

Unconventional properties of non-centrosymmetric superconductors

Von der Fakultät Mathematik und Physik der Universität Stuttgart
zur Erlangung der Würde eines Doktors der Naturwissenschaften
(Dr. rer. nat.) genehmigte Abhandlung

Vorgelegt von

Ludwig Klam

aus Heidenheim an der Brenz

Hauptberichter:	Prof. Dr. Walter Metzner
Mitberichter:	Prof. Dr. Alejandro Muramatsu
Mitberichter:	PD Dr. Dirk Manske
Tag der mündlichen Prüfung:	28. Oktober 2010

Max-Planck-Institut für Festkörperforschung
Stuttgart, 2010

Contents

1	Introduction	15
1.1	Antisymmetric spin–orbit coupling in NCS	18
1.2	Phenomenological theory of Cooper–pairing	21
2	Response and transport in the presence of ASOC	23
2.1	Introduction	23
2.2	Derivation of the transport equations	24
2.3	Solution by Bogoliubov transformation	28
2.4	Gauge invariance	34
2.5	Applications	36
2.5.1	Normal and superfluid density	36
2.5.2	Specific heat capacity	38
2.6	Summary	39
3	New gauge modes	41
3.1	Introduction	41
3.2	Role of phase fluctuations	42
3.3	Results for the gauge modes in NCS	45
3.4	Summary and discussion	48
4	Theory of Raman response	51
4.1	Introduction	52
4.2	Raman vertices and pure triplet response	54
4.3	Mixed–parity results: determination of the singlet–triplet ratio	56
4.4	Summary	65
5	Dynamical spin and charge responses in CePt₃Si	67
5.1	Introduction	67
5.2	Spin–susceptibility with ASOC	68
5.3	Role of band structure in CePt ₃ Si	72
5.3.1	Tight–binding model and DoS	73
5.3.2	Fermi surface nesting	77
5.4	Results	81
5.4.1	Inelastic neutron scattering	81
5.4.2	Consequences for the Cooper–pairing	85

5.4.3	Kohn anomalies in CePt ₃ Si	91
5.5	Summary	97
6	Summary	99
A	Small q–expansion	103
B	Derivation of the Raman vertices	107
C	Tight–binding fit	113
D	Algorithms to calculate the DoS and susceptibility	119
D.1	Numerical convolution	121
D.2	Trilinear interpolation	124
D.3	DoS in 3D	125
	Acknowledgments	139
	Curriculum vitae	141

List of Figures

1.1	Crystal and magnetic structure of CePt ₃ Si	16
1.2	Spin–orbit coupling for tetragonal and cubic point group	19
1.3	Phase diagram of the phenomenological theory	21
3.1	Gauge modes in NCS	46
3.2	Slope of the gauge modes in NCS	48
4.1	Raman spectra for a pure triplet order parameter	55
4.2	Raman spectra for the point group C_{4v}	57
4.3	Power laws for the Raman response on Δ_- of the point group C_{4v}	59
4.4	Power laws for the Raman response on Δ_+ of the point group C_{4v}	59
4.5	Raman spectra for E and T ₂ symmetry of the point group O	62
4.6	Raman spectra for A ₁ symmetry of the point group O	63
4.7	Area on the Fermi–surface that contributes to the triplet Raman response	64
5.1	Brillouin zone for CePt ₃ Si	73
5.2	Tight–binding fit to the LDA band structure of CePt ₃ Si	74
5.3	Fermi surfaces of CePt ₃ Si	75
5.4	Band structure model with spin–orbit coupling for CePt ₃ Si	76
5.5	Cuts through the β band of CePt ₃ Si	76
5.6	Density of states for CePt ₃ Si	77
5.7	Nesting function band of CePt ₃ Si	78
5.8	Nesting vectors for the β band of CePt ₃ Si	79
5.9	Real part of the susceptibility for the β band of CePt ₃ Si	80
5.10	Calculated INS along q_z for CePt ₃ Si	82
5.11	Calculated INS spectra for CePt ₃ Si	84
5.12	Pairing interaction for the singlet channel in CePt ₃ Si	86
5.13	Pairing interaction for the triplet channel in CePt ₃ Si	87
5.14	Projections of superconducting pairing states on the β band of CePt ₃ Si	89
5.15	Important nesting vector for the pairing interaction in CePt ₃ Si	90
5.16	Feynman diagram for Kohn anomalies	91
5.17	RPA enhancement of $\Re\chi_0$ for CePt ₃ Si along ΓZ	93
5.18	Phonon dispersion for CePt ₃ Si	94
5.19	Kohn anomalies for the β band of CePt ₃ Si along ΓZ	95
5.20	Kohn anomalies for the β band of CePt ₃ Si along ΓX	95
5.21	Kohn anomalies for the β band of CePt ₃ Si along ΓM	96

List of Figures

D.1	Schematic data flow of the susceptibility algorithm	120
D.2	Data alignment for a symmetric convolution	123
D.3	Data alignment for an antisymmetric convolution	124

List of Tables

2.1	External perturbations	25
B.1	Raman vertices for $\mathcal{G} = C_{4v}$	111
B.2	Raman vertices for $\mathcal{G} = O$	112

Acronyms

ABM	Anderson–Brinkman–Morel
AFM	Antiferromagnetism
ARPES	Angle-resolved photoemission spectroscopy
ASOC	Antisymmetric spin–orbit coupling
BCS	Bardeen–Cooper–Schrieffer
BQP	Bogoliubov quasiparticle
BW	Balian–Werthamer
DCT	Discrete cosine transformation
DFT	Density functional theory
DoS	Density of states
DST	Discrete sine transformation
INS	Inelastic neutron scattering
LDA	Local-density approximation
MKE	Matrix–kinetic equation
NCS	Non–centrosymmetric superconductors
pha	Particle–hole asymmetric
RPA	Random phase approximation
SBSOS	Spontaneously broken spin orbit symmetry
SOC	Spin–orbit coupling

Zusammenfassung

Eine kinetische Theorie für nicht-inversionssymmetrische Supraleiter (NCS) wird im reinen Grenzfall und für tiefe Temperaturen formuliert. Die Transportgleichungen wurden ganz allgemein für beliebige antisymmetrische Spin-Bahn-Kopplung (ASOC) und in einem erweiterten Impuls- und Frequenz-Bereich gelöst. Es ergibt sich eine Teilchen-Loch-symmetrische, eichinvariante und ladungserhaltende Beschreibung, mit deren Hilfe der Strom-Response, die spezifische Wärmekapazität und der Raman-Response berechnet wird. Eine detaillierte Betrachtung der Eichinvarianz und der dazugehörigen Phasenfluktuationen des supraleitenden Ordnungsparameters offenbart zwei Eichmoden: Einerseits die Anderson-Bogoliubov Mode und andererseits eine neue Eichmode, die stark von der Symmetrie der ASOC abhängt.

Als Anwendung der kinetischen Theorie wird der polarisationsabhängige elektronische Raman-Response für $T = 0$ in zwei wichtigen Gruppen von NCS erforscht, die sich nach der ASOC klassifizieren lassen. Vertreter dieser beiden Gruppen sind CePt_3Si und $\text{Li}_2\text{Pd}_x\text{Pt}_{3-x}\text{B}$. Für die Raman-Vertices werden analytische Ausdrücke hergeleitet und Potenzgesetze im Frequenzbereich sowie die Paarbrechungs-Peaks berechnet. Eine charakteristische Doppelpeak-Struktur wird für NCS vorhergesagt, die dazu dienen kann das unbekanntes Verhältnis der Spin-Singulett- und Triplett-Komponente im supraleitenden Ordnungsparameter zu bestimmen.

Um die dynamische Spin- und Ladungs-Suszeptibilität von CePt_3Si für eine itinerante Beschreibung von Elektronen zu berechnen wird eine effiziente numerische Methode vorgestellt. Mithilfe einer realistischen Parametrisierung der Bandstruktur werden die Nesting-Funktion, Wirkungsquerschnitte für inelastische Neutronenstreuung und Kohn-Anomalien für ein ausgewähltes Band im nichtmagnetischen Normalzustand berechnet. Ausgehend von der Spin- und Ladungs-Suszeptibilität wird eine supraleitende Paarwechselwirkung für eine Gap-Gleichung in schwacher Kopplung konstruiert. Eine Vorzeichenbetrachtung der entkoppelten Gap-Gleichung stützt die experimentellen Hinweise für einen starken Triplett-Beitrag im Ordnungsparameter von CePt_3Si . Speziell für diese Verbindung kann man zeigen, dass eine zunehmende Rashba-artige Spin-Bahn-Kopplung den Triplett-Beitrag stärkt.

Abstract

A kinetic theory for non-centrosymmetric superconductors (NCS) is formulated for low temperatures and in the clean limit. The transport equations are solved quite generally for any kind of antisymmetric spin-orbit coupling (ASOC) in an extended momentum and frequency range. The result is a particle-hole symmetric, gauge-invariant and charge conserving description, which is used to calculate the current response, the specific heat capacity, and the Raman response function. A detailed analysis of the gauge invariance and the associated phase fluctuations of the superconducting order parameter revealed two gauge modes: the Anderson-Bogoliubov mode on the one side and a new gauge mode on the other side, which strongly depends on the symmetry of the ASOC.

As application of the kinetic theory, the polarization-dependence of the $T = 0$ electronic Raman response in NCS is studied for two important classes of ASOC with the representative systems CePt_3Si and $\text{Li}_2\text{Pd}_x\text{Pt}_{3-x}\text{B}$. Analytical expressions for the Raman vertices are derived, and the frequency power laws and pair-breaking peaks are calculated. A characteristic two-peak structure is predicted for NCS and might serve as an indicator for the unknown relative magnitude of the singlet and triplet contributions to the superconducting order parameter.

An efficient numerical method is introduced in order to calculate the dynamical spin and charge response of CePt_3Si , using an itinerant description for the electrons. With a realistic parameterization of the band structure, the nesting function, inelastic neutron scattering cross sections, and Kohn anomalies are calculated for a selected band in the normal non-magnetic state. From the spin and charge susceptibility, a superconducting pairing interaction is constructed for the weak-coupling gap equation. A sign analysis of the decoupled gap equation supports the experimental evidence of a strong triplet contribution to the order parameter in CePt_3Si . In particular for this compound, it can be shown that an increasing Rashba-type of spin-orbit coupling strengthens the triplet contribution.

1 Introduction

Triplet superconductors are by far more exciting and interesting than singlet superconductors, because they open a new degree of freedom: the spin. Unfortunately there are very few examples of confirmed spin triplet superconductors. According to Anderson's theorem [1] a necessary precondition for triplet superconductivity is time reversal symmetry and, in addition, the existence of an inversion center. In brief, Anderson's argument reads as follows: For singlet superconductors the Cooper pairs are made up of electrons with $|\mathbf{k}, \uparrow\rangle$ and $|\mathbf{-k}, \downarrow\rangle$. If, for example, an applied magnetic field lifts the degeneracy between these two states, superconductivity breaks down. Since time reversal symmetry T connects both states through $T|\mathbf{k}, \uparrow\rangle = |\mathbf{-k}, \downarrow\rangle$, this symmetry is necessary for singlet superconductors. Analogously, for triplet superconductors the states $|\mathbf{k}, \uparrow\rangle$, $|\mathbf{-k}, \uparrow\rangle$, $|\mathbf{k}, \downarrow\rangle$ and $|\mathbf{-k}, \downarrow\rangle$ have to be degenerate. This can only be achieved, when an inversion symmetry I is additionally present, since $I|\mathbf{k}, \uparrow\rangle = |\mathbf{-k}, \uparrow\rangle$. Thus, a combination of T and I connects all of these four states. Triplet superconductivity can occur only if these two requirements are fulfilled.

Based on this argument, the discovery of bulk superconductivity in CePt_3Si without inversion symmetry by Bauer *et al.* (2004) [2] seemed quite surprising and attracted great interest, since signatures of a singlet as well as a triplet order parameter were observed in different response and transport measurements [3]. The resolution of this contradiction was pointed out by Frigeri *et al.* [4, 5, 6]: The absence of an inversion center in the crystal structure gives rise to an antisymmetric spin-orbit coupling (ASOC), which invalidates the classification of the superconducting order parameter with respect to spin singlet/even parity and spin triplet/odd parity. Thus, a linear combination of a singlet and triplet component to the gap is, in general, possible for non-centrosymmetric superconductors (NCS).

Even today CePt_3Si is one of the most studied NCS and the symmetry components of the order parameter is still under debate, especially the ratio between the singlet and triplet components to the gap. For example, Chapter 5 will deal with an itinerant model of CePt_3Si , therefore I wish to give a brief summary about the experimental work on this compound. The crystal structure of CePt_3Si is tetragonal and belongs to the space group $P4mm$ with the generating point group C_{4v} and five atoms in one unit cell. This point group has a fourfold symmetry along the c -axes but no mirror plane perpendicular to this axes, which breaks the inversion symmetry. Furthermore, antiferromagnetic order sets in at $T_N \approx 2.2K$ followed by heavy fermion superconductivity below $T_c \approx 0.75K$. The staggered antiferromagnetic order was studied by neutron scattering experiments in Ref. [7] and the result is displayed in Fig. 1.1 together with the crystal structure.

In the superconducting phase, the high critical upper field $H_{c2}(0) \simeq 5T$ exceeds by far the Pauli paramagnetic limiting field and thus indicates spin-triplet superconductivity. Muon-spin rotation seems to confirm the microscopic coexistence of magnetism with a small magnetic moment of about $0.16\mu_B/\text{Ce}$ and superconductivity [7, 8, 9]. First measurements for polycrystal

1 Introduction

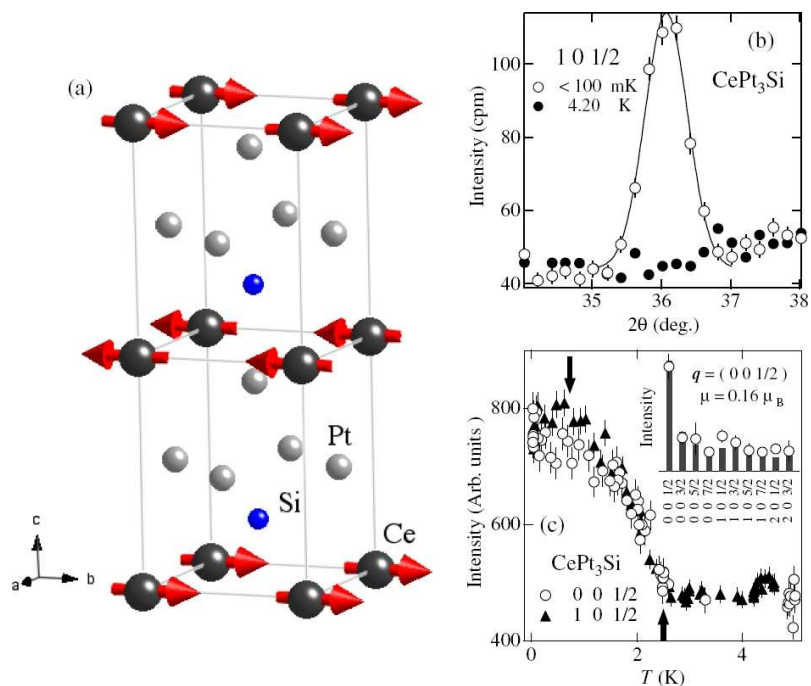


Figure 1.1: Magnetic structure of CePt₃Si as determined from neutron scattering experiments by Metoki *et al.* [7]. (a) Crystal and magnetic structure of CePt₃Si. The red arrows on the Ce atoms represent the magnetic moments which are oriented along the a–b–plane in an unspecific direction but antiferromagnetically staggered. (b) The antiferromagnetic Bragg reflection at (1 0 1/2). (c) The intensity of the magnetic reflection as a function of temperature.

samples on the spin–lattice relaxation rate showed a clear Hebel–Slichter peak, which is usually an indication for spin singlet superconductivity. However, Mukuda *et al.* [10] claim in an NMR study on a single crystal, that the singlet contribution to the order parameter is due to a contamination of pure singlet domains, because the single crystal sample showed no Hebel–Slichter peak. The pressure phase diagram shows that the SC phase is not entirely enclosed in the antiferromagnetic regime [11, 12, 13]. Substituting Si by Ge extends this phase diagram also to negative chemical pressures [14]. Response and transport measurements can serve to identify the symmetry of the underlying order parameter. Among these the London penetration depth [15], thermal conductivity [16] and magnetic relaxation rate $1/T_1T$ of Pt [17, 18] indicate line nodes in the order parameter. Specific heat measurements suggest that there might be two superconducting phase transitions [19], however, these experimental results can be explained by inhomogeneous local pressure [20].

Apart from CePt₃Si, many other exciting NCS have been found meanwhile. Li₂Pd_xPt_{3–x}B [21] compounds are of strong interest because of the tunable concentration of the heavier platinum, which seems to affect the strength of the triplet contribution to the order parameter [22, 23]. Because of this adjustable strength of the ASOC, larger $T_c = 2K - 8K$ [24, 25], absence of

magnetic order and different point group O [26], this NCS will also be of special interest in Chapter 4. Furthermore, UIr is a quite unusual NCS because superconductivity exists inside a ferromagnetic phase [27, 13, 28, 29]. Time reversal symmetry is also broken in LaNiC_2 [30, 31] but without showing any magnetic order [32, 33]. In addition, $\text{Mg}_{10}\text{Ir}_{19}\text{B}_{16}$ might be interesting because of a possible triplet component in the order parameter for certain allowed stoichiometries [34, 35, 36]. The compounds Ln_2C_3 ($\text{Ln}=\text{La}, \text{Y}$) [37, 38] and KO_2O_6 [39] are promising candidates for further investigations, because of the underlying tetrahedral symmetry [40]. There exists also a whole family of NCS with the elemental formula AMSi_3 [41, 42, 43, 44, 45] with $\text{A}=\text{Ca}, \text{Sr}, \text{Ba}$ and $\text{M}=\text{Co}, \text{Rh}, \text{Ir}, \text{Ni}, \text{Pd}, \text{Pt}$ and many other NCS which can be explained within a BCS-like theory as Rh_2Ga_9 , Ir_2Ga_9 [46] and Re_2W [47], to mention only a few examples.

Theoretical work on NCS started directly after the discovery of CePt_3Si with symmetry considerations about the superconducting order parameter and phenomenological models [5, 6, 48, 40]. A lot of work has been done on the (static) spin-susceptibility in NCS [4, 49] as well as attempts of a microscopic pairing theory based on such calculations [50, 51, 52]. Another important issue is impurity scattering and how it affects the superconducting state [53, 54, 55]. Furthermore, Andreev reflection and surface bound states have been addressed in Ref. [56, 57, 58, 59]. Of particular theoretical interest in CePt_3Si as well as in $\text{Li}_2\text{Pt}_3\text{B}$ are unusual Vortex effects [60, 61, 62]. Finally topologically protected states are also an interesting field of research in NCS [63, 64].

Nevertheless, there are still unexplored topics and a lot of exciting open questions about NCS. In particular many response and transport properties in the presence of the involved antisymmetric spin-orbit coupling (ASOC) remain unknown. In this thesis I want to address this issue on different levels: a generalized theory which provides expressions for various response and transport functions in a comprehensive, systematic way, and material specific results. For example, one open question concerns the gauge modes, which are of special theoretical interest, and their dispersion in NCS. Furthermore, I emphasized on the electronic Raman response and how it is affected by the ASOC. Another important issue in NCS is the triplet-singlet ratio of the superconducting order parameter. Despite many efforts and different suggestions to determine this ratio in NCS [65, 57, 58], it remains still unknown for the most interesting compounds. Hence, are there alternatives to determine the triplet-singlet ratio? Apart from that, it is commonly argued that an increasing strength of the ASOC leads to a larger triplet component in the order parameter (see publications on $\text{Li}_2\text{Pd}_x\text{Pt}_{3-x}\text{B}$). Can this assumption be justified? One main objective of this thesis is also an improved material specific description, in particular for CePt_3Si . Published theoretical work on NCS is restricted to simple band structure models and to static calculations, for instance, of the spin susceptibility. Thus, one may ask to what extent it is possible to describe the properties of CePt_3Si within an itinerant model and whether Fermi surface nesting supports the antiferromagnetic state. Using such a model, the goal is to calculate explicitly inelastic neutron scattering cross sections and Kohn anomalies with special attention to the effect of the ASOC. Finally, such a model should allow a discussion of the microscopic pairing mechanism for superconductivity and of the triplet-singlet ratio in CePt_3Si .

This thesis is organized as follows. In the subsequent sections of this introduction, I will define the model including the antisymmetric spin-orbit coupling (ASOC) and refer to the work done before to solve the phenomenological superconducting gap equation for NCS. Chapter 2 deals with a generalized description of response and transport in NCS. Here, a set of kinetic equations

1 Introduction

at low temperatures in the clean limit is derived, and the equations are solved analytically. Special emphasis will be placed on the gauge invariance of this theory in Section 2.4. The applications, discussed in Section 2.5 concern the static and homogenous limit of the normal and superfluid density and the specific heat capacity. These are brief examples for the validity of this kinetic theory. The subsequent Chapters 3 and 4 will both use the formalism established in Chapter 2. In Chapter 3, I will analyze in detail the role of the phase fluctuations of the order parameter in NCS and add the proof for the gauge invariance of the kinetic theory in Chapter 2. Based on the expression for the phase fluctuations, I will present analytical results in Section 3.3 for the dispersion of the gauge modes in NCS. Chapter 4 is an application of this gauge invariant kinetic theory. I will analyze the electronic Raman response for two important classes of ASOC. To this end, the corresponding Raman vertices are first derived in Section 4.2. Based on this, I will present the mixed-parity results, which may be used to determine the unknown singlet-triplet ratio in NCS (4.3). The last part of this thesis, Chapter 5, uses a Green's function approach to calculate the spin and charge responses for CePt₃Si. While the previous chapters contain mainly analytical results, Section 5.2 introduces a numerical method to calculate the material specific dynamical spin and charge susceptibilities. In this connection, I will present a band structure model for CePt₃Si in Section 5.3, including an evaluation of the density of states and the Fermi surface nesting. The results for the dynamical spin and charge susceptibilities will be used in Section 5.4 in order to present three applications with special emphasis on a comparison of the results with and without an ASOC. In Section 5.4.1, I calculate inelastic neutron scattering cross sections. Section 5.4.2 discusses the consequences for possible pairing scenarios based on a pairing interaction mediated by spin fluctuations. Third, I examine Kohn anomalies (Section 5.4.3) in CePt₃Si. Finally, in Chapter 6 one may find the conclusions drawn from the main results.

1.1 Antisymmetric spin-orbit coupling in NCS

The peculiarity of non-centrosymmetric crystal structures is the presence of an antisymmetric spin-orbit coupling (ASOC) ¹, which has many impacts on the electronic structure and the superconducting order parameter. The starting point is a model Hamiltonian for noninteracting electrons in a non-centrosymmetric crystal [53]

$$\hat{H} = \sum_{\mathbf{k}\sigma\sigma'} \hat{c}_{\mathbf{k}\sigma}^\dagger [\xi_{\mathbf{k}}\delta_{\sigma\sigma'} + \boldsymbol{\gamma}_{\mathbf{k}} \cdot \boldsymbol{\tau}_{\sigma\sigma'}] \hat{c}_{\mathbf{k}\sigma'} , \quad (1.1)$$

where $\xi_{\mathbf{k}}$ represents the bare band dispersion assuming time reversal symmetry ($\xi_{-\mathbf{k}} = \xi_{\mathbf{k}}$), $\sigma, \sigma' = \uparrow, \downarrow$ label the spin state, and $\boldsymbol{\tau}$ are the Pauli matrices. The second term describes an ASOC with a (vectorial) coupling constant $\boldsymbol{\gamma}_{\mathbf{k}}$. The pseudovector function $\boldsymbol{\gamma}_{\mathbf{k}}$ has the following symmetry properties: $\boldsymbol{\gamma}_{-\mathbf{k}} = -\boldsymbol{\gamma}_{\mathbf{k}}$ and $g\boldsymbol{\gamma}_{g^{-1}\mathbf{k}} = \boldsymbol{\gamma}_{\mathbf{k}}$ [66]. Here g denotes any symmetry operation of the point group \mathcal{G} of the crystal under consideration. In particular, I am interested in the tetragonal point group C_{4v} (applicable to the heavy Fermion compound CePt₃Si with $T_c=0.75$ K [2], for example) and the cubic point group O (applicable to the system Li₂Pd_{*x*}Pt_{3-*x*}B with $T_c=2.2-2.8$ K

¹See Ref. [4, 53] for a detailed derivation of the ASOC.

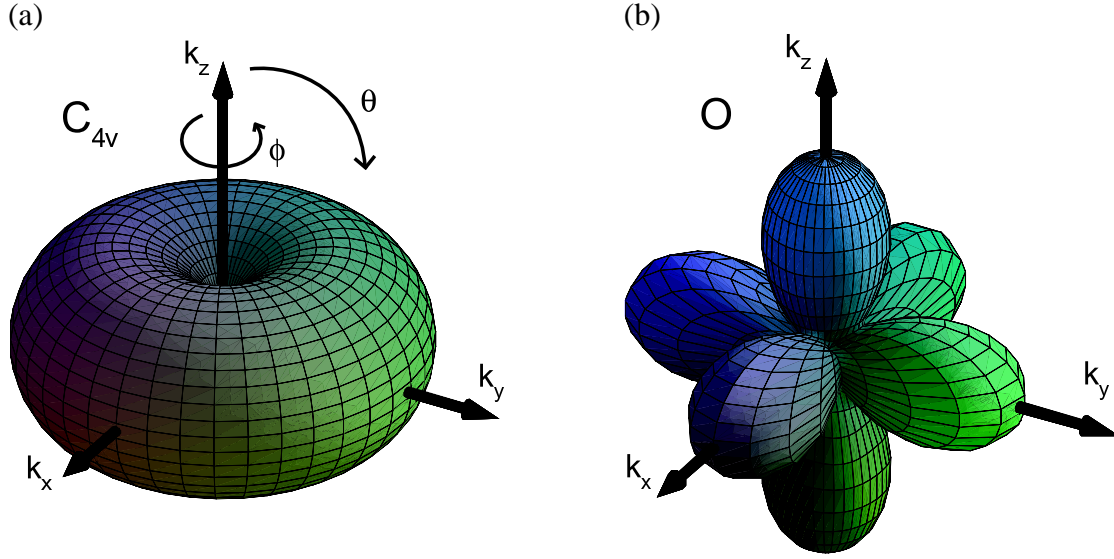


Figure 1.2: Spherical plots of the angular dependence of $|\gamma_{\mathbf{k}}|$ for the point groups C_{4v} (a) and O (b). Since $\mathbf{d}_{\mathbf{k}} \parallel \gamma_{\mathbf{k}}$, these plots show also the magnitude of the gap function in the pure triplet case for both point groups.

for $x=0$ and $T_c=7.2\text{--}8$ K for $x=3$ [21])². An overview for all non-centrosymmetric point groups and their $\gamma_{\mathbf{k}}$ -vectors is presented in Ref. [66]. For $\mathcal{G} = C_{4v}$ the ASOC reads [4, 53]

$$\gamma_{\mathbf{k}} = g_{\perp}(\hat{\mathbf{k}} \times \hat{\mathbf{e}}_z) + g_{\parallel} \hat{k}_x \hat{k}_y \hat{k}_z (\hat{k}_x^2 - \hat{k}_y^2) \hat{\mathbf{e}}_z. \quad (1.2)$$

In the purely two-dimensional case ($g_{\parallel} = 0$) one recovers the so-called Rashba interaction [67, 68, 69]. I choose $g_{\parallel} = 0$ for this thesis in the absence of any experimental or theoretical estimation of this coefficient. For the cubic point group $\mathcal{G} = O$, $\gamma_{\mathbf{k}}$ reads [65]

$$\gamma_{\mathbf{k}} = g_1 \hat{\mathbf{k}} - g_3 \left[\hat{k}_x (\hat{k}_y^2 + \hat{k}_z^2) \hat{\mathbf{e}}_x + \hat{k}_y (\hat{k}_z^2 + \hat{k}_x^2) \hat{\mathbf{e}}_y + \hat{k}_z (\hat{k}_x^2 + \hat{k}_y^2) \hat{\mathbf{e}}_z \right], \quad (1.3)$$

where the ratio $g_3/g_1 \simeq 3/2$ is estimated by Ref. [65]. Because of the larger prefactor $g_3 > g_1$, I will keep the higher order term for all further considerations. Thus, in terms of spherical angles, $\hat{\mathbf{k}} = (\cos \phi \sin \theta, \sin \phi \sin \theta, \cos \theta)$, the angular dependence of $|\gamma_{\mathbf{k}}|$ for both point groups, illustrated in Fig. 1.2, reads

$$|\gamma_{\mathbf{k}}| \propto \sin \theta \quad \text{for } C_{4v} \quad (1.4)$$

$$|\gamma_{\mathbf{k}}| \propto \sqrt{1 - \frac{15}{16} \sin^2 2\theta - \frac{3}{16} \sin^4 \theta \sin^2 2\phi (9 \sin^2 \theta - 4)} \quad \text{for } O \quad (1.5)$$

²Point groups will be labeled in Schönflies notation.

1 Introduction

where $g_3/g_1 = 3/2$ is used. Further, it is convenient to define

$$\hat{\gamma}_{\mathbf{k}} = \frac{\gamma_{\mathbf{k}}}{\sqrt{\langle |\gamma_{\mathbf{k}}|^2 \rangle_{FS}}} . \quad (1.6)$$

By diagonalizing the Hamiltonian [Eq. (1.1)], one finds the eigenvalues $\xi_{\lambda}(\mathbf{k}) = \xi_{\mathbf{k}} + \lambda|\gamma_{\mathbf{k}}|$, which physically corresponds to the lifting of the Kramers degeneracy between the two spin states at a given \mathbf{k} in the presence of ASOC. The basis in which the band is diagonal can be referred to as the *band basis* where the Fermi surface defined by $\xi_{\pm}(\mathbf{k}) = 0$ is split into two pieces labeled \pm . Sigrist and co-workers have shown that the presence of the ASOC generally allows for an admixture of a spin-triplet component to the otherwise spin-singlet pairing gap [5]. This implies that one may write down the following ansatz for the energy gap matrix in spin space:

$$\Delta_{\sigma\sigma'}(\mathbf{k}) = \{[\psi_{\mathbf{k}}(T)\mathbf{1} + \mathbf{d}_{\mathbf{k}}(T) \cdot \boldsymbol{\tau}]i\tau^y\}_{\sigma\sigma'} , \quad (1.7)$$

where $\psi_{\mathbf{k}}(T)$ and $\mathbf{d}_{\mathbf{k}}(T)$ reflect the singlet and triplet part of the pair potential, respectively. In the band basis one finds immediately

$$\Delta_{\pm}(\mathbf{k}) = \psi_{\mathbf{k}}(T) \pm |\mathbf{d}_{\mathbf{k}}(T)| . \quad (1.8)$$

It has been demonstrated that a large ASOC compared to $k_{\text{B}}T_c$ is not destructive for triplet pairing if one assumes $\mathbf{d}_{\mathbf{k}} \parallel \gamma_{\mathbf{k}}$ [5, 40]:

$$\mathbf{d}_{\mathbf{k}}(T) = d(T)\hat{\gamma}_{\mathbf{k}} , \quad (1.9)$$

where the temperature-dependent magnitudes $\psi(T)$ and $d(T)$ of the spin-singlet and triplet energy gaps are solutions of coupled self-consistency equations. Thus, the energy gap in Eq. (1.8) can be written as:

$$\Delta_{\pm}(\mathbf{k}) = \psi(T) \pm d(T)|\hat{\gamma}_{\mathbf{k}}| . \quad (1.10)$$

For the $T = 0$ Raman response in Chapter 4 I will use the following ansatz for the gap function on both bands (+ and -) [48]:

$$\Delta_{\pm}(\mathbf{k}) = \psi \pm d|\gamma_{\mathbf{k}}| = \psi(1 \pm p|\gamma_{\mathbf{k}}|) \equiv \Delta_{\pm} , \quad (1.11)$$

where the parameter $p = d/\psi$ represents the unknown triplet-singlet ratio. For brevity the argument \mathbf{k} is omitted, especially in lengthy expressions. Accordingly, the Bogoliubov-quasiparticle dispersion is given by $E_{\pm}^2(\mathbf{k}) = \xi_{\pm}^2(\mathbf{k}) + \Delta_{\pm}^2(\mathbf{k})$. If one assumes no \mathbf{q} -dependence of the order parameter, $\Delta_{\lambda}(\mathbf{k})$ [and also $E_{\lambda}(\mathbf{k})$] is of even parity i.e. $\Delta_{\lambda}(-\mathbf{k}) = \Delta_{\lambda}(\mathbf{k})$. It is quite remarkable that although the spin representation of the order parameter $\Delta_{\sigma\sigma'}(\mathbf{k})$ does not have well-defined parity w.r.t. $\mathbf{k} \rightarrow -\mathbf{k}$, as easily seen in Eq. (1.7), the energy gap in band representation does. Note that for $\text{Li}_2\text{Pd}_x\text{Pt}_{3-x}\text{B}$ the parameter p seems to be directly related to the substitution of platinum by palladium, since the larger spin-orbit coupling of the heavier platinum is expected to enhance the triplet contribution [22]. This seems to be confirmed by penetration depth experiments [70, 65].

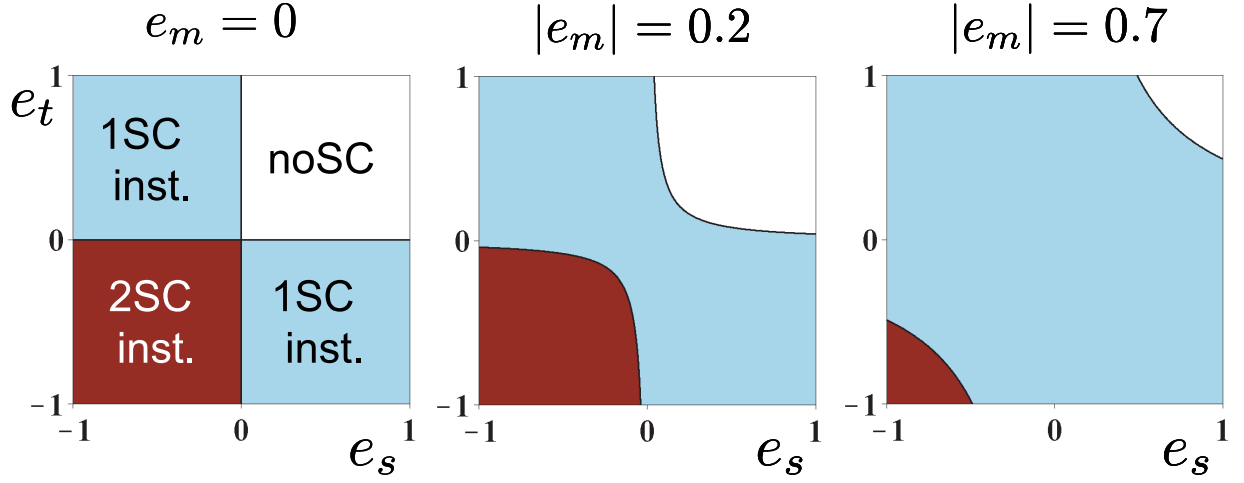


Figure 1.3: Phase diagram for different strength of the singlet (e_s), triplet (e_t) and mixing (e_m) contribution to the pairing interaction. The white, cyan and red areas display no superconductivity, one or two superconducting instabilities, respectively.

1.2 Phenomenological theory of Cooper–pairing

As a first step towards a microscopic description, I explored possible solutions of the gap equation for NCS following the arguments of Frigeri *et al.* [48]. For this purpose one has to perform an unitary transformation to the helicity or band basis, which will be explained in detail in Chapter 2 and also in Chapter 5. The self–consistent gap equation then reads

$$\Delta(\mathbf{k}) = -k_B T \int \frac{d\mathbf{k}'}{(2\pi)^3} \sum_{i\omega_n} \mathbf{V}(\mathbf{k}, \mathbf{k}') \mathbf{F}(\mathbf{k}', i\omega_n) \quad (1.12)$$

in terms of the anomalous Green's functions

$$F_\lambda(\mathbf{k}, i\omega_n) = \frac{\Delta_\pm(\mathbf{k})}{\omega_n^2 + |\Delta_\pm(\mathbf{k})|^2 + \xi_\pm^2(\mathbf{k})}, \quad (1.13)$$

where $\Delta(\mathbf{k}) = (\Delta_+, \Delta_-)$ is the two component order parameter and $\mathbf{F}(\mathbf{k}', i\omega_n)$ denotes the anomalous Green's function, both in the band basis. Performing the Matsubara frequency sum, the weak–coupling gap Equation (1.12) for NCS reads

$$\Delta_\lambda(\mathbf{k}, T) = - \sum_{\mathbf{k}', \mu} V_{\mathbf{k}\mathbf{k}'}^{\lambda\mu} \Delta_\mu(\mathbf{k}', T) \theta_\mu(\mathbf{k}') \quad (1.14)$$

with

$$\theta_\lambda(\mathbf{k}) = \frac{1}{2E_\lambda(\mathbf{k})} \tanh \frac{E_\lambda(\mathbf{k})}{2k_B T}. \quad (1.15)$$

1 Introduction

This gap equation represents an eigenvalue problem which can be solved analytically for a phenomenological pairing interaction that can be parameterized as follows (extensively discussed in Ref. [48]):

$$\begin{aligned} \mathbf{V}(\mathbf{k}, \mathbf{k}') = & \frac{V}{2} [(e_s + e_t |\gamma_{\mathbf{k}}| |\gamma_{\mathbf{k}'}|) \boldsymbol{\sigma}_0 + (e_s - e_t |\gamma_{\mathbf{k}}| |\gamma_{\mathbf{k}'}|) \boldsymbol{\sigma}_x \\ & - e_m (|\gamma_{\mathbf{k}}| + |\gamma_{\mathbf{k}'}|) \boldsymbol{\sigma}_z - i e_m (|\gamma_{\mathbf{k}}| - |\gamma_{\mathbf{k}'}|) \boldsymbol{\sigma}_y] . \end{aligned} \quad (1.16)$$

Here e_s , e_t , e_m denote the singlet, triplet and mixed parity contribution to the pairing interaction, respectively³. In this ansatz, the singlet contribution is constant and the triplet contribution is proportional to $|\gamma_{\mathbf{k}}| |\gamma_{\mathbf{k}'}|$, where the vector function $\gamma_{\mathbf{k}}$ arises from the antisymmetric spin-orbit coupling defined in the previous section. Fig. 1.3 displays an alternative representation of Frigeri's results (see Ref. [48]). Since the gap equation for NCS is in general a 2×2 matrix equation (for Δ_+ , Δ_- or alternatively for the singlet and triplet contribution to the gap), one expects up to two superconducting instabilities. As usual, a negative contribution to the pairing interaction is attractive and a positive contribution repulsive. Thus, superconducting states with a large singlet contribution are located on the upper left corner of the phase diagram and triplet states can be found predominantly on the lower right corner. Mixed parity states are close to the diagonal. Depending on the three parameters, the gap equation has either no solution (white area) or reveals one (cyan area) or two superconducting instabilities (red area). If the mixing term e_m increases, one mainly finds a single superconducting transition and the possibility of zero or two instabilities is suppressed. Interestingly, the phase diagram depends only on the absolute value of the mixing term. As mentioned previously, it is still unclear from (specific heat) experiments, whether CePt₃Si displays one or two superconducting instabilities. From the theoretical point of view, both possibilities can exist. However, most evidence (strong triplet contribution from various response and transport measurements combined with the larger phase space in Fig. 1.3) points towards only one superconducting transition.

In Chapter 2 and 3 I will use the phenomenological pairing interaction of Eq. (1.16) with $e_m = 0$ in the parameter space with one superconducting instability (see Fig. 1.3). In this case, the separable ansatz for the pairing interaction reads

$$V_{\mathbf{k}\mathbf{k}'}^{\lambda\mu} = \Gamma_s + \lambda\mu\Gamma_t |\hat{\gamma}_{\mathbf{k}}| |\hat{\gamma}_{\mathbf{k}'}| , \quad (1.17)$$

where Γ_s and Γ_t represent the singlet and triplet contributions, respectively. With this choice, it is possible to proceed analytically and to demonstrate the gauge invariance of the kinetic theory in Chapter 2 and to calculate the properties of the gauge modes in NCS (Chapter 3). In Chapter 5 and in particular in Section 5.4.2, the pairing interaction will be justified by a microscopic model involving spin fluctuations.

³It can be shown that the Dzyaloshinskii–Moriya interaction contributes to the mixing term e_m , see e.g. Ref. [48].

2 Response and transport in the presence of ASOC

In this chapter, I formulate a kinetic theory for non-centrosymmetric superconductors at low temperatures in the clean limit. The transport equations are solved quite generally in spin- and particle-hole (Nambu) space by performing first a transformation into the band basis and second a Bogoliubov transformation into the quasiparticle-quasihole phase space. As a result, I obtain a particle-hole-symmetric, gauge-invariant and charge conserving description, which is valid in the whole quasiclassical regime, i.e. for the transferred momentum $|\mathbf{q}| \ll k_F$ and the frequency $\omega \ll E_F$ of any applied external perturbation¹. As an example, I calculate in the stationary and long-wavelength limit the current response and the specific heat capacity. The Chapter 3 about new gauge modes in NCS and Chapter 4 on electronic Raman scattering in NCS are based on the theoretical framework of this chapter.

2.1 Introduction

The theoretical study of response and transport properties at low temperatures is particularly interesting, since superconductivity in NCS covers a rich variety of different new features and concepts. I will use the framework of a kinetic theory described by a set of generalized Boltzmann equations, which I used successfully before in Ref. [71] to derive various response and transport functions such as the normal and superfluid density, the specific heat capacity, and in particular the electronic Raman response in NCS, which will be examined in an separate chapter.

A few general remarks about the connection between response and transport phenomena are appropriate at this stage. Traditionally, the notion of transport implies that the theoretical description takes into account the effects of quasiparticle scattering processes by a scattering rate Γ . Therefore, I would like to demonstrate with a simple example, how response and transport are intimately connected: consider the density response of normal metal electrons to the presence of the two electromagnetic potentials $\Phi^{\text{ext.}}$ and $\mathbf{A}^{\text{ext.}}$, which generate the gauge-invariant form of the electric field $\mathbf{E} = -\nabla\Phi^{\text{ext.}} - \partial\mathbf{A}/c\partial t$. In Fourier space ($\nabla \rightarrow i\mathbf{q}$, $\partial/\partial t \rightarrow -i\omega$) one may write for the response of the charge density:

$$\delta n_e = e^2 i\mathbf{q} \cdot \mathbf{M}_0(\mathbf{q}, \omega) \cdot \mathbf{E} ,$$

with \mathbf{M}_0 the Lindhard tensor and $\mathbf{q} \cdot \mathbf{M}_0 \cdot \mathbf{q} \equiv M_0$ the Lindhard function, appropriately renor-

¹ $\hbar = 1$ is used in the whole thesis.

2 Response and transport in the presence of ASOC

malized by collision effects [72]:

$$M_0(\mathbf{q}, \omega) = \frac{\mathcal{L}_0(\mathbf{q}, \omega + i\Gamma)}{1 - \frac{i\Gamma}{\omega + i\Gamma} \left[1 - \frac{\mathcal{L}_0(\mathbf{q}, \omega + i\Gamma)}{\mathcal{L}_0(\mathbf{q}, 0)} \right]} .$$

Here $\mathcal{L}_0(\mathbf{q}, \omega)$ denotes the unrenormalized Lindhard function in the collisionless limit $\Gamma \rightarrow 0$:

$$\mathcal{L}_0(\mathbf{q}, \omega) = \frac{1}{V} \sum_{\mathbf{p}\sigma} \frac{n_{\mathbf{p}+\mathbf{q}/2}^0 - n_{\mathbf{p}-\mathbf{q}/2}^0}{\epsilon_{\mathbf{p}+\mathbf{q}/2} - \epsilon_{\mathbf{p}-\mathbf{q}/2} - \omega} .$$

In this definition of the Lindhard function, $n_{\mathbf{k}}^0$ denotes the equilibrium Fermi–Dirac distribution function and $\epsilon_{\mathbf{k}} = \xi_{\mathbf{k}} + \mu$ represents the band structure. Now the aspect of transport comes into play by the observation that $M_0(\mathbf{q}, \omega)$ may be expressed through the full dynamic conductivity tensor $\boldsymbol{\sigma}(\mathbf{q}, \omega) = e^2(\partial n/\partial \mu)\mathbf{D}(\mathbf{q}, \omega)$ of the electron system as follows:

$$M_0(\mathbf{q}, \omega) \equiv \frac{\mathbf{q} \cdot \boldsymbol{\sigma}(\mathbf{q}, \omega) \cdot \mathbf{q}}{i\omega - \mathbf{q} \cdot \mathbf{D}(\mathbf{q}, \omega) \cdot \mathbf{q}/(1 - i\omega\tau)} ,$$

with $\mathbf{q} \cdot \boldsymbol{\sigma} \cdot \mathbf{q} \stackrel{\Gamma \rightarrow 0}{\equiv} i\omega e^2 \mathcal{L}_0(\mathbf{q}, \omega)$ and with the so-called diffusion pole in the denominator of $M_0(\mathbf{q}, \omega)$ reflecting the charge conservation law. This expression for the Lindhard response function M_0 clearly demonstrates the connection between response (represented by M_0 itself) and transport (represented by the conductivity $\boldsymbol{\sigma}$), which can be evaluated both in the clean limit $\Gamma \rightarrow 0$ and in the presence of collisions $\Gamma \neq 0$. In this sense, the notions of response and transport are closely connected and therefore equitable. In this whole chapter I consider the collisionless case.

2.2 Derivation of the transport equations

In this section, I study the linear response of a NCS to an effective external perturbation potential of the form [73, 74]

$$\delta \xi_{\mathbf{k}\sigma\sigma'}^{\text{ext.}} = \left[e\Phi^{\text{ext.}}(\mathbf{q}, \omega) - \frac{e}{c} \mathbf{v}_{\mathbf{k}} \cdot \mathbf{A}^{\text{ext.}}(\mathbf{q}, \omega) + \frac{e^2}{c^2} \mathbf{A}_i^I(\mathbf{q}, \omega) \frac{\partial^2 \epsilon_{\mathbf{k}}}{\partial k_i \partial k_j} \mathbf{A}_j^S(\mathbf{q}, \omega) \right] \delta_{\sigma\sigma'} . \quad (2.1)$$

Here $\Phi^{\text{ext.}}$ and $\mathbf{A}^{\text{ext.}}$ denote the electromagnetic scalar and vector potential. Electronic Raman scattering is described in addition by the third term. Of course, an experiment measures either the electromagnetic response or the Raman response. However, it is elegant and convenient to treat any possible perturbation of a superconductor on equal footing. The last term in Eq. (2.1) describes a Raman process where an incoming photon with vector potential \mathbf{A}^I , polarization $\hat{\mathbf{e}}^I$ and frequency ω_I is scattered off an electronic excitation. The scattered photon with vector potential \mathbf{A}^S , polarization $\hat{\mathbf{e}}^S$ and frequency $\omega_S = \omega_I - \omega$ gives rise to a Raman signal (Stokes process) and creates an electronic excitation with momentum transfer \mathbf{q} . Furthermore, the Raman

Table 2.1: External perturbations can be decomposed into a vertex–function and a potential. The vertex–function is characteristic for each response function and can be classified according to parity (w.r.t. $\mathbf{k} \rightarrow -\mathbf{k}$) and dimension.

vertex	(fictive) potential	parity	dimension	response
$a_{\mathbf{k}}$	$\delta\xi_a$			
e	$\Phi^{\text{ext.}}$	even	scalar	charge and
$e\mathbf{v}_{\mathbf{k}}$	$\mathbf{A}^{\text{ext.}}$	odd	vector	current
$\left(\frac{E_{\lambda}(\mathbf{k})}{T} - \frac{\partial E_{\lambda}(\mathbf{k})}{\partial T}\right)$	δT	even	scalar	specific heat capacity
$m(\mathbf{M}_{\mathbf{k}}^{-1})_{i,j}$	$r_0 A_i^I A_j^S$	even	tensor	Raman

vertex in the so–called effective–mass approximation reads

$$\gamma_{\mathbf{k}}^{(R)} = m \sum_{i,j} \hat{\mathbf{e}}_i^S \frac{\partial^2 \epsilon(\mathbf{k})}{\partial k_i \partial k_j} \hat{\mathbf{e}}_j^I. \quad (2.2)$$

In general, an external perturbation can be decomposed into a vertex function $a_{\mathbf{k}}$ and a related potential $\delta\xi_a$:

$$\delta\xi_{\mathbf{k}}^{\text{ext.}} = \sum_a a_{\mathbf{k}} \delta\xi_a. \quad (2.3)$$

A list of all relevant vertex functions and potentials, that will be discussed in this chapter, is given in Table 2.1. The table is confined to the transport and response functions that I will treat in this thesis, however, it can be extended to contain also other interesting transport properties as, for example, the ultrasound attenuation which is closely related to the Raman response in 2D systems [71]. The charge density response to the electric field $\mathbf{E} = -\nabla\Phi^{\text{ext.}} - \partial\mathbf{A}^{\text{ext.}}/\partial t$ is characterized by a constant vertex $a_{\mathbf{k}} = e$ (electron charge) and thus of even parity (w.r.t. $\mathbf{k} \rightarrow -\mathbf{k}$), whereas the current response to the vector potential $\mathbf{A}^{\text{ext.}}$ depends on the odd vertex–function $a_{\mathbf{k}} = e\mathbf{v}_{\mathbf{k}}$ (electron velocity). In case of the specific heat capacity $C_V(T)$, the role of the fictive potential is played by the temperature change δT , which couples to the energy variable $\xi_{\mathbf{k}}$. For the Raman response, this fictive potential depends essentially on the vector potential and, hence, on the polarization of the incoming and scattered light. The response and transport functions will be obtained as moments of the momentum distribution functions with the corresponding vertex (see Section 2.5.1 and Chapter 4). Whereas the charge, current, and Raman response are related to the momentum distribution function of the electrons, the specific heat capacity is related to the (Bogoliubov) quasiparticles and hence to their distribution function. This will become clear in Section 2.5.2.

In addition to the external perturbation potentials, also molecular potentials can and have to be

2 Response and transport in the presence of ASOC

taken into account, here, within a mean–field approximation:

$$\delta\xi_{\mathbf{k}} = \delta\xi_{\mathbf{k}}^{\text{ext.}} + \sum_{\mathbf{p}\sigma} (f_{\mathbf{k}\mathbf{p}}^s + V_{\mathbf{q}}) \delta n_{\mathbf{p}} = \sum_a a_{\mathbf{k}} \delta\xi_a + V_{\mathbf{q}} \delta n_1 + \sum_{\mathbf{p}\sigma} f_{\mathbf{k}\mathbf{p}}^s \delta n_{\mathbf{p}}. \quad (2.4)$$

The short–range Fermi–liquid interaction $f_{\mathbf{k}\mathbf{p}}^s$ leads to a renormalization of the electron mass [75] and the long–range Coulomb interaction with $V_{\mathbf{q}} = 4\pi e^2/q^2$ is included self–consistently through the macroscopic density fluctuations $\delta n_1 = \sum_{\mathbf{p}\sigma} \delta n_{\mathbf{p}}$ with the non–equilibrium momentum distribution function $\delta n_{\mathbf{p}}$.

The potentials $\delta\xi_{\mathbf{k}}^{\text{ext.}}$ are assumed to vary in time and space $\propto \exp(i\mathbf{q}\cdot\mathbf{r} - i\omega t)$. Then, the response to the perturbation potentials can generally be described by a nonequilibrium momentum distribution function $\underline{n}_{\mathbf{p}\mathbf{p}'}$, which is a matrix in Nambu, momentum and spin space with $\mathbf{p} = \mathbf{k} + \mathbf{q}/2$ and $\mathbf{p}' = \mathbf{k} - \mathbf{q}/2$. The evolution of the nonequilibrium matrix distribution function in time and space is governed by the matrix–kinetic (von Neumann) equation [76, 77]

$$\omega \underline{n}_{\mathbf{p}\mathbf{p}'} + \sum_{\mathbf{p}''} \left[\underline{n}_{\mathbf{p}\mathbf{p}'}, \underline{\xi}_{\mathbf{p}''\mathbf{p}'} \right]_- = 0, \quad (2.5)$$

in which the full quasiparticle energy $\underline{\xi}_{\mathbf{p}\mathbf{p}'}$ plays the role of the Hamiltonian of the system. This equation holds for $\omega \ll E_F$ and $|\mathbf{q}| \ll k_F$. In general, a collision integral (see e.g. Ref. [77]), that accounts for the relaxation of the system into local equilibrium through collisions, could be inserted on the right–hand side of Eq. (2.5). In the following I will work in the collisionless limit². After linearization according to

$$\underline{n}_{\mathbf{p}''\mathbf{p}'} = \underline{n}_{\mathbf{k}}(\mathbf{q}, \omega) = \underline{n}_{\mathbf{k}}^0 \delta_{\mathbf{q},0} + \delta \underline{n}_{\mathbf{k}}(\mathbf{q}, \omega) \quad (2.6)$$

$$\underline{\xi}_{\mathbf{p}''\mathbf{p}'} = \underline{\xi}_{\mathbf{k}}(\mathbf{q}, \omega) = \underline{\xi}_{\mathbf{k}}^0 \delta_{\mathbf{q},0} + \delta \underline{\xi}_{\mathbf{k}}(\mathbf{q}, \omega), \quad (2.7)$$

the matrix–kinetic equation assumes the following form in spin–space:

$$\omega \delta \underline{n}_{\mathbf{k}} + \delta \underline{n}_{\mathbf{k}} \underline{\xi}_{\mathbf{k}-}^0 - \underline{\xi}_{\mathbf{k}+}^0 \delta \underline{n}_{\mathbf{k}} = \delta \underline{\xi}_{\mathbf{k}} \underline{n}_{\mathbf{k}-}^0 - \underline{n}_{\mathbf{k}+}^0 \delta \underline{\xi}_{\mathbf{k}}. \quad (2.8)$$

Here, ω is the frequency and $\mathbf{k}\pm = \mathbf{k}\pm\mathbf{q}/2$, with \mathbf{q} representing the wave number of the external perturbation. The equilibrium distribution function $\underline{n}_{\mathbf{k}}^0$ and quasiparticle energy $\underline{\xi}_{\mathbf{k}}^0$ are matrices in Nambu and spin space:

$$\underline{n}_{\mathbf{k}}^0 = \begin{pmatrix} \mathbf{n}_{\mathbf{k}} & \mathbf{g}_{\mathbf{k}} \\ \mathbf{g}_{\mathbf{k}}^\dagger & \mathbf{1} - \mathbf{n}_{-\mathbf{k}} \end{pmatrix} \quad (2.9)$$

$$\underline{\xi}_{\mathbf{k}}^0 = \begin{pmatrix} \underline{\xi}_{\mathbf{k}} + \gamma_{\mathbf{k}} \cdot \boldsymbol{\tau} & \Delta_{\mathbf{k}} \\ \Delta_{\mathbf{k}}^\dagger & -[\underline{\xi}_{\mathbf{k}} - \gamma_{\mathbf{k}} \cdot \boldsymbol{\tau}]^T \end{pmatrix}. \quad (2.10)$$

This ansatz was verified by a diagonalization procedure, which will be explained in detail. The

²An example for collision integrals in the Raman response can be found in Ref. [71].

2.2 Derivation of the transport equations

momentum and frequency–dependent deviations from equilibrium are defined as

$$\delta \underline{n}_{\mathbf{k}}^0 = \begin{pmatrix} \delta \mathbf{n}_{\mathbf{k}} & \delta \mathbf{g}_{\mathbf{k}} \\ \delta \mathbf{g}_{\mathbf{k}}^\dagger & -\delta \mathbf{n}_{-\mathbf{k}} \end{pmatrix} \quad (2.11)$$

and

$$\delta \underline{\xi}_{\mathbf{k}}^0 = \begin{pmatrix} \delta \underline{\xi}_{\mathbf{k}} & \delta \underline{\Delta}_{\mathbf{k}} \\ \delta \underline{\Delta}_{\mathbf{k}}^\dagger & -\delta \underline{\xi}_{-\mathbf{k}} \end{pmatrix}, \quad (2.12)$$

respectively. In the spin basis, the matrix–kinetic Equation (2.8) represents a set of 16 equations, which can be reduced to a set of 8 equations by an unitary transformation into the band basis (also referred to as helicity basis). This SU(2) rotation is given by Ref. [57]

$$\underline{U}_{\mathbf{k}} = \begin{pmatrix} \mathbf{U}_{\mathbf{k}} & 0 \\ 0 & \mathbf{U}_{\mathbf{k}}^* \end{pmatrix} \quad (2.13)$$

$$\mathbf{U}_{\mathbf{k}} = \exp\left(-i\frac{\theta_\gamma}{2}\hat{\mathbf{n}}_\gamma \cdot \boldsymbol{\tau}\right) = \cos\frac{\theta_\gamma}{2} - i\hat{\mathbf{n}}_\gamma \cdot \boldsymbol{\tau} \sin\frac{\theta_\gamma}{2} \quad (2.14)$$

$$\mathbf{n}_\gamma = \frac{\boldsymbol{\gamma}_{\mathbf{k}} \times \hat{\mathbf{z}}}{|\boldsymbol{\gamma}_{\mathbf{k}} \times \hat{\mathbf{z}}|}, \quad (2.15)$$

which corresponds to a rotation in spin space into the $\hat{\mathbf{z}}$ –direction about the polar angle θ_γ between $\boldsymbol{\gamma}_{\mathbf{k}}$ and $\hat{\mathbf{z}}$. Multiplying Eq. (2.8) from left with $\underline{U}_{\mathbf{k}+}^\dagger$ and from right with $\underline{U}_{\mathbf{k}-}$, one may rewrite it as

$$\begin{aligned} \omega \underline{U}_{\mathbf{k}+}^\dagger \delta \underline{n}_{\mathbf{k}} \underline{U}_{\mathbf{k}-} + \underline{U}_{\mathbf{k}+}^\dagger \delta \underline{n}_{\mathbf{k}} \underline{U}_{\mathbf{k}-} \underline{U}_{\mathbf{k}-}^\dagger \underline{\xi}_{\mathbf{k}-}^0 \underline{U}_{\mathbf{k}-} - \underline{U}_{\mathbf{k}+}^\dagger \underline{\xi}_{\mathbf{k}+}^0 \underline{U}_{\mathbf{k}+} \underline{U}_{\mathbf{k}+}^\dagger \delta \underline{n}_{\mathbf{k}} \underline{U}_{\mathbf{k}-} \\ = \underline{U}_{\mathbf{k}+}^\dagger \delta \underline{\xi}_{\mathbf{k}} \underline{U}_{\mathbf{k}-} \underline{U}_{\mathbf{k}-}^\dagger \underline{n}_{\mathbf{k}-}^0 \underline{U}_{\mathbf{k}-} - \underline{U}_{\mathbf{k}+}^\dagger \underline{n}_{\mathbf{k}+}^0 \underline{U}_{\mathbf{k}+} \underline{U}_{\mathbf{k}+}^\dagger \delta \underline{\xi}_{\mathbf{k}} \underline{U}_{\mathbf{k}-} \end{aligned} \quad (2.16)$$

or, more simply

$$\omega \delta \underline{n}_{\mathbf{k}}^b + \delta \underline{n}_{\mathbf{k}}^b \underline{\xi}_{\mathbf{k}-}^b - \underline{\xi}_{\mathbf{k}+}^b \delta \underline{n}_{\mathbf{k}}^b = \delta \underline{\xi}_{\mathbf{k}}^b \underline{n}_{\mathbf{k}-}^b - \underline{n}_{\mathbf{k}+}^b \delta \underline{\xi}_{\mathbf{k}}^b, \quad (2.17)$$

where the equilibrium distribution function and energy shifts in the band basis are given by

$$\underline{n}_{\mathbf{k}}^b = \begin{pmatrix} \frac{1}{2}(1 - \xi_+ \theta_+) & 0 & 0 & -\Delta_+ \theta_+ \\ 0 & \frac{1}{2}(1 - \xi_- \theta_-) & \Delta_- \theta_- & 0 \\ 0 & \Delta_-^* \theta_- & \frac{1}{2}(1 + \xi_- \theta_-) & 0 \\ -\Delta_+^* \theta_+ & 0 & 0 & \frac{1}{2}(1 + \xi_+ \theta_+) \end{pmatrix} \quad (2.18)$$

and

$$\underline{\xi}_{\mathbf{k}}^b = \begin{pmatrix} \xi_+ & 0 & 0 & \Delta_+ \\ 0 & \xi_- & -\Delta_- & 0 \\ 0 & -\Delta_-^* & -\xi_- & 0 \\ \Delta_+^* & 0 & 0 & -\xi_+ \end{pmatrix}. \quad (2.19)$$

The trick consists of adding the identity matrix with the adequate momentum–index in between the quantities of Eq. (2.8). Then, the deviations from equilibrium can be parameterized as fol-

2 Response and transport in the presence of ASOC

lows:

$$\delta \underline{n}_{\mathbf{k}}^b = \underline{U}_{\mathbf{k}+}^\dagger \delta \underline{n}_{\mathbf{k}} \underline{U}_{\mathbf{k}-} = \begin{pmatrix} \delta n_+^b & 0 & 0 & \delta g_+^b \\ 0 & \delta n_-^b & -\delta g_-^b & 0 \\ 0 & -\delta g_-^{b*} & -\delta n_-^b & 0 \\ \delta g_+^{b*} & 0 & 0 & -\delta n_+^b \end{pmatrix} \quad (2.20)$$

$$\delta \underline{\xi}_{\mathbf{k}}^b = \underline{U}_{\mathbf{k}+}^\dagger \delta \underline{\xi}_{\mathbf{k}} \underline{U}_{\mathbf{k}-} = \begin{pmatrix} \delta \xi_+^b & 0 & 0 & \delta \Delta_+^b \\ 0 & \delta \xi_-^b & -\delta \Delta_-^b & 0 \\ 0 & -\delta \Delta_-^{b*} & -\delta \xi_-^b & 0 \\ \delta \Delta_+^{b*} & 0 & 0 & -\delta \xi_+^b \end{pmatrix}. \quad (2.21)$$

Thus, I have now derived a set of equations in spin- and band-basis [Eqs. (2.8) and (2.17)] that allow us to determine the diagonal and off-diagonal non-equilibrium momentum distribution functions. In Section 2.5.1 and in Chapter 4, I will use these distribution functions to determine the normal and superfluid density, specific heat capacity, and the Raman response of NCS. From now on, I will omit the index “*b*” indicating the band-basis, since all further considerations will be made in the band basis.

2.3 Solution by Bogoliubov transformation

In what follows, I will solve the kinetic Equation (2.17), derived in the previous section. For this purpose, I perform first a Bogoliubov transformation into quasiparticle space, where the kinetic equations are easily decoupled and then solved. For the subsequent inverse Bogoliubov transformation I will introduce parity projected quantities to obtain finally a relation between the diagonal and off-diagonal energy-shifts on the one side and the non-equilibrium distribution functions on the other. As a first step towards the solution of the kinetic equations, the momentum distribution matrix $\underline{n}_{\mathbf{k}}$ and the energy matrix $\underline{\xi}_{\mathbf{k}}$ (both in band-basis) are diagonalized through the following Bogoliubov transformation

$$\underline{\nu}_{\mathbf{k}} = \underline{B}_{\mathbf{k}}^\dagger \underline{n}_{\mathbf{k}} \underline{B}_{\mathbf{k}} = \begin{pmatrix} f(E_+) & 0 & 0 & 0 \\ 0 & f(E_-) & 0 & 0 \\ 0 & 0 & f(-E_-) & 0 \\ 0 & 0 & 0 & f(-E_+) \end{pmatrix} \quad (2.22)$$

$$\underline{E}_{\mathbf{k}} = \underline{B}_{\mathbf{k}}^\dagger \underline{\xi}_{\mathbf{k}} \underline{B}_{\mathbf{k}} = \begin{pmatrix} E_+ & 0 & 0 & 0 \\ 0 & E_- & 0 & 0 \\ 0 & 0 & -E_- & 0 \\ 0 & 0 & 0 & -E_+ \end{pmatrix}, \quad (2.23)$$

2.3 Solution by Bogoliubov transformation

with the Fermi–Dirac distribution function $f(E_\lambda) = [\exp(E_\lambda/k_B T) + 1]^{-1}$. The Bogoliubov matrix has been found to read in the band basis

$$\underline{B}_{\mathbf{k}} = \begin{pmatrix} u_+ & 0 & 0 & v_+ \\ 0 & u_- & -v_- & 0 \\ 0 & v_-^* & u_- & 0 \\ -v_+^* & 0 & 0 & u_+ \end{pmatrix}, \quad (2.24)$$

with the coherence factors

$$u_\lambda(\mathbf{k}) = \sqrt{\frac{1}{2} \left(1 + \frac{\xi_\lambda(\mathbf{k})}{E_\lambda(\mathbf{k})} \right)} \quad (2.25)$$

$$v_\lambda(\mathbf{k}) = -\sqrt{\frac{1}{2} \left(1 - \frac{\xi_\lambda(\mathbf{k})}{E_\lambda(\mathbf{k})} \right) \frac{\Delta_\lambda(\mathbf{k})}{|\Delta_\lambda(\mathbf{k})|}}, \quad (2.26)$$

satisfying the condition $|u_\lambda|^2 + |v_\lambda|^2 = 1$, by which the fermionic character of the Bogoliubov quasiparticles is established. As indicated by the coherence factors, the order parameter on each spin–orbit split band $\Delta_\lambda(\mathbf{k})$ is a complex function. In order to solve the transport equation in the band basis (2.17), one may multiply from the left with the Bogoliubov matrix $\underline{B}_{\mathbf{k}+}^\dagger$ and from the right with $\underline{B}_{\mathbf{k}-}$ ³. The result is

$$\begin{aligned} \omega \underline{B}_{\mathbf{k}+}^\dagger \delta n_{\mathbf{k}} \underline{B}_{\mathbf{k}-} + \underline{B}_{\mathbf{k}+}^\dagger \delta n_{\mathbf{k}} \underline{B}_{\mathbf{k}-} \underline{B}_{\mathbf{k}-}^\dagger \underline{\xi}_{\mathbf{k}-}^0 \underline{B}_{\mathbf{k}-} - \underline{B}_{\mathbf{k}+}^\dagger \underline{\xi}_{\mathbf{k}+}^0 \underline{B}_{\mathbf{k}+} \underline{B}_{\mathbf{k}+}^\dagger \delta n_{\mathbf{k}} \underline{B}_{\mathbf{k}-} \\ = \underline{B}_{\mathbf{k}+}^\dagger \delta \underline{\xi}_{\mathbf{k}} \underline{B}_{\mathbf{k}-} \underline{B}_{\mathbf{k}-}^\dagger n_{\mathbf{k}-}^0 \underline{B}_{\mathbf{k}-} - \underline{B}_{\mathbf{k}+}^\dagger n_{\mathbf{k}+}^0 \underline{B}_{\mathbf{k}+} \underline{B}_{\mathbf{k}+}^\dagger \delta \underline{\xi}_{\mathbf{k}} \underline{B}_{\mathbf{k}-} \end{aligned} \quad (2.27)$$

or, more simply

$$\omega \delta \underline{\nu}_{\mathbf{k}} + \delta \underline{\nu}_{\mathbf{k}} \underline{E}_{\mathbf{k}-} - \underline{E}_{\mathbf{k}+} \delta \underline{\nu}_{\mathbf{k}} = \delta \underline{E}_{\mathbf{k}} \underline{\nu}_{\mathbf{k}-} - \underline{\nu}_{\mathbf{k}+} \delta \underline{E}_{\mathbf{k}}. \quad (2.28)$$

The new Bogoliubov–transformed quantities, describing the deviation from equilibrium, are identified from the preceding equations and labeled as follows:

$$\delta \underline{\nu}(\mathbf{k}) = \underline{B}_{\mathbf{k}+}^\dagger \delta n_{\mathbf{k}} \underline{B}_{\mathbf{k}-} = \begin{pmatrix} \delta \nu_+(\mathbf{k}) & 0 & 0 & \delta \gamma_+(\mathbf{k}) \\ 0 & \delta \nu_-(\mathbf{k}) & -\delta \gamma_-(\mathbf{k}) & 0 \\ 0 & -\delta \gamma_-^*(\mathbf{k}) & -\delta \nu_-(-\mathbf{k}) & 0 \\ \delta \gamma_+^*(\mathbf{k}) & 0 & 0 & -\delta \nu_+(-\mathbf{k}) \end{pmatrix} \quad (2.29)$$

$$\delta \underline{E}(\mathbf{k}) = \underline{B}_{\mathbf{k}+}^\dagger \delta \underline{\xi}_{\mathbf{k}} \underline{B}_{\mathbf{k}-} = \begin{pmatrix} \delta E_+(\mathbf{k}) & 0 & 0 & \delta D_+(\mathbf{k}) \\ 0 & \delta E_-(\mathbf{k}) & -\delta D_-(\mathbf{k}) & 0 \\ 0 & -\delta D_-^*(\mathbf{k}) & -\delta E_-(-\mathbf{k}) & 0 \\ \delta D_+^*(\mathbf{k}) & 0 & 0 & -\delta E_+(-\mathbf{k}) \end{pmatrix}. \quad (2.30)$$

³Here as well, identity matrices with the right momentum indices are inserted as for the unitary transformation into the band–basis.

2 Response and transport in the presence of ASOC

The solution of Eq. (2.28) for the quasiparticle distribution functions is the set of the following eight equations ($\lambda = \pm$):

$$\delta\nu_\lambda(\mathbf{k}) = \frac{\eta_\lambda^-(\mathbf{k})}{\omega - \eta_\lambda^-(\mathbf{k})} \tilde{y}_\lambda(\mathbf{k}) \delta E_\lambda(\mathbf{k}) \quad (2.31a)$$

$$\delta\nu_\lambda(-\mathbf{k}) = -\frac{\eta_\lambda^-(\mathbf{k})}{\omega + \eta_\lambda^-(\mathbf{k})} \tilde{y}_\lambda(\mathbf{k}) \delta E_\lambda(-\mathbf{k}) \quad (2.31b)$$

$$\delta\gamma_\lambda(\mathbf{k}) = \frac{\eta_\lambda^+(\mathbf{k})}{\omega - \eta_\lambda^+(\mathbf{k})} \Theta_\lambda(\mathbf{k}) \delta D_\lambda(\mathbf{k}) \quad (2.31c)$$

$$\delta\gamma_\lambda^*(\mathbf{k}) = -\frac{\eta_\lambda^+(\mathbf{k})}{\omega + \eta_\lambda^+(\mathbf{k})} \Theta_\lambda(\mathbf{k}) \delta D_\lambda^*(\mathbf{k}), \quad (2.31d)$$

where I have introduced the following abbreviations:

$$\eta_\lambda^\pm(\mathbf{k}) = E_\lambda(\mathbf{k}+) \pm E_\lambda(\mathbf{k}-) \quad (2.32)$$

$$\tilde{y}_\lambda(\mathbf{k}) = -\frac{f[E_\lambda(\mathbf{k}+)] - f[E_\lambda(\mathbf{k}-)]}{E_\lambda(\mathbf{k}+) - E_\lambda(\mathbf{k}-)}, \quad (2.33)$$

and

$$\Theta_\lambda(\mathbf{k}) = \frac{1 - f[E_\lambda(\mathbf{k}+)] - f[E_\lambda(\mathbf{k}-)]}{E_\lambda(\mathbf{k}+) + E_\lambda(\mathbf{k}-)}. \quad (2.34)$$

The expressions for these quantities in the long-wavelength limit can be found in Appendix A. In this limit, the difference quotient $\tilde{y}_\lambda(\mathbf{k})$ is equal to the Yosida kernel $y_\lambda(\mathbf{k})$, which is given by the derivative of the quasiparticle distribution function

$$y_\lambda(\mathbf{k}) = -\frac{\partial f[E_\lambda(\mathbf{k})]}{\partial E_\lambda(\mathbf{k})} = \frac{1}{4k_B T} \frac{1}{\cosh^2\left(\frac{E_\lambda(\mathbf{k})}{2k_B T}\right)} \quad (2.35)$$

with respect to the quasiparticle energy $E_\lambda(\mathbf{k})$. The Yosida kernel is crucial for the temperature dependence of all response and transport functions. Accordingly, $\Theta_\lambda(\mathbf{k}) \xrightarrow{q \rightarrow 0} \theta_\lambda(\mathbf{k})$ represents the kernel of the self-consistency Equation (1.14). It is instructive to note that the distribution functions $\delta\nu_\lambda(\mathbf{k})$ and $\delta\gamma_\lambda(\mathbf{k})$ have a clear physical meaning: The diagonal component $\delta\nu_\lambda(\mathbf{k}) = \delta\langle\hat{\alpha}_\lambda^\dagger\hat{\alpha}_\lambda\rangle(\mathbf{k})$ describes the response of the Bogoliubov quasiparticles (with the quasiparticle creation and annihilation operators $\hat{\alpha}_\lambda^\dagger, \hat{\alpha}_\lambda$ in the band λ). The off-diagonal component $\delta\gamma_\lambda(\mathbf{k}) = \delta\langle\hat{\alpha}_\lambda\hat{\alpha}_\lambda\rangle(\mathbf{k})$ describes the pair-response. Note that the abbreviations $\eta_\lambda^\pm(\mathbf{k})$ are of even (+) and odd (-) parity w.r.t. $\mathbf{k} \rightarrow -\mathbf{k}$ and become very simple expressions in the small wavelength limit (see Appendix A).

For the inverse Bogoliubov transformation, it is convenient to introduce parity-projected quantities which are labeled by $s = \pm 1$:

$$\delta n_\lambda^{(s)}(\mathbf{k}) = \frac{1}{2} [\delta n_\lambda(\mathbf{k}) + s \delta n_\lambda(-\mathbf{k})] \quad (2.36)$$

2.3 Solution by Bogoliubov transformation

$$\delta\xi_\lambda^{(s)}(\mathbf{k}) = \frac{1}{2} [\delta\xi_\lambda(\mathbf{k}) + s\delta\xi_\lambda(-\mathbf{k})] . \quad (2.37)$$

In almost the same manner also the off-diagonal components are decomposed by

$$\delta g_\lambda^{(s)}(\mathbf{k}) = \frac{1}{2} \left[\delta g_\lambda(\mathbf{k}) \frac{\Delta_\lambda^*(\mathbf{k})}{|\Delta_\lambda(\mathbf{k})|} + s \frac{\Delta_\lambda(\mathbf{k})}{|\Delta_\lambda(\mathbf{k})|} \delta g_\lambda(-\mathbf{k}) \right] , \quad (2.38)$$

and

$$\delta\Delta_\lambda^{(s)}(\mathbf{k}) = \frac{1}{2} \left[\delta\Delta_\lambda(\mathbf{k}) \frac{\Delta_\lambda^*(\mathbf{k})}{|\Delta_\lambda(\mathbf{k})|} + s \frac{\Delta_\lambda(\mathbf{k})}{|\Delta_\lambda(\mathbf{k})|} \delta\Delta_\lambda(-\mathbf{k}) \right] . \quad (2.39)$$

I use the same symmetry classification for the Bogoliubov-transformed quantities. The physical meaning of $\delta\Delta_\lambda(\mathbf{k}, \mathbf{q}, \omega)$ becomes clear after a decomposition into its real and imaginary part

$$\begin{aligned} \delta\Delta_\lambda(\mathbf{k}, \mathbf{q}, \omega) &= a_\lambda(\mathbf{k}, \mathbf{q}, \omega) e^{i\varphi_\lambda(\mathbf{q}, \omega)} - \Delta_\lambda(\mathbf{k}) \\ &= [\delta a_\lambda(\mathbf{k}, \mathbf{q}, \omega) + i\delta\phi_\lambda(\mathbf{q}, \omega) |\Delta_\lambda(\mathbf{k})|] \frac{\Delta_\lambda(\mathbf{k})}{|\Delta_\lambda(\mathbf{k})|} . \end{aligned} \quad (2.40)$$

With Eq. (2.39), one can identify $\delta\Delta_\lambda^{(+)}(\mathbf{k}, \mathbf{q}, \omega) = \delta a_\lambda(\mathbf{k}, \mathbf{q}, \omega)$ as the amplitude fluctuations and $\delta\Delta_\lambda^{(-)}(\mathbf{k}, \mathbf{q}, \omega)/\Delta_\lambda(\mathbf{k}) = i\delta\phi_\lambda(\mathbf{q}, \omega)$ as the phase fluctuations of the order parameter.

The off-diagonal energy shift $\delta\Delta_\lambda^{(s)}(\mathbf{k})$ can be determined from a straightforward variation of the self-consistency Equation (1.14):

$$\delta\Delta_\lambda^{(s)}(\mathbf{k}) = \sum_{\mathbf{k}'\mu} V_{\mathbf{k}\mathbf{k}'}^{\lambda\mu} \delta\mathbf{g}_\mu^{(s)}(\mathbf{k}') , \quad (2.41)$$

with $\delta g_\lambda^{(s)}(\mathbf{k}) = -\theta_\lambda(\mathbf{k}) \delta\Delta_\lambda^{(s)}(\mathbf{k})$. This off-diagonal self-consistency equation will play an important role for the gauge invariance of the theory, as will be discussed in Chapter 3.

From the symmetry-classification, one can assign to each transport and response function (see Table 2.1) the corresponding momentum distribution function $\delta n_\lambda^{(+)}(\mathbf{k})$ or $\delta n_\lambda^{(-)}(\mathbf{k})$: The vertex function of the (charge) density and Raman response is even in \mathbf{k} . Thus, only the even distribution function $\delta n_\lambda^{(+)}(\mathbf{k})$ contributes to those response functions. For the current response (dynamic conductivity), the vertex-function ($a_\sigma(\mathbf{k}) = e\mathbf{v}_\mathbf{k}$) is odd in momentum. Thus, only $\delta n_\lambda^{(-)}(\mathbf{k})$ contributes to the conductivity upon summation over \mathbf{k} . Further, the Bogoliubov-transformation can now be written in this simple form

$$\begin{pmatrix} \delta\nu_\lambda^{(s)}(\mathbf{k}) \\ \delta\gamma_\lambda^{(s)}(\mathbf{k}) \end{pmatrix} = \begin{pmatrix} q_\lambda^{(s)}(\mathbf{k}) & p_\lambda^{(s)}(\mathbf{k}) \\ -p_\lambda^{(s)}(\mathbf{k}) & q_\lambda^{(s)}(\mathbf{k}) \end{pmatrix} \cdot \begin{pmatrix} \delta n_\lambda^{(s)}(\mathbf{k}) \\ \delta g_\lambda^{(s)}(\mathbf{k}) \end{pmatrix} \quad (2.42)$$

$$\begin{pmatrix} \delta E_\lambda^{(s)}(\mathbf{k}) \\ \delta D_\lambda^{(s)}(\mathbf{k}) \end{pmatrix} = \begin{pmatrix} q_\lambda^{(s)}(\mathbf{k}) & p_\lambda^{(s)}(\mathbf{k}) \\ -p_\lambda^{(s)}(\mathbf{k}) & q_\lambda^{(s)}(\mathbf{k}) \end{pmatrix} \cdot \begin{pmatrix} \delta\xi_\lambda^{(s)}(\mathbf{k}) \\ \delta\Delta_\lambda^{(s)}(\mathbf{k}) \end{pmatrix} , \quad (2.43)$$

2 Response and transport in the presence of ASOC

which might easily be inverted by using the sum rule

$$\left[q_\lambda^{(s)}(\mathbf{k}) \right]^2 + \left[p_\lambda^{(s)}(\mathbf{k}) \right]^2 = 1. \quad (2.44)$$

Here, I have defined the real-valued coherence-factors

$$q_\lambda^{(s)}(\mathbf{k}) = |u_\lambda(\mathbf{k}+)u_\lambda(\mathbf{k}-)| - s|v_\lambda(\mathbf{k}+)v_\lambda(\mathbf{k}-)| \quad (2.45)$$

and

$$p_\lambda^{(s)}(\mathbf{k}) = |u_\lambda(\mathbf{k}+)v_\lambda(\mathbf{k}-)| + s|u_\lambda(\mathbf{k}-)v_\lambda(\mathbf{k}+)|, \quad (2.46)$$

with the explicit form

$$q_\lambda^{(s)}(\mathbf{k}) = \sqrt{\frac{1}{2} + \frac{\xi_\lambda(\mathbf{k}+)\xi_\lambda(\mathbf{k}-) - s|\Delta_\lambda(\mathbf{k})|^2}{2E_\lambda(\mathbf{k}+)E_\lambda(\mathbf{k}-)}} \quad (2.47)$$

and

$$p_\lambda^{(s)}(\mathbf{k}) = \sqrt{\frac{1}{2} - \frac{\xi_\lambda(\mathbf{k}+)\xi_\lambda(\mathbf{k}-) - s|\Delta_\lambda(\mathbf{k})|^2}{2E_\lambda(\mathbf{k}+)E_\lambda(\mathbf{k}-)}}. \quad (2.48)$$

From Eqs. (2.43) and (2.28) one finally obtains the following solution of the matrix-kinetic equation

$$\begin{pmatrix} \delta n_\lambda^+(\mathbf{k}) \\ \delta n_\lambda^-(\mathbf{k}) \\ \delta g_\lambda^+(\mathbf{k}) \\ \delta g_\lambda^-(\mathbf{k}) \end{pmatrix} = \begin{pmatrix} N_{11} & N_{12} & N_{13} & N_{14} \\ N_{21} & N_{22} & N_{23} & N_{24} \\ N_{31} & N_{32} & N_{33} & N_{34} \\ N_{41} & N_{42} & N_{43} & N_{44} \end{pmatrix} \cdot \begin{pmatrix} \delta \xi_\lambda^+(\mathbf{k}) \\ \delta \xi_\lambda^-(\mathbf{k}) \\ \delta \Delta_\lambda^+(\mathbf{k}) \\ \delta \Delta_\lambda^-(\mathbf{k}) \end{pmatrix}. \quad (2.49)$$

The vector on the left-hand side contains the non-equilibrium momentum distribution functions [defined in Eq. (2.20)] which can be expressed in terms of the diagonal and off-diagonal energy-shifts [defined in Eq. (2.21) and obtained from Table 2.1 and Eq. (2.41)]. The matrix-elements N_{ij} read in detail:

$$N_{11} = q_\lambda^{(+)^2}(\mathbf{k})\tilde{y}_\lambda^{(+)}(\mathbf{k}) + p_\lambda^{(+)^2}(\mathbf{k})\Theta_\lambda^{(+)}(\mathbf{k}) \quad (2.50a)$$

$$N_{12} = q_\lambda^{(+)}(\mathbf{k})q_\lambda^{(-)}(\mathbf{k})\tilde{y}_\lambda^{(-)}(\mathbf{k}) + p_\lambda^{(+)}(\mathbf{k})p_\lambda^{(-)}(\mathbf{k})\Theta_\lambda^{(-)}(\mathbf{k}) \quad (2.50b)$$

$$N_{13} = q_\lambda^{(+)}(\mathbf{k})p_\lambda^{(+)}(\mathbf{k}) \left[\tilde{y}_\lambda^{(+)}(\mathbf{k}) - \Theta_\lambda^{(+)}(\mathbf{k}) \right] \quad (2.50c)$$

$$N_{14} = q_\lambda^{(+)}(\mathbf{k})p_\lambda^{(-)}(\mathbf{k})\tilde{y}_\lambda^{(-)}(\mathbf{k}) - q_\lambda^{(-)}(\mathbf{k})p_\lambda^{(+)}(\mathbf{k})\Theta_\lambda^{(-)}(\mathbf{k}) \quad (2.50d)$$

$$N_{22} = q_\lambda^{(-)^2}(\mathbf{k})\tilde{y}_\lambda^{(+)}(\mathbf{k}) + p_\lambda^{(-)^2}(\mathbf{k})\Theta_\lambda^{(+)}(\mathbf{k}) \quad (2.50e)$$

$$N_{23} = q_\lambda^{(-)}(\mathbf{k})p_\lambda^{(+)}(\mathbf{k})\tilde{y}_\lambda^{(-)}(\mathbf{k}) - q_\lambda^{(+)}(\mathbf{k})p_\lambda^{(-)}(\mathbf{k})\Theta_\lambda^{(-)}(\mathbf{k}) \quad (2.50f)$$

$$N_{24} = q_\lambda^{(-)}(\mathbf{k})p_\lambda^{(-)}(\mathbf{k}) \left[\tilde{y}_\lambda^{(+)}(\mathbf{k}) - \Theta_\lambda^{(+)}(\mathbf{k}) \right] \quad (2.50g)$$

2.3 Solution by Bogoliubov transformation

$$N_{33} = p_\lambda^{(+2)}(\mathbf{k})\tilde{y}_\lambda^{(+)}(\mathbf{k}) + q_\lambda^{(+2)}(\mathbf{k})\Theta_\lambda^{(+)}(\mathbf{k}) \quad (2.50h)$$

$$N_{34} = p_\lambda^{(+)}(\mathbf{k})p_\lambda^{(-)}(\mathbf{k})\tilde{y}_\lambda^{(-)}(\mathbf{k}) + q_\lambda^{(+)}(\mathbf{k})q_\lambda^{(-)}(\mathbf{k})\Theta_\lambda^{(-)}(\mathbf{k}) \quad (2.50i)$$

$$N_{44} = p_\lambda^{(-2)}(\mathbf{k})\tilde{y}_\lambda^{(+)}(\mathbf{k}) + q_\lambda^{(-2)}(\mathbf{k})\Theta_\lambda^{(+)}(\mathbf{k}) . \quad (2.50j)$$

The matrix–elements N_{ij} are symmetric, i.e. $N_{ij} = N_{ji}$ and the occurring products of coherence–factors can be found in the Appendix A. Above, I have introduced the following abbreviations:

$$\tilde{y}_\lambda^{(s)}(\mathbf{k}) = \frac{\eta_\lambda^{(s)2}(\mathbf{k})}{\omega^2 - \eta_\lambda^{(s)2}(\mathbf{k})}\tilde{y}_\lambda(\mathbf{k}) \quad (2.51)$$

$$\Theta_\lambda^{(s)}(\mathbf{k}) = \frac{\eta_\lambda^{(s)2}(\mathbf{k})}{\omega^2 - \eta_\lambda^{(s)2}(\mathbf{k})}\Theta_\lambda(\mathbf{k}) .$$

The matrix–elements N_{13} , N_{23} and N_{34} are shown to be odd w.r.t. $\xi_\lambda(\mathbf{k}) \rightarrow -\xi_\lambda(\mathbf{k})$. Thus in a particle–hole symmetric theory, these terms will vanish upon integration over $\xi_\lambda(\mathbf{k})$ and are labeled $O(\text{pha})$ which stands for “particle–hole asymmetric”. It is convenient to rewrite these matrix elements in terms of the functions

$$\lambda_\lambda(\mathbf{k}) = \left[p_\lambda^{(+2)}(\mathbf{k}) - q_\lambda^{(-2)}(\mathbf{k}) \right] \left[\tilde{y}_\lambda^{(+)}(\mathbf{k}) - \Theta_\lambda^{(+)}(\mathbf{k}) \right] \quad (2.52)$$

$$\Phi_\lambda(\mathbf{k}) = q_\lambda^{(+2)}\tilde{y}_\lambda(\mathbf{k}) + p_\lambda^{(+2)}\tilde{y}_\lambda(\mathbf{k})\Theta_\lambda(\mathbf{k}) \quad (2.53)$$

$$\frac{\Theta_\lambda^{(+)}(\mathbf{k})}{2} = \frac{\eta_\lambda^{(+2)}(\mathbf{k})\Theta_\lambda(\mathbf{k}) - \eta_\lambda^{(-2)}(\mathbf{k})\tilde{y}_\lambda(\mathbf{k})}{\eta_\lambda^{(+2)}(\mathbf{k}) - \eta_\lambda^{(-2)}(\mathbf{k})} , \quad (2.54)$$

where the first one, $\lambda_\lambda(\mathbf{k})$, is referred to as the Tsuneto–function [78]. A straightforward but lengthy calculation yields

$$N_{11} = \frac{\eta^2\Phi_\lambda(\mathbf{k}) - \omega^2\lambda_\lambda(\mathbf{k})}{\omega^2 - \eta^2} \quad (2.55a)$$

$$N_{12} = \frac{\omega\eta[\Phi_\lambda(\mathbf{k}) - \lambda_\lambda(\mathbf{k})]}{\omega^2 - \eta^2} \quad (2.55b)$$

$$N_{13} = O(\text{pha}) \quad (2.55c)$$

$$N_{14} = \frac{\omega}{2\Delta_\lambda(\mathbf{k})}\lambda_\lambda(\mathbf{k}) \quad (2.55d)$$

$$N_{22} = \frac{\eta^2[\Phi_\lambda(\mathbf{k}) - \lambda_\lambda(\mathbf{k})]}{\omega^2 - \eta^2} \quad (2.55e)$$

$$N_{23} = O(\text{pha}) \quad (2.55f)$$

$$N_{24} = \frac{\eta}{2\Delta_\lambda(\mathbf{k})}\lambda_\lambda(\mathbf{k}) \quad (2.55g)$$

2 Response and transport in the presence of ASOC

$$N_{33} = -\frac{\theta_\lambda^{(+)}(\mathbf{k})}{2} - \frac{\omega^2 - \eta^2 - 4\Delta_\lambda^2(\mathbf{k})}{4\Delta_\lambda^2(\mathbf{k})} \lambda_\lambda(\mathbf{k}) \quad (2.55h)$$

$$N_{34} = O(\text{pha}) \quad (2.55i)$$

$$N_{44} = -\frac{\theta_\lambda^{(+)}(\mathbf{k})}{2} - \frac{\omega^2 - \eta^2}{4\Delta_\lambda^2(\mathbf{k})} \lambda_\lambda(\mathbf{k}) , \quad (2.55j)$$

where $\eta = \mathbf{v}_\mathbf{k} \cdot \mathbf{q}$. Note that all expressions are valid in the whole quasiclassical limit, i.e. for $\mathbf{q} \ll k_F$ and $\omega \ll E_F$. For small wave numbers, as required in the Raman case, the Tsuneto and related functions $\lambda_\lambda(\mathbf{k})$, $\Phi_\lambda(\mathbf{k})$ and $\theta_\lambda^{(+)}$ simplify considerably. The results for such a small- \mathbf{q} expansion can be found in Appendix A. Further considerations for response and transport properties require both main results of this section: The solution of the transport equation in quasiparticle space, given by Eq. (2.31) will be used directly in Section 2.5.2 to derive the specific heat capacity in NCS (see Table 2.1). For the discussion of the gauge mode (Chapter 3), the normal and superfluid density (Section 2.5.1), and the Raman response (Chapter 4) the non-equilibrium distribution functions after an inverse Bogoliubov transformation are necessary [see Eq. (2.49) and Eq. (2.55)].

2.4 Gauge invariance

The gauge invariance of this theory is an important issue, which will be discussed in the following section. To this end, the gauge modes have to be determined (a detailed calculation is found in Chapter 3) and inserted into the transport equations. An integration of these transport equations yields a continuity equation, which demonstrates the gauge invariance of this theory for $\omega \ll E_F$ and $\mathbf{q} \ll k_F$. For this purpose, it is very instructive to rebuild the original distribution function by combining δn_λ^+ and δn_λ^- from Eq. (2.49) and Eq. (2.55):

$$\omega \delta n_\lambda - \eta [\delta n_\lambda + \Phi_\lambda \delta \xi_\lambda] = -\lambda_\lambda [\omega \delta \xi_\lambda^+ + \eta \delta \xi_\lambda^-] + \lambda_\lambda (\omega^2 - \eta^2) \frac{\delta \Delta_\lambda^-}{2\Delta_\lambda} . \quad (2.56)$$

The left-hand side of this equation has the same structure as the linearized Landau-Boltzmann equation of the normal state. In what follows, I want to discuss the right-hand side of the above equation. Note that all terms coupling to $\delta \Delta_\lambda^+$ have vanished because of particle-hole symmetry. This means that the amplitude fluctuations of the order parameter do not contribute to the response in a particle-hole symmetric theory. The phase fluctuations are also given by Eq. (2.49):

$$\delta g_\lambda^- + \left[\frac{\theta_\lambda^+}{2} + \frac{\omega^2 - \eta^2}{4\Delta_\lambda^2} \lambda_\lambda \right] \delta \Delta_\lambda^- = \frac{\omega \delta \xi_\lambda^+ + \eta \delta \xi_\lambda^-}{2\Delta_\lambda} \lambda_\lambda . \quad (2.57)$$

Multiplication with the pairing–interaction $V_{\mathbf{k}\mathbf{k}'}^{\lambda\mu}$ and summation over \mathbf{k}' and the band–index μ yields

$$\begin{aligned} \delta\Delta_{\lambda}^{-}(\mathbf{k}) &+ \sum_{\mathbf{k}'\mu} V_{\mathbf{k}\mathbf{k}'}^{\lambda\mu} \left[\theta_{\mu} + \delta\theta_{\mu} + \frac{\omega^2 - \eta^2}{4\Delta_{\mu}^2} \lambda_{\mu} \right] \delta\Delta_{\mu}^{-}(\mathbf{k}') \\ &= \sum_{\mathbf{k}'\mu} V_{\mathbf{k}\mathbf{k}'}^{\lambda\mu} \frac{\omega\delta\xi_{\mu}^{+}(\mathbf{k}') + \eta\delta\xi_{\mu}^{-}(\mathbf{k}')}{2\Delta_{\mu}(\mathbf{k}')} \lambda_{\mu}(\mathbf{k}') , \end{aligned} \quad (2.58)$$

where I have introduced $\delta\theta_{\lambda} = \theta_{\lambda}^{+}/2 - \theta_{\lambda}$. It can be shown, that the $\xi_{\mu}(\mathbf{k})$ –integral over $\delta\theta_{\mu}$ vanishes identically for all momenta⁴. Using the equilibrium gap Equation (1.14) one arrives at

$$\sum_{\mu} \frac{\delta\Delta_{\mu}^{-}}{|\Delta_{\mu}|} \sum_{\mathbf{k}'} V_{\mathbf{k}\mathbf{k}'}^{\lambda\mu} \frac{\omega^2 - \eta^2}{4|\Delta_{\mu}(\mathbf{k}')|} \lambda_{\mu}(\mathbf{k}') = \sum_{\mathbf{k}'\mu} V_{\mathbf{k}\mathbf{k}'}^{\lambda\mu} \frac{\omega\delta\xi_{\mu}^{+}(\mathbf{k}') + \eta\delta\xi_{\mu}^{-}(\mathbf{k}')}{2\Delta_{\mu}(\mathbf{k}')} \lambda_{\mu}(\mathbf{k}') . \quad (2.59)$$

These are two coupled equations (for $\lambda = \pm$) which determine the phase fluctuations of the order parameter (gauge mode). Note that in the weak coupling BCS theory, there are only two collective excitations possible: the Anderson–Bogoliubov and 2Δ mode. In NCS, there exist two gauge modes due to the band splitting, which can be connected with the particle number conservation law. In addition, due to the existence of a triplet fraction, there could be further collective excitation analogous to Leggett’s SBSOS modes predicted for the superfluid phases of ^3He [80, 81]. The latter should be connectable with the spin conservation law in NCS. Finally, massive collective modes with frequencies below 2Δ may exist in NCS. In Chapter 3, it will be shown, that the right–hand side of Eq. (2.56) vanishes upon \mathbf{k} and λ (band) summation when inserting the above expressions for the gauge mode. This leads to the following continuity equation for the electron density:

$$\omega \sum_{\mathbf{k},\lambda} \delta n_{\lambda}(\mathbf{k}) - \mathbf{q} \cdot \sum_{\mathbf{k},\lambda} \mathbf{v}_{\mathbf{k}} [\delta n_{\lambda}(\mathbf{k}) + \Phi_{\lambda}(\mathbf{k})\delta\xi_{\lambda}(\mathbf{k})] = 0 . \quad (2.60)$$

For a conserved quantity such as the particle $a_{\mathbf{k}} = 1$ or charge density $a_{\mathbf{k}} = e$, one can identify the corresponding generalized density and current density

$$\delta n_a = \sum_{\mathbf{k},\lambda} a_{\mathbf{k}} \delta n_{\lambda}(\mathbf{k}) \quad (2.61)$$

$$\mathbf{j}_a = \sum_{\mathbf{k},\lambda} a_{\mathbf{k}} \mathbf{v}_{\mathbf{k}} [\delta n_{\lambda}(\mathbf{k}) + \Phi_{\lambda}(\mathbf{k})\delta\xi_{\lambda}(\mathbf{k})] , \quad (2.62)$$

obeying the continuity equation

$$\omega \delta n_a - \mathbf{q} \cdot \mathbf{j}_a = 0 . \quad (2.63)$$

⁴This is a straight forward generalization of the calculation in my Diploma thesis [79].

2 Response and transport in the presence of ASOC

That is, I have demonstrated charge conservation and gauge invariance of the theory for $\omega \ll E_F$ and $\mathbf{q} \ll k_F$.

2.5 Applications

The applications, which I will present in the following, are restricted to the long-wavelength and static limit and are intended to demonstrate the validity of the theory through a comparison to simple local equilibrium calculations. Since I solved the transport equations for arbitrary frequency ω and momentum \mathbf{q} , the full potential of this theory would be exploited for a dynamic $\mathbf{q} \neq 0$ calculation of a transport property. At least a finite ω calculation will be presented in an extra chapter, namely the electronic Raman response in NCS. However, let's first derive the expressions for the normal and superfluid density, as well as for the specific heat capacity in NCS.

2.5.1 Normal and superfluid density

The normal and superfluid density are derived in the static and long-wavelength limit ($\omega \rightarrow 0$ and $\mathbf{q} \rightarrow 0$). In order to preserve gauge invariance, gradient terms of the order $O(\mathbf{q})$ are still taken into account. The parity-projected distribution functions are obtained from Eq. (2.49) and from Eq. (2.55)

$$\delta n_{\lambda}^+(\mathbf{k}) = -\phi_{\lambda}(\mathbf{k})\delta\xi_{\lambda}^+(\mathbf{k}) \quad (2.64)$$

$$\delta n_{\lambda}^-(\mathbf{k}) = -[\phi_{\lambda}(\mathbf{k}) - \lambda_{\lambda}(\mathbf{k})]\delta\xi_{\lambda}^-(\mathbf{k}) + \eta\lambda_{\lambda}(\mathbf{k})\frac{\delta\Delta_{\lambda}^-(\mathbf{k})}{2\Delta_{\lambda}(\mathbf{k})}, \quad (2.65)$$

where I made use of the $\mathbf{q} \rightarrow 0$ limit with the coherence-factors $q_{\lambda}^-(\mathbf{k}) \rightarrow 1$, $p_{\lambda}^-(\mathbf{k}) \rightarrow 0$, and $\Phi_{\lambda}(\mathbf{k}) \rightarrow \phi_{\lambda}(\mathbf{k})$, $\tilde{y}_{\lambda}(\mathbf{k}) \rightarrow y_{\lambda}(\mathbf{k})$, as well as the Tsuneto-function $\lambda_{\lambda}(\mathbf{k}) \rightarrow \phi_{\lambda}(\mathbf{k}) - y_{\lambda}(\mathbf{k})$ (see Appendix A). The combined expression for $\delta n_{\lambda}^+(\mathbf{k})$ and $\delta n_{\lambda}^-(\mathbf{k})$ are now inserted in Eq. (2.62) to derive the supercurrent density (vertex-function $a_{\mathbf{k}} = e$):

$$\begin{aligned} \mathbf{j}_i^s &= \sum_{\mathbf{p}\lambda} e \mathbf{v}_{\mathbf{p}i} [\delta n_{\lambda}(\mathbf{p}) + \phi_{\lambda}(\mathbf{p})\delta\xi_{\lambda}^-(\mathbf{p})] \\ &= e \sum_{\mathbf{p}\lambda} \mathbf{v}_{\mathbf{p}i} \mathbf{v}_{\mathbf{p}j} \lambda_{\lambda}(\mathbf{p}) \left(-\frac{e}{c} \mathbf{A} + \frac{1}{2} \nabla \delta\varphi_{\lambda} \right). \end{aligned} \quad (2.66)$$

Here, I used the result from Section 2.3 that $\delta\Delta_{\lambda}^-(\mathbf{k})/\Delta_{\lambda}(\mathbf{k}) = i\delta\varphi_{\lambda}$ represents the phase fluctuations of the order parameter. These phase fluctuations ensure gauge invariance in the above expression for the supercurrent. By rewriting the supercurrent as product of the superfluid density

and the corresponding velocity \mathbf{v}^s , one can easily identify

$$\mathbf{j}^s = e \mathbf{n}^s \cdot \mathbf{v}^s \quad (2.67)$$

$$\mathbf{v}^s = \frac{e}{m} \left(-\frac{e}{c} \mathbf{A} + \frac{1}{2} \nabla \delta \varphi_\lambda \right). \quad (2.68)$$

Therefore, the superfluid and normal fluid density tensor read

$$n_{ij}^s = \sum_{\mathbf{p}\lambda} \mathbf{p}_i \mathbf{v}_{\mathbf{p}j} \lambda_\lambda(\mathbf{p}) \quad (2.69)$$

$$n_{ij}^n = n \delta_{ij} - n_{ij}^s = \sum_{\mathbf{p}\lambda} \mathbf{p}_i \mathbf{v}_{\mathbf{p}j} y_\lambda(\mathbf{p}). \quad (2.70)$$

Thus, in this static and small- \mathbf{q} -limit one obtains a very clear picture: The Yosida-kernel $y_\lambda(\mathbf{k}) = -\partial f[E_\lambda(\mathbf{k})]/\partial E_\lambda(\mathbf{k})$ generates the normal fluid density and the Tsuneto-function $\lambda_\lambda(\mathbf{k})$ gives rise to the superfluid density.

It is important to realize, that this result can be derived in the following alternative simple way from local equilibrium considerations. In terms of the Fermi-Dirac distribution function on both bands $f[E_\lambda(\mathbf{p})]$ for the Bogoliubov quasiparticles, the supercurrent can be written in the standard quantum-mechanical form:

$$\begin{aligned} j_i^s &= n v_i^s + \frac{1}{V} \sum_{\mathbf{p}\lambda} v_{\mathbf{p}i}(\mathbf{p}) f(E_\lambda(\mathbf{p}) + \mathbf{p} \cdot \mathbf{v}^s) \\ &= n v_i^s + \frac{1}{V} \sum_{\mathbf{p}\lambda} v_{\mathbf{p}i} \left\{ f(E_\lambda(\mathbf{p})) + \frac{\partial f(E_\lambda(\mathbf{p}))}{\partial E_\lambda(\mathbf{p})} p_j v_j^s \right\} \\ &= \left\{ n \delta_{ij} - \frac{1}{V} \sum_{\mathbf{p}\lambda} \frac{p_i}{m} \left(-\frac{\partial f(E_\lambda(\mathbf{p}))}{\partial E_\lambda(\mathbf{p})} \right) p_j \right\} v_j^s. \end{aligned} \quad (2.71)$$

This immediately implies the definition of the normal fluid density in the form

$$n_{ij}^n = \frac{1}{V} \sum_{\mathbf{p}\lambda} p_i v_j y_\lambda(\mathbf{p}). \quad (2.72)$$

Thus, the results obtained with this simple local equilibrium picture are in agreement with the results in Ref. [82].

2.5.2 Specific heat capacity

In order to derive the specific heat capacity, I start from an expression for the entropy of a NCS, which has to be written in the general form

$$\begin{aligned} T\sigma(T) &= -\frac{k_B}{V} \sum_{\mathbf{p}\lambda} f[E_\lambda(\mathbf{p})] \ln f[E_\lambda(\mathbf{p})] + \{1 - f[E_\lambda(\mathbf{p})]\} \ln\{1 - f[E_\lambda(\mathbf{p})]\} \\ &= \frac{1}{V} \sum_{\mathbf{p}\lambda} \xi_\lambda^2(\mathbf{p}) y_{\mathbf{p}}^{(\lambda)}. \end{aligned} \quad (2.73)$$

The change of the entropy as a consequence of a temperature change δT can then be written in the form [82]

$$T\delta\sigma(T) = \frac{1}{V} \sum_{\mathbf{p}\lambda} E_\lambda(\mathbf{p}) \delta\nu_\lambda(\mathbf{p}), \quad (2.74)$$

where the quasiparticle distribution function is given by Eq. (2.31). In the static and homogeneous limit, i.e. $\omega \rightarrow 0$ and $\mathbf{q} \rightarrow 0$, this expression simplifies considerably to $\delta\nu_\lambda(\mathbf{k}) = y_\lambda(\mathbf{k})\delta E_\lambda(\mathbf{k})$. The quasiparticle energy shift for a temperature change is $\delta E_\lambda(\mathbf{k}) = (E_\lambda(\mathbf{k})/T - \partial E_\lambda(\mathbf{k})/\partial T)\delta T$ for each band [82]. Hence, the result for the entropy change reads

$$\begin{aligned} T\delta\sigma(T) &= \frac{1}{V} \sum_{\mathbf{p}\lambda} y_\lambda(\mathbf{p}) E_\lambda(\mathbf{p}) \left[E_\lambda(\mathbf{p}) - T \frac{\partial E_\lambda(\mathbf{p})}{\partial T} \right] \delta T \\ &= C_V(T) \delta T \end{aligned} \quad (2.75)$$

and one may easily identify the specific heat capacity as

$$C_V(T) = \frac{1}{V} \sum_{\mathbf{p}\lambda} y_\lambda(\mathbf{p}) \left[E_\lambda^2(\mathbf{p}) - \frac{T}{2} \frac{\partial \Delta_\lambda^2(\mathbf{p})}{\partial T} \right]. \quad (2.76)$$

An alternative way to derive the specific heat capacity employs again the concept of local equilibrium:

$$T\delta\sigma(T) = \frac{1}{V} \sum_{\mathbf{p}\lambda} E_\lambda(\mathbf{p}) \delta f(E_\lambda(\mathbf{p})). \quad (2.77)$$

The change of the BQP (Fermi–Dirac) distribution function with temperature has two causes: first the direct change $T \rightarrow T + \delta T$ and second the change of the BQP energy with temperature through the T -dependence of the energy gap:

$$\delta f(E_\lambda(\mathbf{p})) = f\left(\frac{E_\lambda(\mathbf{p}) + \frac{\partial E_\lambda(\mathbf{p})}{\partial T} \delta T}{k_B [T + \delta T]}\right) - f\left(\frac{E_\lambda(\mathbf{p})}{k_B T}\right) \quad (2.78)$$

$$\delta f(E_\lambda(\mathbf{p})) = \underbrace{\left(-\frac{\partial f(E_\lambda(\mathbf{p}))}{\partial E_\lambda(\mathbf{p})} \right)}_{y_\lambda(\mathbf{p})} \left(\frac{E_{\mathbf{p}\lambda}^0}{T} - \frac{\partial E_\lambda(\mathbf{p})}{\partial T} \right) \delta T. \quad (2.79)$$

Hence, one arrives at the same result for the entropy change

$$\begin{aligned} T\delta\sigma(T) &= \frac{1}{V} \sum_{\mathbf{p}\lambda} y_\lambda(\mathbf{p}) E_\lambda(\mathbf{p}) \left[E_\lambda(\mathbf{p}) - T \frac{\partial E_\lambda(\mathbf{p})}{\partial T} \right] \delta T \\ &= C_V(T) \delta T \end{aligned} \quad (2.80)$$

and the result for the specific heat capacity is confirmed. Again, like in the case of the normal and superfluid density, the result for the specific heat capacity can be viewed to consist of contributions from the two bands, in the sense that the sum over the spin projections $\sigma = \pm 1$ is replaced by a sum over the pseudospin variable $\lambda = \pm$.

2.6 Summary

In this chapter, I derived response and transport functions for non-centrosymmetric superconductors from a kinetic theory. The starting point is a generalized von Neumann equation which describes the evolution of the momentum distribution function in time and space, and I derived a linearized matrix-kinetic (Boltzmann) equation in ω - \mathbf{q} -space. This kinetic equation (MKE) is a 4×4 matrix equation in both particle-hole (Nambu) and spin space. I explored the Nambu-structure and solved the kinetic equation quite generally by first performing an SU(2) rotation into the band-basis and second applying a Bogoliubov-transformation into quasiparticle space. The theory is particle-hole symmetric, applies to any kind of antisymmetric spin-orbit coupling, and holds for arbitrary quasiclassical frequency and momentum with $\omega \ll E_F$ and $|\mathbf{q}| \ll k_F$. The main results of this chapter are represented by the following equations:

- Eq. (2.8) describes the kinetics in NCS. An important point consisted in the clarification of the Nambu-structure of the involved quantities. The MKE transformed to the band-basis is given by Eq. (2.17) and the Bogoliubov-transformed MKE is found in Eq. (2.28).
- In quasiparticle space the solution of the MKE is given in Eq. (2.31), which is used e.g. in Section 2.5.2 in order to derive the specific heat capacity.
- The general analytical solution of the MKE is found in Eq. (2.49) with the matrix elements in Eq. (2.50) or in a more convenient form in Eq. (2.55). Together with the characteristic vertex-functions listed in Table 2.1, this solution of the MKE provides any response or transport function for NCS.

Furthermore, assuming a separable ansatz for the pairing interaction, I discussed the gauge invariance and charge conservation for this theory. A detailed analysis about the gauge invariance and the associated collective order parameter modes will be presented in Chapter 3. Within this

2 Response and transport in the presence of ASOC

framework, I derived expressions for the normal and superfluid density and compared the results in the static and long-wavelength limit with those from a local equilibrium analysis. The same investigations were done for the specific heat capacity. In both cases the same results were recovered, as expected.

3 New gauge modes

The following chapter is devoted to an interesting consequence that emerges when solving the matrix–kinetic equation in Chapter 2 and deserves its own chapter. By demonstrating the gauge invariance of this theory, I recognized, that there are two gauge modes with interesting properties in NCS. Since the observability of gauge modes in superconductors is rather limited (see summary of this chapter), this topic is interesting for other reasons. It is well–known that the original BCS description is lacking gauge invariance, and associated with this, violates the number conservation. Nambu, who received the Nobel Prize in 2008 “for the discovery of the mechanism of spontaneous broken symmetry in subatomic physics”, points out in his Nobel lecture [83], that the pairing interaction, which gives rise to the Cooper–instability, causes also collective excitations in the superconductor. In the BCS–case these are on the one hand the amplitude fluctuations and on the other hand the phase fluctuations of the order parameter. The phase fluctuations couple to the density and current response, restore the particle number conservation, and with it the gauge invariance. Hence, the mode connected to these fluctuations is called gauge mode. Other names are Nambu–Goldstone mode [83] or Anderson–Bogoliubov mode [84, 85].

3.1 Introduction

An excellent introduction to collective order parameter modes is found in the book “The superfluid phases of helium 3” by Vollhardt and Wölfle [86]. In spin–triplet systems, Leggett predicted the SBSOS¹ modes [80, 81]. There, the order parameter can be described by a complex vector, where each component can oscillate against each other. Combined, these are 18 possible collective modes, which were classified in detail by Wölfle [87]. The temperature dependence of these modes (called e.g. clapping, normal–flapping, super–flapping) was analyzed in Ref. [88, 89]. Leggett predicted also a collective mode in two–band superconductors which arises from fluctuations of the phase difference between the order parameters on both bands [90]. More than 40 years later this mode could finally be observed experimentally in MgB₂ [91] and is still attracting interest [92]. The gauge modes, I will discuss in the following, are probably different from Leggett’s mode, since the order parameters on both bands in NCS are not independent of each other.

In charged Fermi systems, the gauge modes are shifted to the plasma frequency through the Anderson–Higgs mechanism [93]. Within the kinetic–theory approach described in Chapter 2 this is done by taking the long–range Coulomb interaction into account. For centrosymmetric unconventional superconductors this is explained in Ref. [71]. In this chapter, I will investigate the gauge modes before Coulomb renormalization.

¹spontaneously broken spin orbit symmetry

3.2 Role of phase fluctuations

The gauge modes are derived from the phase fluctuations of the order parameter $\delta\Delta_\mu^-$ on both sheets of the Fermi surface $\mu = \pm$. Using the equilibrium gap equation and a separable pairing–interaction $V_{\mathbf{k}\mathbf{k}'}^{\mu\nu} = \Gamma_s + \mu\nu\Gamma_t|\hat{\gamma}_\mathbf{k}||\hat{\gamma}_{\mathbf{k}'}$ where Γ_s and Γ_t represent the singlet and triplet contribution, one arrives at [see Eq. (2.59) in Chapter 2]:

$$\sum_\nu \frac{\delta\Delta_\nu^-(\mathbf{k})}{|\Delta_\nu^-(\mathbf{k})|} \sum_{\mathbf{k}'} V_{\mathbf{k}\mathbf{k}'}^{\mu\nu} \frac{\omega^2 - \eta_\nu^2}{4|\Delta_\nu^-(\mathbf{k}')|} \lambda_\nu(\mathbf{k}') = \sum_{\mathbf{k}'\nu} V_{\mathbf{k}\mathbf{k}'}^{\mu\nu} \frac{\omega\delta\xi_\nu^+(\mathbf{k}') + \eta_\nu\delta\xi_\nu^-(\mathbf{k}')}{2\Delta_\nu^-(\mathbf{k}')} \lambda_\nu(\mathbf{k}') . \quad (3.1)$$

These are two coupled equations (for $\mu = \pm$) which determine the phase fluctuations of the order parameter $\delta\Delta_\nu^-(\mathbf{k})/2|\Delta_\nu^-(\mathbf{k})|$. In NCS, one finds fluctuations on both spin–orbit split bands. The gauge invariance of the kinetic theory and charge conservation can only be demonstrated by taking both phase fluctuations into account.

In order to calculate the dispersion of the gauge modes, it is convenient to introduce as an additional parameter the strength of the spin–orbit coupling α , which can be used as expansion parameter. In agreement with the previous definition (see Section 1.1), α is just the magnitude of the spin–orbit vector:

$$\gamma_\mathbf{k} = \alpha\hat{\gamma}_\mathbf{k} \quad (3.2)$$

$$\hat{\gamma}_\mathbf{k} = \frac{\gamma_\mathbf{k}}{\sqrt{\langle |\gamma_\mathbf{k}|^2 \rangle_{FS}}} . \quad (3.3)$$

Thus, the energy dispersion and the order parameter on both bands read:

$$\xi_\pm(\mathbf{k}) = \xi_\mathbf{k} \pm \alpha|\hat{\gamma}_\mathbf{k}| \quad (3.4)$$

$$\Delta_\pm(\mathbf{k}) = \psi \pm d\alpha|\hat{\gamma}_\mathbf{k}| . \quad (3.5)$$

In order to proceed analytically, the following two assumptions were required

- The equilibrium phase of the order parameter is independent of \mathbf{k} and band index μ : $\hat{\Delta}_\mu(\mathbf{k}) = \Delta_\mu(\mathbf{k})/|\Delta_\mu(\mathbf{k})| = e^{i\phi} \equiv \hat{\Delta}$. This means together with the ansatz $\Delta_\pm(\mathbf{k}) = \psi \pm \alpha d|\hat{\gamma}_\mathbf{k}|$ that I allow for an overall phase ϕ , which has to be the same for each band and therefore is also fixed between the singlet and triplet contribution. Whether fluctuations of the phase difference between both bands like Leggett’s mode are possible, might be an issue for further investigations.
- The usual assumption, that the phase fluctuations are independent of \mathbf{k} : $\delta\Delta_\mu^-(\mathbf{k})/2|\Delta_\mu^-(\mathbf{k})| \equiv i\delta\phi_\mu(\mathbf{q}, \omega)/2$.

With these assumptions, the amplitude ($\delta\Delta_\mu^+$) and phase fluctuations ($\delta\Delta_\mu^-$) decouple. The phase fluctuations are then determined from Eq. (3.1) by solving this system of linear equations and

inserting the pairing–interaction. The result reads:

$$\frac{\delta\Delta_+^-}{2|\Delta_+|} = \frac{\sum_{\mathbf{p},\mathbf{p}'} B_+(\mathbf{p})A_-(\mathbf{p}') [|\hat{\gamma}_{\mathbf{p}}| + |\hat{\gamma}_{\mathbf{p}'}|] + B_-(\mathbf{p})A_-(\mathbf{p}') [|\hat{\gamma}_{\mathbf{p}'}| - |\hat{\gamma}_{\mathbf{p}}|]}{\sum_{\mathbf{p},\mathbf{p}'} A_-(\mathbf{p})A_+(\mathbf{p}') [|\hat{\gamma}_{\mathbf{p}}| + |\hat{\gamma}_{\mathbf{p}'}|]} \quad (3.6)$$

$$\frac{\delta\Delta_-^-}{2|\Delta_-|} = \frac{\sum_{\mathbf{p},\mathbf{p}'} B_+(\mathbf{p})A_+(\mathbf{p}') [|\hat{\gamma}_{\mathbf{p}'}| - |\hat{\gamma}_{\mathbf{p}}|] + B_-(\mathbf{p})A_+(\mathbf{p}') [|\hat{\gamma}_{\mathbf{p}}| + |\hat{\gamma}_{\mathbf{p}'}|]}{\sum_{\mathbf{p},\mathbf{p}'} A_-(\mathbf{p})A_+(\mathbf{p}') [|\hat{\gamma}_{\mathbf{p}}| + |\hat{\gamma}_{\mathbf{p}'}|]}, \quad (3.7)$$

with the abbreviations

$$A_\mu = \frac{\omega^2 - \eta_\mu^2}{2|\Delta_\mu|} \lambda_\mu, \quad B_\mu = \frac{\omega\delta\xi_\mu^+ + \eta_\mu\delta\xi_\mu^-}{2\Delta_\mu} \lambda_\mu. \quad (3.8)$$

In what follows, I will demonstrate particle conservation for arbitrary momentum \mathbf{q} in NCS. For this purpose, the sum rules

$$\frac{1}{2} \sum_{\mu} V_{\mathbf{k}\mathbf{p}}^{\mu\nu} = \Gamma_s \quad \text{singlet projection} \quad (3.9)$$

$$\frac{1}{2} \sum_{\mu} \mu V_{\mathbf{k}\mathbf{p}}^{\mu\nu} = \nu \Gamma_t |\hat{\gamma}_{\mathbf{k}}| |\hat{\gamma}_{\mathbf{p}}| \quad \text{triplet projection} \quad (3.10)$$

for the pairing interaction are quite useful. Applying both sum rules to Eq. (3.1) one gets

$$\sum_{\mathbf{p}\nu} \frac{\omega^2 - \eta_\nu^2(\mathbf{p})}{2|\Delta_\nu(\mathbf{p})|} \lambda_\nu(\mathbf{p}) \frac{\delta\Delta_\nu^-(\mathbf{k})}{2|\Delta_\nu(\mathbf{k})|} = \sum_{\mathbf{p}\nu} \frac{\omega\delta\xi_\nu^+(\mathbf{p}) + \eta_\nu(\mathbf{p})\delta\xi_\nu^-(\mathbf{p})}{2|\Delta_\nu(\mathbf{p})|} \lambda_\nu(\mathbf{p}) \quad (3.11)$$

$$\sum_{\mathbf{p}\nu} \nu |\hat{\gamma}_{\mathbf{p}}| \frac{\omega^2 - \eta_\nu^2(\mathbf{p})}{2|\Delta_\nu(\mathbf{p})|} \lambda_\nu(\mathbf{p}) \frac{\delta\Delta_\nu^-(\mathbf{k})}{2|\Delta_\nu(\mathbf{k})|} = \sum_{\mathbf{p}\nu} \nu |\hat{\gamma}_{\mathbf{p}}| \frac{\omega\delta\xi_\nu^+(\mathbf{p}) + \eta_\nu(\mathbf{p})\delta\xi_\nu^-(\mathbf{p})}{2|\Delta_\nu(\mathbf{p})|} \lambda_\nu(\mathbf{p}). \quad (3.12)$$

With the abbreviations, defined in Eq. (3.8), this simplifies to

$$\sum_{\mathbf{p}\nu} A_\nu(\mathbf{p}) \frac{\delta\Delta_\nu^-(\mathbf{k})}{2|\Delta_\nu(\mathbf{k})|} = \sum_{\mathbf{p}\nu} B_\nu(\mathbf{p}) \quad (3.13)$$

$$\sum_{\mathbf{p}\nu} \nu |\hat{\gamma}_{\mathbf{p}}| A_\nu(\mathbf{p}) \frac{\delta\Delta_\nu^-(\mathbf{k})}{2|\Delta_\nu(\mathbf{k})|} = \sum_{\mathbf{p}\nu} \nu |\hat{\gamma}_{\mathbf{p}}| B_\nu(\mathbf{p}). \quad (3.14)$$

Now, one has to go back to Eq. (2.56) in Chapter 2:

$$\omega\delta n_\mu - \eta_\mu [\delta n_\mu + \Phi_\mu \delta\xi_\mu] = -\lambda_\mu [\omega\delta\xi_\mu^+ + \eta_\mu\delta\xi_\mu^-] + \lambda_\mu (\omega^2 - \eta_\mu^2) \frac{\delta\Delta_\mu^-}{2\Delta_\mu}. \quad (3.15)$$

3 New gauge modes

The r.h.s. of this equation may be rewritten with the abbreviations used in Eq. (3.8):

$$\text{r.h.s.} = 2\Delta_\mu(\mathbf{k}) \left[A_\mu(\mathbf{k}) \frac{\delta\Delta_\mu^-(\mathbf{k})}{2|\Delta_\mu(\mathbf{k})|} - B_\mu(\mathbf{k}) \right]. \quad (3.16)$$

Performing the sum $\sum_{\mathbf{k}\mu} \dots$ on both sides of Eq. (3.15) finally leads to

$$\omega\delta n - \mathbf{q} \cdot \mathbf{j} = 2\psi \sum_{\mathbf{k}\mu} \underbrace{A_\mu(\mathbf{k}) \frac{\delta\Delta_\mu^-(\mathbf{p})}{2|\Delta_\mu(\mathbf{p})|} - B_\mu(\mathbf{k})}_{=0, \text{ c.f. Eq. (3.13)}} \quad (3.17)$$

$$+ 2d \sum_{\mathbf{k}\mu} \underbrace{\mu|\hat{\gamma}_{\mathbf{k}}| A_\mu(\mathbf{k}) \frac{\delta\Delta_\mu^-(\mathbf{p})}{2|\Delta_\mu(\mathbf{p})|} - |\hat{\gamma}_{\mathbf{k}}| B_\mu(\mathbf{k})}_{=0, \text{ c.f. Eq. (3.14)}} \quad (3.18)$$

$$\omega\delta n - \mathbf{q} \cdot \mathbf{j} = 0, \quad (3.19)$$

with the particle density n and the current density \mathbf{j} . Thus, through this continuity equation, I demonstrated the most important role of the phase fluctuations, namely to restore the number conservation law and, accompanied with this, the gauge invariance for arbitrary frequencies ω and momentum transfers \mathbf{q} .

Now it is instructive to take a look at the homogeneous, i.e. $\mathbf{q} \rightarrow 0$ limit. In this limit, Eq. (3.15) reads (see Appendix A for the $\mathbf{q} \rightarrow 0$ -expansion of all quantities):

$$\delta n_\mu(\mathbf{k}) = \lambda_\mu(\mathbf{k}) \left[-\xi_\mu^+(\mathbf{k}) + \omega \frac{\delta\Delta_\mu^-(\mathbf{k})}{2|\Delta_\mu(\mathbf{k})|} \right]. \quad (3.20)$$

For the electromagnetic response, one may insert for the external perturbations $\xi_\mu^+(\mathbf{k}) = e\Phi^{\text{ext.}}$, even in \mathbf{k} , the scalar electromagnetic potential $\Phi^{\text{ext.}}$ as described in Section 2.2 and in particular in Table 2.1. The phase fluctuations may be abbreviated by $i\delta\phi_\mu(\mathbf{q}, \omega)/2$ (see assumptions) and going back from Fourier-space into the time-domain, the above equation is equivalent to

$$\delta n_\mu(\mathbf{k}) = -e\lambda_\mu(\mathbf{k}) \left[\Phi^{\text{ext.}} - \frac{1}{c} \frac{\partial}{\partial t} \left(-\frac{c}{2e} \delta\phi_\mu \right) \right]. \quad (3.21)$$

Clearly, the last term $-c/2e \delta\phi_\mu$ is the gauge field for NCS (see Nambu's Nobel lecture for the BCS analoge in Ref. [83]). The phase fluctuations $\delta\phi_\mu$ can be evaluated from Eq. (3.1) for $\mathbf{q} \rightarrow 0$ with the result:

$$\frac{i}{2} \delta\phi_\mu(\mathbf{q}, \omega) = \frac{\delta\Delta_\mu^-(\mathbf{k})}{2|\Delta_\mu(\mathbf{k})|} = \frac{e\Phi^{\text{ext.}}}{\omega}. \quad (3.22)$$

This equation is nothing else than the well-known Josephson equation for NCS in Fourier-space, since it connects the time-derivative of the superconducting phase with an applied electromag-

netic potential. In that sense, Eqs. (3.6) and (3.7) are finite- \mathbf{q} generalizations of the Josephson relation for NCS. Finally, inserting this expression into Eq. (3.21), one recovers again the density conservation (in the homogenous limit):

$$\delta n_\mu(\mathbf{k}) = \lambda_\mu(\mathbf{k}) \left[-e\Phi^{\text{ext.}} + \omega \frac{e\Phi^{\text{ext.}}}{\omega} \right] = 0. \quad (3.23)$$

Here, one can see that the densities on both bands $\mu = \pm$ are conserved separately. The two gauge modes, and therefore the two gauge bosons in NCS superconductors, thus reflect through the Goldstone theorem [94] the (charge) density conservation on each band.

3.3 Results for the gauge modes in NCS

In order to calculate the dispersion of the gauge modes, one has to examine the phase fluctuations given in Eqs. (3.6) and (3.7). Since the denominator is the same for the phase fluctuations on both bands, the gauge modes are obtained from the poles of $\delta\Delta_\mu^-/2\Delta_\mu$:

$$\left\langle \frac{\omega^2 - \eta_-^2}{4|\Delta_-|} \lambda_- |\hat{\gamma}_\mathbf{k}| \right\rangle \left\langle \frac{\omega^2 - \eta_+^2}{4|\Delta_+|} \lambda_+ \right\rangle + \left\langle \frac{\omega^2 - \eta_-^2}{4|\Delta_-|} \lambda_- \right\rangle \left\langle \frac{\omega^2 - \eta_+^2}{4|\Delta_+|} \lambda_+ |\hat{\gamma}_\mathbf{k}| \right\rangle = 0, \quad (3.24)$$

with $\langle \dots \rangle = \sum_{\mathbf{k}} \dots$. This is a fourth order equation in ω which can be solved analytically with the result:

$$\omega_\pm^2 = \frac{1}{2} \left[\frac{\beta_{1+} + \beta_{1-}}{\alpha_+ + \alpha_-} + \frac{\alpha_- \beta_{0+} + \alpha_+ \beta_{0-}}{\alpha_+ + \alpha_-} \right] \pm \frac{r}{2} \left| \frac{\beta_{1+} + \beta_{1-}}{\alpha_+ + \alpha_-} - \frac{\alpha_- \beta_{0+} + \alpha_+ \beta_{0-}}{\alpha_+ + \alpha_-} \right|, \quad (3.25)$$

using the following abbreviations:

$$r = \sqrt{1 + 4 \frac{(\beta_{0+} - \beta_{0-})(\alpha_- \beta_{1+} - \alpha_+ \beta_{1-})}{(\beta_{1+} + \beta_{1-} - \alpha_- \beta_{0+} - \alpha_+ \beta_{0-})^2}} \xrightarrow{\text{no SOC}} 1; \quad (3.26)$$

$$\alpha_\mu = \frac{\langle |\hat{\gamma}_\mathbf{k}| \frac{\lambda_{\mathbf{k}\mu}}{2\Delta_{\mathbf{k}\mu}} \rangle}{\langle \frac{\lambda_{\mathbf{k}\mu}}{2\Delta_{\mathbf{k}\mu}} \rangle}; \quad \beta_{n\mu} = \frac{\langle |\hat{\gamma}_\mathbf{k}|^n (\mathbf{v}_\mathbf{k} \cdot \mathbf{q})^2 \frac{\lambda_{\mathbf{k}\mu}}{2\Delta_{\mathbf{k}\mu}} \rangle}{\langle \frac{\lambda_{\mathbf{k}\mu}}{2\Delta_{\mathbf{k}\mu}} \rangle}. \quad (3.27)$$

Note that Eq. (3.25) is an exact, but implicit solution. For larger frequencies corrections from the ω -dependent Tsuneto-function $\lambda_\mu(\mathbf{k}, \mathbf{q}, \omega)$ have also to be taken into account. However, I am interested in the asymptotic behavior $\omega, \mathbf{q} \rightarrow 0$, only. In this limit (see Appendix A), the Tsuneto-function is just constant w.r.t. the frequency and momentum transfer. In order to continue an analytical evaluation, it is convenient to expand the solution (3.25) to the lowest

3 New gauge modes

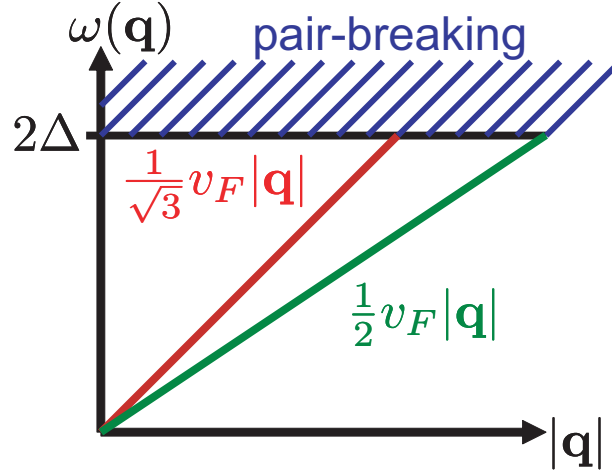


Figure 3.1: Illustration of the gauge modes for NCS of tetragonal, tetrahedral and cubic symmetry before charge renormalization. Both modes disperse for small momenta linear in q but with different slopes.

order in the spin-orbit coupling parameter α^2 :

$$\omega_{1,2}^2 = \frac{1}{2} \left[\frac{\langle \eta^2 |\hat{\gamma}_{\mathbf{k}}| \lambda \rangle}{\langle |\hat{\gamma}_{\mathbf{k}}| \lambda \rangle} + \frac{\langle \eta^2 \lambda \rangle}{\langle \lambda \rangle} \right] + \mathcal{O}(\alpha^2) \pm \left[\frac{1}{2} \left| \frac{\langle \eta^2 |\hat{\gamma}_{\mathbf{k}}| \lambda \rangle}{\langle |\hat{\gamma}_{\mathbf{k}}| \lambda \rangle} - \frac{\langle \eta^2 \lambda \rangle}{\langle \lambda \rangle} \right| + \mathcal{O}(\alpha^2) \right]. \quad (3.28)$$

Here, I neglected the effect of the spin-orbit split bands, since $\xi_{\mu}(\mathbf{k}) = \xi_{\mathbf{k}} + \mu\alpha|\hat{\gamma}_{\mathbf{k}}| \xrightarrow{\alpha \rightarrow 0} \xi(\mathbf{k})$. The prefactors of both $\mathcal{O}(\alpha^2)$ -terms are lengthy and not shown here. Note that $|\hat{\gamma}_{\mathbf{k}}|$ does not cancel in the numerator and denominator. Thus there are two distinct dispersions, even for arbitrary small ASOC. For vanishing ASOC, i.e. $\alpha = 0$, the well-known result for the Anderson-Bogoliubov mode is recovered [85, 84]:

$$\omega_{\text{AB}}^2 = \frac{\langle \eta^2 \lambda \rangle}{\langle \lambda \rangle} \xrightarrow{\omega \rightarrow 0} \frac{1}{3} v_F^2 |\mathbf{q}|^2. \quad (3.29)$$

Performing the momentum-integration

$$\langle \dots \rangle = N_F \int_{-\infty}^{\infty} d\xi_{\mathbf{k}} \langle \dots \rangle_{\text{FS}}, \quad (3.30)$$

it is now possible to examine the dispersion of the gauge modes for low frequencies and different

²Note that this expression is not valid for exactly $\alpha = 0$, since on the one hand broken inversion symmetry is assumed and on the other hand, the strength of the ASOC as well as the triplet-contribution to the gap is infinitesimal small. An expression for $\alpha = 0$ is given in the following Eq. (3.29).

3.3 Results for the gauge modes in NCS

type of ASOC. Additional to the tetragonal symmetry ($\mathcal{G} = C_{4v}$) and to the cubic symmetry ($\mathcal{G} = O$) defined in Section 1.1, I want to introduce here another class of NCS with tetrahedral point group $\mathcal{G} = T_d$ which is also of interest [39, 38]. For the tetrahedral point group, the spin-orbit vector $\gamma_{\mathbf{k}}$ reads [66]

$$\gamma_{\mathbf{k}} = g \left[\hat{k}_x(\hat{k}_y^2 - \hat{k}_z^2)\hat{\mathbf{e}}_x + \hat{k}_y(\hat{k}_z^2 - \hat{k}_x^2)\hat{\mathbf{e}}_y + \hat{k}_z(\hat{k}_x^2 - \hat{k}_y^2)\hat{\mathbf{e}}_z \right]. \quad (3.31)$$

In spherical coordinates and normalized, this yields:

$$|\hat{\gamma}_{\mathbf{k}}| = \frac{\sqrt{35}}{2} |\sin \theta| \sqrt{\cos^2 \theta - \cos^2 \phi \sin^2 \phi \sin^2 \theta (8 - 9 \sin^2 \theta)}. \quad (3.32)$$

Thus, I get for ω , \mathbf{q} , $\alpha \rightarrow 0$ and $|\hat{\gamma}_{\mathbf{k}}| \propto \sin \theta$ (Rashba-type of SOC, as e.g. in CePt₃Si):

$$\frac{\langle \eta^2 |\hat{\gamma}_{\mathbf{k}}|\lambda \rangle}{\langle |\hat{\gamma}_{\mathbf{k}}|\lambda \rangle} = \frac{1}{4} v_{\text{F}}^2 |\mathbf{q}|^2. \quad (3.33)$$

For a $\hat{\gamma}_{\mathbf{k}}$ -vector with cubic or tetrahedral symmetry (as e.g. in Li₂Pd_xPt_{3-x}B or Ln₂C₃ with Ln=La, Y), one gets

$$\frac{\langle \eta^2 |\hat{\gamma}_{\mathbf{k}}|\lambda \rangle}{\langle |\hat{\gamma}_{\mathbf{k}}|\lambda \rangle} = \frac{1}{3} v_{\text{F}}^2 |\mathbf{q}|^2. \quad (3.34)$$

For the highly symmetric cubic point group, this result is not surprising, since the first term $\hat{\gamma}_{\mathbf{k}} \propto \hat{\mathbf{k}}$ is pseudo-isotropic. Interestingly, the second term for the cubic symmetry does not affect the prefactor 1/3. Finally for small ASOC the dispersion of both gauge modes reads:

$$\omega_+^2 = \frac{1}{3} v_{\text{F}}^2 |\mathbf{q}|^2 + \mathcal{O}(\alpha^2) \quad \text{Anderson-Bogoliubov mode} \quad (3.35)$$

$$\omega_-^2 = \begin{cases} \frac{1}{4} v_{\text{F}}^2 |\mathbf{q}|^2 + \mathcal{O}(\alpha^2) & \text{for } \mathcal{G} = C_{4v} \\ \frac{1}{3} v_{\text{F}}^2 |\mathbf{q}|^2 + \mathcal{O}(\alpha^2) & \text{for } \mathcal{G} = O \text{ and } \mathcal{G} = T_d \end{cases} \quad (3.36)$$

Thus, I found two gauge modes with linear $|\mathbf{q}|$ -dispersion for NCS (see Fig 3.1 for a schematic illustration). Of course, in charged Fermi systems, the gauge modes are shifted to the plasma frequency, usually above the pair-breaking continuum, but this should not change the different behaviors in the slope. One gauge mode (ω_+) can be identified (for $\alpha \rightarrow 0$) as the well-known Anderson-Bogoliubov mode. The second one (ω_-) appears for broken inversion symmetry and depends on the symmetry of the spin-orbit vector $\hat{\gamma}_{\mathbf{k}}$ (which is determined by the symmetry of the crystal structure). The slope of both dispersions is modified by the strength of the ASOC (α) according to $\mathcal{O}(\alpha^2)$ and can be different even for arbitrarily small (but non-vanishing) ASOC, which is displayed schematically in Fig. 3.2.

3 New gauge modes

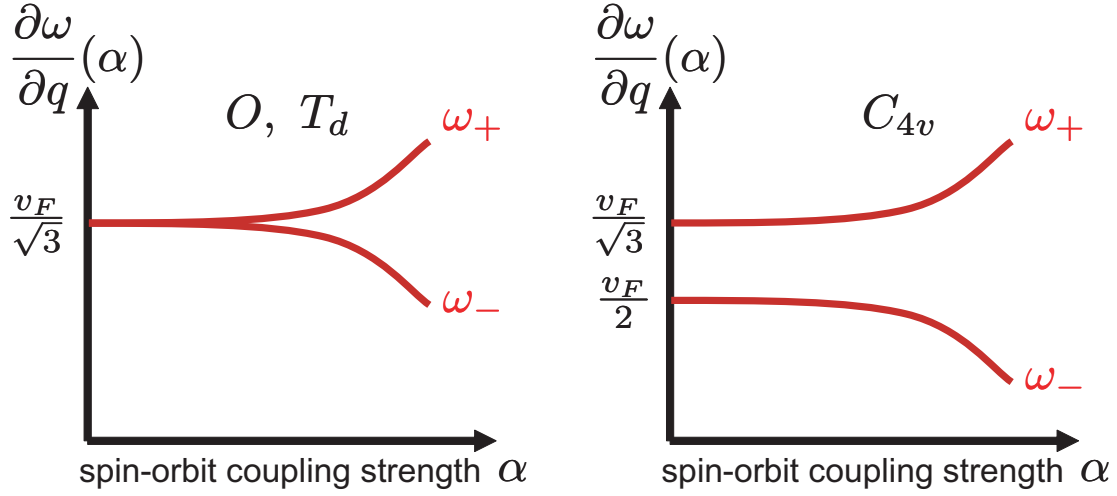


Figure 3.2: Illustration of the slope at $\mathbf{q} \rightarrow 0$ of the gauge modes in NCS before charge renormalization as a function of the spin-orbit coupling strength α (defined through $\gamma_{\mathbf{k}} = \alpha \hat{\gamma}_{\mathbf{k}}$). The behavior for the cubic and tetrahedral symmetry (left-hand side) is clearly different from the tetragonal case (right-hand side).

3.4 Summary and discussion

For any superconductor with inversion symmetry (singlet or triplet), the gauge mode disperses according to $\omega(\mathbf{q}) = v_F/\sqrt{3}|\mathbf{q}|$, gives rise to a generalized Josephson relation, and preserves gauge invariance for the density and current response. At the same time, the particle number conservation is restored, when phase fluctuations are taken into account. I calculated the phase fluctuations in non-centrosymmetric superconductors (NCS) for each of the two spin-orbit split bands for a separable pairing interaction (neglecting the singlet-triplet mixing term, i.e. without Dzyaloshinskii-Moriya interaction). It remains the subject of further investigations, how gauge invariance could be demonstrated with a singlet-triplet mixing term in the pairing interaction. It turns out that the phase fluctuations give rise to two gauge modes in NCS. One of them reflects the singlet contribution of the order parameter and is identical to the Anderson-Bogoliubov mode in the limit of vanishing ASOC. Most importantly, I discovered that the second gauge mode, which reflects the triplet contribution of the order parameter, is (a) unique to NCS and (b) depends on the symmetry of the $\gamma_{\mathbf{k}}$ -vector: I obtain for cubic and tetrahedral symmetry $v_F/\sqrt{3}$ for the slope of this gauge mode, whereas for tetragonal symmetry I find $v_F/2$.

The observability of these collective modes is inhibited, since the gauge modes are shifted to the plasma frequency, which usually lies well above the pair-breaking continuum and thus leads to strong damping [95]. However, in some highly anisotropic compounds, the plasma frequency may be located below the pair-breaking continuum, which may favor the observability [96]. The amplitude fluctuations of the order parameter (which start dispersing at 2Δ) were for the first time observed in NbSe₂ [97, 98] by Raman spectroscopy. Since the gauge modes couple to the charge

3.4 *Summary and discussion*

channel, many different experimental techniques are in principle suitable. Hirschfeld proposed e.g. electromagnetic power absorption measurements to detect collective modes in unconventional superconductors [99]. However, the most natural way to analyze gauge modes, especially in neutral superfluids, is via sound propagation measurements as e.g. ultrasound attenuation [86].

4 Theory of Raman response

Inelastic light scattering is a powerful tool to analyze vibrational and electronic properties of a system (see e.g. the review in Ref. [100]). Through photons, many different types of excitations can be generated, such as phonons, electronic excitations and magnons. Because of this, a typical Raman spectrum consists of a broad electronic background, superimposed with sharp phonon peaks at well-defined frequencies and for a well-known polarization setup. In the presence of antiferromagnetic correlations, broad two-magnon features are seen at higher frequencies. Particularly interesting is the Raman response in superconductors: Spectral weight is transferred from low frequencies to higher ones, low frequency power laws and pair-breaking peaks may occur, and the electron-phonon interaction changes the shape and position of the phonons.

In a side-project, I contributed to an experimental work on “Electronic and phononic Raman scattering in detwinned $\text{YBa}_2\text{Cu}_3\text{O}_{6.95}$ and $\text{Y}_{0.85}\text{Ca}_{0.15}\text{Ba}_2\text{Cu}_3\text{O}_{6.95}$: s -wave admixture to the $d_{x^2-y^2}$ -wave order parameter” by Bakr *et al.* [74]. We studied the electronic Raman effect as well as phonon anomalies in detwinned, slightly overdoped $\text{YBa}_2\text{Cu}_3\text{O}_{6.95}$ ($\text{YBCO}_{6.95}$) and moderately overdoped $\text{Y}_{0.85}\text{Ca}_{0.15}\text{Ba}_2\text{Cu}_3\text{O}_{6.95}$ ($\text{YBCO}_{6.95}:\text{Ca}$) single crystals. As a result of the detwinning, in both samples, modifications due to the a - b axis anisotropy could be observed in several phonon lineshapes. Since the theoretical model in this reference takes both, electronic and phononic contributions to the Raman response into account, we were able to disentangle both contributions. We concluded, that the Raman spectra are consistent with an s -wave admixture with an upper limit of 20%.

In the presence of nonmagnetic impurities the electronic Raman response changes significantly: additional weight at lower frequencies in the Raman spectra hides the low frequency power laws. Furthermore, the low temperature Raman response shows in certain symmetries a peculiarity called universal transport, i.e. the Raman response becomes independent of scattering parameters. More about these interesting properties are discussed in a publication together with Einzel [71]. Other results of this work were modified low temperature power laws and a connection between Raman response and ultrasound attenuation.

Raman response for singlet superconductors has been extensively studied for all different kinds of orbital anisotropies of the order parameter (see e.g. Ref. [101, 102]). For triplet order parameters such a detailed analysis has not yet been done. Only for Sr_2RuO_4 a few publications exist [103, 104], which focused mainly on the clapping mode, because in this two-dimensional analysis the order parameter is pseudo-isotropic and thus the Raman response is BCS-like. The only non-trivial example for calculated Raman spectra of a possible pairing state in a triplet superconductor is found in Ref. [105]. Since the pure triplet states can be realized in NCS as a limiting case, I will additionally discuss the spectra of the most common triplet states as e.g. the Balian-Werthamer (BW) state, the Anderson-Brinkman-Morel (ABM or axial) state, and the polar state.

4 Theory of Raman response

An important and unresolved issue for NCS is the determination of the triplet–singlet ratio in the superconducting order parameter. Analogous to the question about the size of an s –wave contribution in cuprates, the size of the triplet–singlet ratio in NCS remains a very interesting topic. For all NCS this ratio is still unknown, however, there are several proposals how to determine this ratio: Yuan *et al.* [65] analyzed the temperature–dependent penetration depth to estimate the triplet–singlet ratio for $\text{Li}_2\text{Pd}_x\text{Pt}_{3-x}\text{B}$, Vorontsov *et al.* [57] suggested spin currents, Fujimoto recommended Andreev reflection [58], and I propose electronic Raman scattering as a probe of the triplet–singlet ratio in NCS.

In the following, I will discuss the electronic Raman response in NCS for the most simple case: for $T = 0$, assuming spherical Fermi–surfaces, without impurities (i.e. collisionless limit) and for the inverse effective mass approximation for the Raman vertex without higher order vertex corrections¹. Precisely because of these simplifying assumptions, the results become particularly clear, even though analytical expressions could only be obtained in special cases.

4.1 Introduction

A Raman experiment detects the intensity of the scattered light with frequency–shift $\omega = \omega_I - \omega_S$, where the incoming photon of frequency ω_I is scattered on an elementary excitation and gives rise to a scattered photon with frequency ω_S and a momentum transfer \mathbf{q} . The differential photon scattering cross section of this process is given by Ref. [107]:

$$\frac{\partial^2 \sigma}{\partial \omega \partial \Omega} = \frac{\omega_S}{\omega_I} r_0^2 S_{\gamma\gamma}(\mathbf{q}, \omega), \quad (4.1)$$

with the solid angle Ω and the Thompson radius $r_0 = e^2/mc^2$. The generalized structure function $S_{\gamma\gamma}(\mathbf{q}, \omega)$ is connected through the fluctuation–dissipation theorem to the imaginary part of the Raman response function $\chi_{\gamma\gamma}(\mathbf{q}, \omega)$:

$$S_{\gamma\gamma}(\mathbf{q}, \omega) = -\frac{1}{\pi} [1 + n(\omega)] \chi''_{\gamma\gamma}(\mathbf{q}, \omega). \quad (4.2)$$

Here, $n(\omega) = [\exp(\omega/k_B T) - 1]^{-1}$ denotes the Bose distribution function. After Coulomb renormalization and in the long–wavelength limit ($\mathbf{q} = 0$), the Raman response function is given by the imaginary part of (see also Ref. [108])

$$\chi_{\gamma\gamma}(\omega) = \chi_{\gamma\gamma}^{(0)}(\omega) - \frac{[\chi_{\gamma 1}^{(0)}(\omega)]^2}{\chi_{11}^{(0)}(\omega)}. \quad (4.3)$$

¹Differences in the Raman spectra from vertex corrections are discussed in Ref. [101, 102, 106].

Within the notation developed in Chapter 2, the unscreened Raman response reads

$$\chi_{ab}^{(0)}(\omega) = \frac{1}{V} \sum_{\mathbf{p}, \sigma} a_{\mathbf{p}} b_{\mathbf{p}} \lambda_{\mathbf{p}}(\omega), \quad (4.4)$$

where the vertex-functions $a_{\mathbf{p}}, b_{\mathbf{p}}$ are either 1 or the corresponding momentum-dependent Raman vertex $\gamma \equiv \gamma_{\mathbf{k}}^{(R)}$ that describes the coupling of polarized light to the sample. The long-wavelength limit of the Tsuneto-function $\lambda_{\mathbf{p}}(\mathbf{q} = 0) = 4\Delta_{\mathbf{p}}^2 \theta_{\mathbf{p}} / (4E_{\mathbf{p}}^2 - \omega^2)$ is given in Appendix A and since I am interested in the $T = 0$ Raman response, it is possible to perform the integration on the energy variable $\xi_{\mathbf{k}}$ with the result (see also Ref. [101, 102]):

$$\Re \chi_{ab}^{(0)}(\omega) = \frac{N_{\text{F}}}{\omega} \begin{cases} \left\langle a_{\mathbf{k}} b_{\mathbf{k}} \frac{4|\Delta_{\mathbf{k}}|^2}{\sqrt{4|\Delta_{\mathbf{k}}|^2 - \omega^2}} \arctan \frac{\omega}{\sqrt{4|\Delta_{\mathbf{k}}|^2 - \omega^2}} \right\rangle_{FS} & \text{for } 2|\Delta_{\mathbf{k}}| > \omega \\ \left\langle a_{\mathbf{k}} b_{\mathbf{k}} \frac{2|\Delta_{\mathbf{k}}|^2}{\sqrt{\omega^2 - 4|\Delta_{\mathbf{k}}|^2}} \ln \frac{\omega - \sqrt{\omega^2 - 4|\Delta_{\mathbf{k}}|^2}}{\omega + \sqrt{\omega^2 - 4|\Delta_{\mathbf{k}}|^2}} \right\rangle_{FS} & \text{for } 2|\Delta_{\mathbf{k}}| \leq \omega \end{cases} \quad (4.5)$$

$$\Im \chi_{ab}^{(0)}(\omega) = \frac{\pi N_{\text{F}}}{\omega} \left\langle a_{\mathbf{k}} b_{\mathbf{k}} \Re \frac{2|\Delta_{\mathbf{k}}|^2}{\sqrt{\omega^2 - 4|\Delta_{\mathbf{k}}|^2}} \right\rangle_{FS}. \quad (4.6)$$

Here the Fermi-surface average is defined as

$$\langle \dots \rangle_{FS} = \int_0^{2\pi} \frac{d\phi}{4\pi} \int_0^{\pi} d\theta \sin \theta \dots \quad (4.7)$$

Note that the second term in Eq. (4.3) is often referred to as the screening contribution and originates from the gauge invariance. It becomes important for the A_1 symmetry and accounts for the particle conservation². Since the ASOC leads to a splitting of the Fermi surface, the total Raman response is given by $\chi_{\gamma\gamma}^{\text{total}} = \sum_{\lambda=\pm} \chi_{\gamma\gamma}^{\lambda}$ with $\chi_{\gamma\gamma}^{\pm} = \chi_{\gamma\gamma}(\Delta_{\pm})$, in which the usual summation over the spin variable σ is replaced by a summation over the pseudo-spin (band) index λ . With Eq. (1.11) the unscreened Raman response for both bands in the clean limit [$l \gg \xi(0)$ with the mean free path l and the coherence length $\xi(T = 0)$] can be analytically expressed as³

$$\Im \chi_{\gamma\gamma}^{(0)\pm} = \frac{\pi N_{\text{F}}^{\pm} \psi}{\omega} \Re \left\langle \gamma_{\mathbf{k}}^{(R)2} \frac{|1 \pm p|\gamma_{\mathbf{k}}|^2}{\sqrt{(\frac{\omega}{2\psi})^2 - |1 \pm p|\gamma_{\mathbf{k}}|^2}} \right\rangle_{FS}. \quad (4.8)$$

Here, N_{F}^{\pm} reflect the different densities of states on both bands and $\langle \dots \rangle_{FS}$ denotes an average

²According to a recent publication by Klein [92], this screening contribution vanishes in all symmetries (even in A_1) for two-band superconductors when vertex-corrections are taken into account (and for $\mathbf{q} = 0$). However, it is not yet clear, whether this result applies to NCS. This is an additional reason why I will show in all following graphs the screening contribution for the A_1 symmetry separately.

³Interband scattering processes are neglected.

4 Theory of Raman response

over the Fermi surface.

4.2 Raman vertices and pure triplet response

Raman scattering takes place at the center of the Brillouin zone. Therefore, I consider small momentum transfers ($\mathbf{q} \rightarrow 0$). This is due to the fact that the maximum momentum transfer by light q_{\max} is typically three orders of magnitude smaller than a typical wave vector k_{BZ} or k_F . Furthermore, I assume non-resonant scattering, which is the case when the photon energy is less than the optical band gap⁴. Then, the inverse effective mass approximation for the Raman tensor is usually a good approximation [110, 111]

$$\gamma_{\mathbf{k}}^{(R)} = m \sum_{i,j} \hat{\mathbf{e}}_i^S \frac{\partial^2 \epsilon(\mathbf{k})}{\partial k_i \partial k_j} \hat{\mathbf{e}}_j^I, \quad (4.9)$$

where $\hat{\mathbf{e}}^{S,I}$ denote the unit vectors of scattered and incident polarization light, respectively. The light polarization selects elements of this Raman tensor, where $\gamma_{\mathbf{k}}^{(R)}$ can be decomposed into its symmetry components and, after a straightforward calculation (see Appendix B), expanded into a set of basis functions on a spherical Fermi surface.

The results for the tetragonal group C_{4v} are

$$\gamma_{A_1}^{(R)} = \sum_{k=0}^{\infty} \sum_{l=0}^{l \leq k/2} \gamma_{k,l}^{(R)} \cos 4l\phi \sin^{2k} \theta \quad (4.10a)$$

$$\gamma_{B_1}^{(R)} = \sum_{k=1}^{\infty} \sum_{l=1}^{l \leq (k+1)/2} \gamma_{k,l}^{(R)} \cos(4l-2)\phi \sin^{2k} \theta \quad (4.10b)$$

$$\gamma_{B_2}^{(R)} = \sum_{k=1}^{\infty} \sum_{l=1}^{l \leq (k+1)/2} \gamma_{k,l}^{(R)} \sin(4l-2)\phi \sin^{2k} \theta, \quad (4.10c)$$

and for the cubic group O , I obtain

$$\gamma_{A_1}^{(R)} = \sum_{k=0}^{\infty} \sum_{l=0}^{l \leq k/2} \gamma_{k,l}^{(R)} \cos 4l\phi \sin^{2k} \theta \quad (4.11a)$$

$$\gamma_{E^{(1)}}^{(R)} = \gamma_0^{(R)} (2 - 3 \sin^2 \theta) + \dots \quad (4.11b)$$

$$\gamma_{E^{(2)}}^{(R)} = \sum_{k=1}^{\infty} \sum_{l=1}^{l \leq (k+1)/2} \gamma_{k,l}^{(R)} \cos(4l-2)\phi \sin^{2k} \theta \quad (4.11c)$$

⁴Since I am interested in the low-frequency power laws in the Raman signal, resonance-enhanced Raman scattering is not helpful in order to extract the nodal structure of the superconducting order parameter, because the corresponding low-energy power laws are then changed, see e.g. Ref. [109].

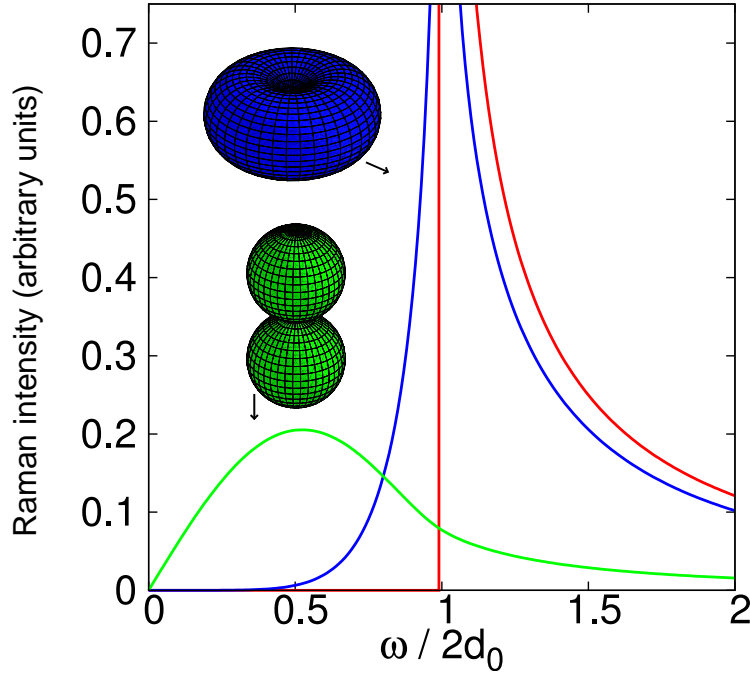


Figure 4.1: Raman spectra for a pure triplet order parameter ($\psi = 0$) for $B_{1,2}$ polarization of the point group C_{4v} in backscattering geometry. The ABM (axial) state with $|\mathbf{d}_{\mathbf{k}}| = d_0 \sin \theta$ is displayed in blue and the polar state with $|\mathbf{d}_{\mathbf{k}}| = d_0 |\cos \theta|$ in green. For a comparison, also the Raman response for the BW state (red) with $|\mathbf{d}_{\mathbf{k}}| = d_0$ is shown.

$$\gamma_{T_2}^{(R)} = \sum_{k=1}^{\infty} \sum_{l=1}^{l \leq (k+1)/2} \gamma_{k,l}^{(R)} \sin(4l-2)\phi \sin^{2k} \theta \quad (4.11d)$$

in a backscattering–geometry experiment ($z\bar{z}$). The Raman vertices corresponding to $E^{(1)}$ and $E^{(2)}$ seem to be quite different, but it turns out that the Raman response is exactly the same because $E^{(1)}$ and $E^{(2)}$ are both elements of the same symmetry class. In what follows, I neglect higher harmonics and thus use only the leading term in the expansions of $\gamma_{\mathbf{k}}^{(R)}$. Due to screening, the constant term ($k=0, l=0$) in the A_1 vertex generates no Raman response, thus I used ($k=1, l=0$). For all other vertices the leading term is given by ($k=1, l=1$).

In general, due to the mixing of a singlet and a triplet component to the superconducting gap, one expects a two–peak structure in NCS, reflecting both pair–breaking peaks for the linear combination [see Eq. (1.11)] of the singlet order parameter $\psi_{\mathbf{k}}$ and the triplet order parameter $\mathbf{d}_{\mathbf{k}}$ (shown in Fig. 4.1), respectively. The ratio $p = d/\psi$, however, is unknown for both types of ASOCs.

How does the Raman spectrum look like for a pure triplet p –wave state? Some representative examples, see Fig. 4.1, are the Balian–Werthamer (BW) state, the Anderson–Brinkman–Morel (ABM or axial) state, and the polar state. The simple pseudoisotropic BW state with $\mathbf{d}_{\mathbf{k}} = d_0 \hat{\mathbf{k}}$ [equivalent to Eq. (1.3) for $g_3 = 0$], as well as previous work on triplet superconductors,

4 Theory of Raman response

restricted on a (cylindrical) 2D Fermi surface, generates the same Raman response as an s -wave superconductor [103]. However, in three dimensions one obtains more interesting results for the axial state with $\mathbf{d}_{\mathbf{k}} = d_0(\hat{k}_y\hat{e}_x - \hat{k}_x\hat{e}_y)$ [equivalent to Eq. (1.2) for $g_{\parallel} = 0$]. The Raman response for this axial state in B_1 and B_2 polarizations for $\mathcal{G} = C_{4v}$ is given by

$$\chi''_{B_{1,2}}(x) = \frac{\pi N_F \gamma_0^{(R)2}}{128} \times \left(-10 - \frac{28}{3}x^2 - 10x^4 + \frac{5 + 3x^2 + 3x^4 + 5x^6}{x} \ln \left| \frac{x+1}{x-1} \right| \right) \quad (4.12)$$

with the dimensionless frequency $x = \omega/2d_0$. An expansion for low frequencies reveals a characteristic exponent [$\chi''_{B_{1,2}} \propto (\omega/2d_0)^6$], which is due to the overlap between the gap- and the vertex-function: Since the Raman vertex has no weight at the two point-nodes along the k_z -axis (see table B.1 in Appendix B), the Raman response looks similar to the one from an isotropic gap, leading to such a high exponent in the low-frequency expansion. Moreover, I calculated the Raman response for the polar state with $\mathbf{d}_{\mathbf{k}} = d_0\hat{k}_z\hat{e}_x$; in this case one equatorial line node crosses the Fermi surface and one obtains:

$$\chi''_{B_{1,2}}(x) = \frac{\pi N_F \gamma_0^{(R)2}}{8x} \begin{cases} \frac{\pi}{2}x^2 - \frac{3\pi}{4}x^4 + \frac{5\pi}{16}x^6 & x \leq 1 \\ (x^2 - \frac{3}{2}x^4 + \frac{5}{8}x^6) \arcsin \frac{1}{x} & x > 1 \\ -(\frac{1}{3} - \frac{13}{12}x^2 + \frac{5}{8}x^4) \sqrt{x^2 - 1} & \end{cases} \quad (4.13)$$

with the trivial low frequency expansion $\chi''_{B_{1,2}} \propto \omega/2d_0$. While the pair-breaking peaks for the BW and ABM state were both located at $\omega = 2d_0$ (similar to the B_{1g} polarization in the singlet d -wave case, which is peaked at $2\Delta_0$), for the polar state this peak is significantly shifted to lower frequencies ($\omega = 1.38d_0$).

4.3 Mixed-parity results: determination of the singlet-triplet ratio

Let me now turn to the predicted Raman spectra for the tetragonal point group $\mathcal{G} = C_{4v}$. In Fig. 4.2 I show the calculated Raman response using Eq. (1.2) with $g_{\parallel} = 0$. This Rashba-type of ASOC splits the Fermi surface into two bands; while on the one band the gap function is $\Delta_{\mathbf{k}} = \psi(1 + p|\gamma_{\mathbf{k}}|) \equiv \Delta_+$, it is $\Delta_- \equiv \psi(1 - p|\gamma_{\mathbf{k}}|)$ on the other band. Thus, depending on the ratio $p = d/\psi$, four different cases (see polar diagrams in the insets) have to be considered: (a) no nodes; (b) one (equatorial) line node (Δ_- band); (c) two line nodes (Δ_- band); and (d) two point nodes on both bands. Below, I will first describe all features in the numerically calculated spectra of Fig. 4.2 according to these four cases and then a curve sketching with detailed information about the analytical results (i.e. the peak and kink positions) will follow. Since the Raman intensity in NCS is proportional to the imaginary part of

$$\chi_{\gamma\gamma}^{\text{total}} = \chi_{\gamma\gamma}(\Delta_-) + \chi_{\gamma\gamma}(\Delta_+) , \quad (4.14)$$

4.3 Mixed-parity results: determination of the singlet-triplet ratio

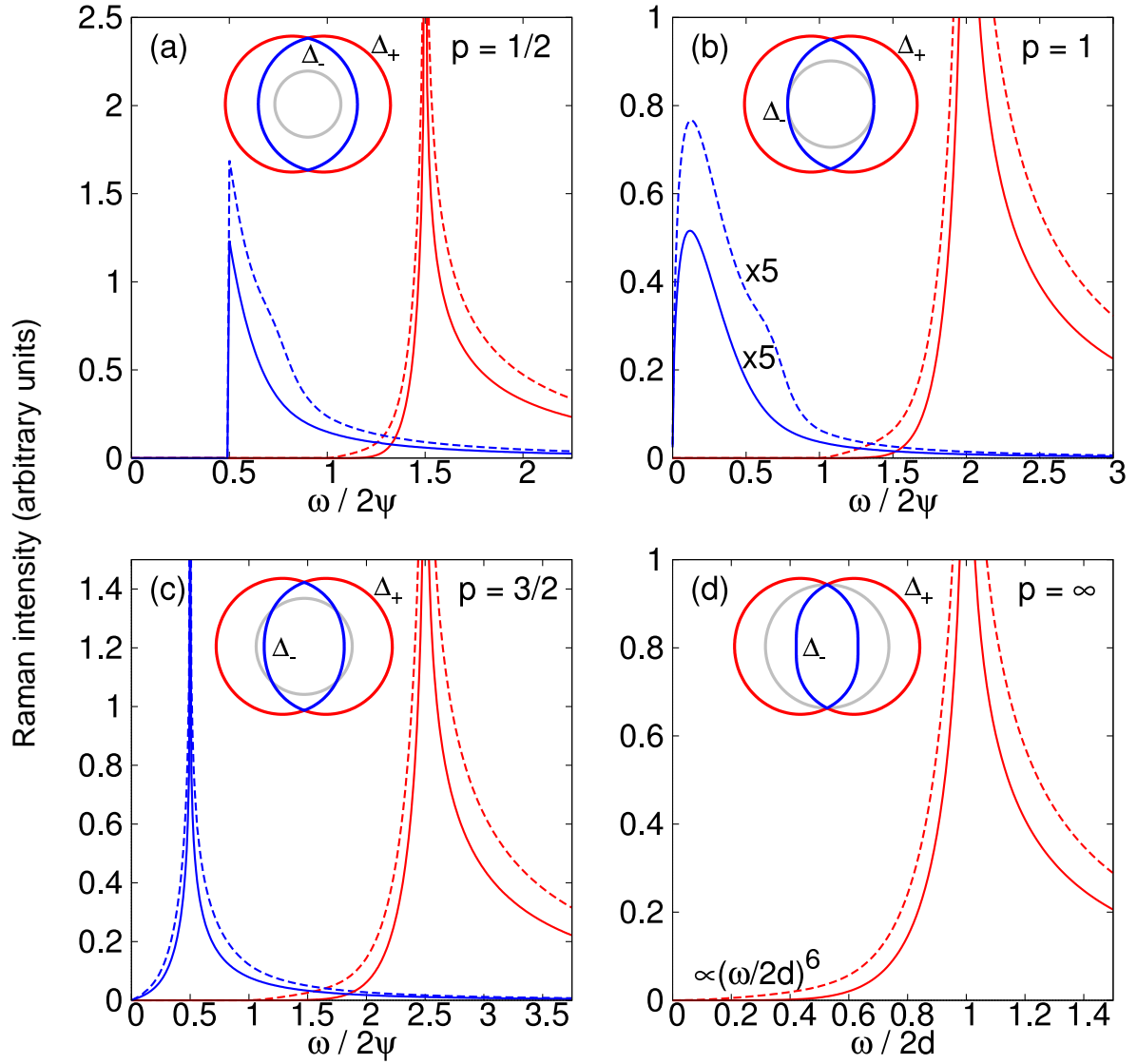


Figure 4.2: Calculated Raman spectra $\chi''_{\gamma\gamma}(\Delta_-)$ [blue] and $\chi''_{\gamma\gamma}(\Delta_+)$ [red] for $B_{1,2}$ (solid lines) and for A_1 (dashed lines) polarizations for the point group C_{4v} . One obtains the same spectrum for the B_1 and B_2 symmetry. The polar diagrams in the insets demonstrate the four qualitative different cases for the unknown ratio $p = d/\psi$.

4 Theory of Raman response

it is interesting to display both contributions separately (blue and red lines, respectively). Although (except for $\psi = 0$) one always finds two pair-breaking peaks at

$$\frac{\omega}{2\psi} = |1 \pm p|, \quad (4.15)$$

I want to stress that these results for NCS are not just a superposition of a singlet and a triplet spectrum. This is clearly demonstrated in Fig. 4.2(a), for example, in which the results for a small triplet contribution ($p = 1/2$) are shown. For $\chi''_{\gamma\gamma}(\Delta_-)$ I find a threshold behavior with an adjacent maximum value of $\chi''_{B_{1,2}}(\Delta_-) = N_F^- \gamma_0^{(R)2} \pi^2/8 \sqrt{p^{-1} - 1}$. In contrast for $\chi''_{\gamma\gamma}(\Delta_+)$ a zero Raman signal to twice the singlet contribution followed by a smooth increase and a singularity is obtained⁵. Note that even though the gap function does not depend on ϕ (see Fig. 1.2 in Chapter 1), one obtains a small polarization-dependence. This unusual behavior occurs only in A_1 symmetry, is due to screening, and leads to a small shoulder for $p \leq 1$. Except from this, the screened spectra show the same peak positions and differ only by a scaling factor. Since this calculation does not predict the absolute intensities (neither the relative intensities between different polarization setups), the scaling is arbitrary as indicated by the y-axis labeling. In the special case, in which the singlet contribution equals the triplet one ($p = 1$), the gap function Δ_- displays an equatorial line node without sign change. This is displayed in Fig. 4.2(b). Because of this nodal structure and strong weight from the vertex function ($\propto \sin^2 \theta$), many low energetic quasiparticles can be excited, which leads to a square-root increase in the Raman intensity (see Fig. 4.3). In this special case the pair-breaking peak is located very close to elastic scattering ($\omega = 0.24\psi$). In Fig. 4.2(c) the gap function Δ_- displays two circular line nodes. The corresponding Raman response for $p > 1$ shows two singularities with different low frequency power laws, namely $\chi''_{B_{1,2}}(\Delta_-) \propto \omega/2\psi$ and $\chi''_{B_{1,2}}(\Delta_+) \propto (\omega/2\psi - 1)^{11/2}$. The different power laws were derived analytically and compared to the numerical calculations in Fig. 4.3 for Δ_- and in Fig. 4.4 for Δ_+ . Especially for the large exponents, the agreement is perfect⁶. Finally, for $p \gg 1$ one recovers the pure triplet cases (d) which is given analytically by Eq. (4.12).

In what follows, I want to discuss exemplarily for the tetragonal case (C_{4v}) the Raman response function without screening (i.e. for the $B_{1,2}$ symmetries). Inserting in Eq. (4.8) the expression for the spin-orbit vector (see Eq. (1.2) in Chapter 1) and the Raman vertex for the B_1 or B_2 symmetry [see Eq. (4.10)], performing the ϕ -integration and after several substitutions, the Raman response reads

$$\Im \chi_{B_{1,2}}^{(0)\pm}(x) = \frac{\pi \gamma_0^2 N_F^\pm}{4x} \Re \int_0^1 \frac{dt t^5 (1 \pm pt)^2}{\sqrt{1-t^2} \sqrt{x^2 - |1 \pm pt|^2}} \quad (4.16)$$

with $x = \omega/2\psi$ and the triplet singlet ratio $p = d/\psi$ which goes from zero (pure singlet) to infinity (pure triplet). For the peaks, kinks and singularities, the denominator of the above expression

⁵A singlet gap and a triplet gap on separated bands cannot produce this features.

⁶For small exponents, good agreement is only expected for smaller frequencies.

4.3 Mixed-parity results: determination of the singlet-triplet ratio

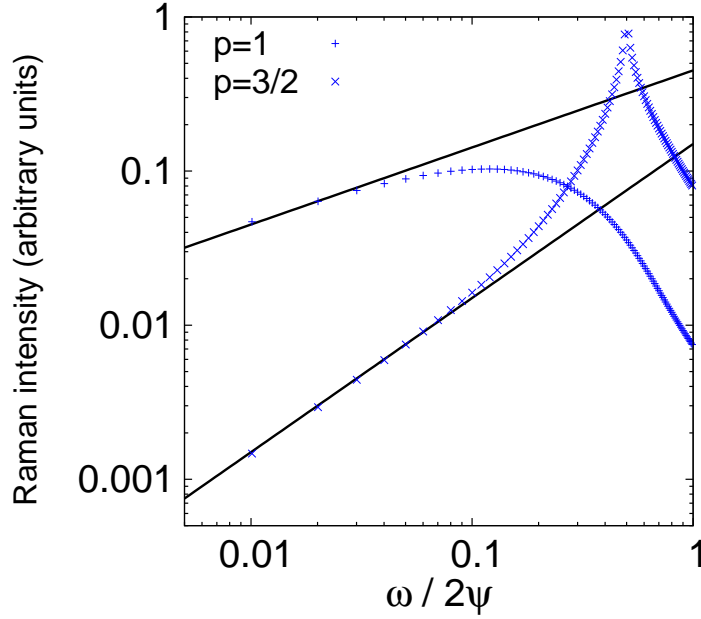


Figure 4.3: Calculated Raman spectra $\chi_{\gamma\gamma}(\Delta_-)$ for $B_{1,2}$ polarization for the point group C_{4v} [same as blue graphs in Fig. 4.2(b) and (c)] on a double logarithmic scale. The solid lines correspond to the power laws $\chi''_{B_{1,2}}(\Delta_-) \propto \sqrt{\omega/2\psi}$ for $p = 1$ and $\chi''_{B_{1,2}}(\Delta_-) \propto \omega/2\psi$ for $p = 3/2$.

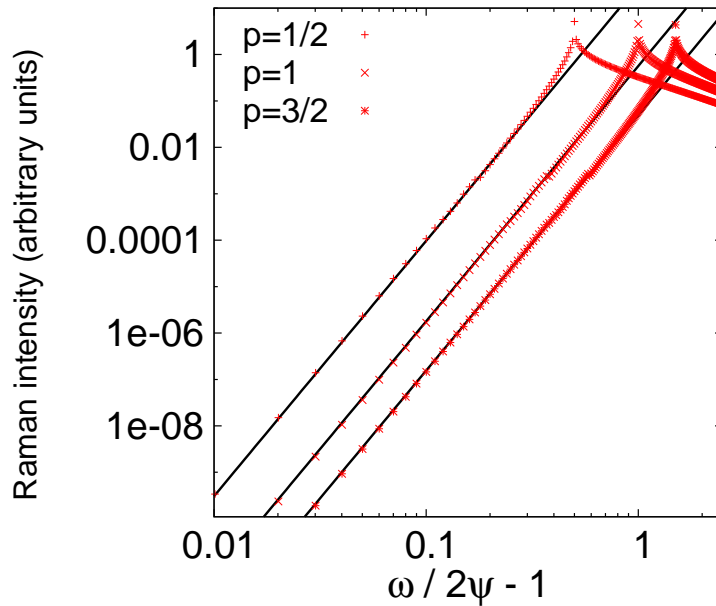


Figure 4.4: Calculated Raman spectra $\chi_{\gamma\gamma}(\Delta_+)$ for $B_{1,2}$ polarization for the point group C_{4v} [same as red graphs in Fig. 4.2(a),(b) and (c)] on a double logarithmic scale. The solid lines correspond to the power law $\chi''_{B_{1,2}}(\Delta_+) \propto (\omega/2\psi - 1)^{11/2}$.

4 Theory of Raman response

is decisive – it can be rewritten more conveniently:

$$\text{denominator} = \sqrt{(1+t)(1-t)}\sqrt{(x+|1\pm pt|)(x-|1\pm pt|)}. \quad (4.17)$$

First, I will discuss the Raman response for the “+”-band associated with the order parameter Δ_+ (singlet+triplet), displayed in red in Fig. 4.2. One can identify four different cases:

- (i) $x < 1$:
With $(x - 1 - pt) < 0$ the denominator is purely imaginary, therefore the Raman response is zero.
- (ii) $1 < x < 1 + p$:
The denominator is real for $(x - 1 - pt) > 0 \Leftrightarrow t < (x - 1)/p$. Thus, the Raman response increases in this range according to

$$\Im\chi_{B_{1,2}}^{(0)+}(1 < x < 1 + p) = \frac{\pi\gamma_0^2 N_F^+}{4x} \int_0^{(x-1)/p} \frac{dt t^5 (1+pt)^2}{\sqrt{1-t^2} \sqrt{x^2 - (1+pt)^2}}. \quad (4.18)$$

- (iii) $x = 1 + p$:
For this case the denominator is proportional to $(1 - t)$, which causes a singularity in the Raman response.
- (iv) $x > 1 + p$:
Here the denominator is purely real, hence, the Raman response decreases with increasing frequency x .

The second case, associated with the order parameter Δ_- (singlet–triplet), blue in Fig. 4.2, needs a more detailed case by case analysis:

(1) $p < 1$: singlet+small triplet contribution

For small triplet contribution, the Raman spectra for this case are displayed in Fig. 4.2(a). From the denominator

$$\text{denominator} = \sqrt{(1+t)(1-t)}\sqrt{(x+1-pt)(x-1+pt)} \quad (4.19)$$

one can identify four cases:

- (i) $x < 1 - p$:
The Raman spectra in this range are gapped, because the denominator is purely imaginary ($(x - 1 + pt) < 0$).
- (ii) $x = 1 - p$:
Considering the limiting behavior (from larger frequencies), the Raman response shows a step-like increase to the value

$$\Im\chi_{B_{1,2}}^{(0)-}(x = 1 - p) = \frac{\pi^2\gamma_0^2 N_F^-}{8} \sqrt{\frac{1-p}{p}}. \quad (4.20)$$

4.3 Mixed-parity results: determination of the singlet-triplet ratio

(iii) $1 - p < x < 1$:

Here, the denominator is real for $(x - 1 + pt) > 0 \Leftrightarrow t > (1 - x)/p$. This means, the Raman response reads:

$$\Im \chi_{B_{1,2}}^{(0)-}(1 - p < x < 1) = \frac{\pi \gamma_0^2 N_F^-}{4x} \int_{(1-x)/p}^1 \frac{dt t^5 (1 - pt)^2}{\sqrt{1 - t^2} \sqrt{x^2 - (1 - pt)^2}}. \quad (4.21)$$

For very small triplet contributions, there might appear another maximum in this interval.

(iv) $x > 1$:

For this case, the denominator is purely real and the response function decreases with increasing frequency.

(2) $p = 1$: equal singlet and triplet contribution

This case corresponds to the blue curve in Fig. 4.2(b). Here the Raman response simplifies to

$$\Im \chi_{B_{1,2}}^{(0)-}(p = 1) = \frac{\pi \gamma_0^2 N_F^-}{4x} \Re \int_0^1 \frac{dt t^5 (1 - t)^2}{\sqrt{1 - t^2} \sqrt{x^2 - (1 - t)^2}}, \quad (4.22)$$

which can be evaluated analytically for $x < 1$ to

$$\begin{aligned} \Im \chi_{B_{1,2}}^{(0)-}(x < 1) &= \frac{\pi \gamma_0^2 N_F^-}{4x} \left[\frac{x^{3/2}}{240} (105 + 699x + 404x^2 + 1022x^3 + 75x^4 + 75x^5) \right. \\ &\quad \times K \left(\frac{1}{2} \sqrt{2 + x} \right) - \frac{x^{1/2}}{120} (-75 + 474x^2 + 437x^4) E \left(\frac{1}{2} \sqrt{2 + x} \right) \\ &\quad \left. - \frac{x^{1/2}}{16} (5 + 15x^2 + 39x^4 + 5x^6) \Pi \left(\frac{1}{2}, \frac{1}{2} \sqrt{2 + x} \right) \right], \quad (4.23) \end{aligned}$$

where K , E and Π denote the complete elliptic integrals of the first, second and third kind, respectively. This above function has a maximum at $x = 0.11829 \dots$ and its low frequency expansion is proportional to \sqrt{x} .

(3) $p > 1$: triplet and small singlet contribution

This case corresponds to the blue graph in Fig. 4.2(b) and (c). Here the denominator reads

$$\text{denominator} = \sqrt{(1 + t)(1 - t)} \sqrt{(x + |1 - pt|)(x - |1 - pt|)}. \quad (4.24)$$

Clearly, for all frequencies $x > 0$ the denominator contributes to the Raman response and at $x = p - 1$ one obtains a singularity.

4 Theory of Raman response

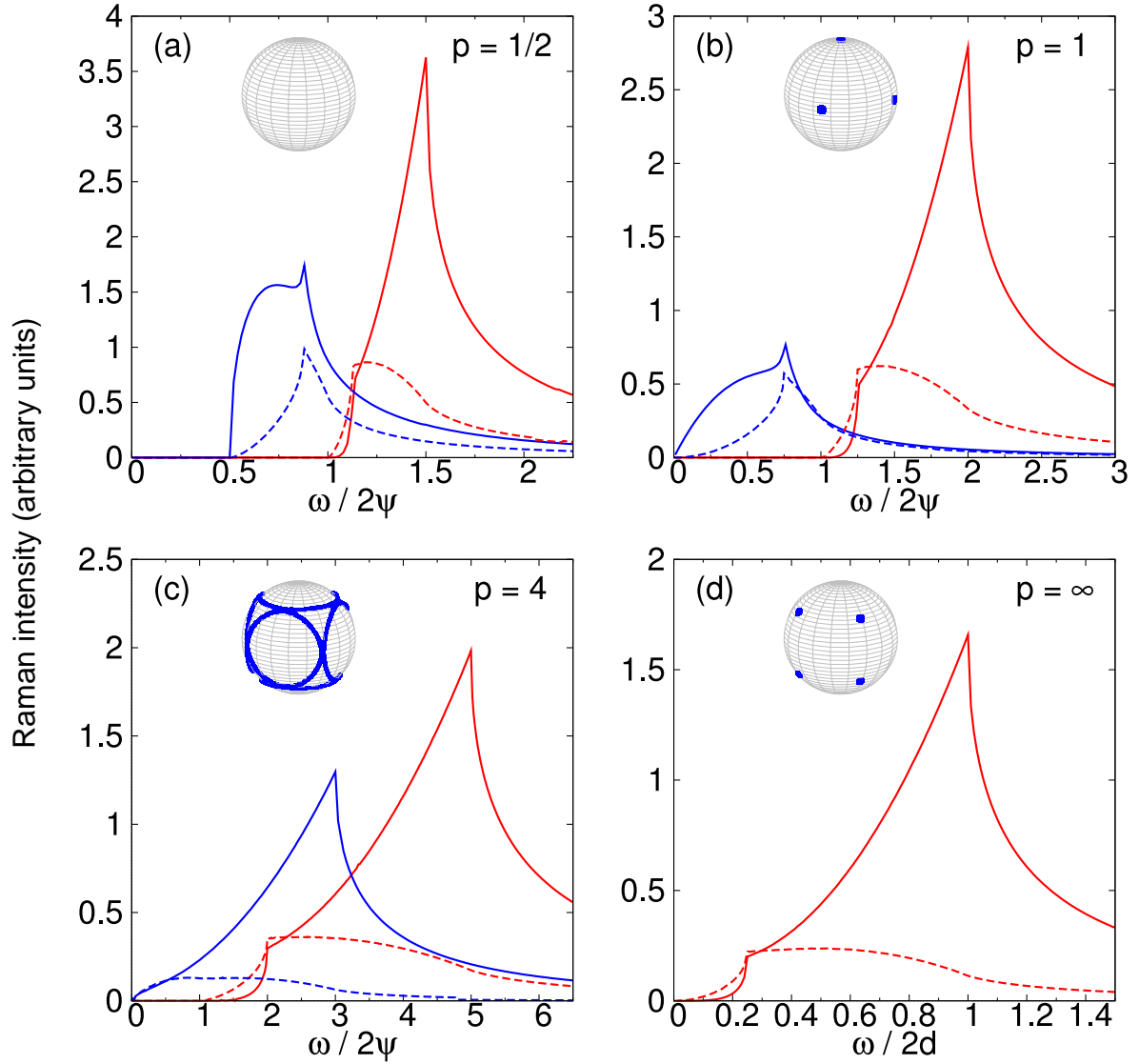


Figure 4.5: Calculated Raman spectra $\chi_{\gamma\gamma}(\Delta_-)$ [blue] and $\chi_{\gamma\gamma}(\Delta_+)$ [red] for E (solid lines) and T_2 (dashed lines) polarizations for the point group O . The insets display the point and line nodes of the gap function Δ_- .

The Raman response for the point group O , using Eq. (1.3), is shown in Fig. 4.5 for the E and T_2 symmetries and in Fig. 4.6 for the A_1 symmetry with and without screening. As in the previous (tetragonal) case, there is only little difference between the unscreened and the screened Raman response. Except from a scaling, no additional features appear from the screening term. I again consider four different cases: (a) no nodes; (b) six point nodes (Δ_- band); (c) six connected line nodes (Δ_- band); and (d) 8 point nodes (both bands) as illustrated in the insets. Obviously, the pronounced angular dependence of $|\gamma_{\mathbf{k}}|$ leads to a strong polarization-dependence. Thus one gets different peak positions for the E and T_2 polarizations in $\chi''_{\gamma\gamma}(\Delta_+)$. As a further consequence,

4.3 Mixed-parity results: determination of the singlet-triplet ratio

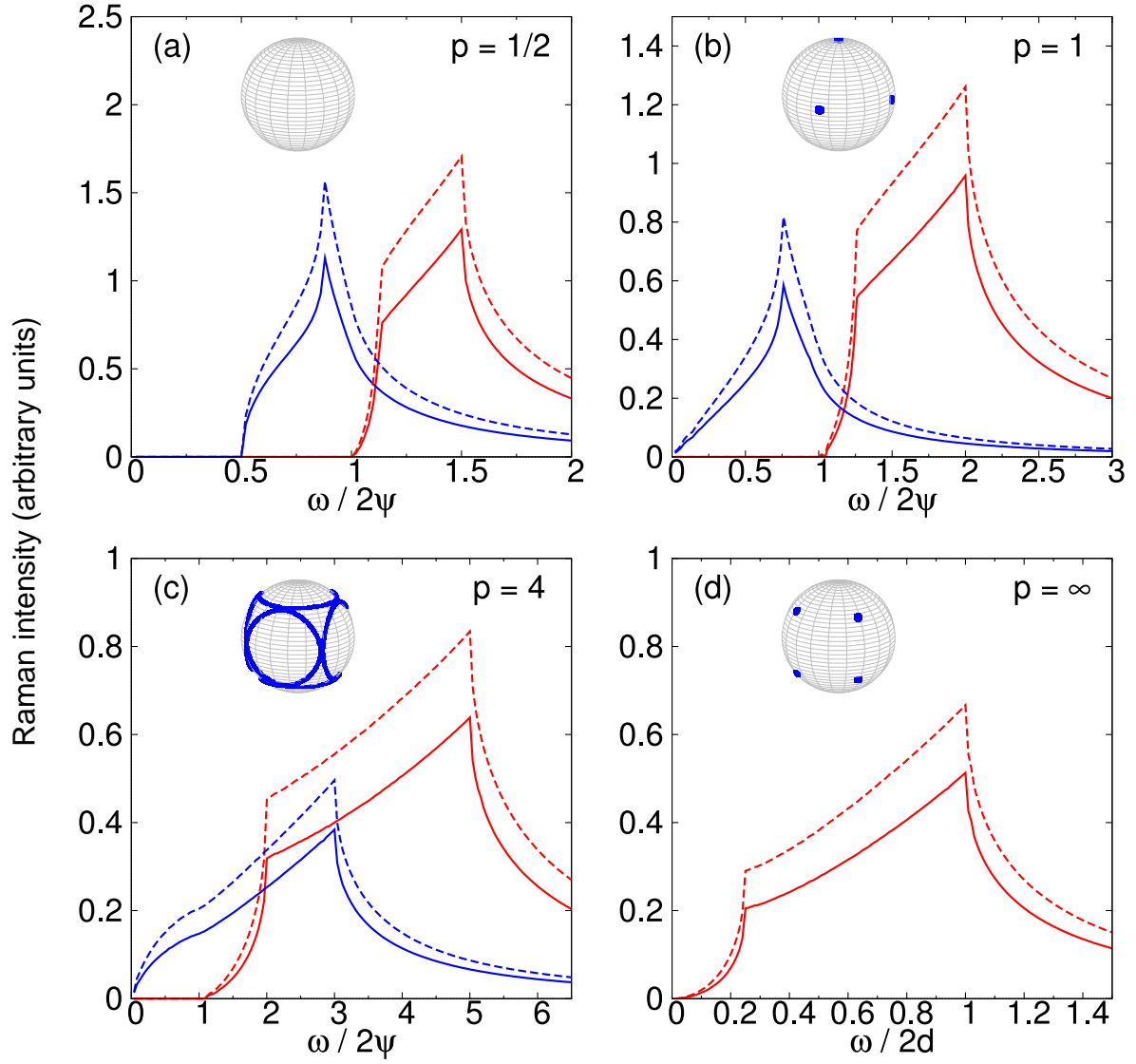


Figure 4.6: Calculated Raman spectra $\chi_{\gamma\gamma}(\Delta_-)$ [blue] and $\chi_{\gamma\gamma}(\Delta_+)$ [red] for A_1 polarization with screening (solid lines) and without screening (dashed lines) for the point group O . The insets display the point and line nodes of the gap function Δ_- .

4 Theory of Raman response

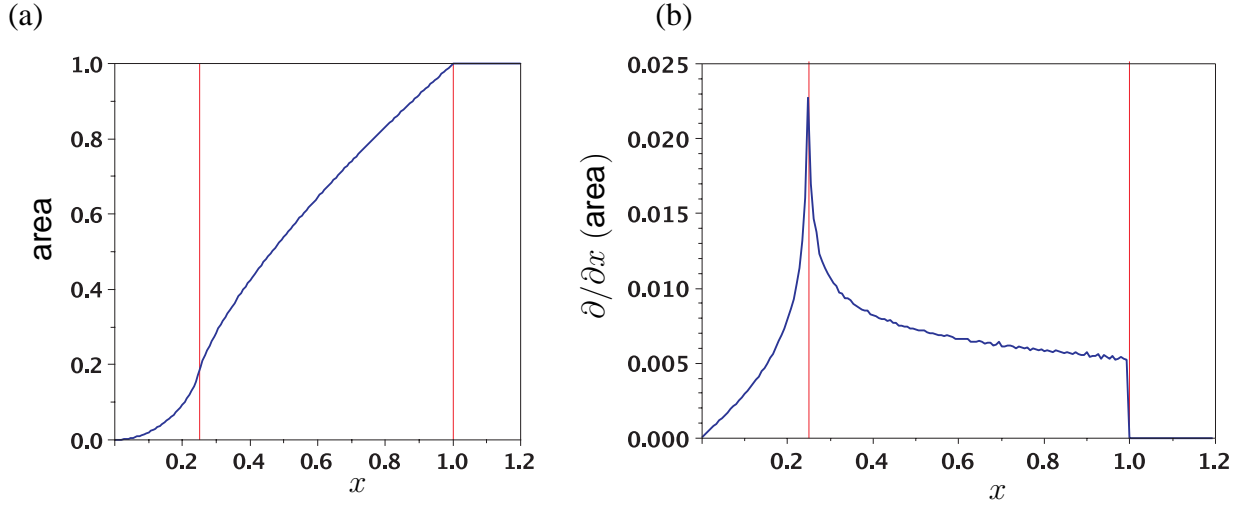


Figure 4.7: (a) Fraction of the area on the Fermi-surface that contributes to the pure triplet Raman response for the cubic point group O in dependence of the normalized frequency $x = \omega/2d$. (b) Derivative of the area displayed in (a) with respect to x . The change in slope at $x = 1/4$ in (a) becomes visible as kink in (b).

the Raman spectra reveal up to two kinks on each band (+, -) at

$$\frac{\omega}{2\psi} = |1 \pm p/4| \quad (4.25)$$

and

$$\frac{\omega}{2\psi} = |1 \pm p|. \quad (4.26)$$

Interestingly, the T_2 symmetry displays only a change in slope at $\omega/2\psi = |1 + p|$ instead of a kink, which is due to the small overlap between the gap- and the vertex-function. Furthermore, due to the non-trivial ϕ -integration, no singularities are present. Nevertheless, the main feature, namely the two-peak structure, is still present and one can directly deduce the value of p from the peak and kink positions.

Finally, for $p \gg 1$ one recovers the pure triplet case (d), in which the unscreened Raman response is given by

$$\chi''_{\gamma\gamma}(\omega) \propto \frac{2d}{\omega} \Re \left\langle \gamma_{\mathbf{k}}^{(R)2} \frac{|\gamma_{\mathbf{k}}|^2}{\sqrt{(\omega/2d + |\gamma_{\mathbf{k}}|)(\omega/2d - |\gamma_{\mathbf{k}}|)}} \right\rangle_{\text{FS}}. \quad (4.27)$$

Clearly, only the area on the Fermi surface with $\omega/2d > |\gamma_{\mathbf{k}}|$ contributes to the Raman intensity. Since $|\gamma_{\mathbf{k}}| \in [0, 1]$ has a saddle point at $|\gamma_{\mathbf{k}}| = 1/4$, one finds kinks at characteristic frequencies $\omega/2d = 1/4$ and $\omega/2d = 1$. This is illustrated in Fig. 4.7, where I plotted exemplary the area on the (spherical) Fermi-surface that contributes to the above Raman response. Especially in the derivative one can identify a kink at $\omega/2d = 1/4$ and a jump at $\omega/2d = 1$. The full discussion of the peak and kink positions for the cubic point group is completely analogue to the presented

analysis in the tetragonal case, however, for mixed-parity it is lengthier, because more cases have to be distinguished. In contrast to the Rashba-type of SOC, I find a characteristic low energy expansion $\propto (\omega/2d)^2$ for both the A_1 and E symmetry, while $\propto (\omega/2d)^4$ for the T_2 symmetry. Also all power laws for the cubic symmetry are obtained analytically and they are in perfect agreement with the numerical results.

4.4 Summary

In this chapter I presented analytical and numerical results for the electronic (pair-breaking) Raman response in non-centrosymmetric superconductors for zero temperature. To this end I analyzed the two most interesting classes of tetragonal and cubic symmetry, applying for example to CePt_3Si ($\mathcal{G} = C_{4v}$) and $\text{Li}_2\text{Pd}_x\text{Pt}_{3-x}\text{B}$ ($\mathcal{G} = O$). Accounting for the antisymmetric spin-orbit coupling, I provide various analytical results such as the Raman vertices for both point groups, the Raman response for several pure triplet states, power laws and kink positions for mixed-parity states. The numerical results cover all relevant cases from weak to strong triplet-singlet ratio and demonstrate a characteristic two-peak structure for Raman spectra of NCS. These theoretical predictions can be used to analyze the underlying condensate in parity-violating NCS and allow the determination of the unknown triplet-singlet ratio. I published a short version of this chapter in Ref. [112]. Finally, some words about the observability of these predictions are appropriate. Because of the low T_c , especially of CePt_3Si (0.75K), measurements of the electronic Raman effect appear at least challenging if not impossible. Even experiments on $\text{Li}_2\text{Pd}_x\text{Pt}_{3-x}\text{B}$ with a T_c between 2K and 8K might be very demanding. A look at published experiments on electronic Raman scattering reveals that already in 1980 Sooryakumar and Klein presented in Ref. [97] beautiful electronic Raman spectra for 2H-NbSe_2 with $T_c=7.2\text{K}$ and performed measurements between 1.5K and 2K. Furthermore, in Ref. [113], Gasparov *et al.* described a technique, where sample heating due to laser radiation can be reduced when the sample is surrounded by superfluid He because of the huge thermal conductivity⁷. Therefore, Raman measurements on materials with low T_c 's should be possible. Another important point is the following: Since the theory is formulated in terms of the characteristic spin-orbit coupling, the results apply to a whole class of tetragonal and cubic NCS (known and unknown). The materials CePt_3Si and $\text{Li}_2\text{Pd}_x\text{Pt}_{3-x}\text{B}$ are only examples of these classes, while the validity of this result is much broader. The point group of the crystal structure and the spin-orbit coupling are the only material specific quantities that enter the calculation of this chapter. Hence, these results apply to a whole class of tetragonal and cubic NCS.

⁷Sample heating can never be completely reduced due to the Kapitza resistance between the sample-liquid He interface.

5 Dynamical spin and charge responses in CePt₃Si

So far, the previous chapters dealt with general properties of NCS. For these analytical considerations, especially the gauge invariance in Chapter 3, it was indispensable to use a (phenomenological) separable ansatz for the pairing interaction. Now as a case study, I want to focus among other things on a microscopic justification of the pairing interaction based on spin fluctuations in CePt₃Si. For this purpose, I introduce a numerical approach to calculate the spin and charge response and apply it to this particular NCS. CePt₃Si is still six years after its discovery one of the most interesting NCS, because it undergoes interesting phase transitions: antiferromagnetic order ($T_N \approx 2.2K$) and in coexistence with this, one or even two superconducting orders ($T_c \approx 0.75K$). Therefore, more material specific models are needed. One of the interesting questions is, to what extent the band structure plays a role in this compound. Hence, I use an itinerant description to calculate the dynamical spin and charge susceptibilities in the presence of an ASOC. Since it is a challenge to evaluate numerically the ω dependent susceptibility in the whole three dimensional Brillouin zone, I have to confine the calculations to the normal state in the vicinity of the antiferromagnetic order. Nevertheless, all calculations were done for $T = 0$ to obtain sharper results. The following introduction compares the method to published results. In Section 5.2 I derive quite general the main equations for the susceptibility using a Green's function approach, and together with the model band structure in Section 5.3, finally some numerical results for inelastic neutron scattering, a discussion of possible superconducting pairing scenarios, and Kohn anomalies in CePt₃Si will be presented.

5.1 Introduction

There are different possibilities to calculate the (dynamical) susceptibility on the whole Brillouin zone numerically. In this case, it is convenient to take advantage of the convolution theorem for the Green's function. The first decision is, whether the calculation is done for Matsubara frequencies on the imaginary axis or on the real frequency axis. The first method has the advantage that one can choose a relatively small grid in momentum space, since the Matsubara Green's functions are relatively smooth. The obvious disadvantage is the large sum of Matsubara frequencies, which has to be evaluated to reach low temperatures¹. The calculation on the real axis on the other hand can easily be performed for low temperatures and especially for $T = 0$. The

¹The calculation e.g. of Yanase *et al.* [114] for the superconducting state done at $30K$ (without ω -dependence), which is quite large compared to the actual T_c of $0.75K$.

5 Dynamical spin and charge responses in CePt₃Si

disadvantage of this method is the fine \mathbf{q} grid which has to be adapted such that the peaks in the spectral function are well sampled. In the following section, I will describe exactly this method.

Furthermore, I want to calculate the *dynamical* susceptibility. Published results till now are restricted to the static susceptibility [51, 115, 114, 52]. In the next sections some results will be presented which support the idea that dynamic nesting may play an important role in CePt₃Si. The numerical evaluation of the dynamical susceptibility for a three dimensional Brillouin zone in the presence of an ASOC is connected with some computational efforts, which I could overcome through a very efficient algorithm which is in detail explained in the following section and in Appendix D.

5.2 Spin–susceptibility with ASOC

In general, the dynamical spin susceptibility for NCS superconductors is given by (see Ref. [53])

$$\chi_{ij}(\mathbf{q}, i\nu_m) = -\frac{1}{\beta} \sum_{\mathbf{k}, i\omega_n} \text{Tr} \left[\sigma_i \hat{\mathbf{G}}(\mathbf{k}, i\omega_n) \sigma_j \hat{\mathbf{G}}(\mathbf{k} + \mathbf{q}, i\omega_n + i\nu_m) - \sigma_i \hat{\mathbf{F}}(\mathbf{k}, i\omega_n) \sigma_j^\top \hat{\mathbf{F}}^\dagger(\mathbf{k} + \mathbf{q}, i\omega_n + i\nu_m) \right], \quad (5.1)$$

where Tr denotes the trace, with the Pauli matrices σ_i , the inverse temperature $\beta = (k_B T)^{-1}$, the fermionic Matsubara frequency $\omega_n = (2n + 1)\pi k_B T$ and the bosonic Matsubara frequency $\nu_m = 2m\pi k_B T$. The single particle normal and anomalous Matsubara Green's function in the spin basis are denoted by $\hat{\mathbf{G}}$ and $\hat{\mathbf{F}}$, respectively. With an unitary transformation (see Section 2.2 for this SU(2) spin–rotation) they can be rewritten in terms of the Matsubara Green's function in the band basis [48]:

$$\hat{\mathbf{G}}(\mathbf{k}, i\omega_n) = G_+(\mathbf{k}, i\omega_n) \hat{\sigma}_+(\mathbf{p}) + G_-(\mathbf{k}, i\omega_n) \hat{\sigma}_-(\mathbf{p}) \quad (5.2)$$

$$\hat{\mathbf{F}}(\mathbf{k}, i\omega_n) = [F_+(\mathbf{k}, i\omega_n) \hat{\sigma}_+(\mathbf{p}) + F_-(\mathbf{k}, i\omega_n) \hat{\sigma}_-(\mathbf{p})] i\sigma_y \quad (5.3)$$

with the matrices

$$\hat{\sigma}_\pm(\mathbf{k}) = \frac{1}{2} [\sigma_0 \pm \hat{\gamma}_\mathbf{k} \cdot \boldsymbol{\sigma}], \quad (5.4)$$

and the identity matrix σ_0 . Here, a different normalization of $\gamma_\mathbf{k}$ compared to the previous chapters is used:

$$\hat{\gamma}_\mathbf{k} = \frac{\gamma_\mathbf{k}}{\sqrt{\gamma_\mathbf{k}^2}} \quad (5.5)$$

The Green's functions in band basis are obtained from the solution of the Gor'kov equations and read [48]:

$$G_{\pm}(\mathbf{k}, i\omega_n) = -\frac{i\omega_n + \xi_{\pm}}{\omega_n^2 + |\Delta_{\pm}|^2 + \xi_{\pm}^2} \quad (5.6)$$

$$F_{\pm}(\mathbf{k}, i\omega_n) = \frac{\Delta_{\pm}}{\omega_n^2 + |\Delta_{\pm}|^2 + \xi_{\pm}^2}. \quad (5.7)$$

Again, the energy dispersion and the order parameter on both bands read

$$\xi_{\lambda}(\mathbf{k}) = \xi_{\mathbf{k}} + \lambda\alpha|\gamma_{\mathbf{k}}| \quad (5.8)$$

$$\Delta_{\pm}(\mathbf{k}) = \psi \pm d|\gamma_{\mathbf{k}}|, \quad (5.9)$$

with the spin-orbit coupling strength α . In order to account for the periodicity of the $\gamma_{\mathbf{k}}$ -vector in the Brillouin zone, it is convenient to define $\gamma_{\mathbf{k}}$ as derivative of the band structure [66, 51]:

$$\gamma_{\mathbf{k}} = \frac{1}{v_{\text{avg}}} \begin{pmatrix} -v_y(\mathbf{k}) \\ v_x(\mathbf{k}) \\ 0 \end{pmatrix}, \quad (5.10)$$

$$v_{\text{avg}}^2 = \int_{B.Z.} d\mathbf{k} v_x^2(\mathbf{k}) + v_y^2(\mathbf{k}),$$

$$v_{x,y} = \frac{\partial \xi_{\mathbf{k}}}{\partial k_{x,y}}.$$

At this stage a parameterization of the band structure $\xi_{\mathbf{k}}$ is not necessary, it will be specified in the following Section 5.3. Note that for the non-isotropic case (i.e. in the presence of an ASOC), the following nine different components have to be evaluated separately:

$$\chi(\mathbf{q}, i\nu_m) = \begin{pmatrix} \chi_{11} & \chi_{12} & \chi_{13} \\ \chi_{21} & \chi_{22} & \chi_{23} \\ \chi_{31} & \chi_{32} & \chi_{33} \end{pmatrix}. \quad (5.11)$$

In view of the application to inelastic neutron scattering, I will confine the evaluation to the diagonal components of the susceptibility matrix. Furthermore, from now on I will only consider the normal state².

Inserting Eq. (5.6) and the following definitions into the expression for the dynamical spin susceptibility, Eq. (5.1), and evaluation the trace, yields after a straightforward, but tedious

²Numerical calculations in the superconducting state are at least twice as expensive, w.r.t. the memory consumption and computational time. However the generalization is straightforward and already included in the algorithm described in Appendix D.

5 Dynamical spin and charge responses in CePt₃Si

calculation

$$\chi_{00}(\mathbf{q}, i\nu_m) = \chi_{++00} + \chi_{++xx} + \chi_{++yy} \quad (5.12)$$

$$+ \chi_{+-00} - \chi_{+-xx} - \chi_{+-yy}$$

$$+ \chi_{-+00} - \chi_{-+xx} - \chi_{-+yy}$$

$$+ \chi_{--00} + \chi_{--xx} + \chi_{--yy}$$

$$\chi_{11}(\mathbf{q}, i\nu_m) = \chi_{++00} + \chi_{++xx} - \chi_{++yy} \quad (5.13)$$

$$+ \chi_{+-00} - \chi_{+-xx} + \chi_{+-yy}$$

$$+ \chi_{-+00} - \chi_{-+xx} + \chi_{-+yy}$$

$$+ \chi_{--00} + \chi_{--xx} - \chi_{--yy}$$

$$\chi_{22}(\mathbf{q}, i\nu_m) = \chi_{++00} - \chi_{++xx} + \chi_{++yy} \quad (5.14)$$

$$+ \chi_{+-00} + \chi_{+-xx} - \chi_{+-yy}$$

$$+ \chi_{-+00} + \chi_{-+xx} - \chi_{-+yy}$$

$$+ \chi_{--00} - \chi_{--xx} + \chi_{--yy}$$

$$\chi_{33}(\mathbf{q}, i\nu_m) = \chi_{++00} - \chi_{++xx} - \chi_{++yy} \quad (5.15)$$

$$+ \chi_{+-00} + \chi_{+-xx} + \chi_{+-yy}$$

$$+ \chi_{-+00} + \chi_{-+xx} + \chi_{-+yy}$$

$$+ \chi_{--00} - \chi_{--xx} - \chi_{--yy} ,$$

with the abbreviation:

$$\chi_{\alpha\beta ij} = \frac{1}{8} \frac{1}{\beta} \sum_{\mathbf{p}, n} \hat{\gamma}_i(\mathbf{p}) G_{\alpha}^{(0)}(\mathbf{p}, i\omega_n) G_{\beta}^{(0)}(\mathbf{p} + \mathbf{q}, i\omega_n + i\nu_m) \hat{\gamma}_j(\mathbf{p} + \mathbf{q}) . \quad (5.16)$$

For the sake of completeness, I added the zeroth component of the susceptibility tensor in Eq. (5.12), referred to as the charge susceptibility. The indices α, β denote the spin-orbit split bands

$$\alpha, \beta = \begin{cases} + & \text{"+"-band} & \rightarrow & \text{use } \xi_+(\mathbf{k}) \\ 0 & \text{no SOC} & \rightarrow & \text{use } \xi_{\mathbf{k}} \\ - & \text{"-"-band} & \rightarrow & \text{use } \xi_-(\mathbf{k}) \end{cases} \quad (5.17)$$

and the indices i, j select components of the $\hat{\gamma}_{\mathbf{k}}$ -vector

$$i, j = \begin{cases} 0 & \hat{\gamma}_0 \equiv 1 \text{ (definition)} \\ 1, 2, 3 & \hat{\gamma}_{1,2,3}(\mathbf{k}) = \hat{\gamma}_{x,y,z}(\mathbf{k}) \end{cases} \quad (5.18)$$

where I used the convenient definition that the zeroth index of $\hat{\gamma}_0 \equiv 1$. In order to evaluate the susceptibility on the real frequency axis rather than on the Matsubara points on the imaginary

axis, I use the spectral representation of the normal Green's function [116]

$$G(\mathbf{k}, i\omega_n) = \int_{-\infty}^{\infty} \frac{d\omega}{2\pi} \frac{A(\mathbf{k}, \omega)}{i\omega_n - \omega}, \quad (5.19)$$

$$A(\mathbf{k}, \omega) = -2\Im [G(\mathbf{k}, \omega + i\delta)]. \quad (5.20)$$

Inserting the spectral representation into Eq. (5.16) and performing the Matsubara frequency sum according to

$$\frac{1}{\beta} \sum_{\omega_n} \frac{1}{(i\omega_n + i\nu_m - y)(i\omega_n - x)} = \frac{f(x) - f(y)}{i\nu_m + x - y} \quad (5.21)$$

yields finally:

$$\chi''_{\alpha\beta ij}(\mathbf{q}, \omega) = -\frac{\pi}{8} \int_{-\infty}^{\infty} d\nu \mathcal{C}_{\alpha\beta ij}(\mathbf{q}, \omega + \nu, \nu) [f(\nu) - f(\omega + \nu)], \quad (5.22)$$

$$\mathcal{C}(\mathbf{q}, \epsilon, \nu) = \frac{1}{\pi^2} \int_{BZ} d^3k \hat{\gamma}_i(\mathbf{k}) G''_{\alpha}(\mathbf{k}, \epsilon) G''_{\beta}(\mathbf{k} + \mathbf{q}, \nu) \hat{\gamma}_j(\mathbf{k} + \mathbf{q}). \quad (5.23)$$

Here $f(x)$ denotes the Fermi-Dirac distribution function. In order to derive this expression, I did first the analytical continuation $i\nu_m \rightarrow \omega + i\delta$, applied then

$$\lim_{\delta \rightarrow 0} \frac{1}{x \pm i\delta} = P \left(\frac{1}{x} \right) \mp i\pi\delta(x) \quad (5.24)$$

with P being the Cauchy principal value, and eventually extracted the imaginary part of the susceptibility. Note that Eq. (5.22) can be further simplified for zero temperature. In this case the boundaries of the integral can be replaced according to $\int_{-\infty}^{\infty} \rightarrow \int_{-\omega}^0$ by removing the step-like Fermi-Dirac distribution function. For finite temperature, it is sufficient to add a small interval of several $k_B T$ around this integration range. Finally, Eq. (5.22) together with Eq. (5.23) can now be used to calculate the susceptibility numerically. For this purpose, I used the following model for the imaginary part of the Green's function (which is proportional to the spectral function, see above), anticipating a generalization to the superconducting state:

$$\Im G_0(\mathbf{k}, \omega) = -u_{\mathbf{k}}^2 \frac{\delta_0}{(\omega - E_{\mathbf{k}})^2 + \delta_0^2} - v_{\mathbf{k}}^2 \frac{\delta_0}{(\omega + E_{\mathbf{k}})^2 + \delta_0^2} \quad (5.25)$$

$$\Im F_0(\mathbf{k}, \omega) = -u_{\mathbf{k}} v_{\mathbf{k}} \left[\frac{\delta_0}{(\omega - E_{\mathbf{k}})^2 + \delta_0^2} + \frac{\delta_0}{(\omega + E_{\mathbf{k}})^2 + \delta_0^2} \right], \quad (5.26)$$

where δ_0 is a small (real) number which represents the quasiparticle width/damping. In all fol-

5 Dynamical spin and charge responses in CePt₃Si

lowing calculations, I used $\delta_0 = 2\text{meV}$ ³. The usual coherence factors read:

$$\begin{aligned} u_{\mathbf{k}}^2 &= \frac{1}{2} \left(1 + \frac{\xi_{\mathbf{k}}}{E_{\mathbf{k}}} \right) \\ v_{\mathbf{k}}^2 &= \frac{1}{2} \left(1 - \frac{\xi_{\mathbf{k}}}{E_{\mathbf{k}}} \right) \\ u_{\mathbf{k}}v_{\mathbf{k}} &= \frac{\Delta_{\mathbf{k}}}{2E_{\mathbf{k}}}. \end{aligned} \quad (5.27)$$

It is self-explanatory, that any another model e.g. with self-energy effects and mass-renormalization could also be chosen. Ideally, ARPES measurements⁴, which provide the spectral function, could be used to calculate the susceptibility and then compare the results to data from inelastic neutron scattering experiments.

At this stage, some remarks about the method to calculate $\chi''_{\alpha\beta ij}$ from Eq. (5.22) and Eq. (5.23) may be appropriate. Clearly, Eq. (5.23) describes a correlation in momentum-space, it can be rewritten symbolically (every term is now a 3D matrix in momentum-space) using the cross-correlation/convolution theorem

$$\begin{aligned} \mathcal{C}_{\alpha\beta ij}(\epsilon, \nu) &= \frac{1}{\pi^2} [\hat{\gamma}_i G''_{\alpha}(\epsilon)] \otimes [G''_{\beta}(\nu) \hat{\gamma}_j] \\ &= \frac{1}{\pi^2} \mathcal{F}^{-1} \{ \mathcal{F} [\hat{\gamma}_i G''_{\alpha}(\epsilon)]^* \times \mathcal{F} [G''_{\beta}(\nu) \hat{\gamma}_j] \} \end{aligned} \quad (5.28)$$

where \otimes denotes the cross-correlation, \times is an element by element multiplication, $*$ denotes the conjugate complex and \mathcal{F} denotes the Fourier transformation. Instead of a Fourier or fast Fourier transform, I use the even faster (and less memory consuming) discrete sine and cosine transform (DST, DCT) [118], taking into account all symmetries⁵. Details about the algorithm, can be found in Appendix D.

5.3 Role of band structure in CePt₃Si

The previous considerations apply to any NCS with ASOC. From now on I will take a closer look at the best studied compound, namely CePt₃Si. To this end, a sophisticated band structure model for the three closest bands to the Fermi edge will be derived from LDA calculations performed by Heid. All further considerations are then confined on the most interesting β band, since the spin susceptibility reveals a strong nesting vector at $\mathbf{Q} = (0, 0, \pi)$, which is exactly the AFM ordering vector. This is a strong evidence, that an itinerant description including the band structure is at

³For such a small damping one has to choose a very fine-meshed grid. I used therefore $500 \times 500 \times 500$ k-points in 1/8th of the Brillouin zone. Calculations with an even finer mesh showed no further improvement.

⁴ARPES data are not yet available on CePt₃Si, however, for non-centrosymmetric CeIrSi₃ ARPES data can be found in Ref. [117].

⁵That is in detail the time reversal symmetry, the tetragonal symmetry and the fact that the spectral function and $\hat{\gamma}_{\mathbf{k}}$ are real.

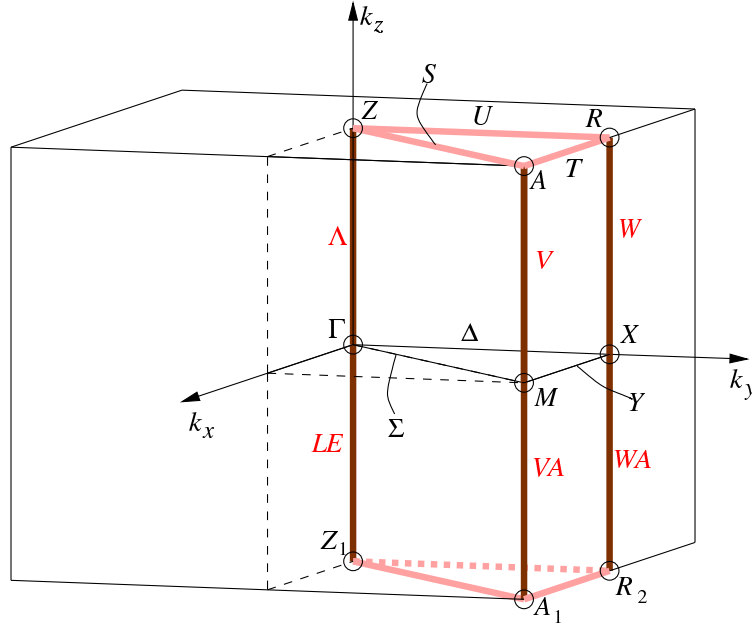


Figure 5.1: Brillouin zone for the space group $P4mm$, applying to CePt_3Si . From bilbao crystallographic server [127].

least one important part to describe the properties of CePt_3Si .

A review about Fermi surface reconstructions for Ce-based heavy-fermion superconductors can be found in Ref. [119]. In particular for CePt_3Si two different LDA calculations by Samokhin *et al.* [120, 121] and Hashimoto *et al.* [122] are published and will be compared to the LDA results obtained by Heid [123] in the following section. For the isostructural LaPt_3Si , LDA calculations are found in Ref. [122, 124]. Contributions from the experimental side to clarify the Fermi surface can be found e.g. in Ref. [122, 125, 119] with de Haas-van Alphen measurements. An interesting suggestion from Mineev *et al.* to extract the strength of the ASOC α from de Haas-van Alphen experiments should also be mentioned [126].

For the definition of the high symmetry points in the Brillouin zone of CePt_3Si , belonging to the point group C_{4v} (space group $P4mm$), see Fig. 5.1. In the following section I will present a tight binding band structure model for this tetragonal symmetry and calculate from it the density of states (DoS). In Section 5.3.2, the nesting vectors in the β band of CePt_3Si will be identified.

5.3.1 Tight-binding model and DoS

In order to calculate the density of states, the nesting vectors, the spin and charge susceptibility of CePt_3Si , first a model for the band structure is needed. Using a mixed-basis-pseudopotential code ⁶ Heid calculated in LDA approximation the band structure of “Ce” Pt_3Si [123]. The result for the three closest bands to the Fermi surface is shown along the high symmetry points

⁶The implementation of this method, which was developed by Meyer *et al.* [128] is described in Ref. [129].

5 Dynamical spin and charge responses in CePt_3Si

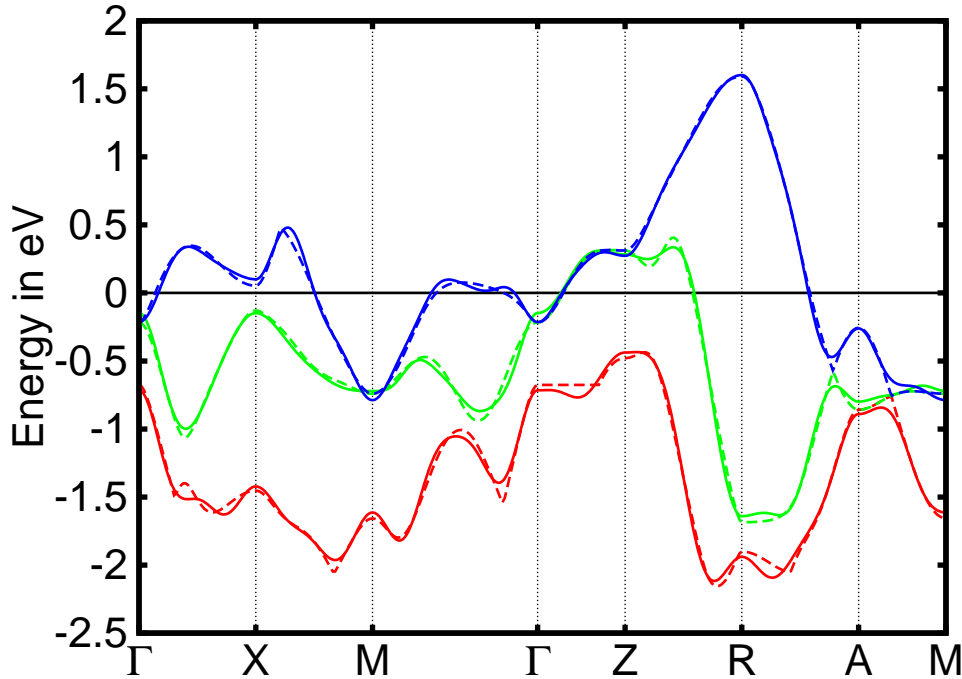


Figure 5.2: Tight-binding fit to the LDA band structure of CePt_3Si for the closest bands to the Fermi surface: α band (red), β band (green), and γ band (blue). The dashed line corresponds to the LDA calculation and the solid line is a tight binding fit to this band structure including 4th nearest neighbors in a tetragonal lattice.

in Fig. 5.2 (dashed lines). The LDA calculation was performed for the electronic structure of LaPt_3Si plus one negative background charge in order to account for the one 4f electron. However, the experimental crystal structure from diffraction measurements [2] was used (without relaxation). The additional background charge affects mainly the dispersion by shifting the chemical potential. The calculation was done without taking spin-orbit coupling into account. Further, the grid has $11 \times 11 \times 9$ (=1089) k-points in the irreducible Brillouin zone, which corresponds to a $20 \times 20 \times 16$ grid in the whole Brillouin zone. As reference also the band structure for LaPt_3Si was calculated and compared to the calculations by Hashimoto in Ref. [122]. The agreement for LaPt_3Si was good (not shown here), whereas the band structure of “Ce” Pt_3Si shows significant differences compared to the published results by Samokhin *et al.* [120, 121]: In Heid’s calculation, the so-called α band does not cross the Fermi surface at all, while Samokhin’s calculation shows a small hole pocket around the Z-point. Further, a lot of low lying f-bands around 400meV above the Fermi surface flattens the dispersion of the γ band above the Fermi surface. I assume, that all these differences are due to the approximation for the Ce-4f state.

However, I used this LDA-result for “Ce” Pt_3Si to fit the coefficients of a tight-binding model with tetragonal lattice. The model includes 4th nearest neighbors to fit the α , β , and γ band. In

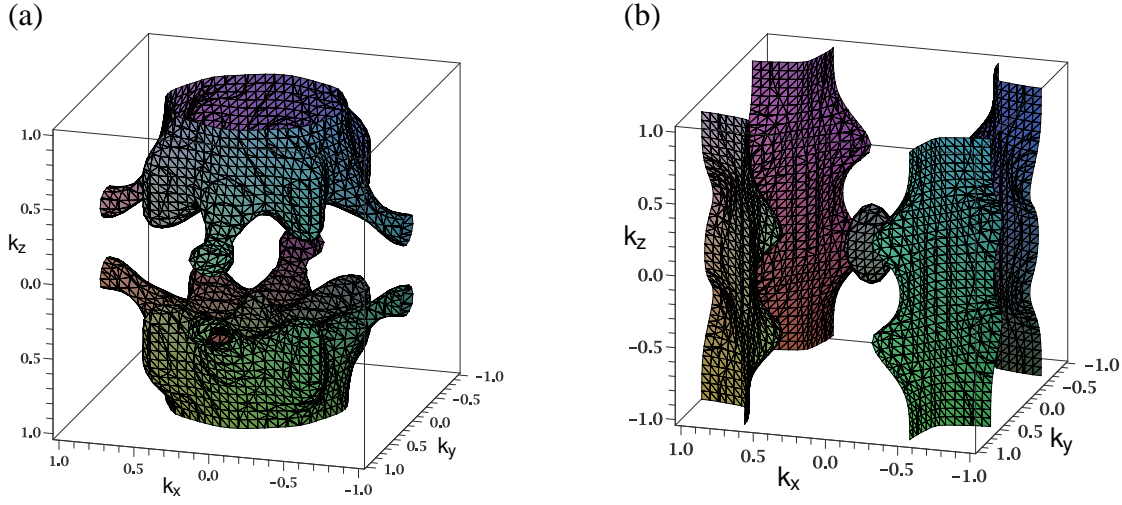


Figure 5.3: Fermi surfaces of CePt₃Si: (a) the β band and (b) the γ band.

general, the band structure can be written as

$$\xi_{\mathbf{k}} = \sum_{(i,j,k) \neq (0,0,0)} t_{(i,j,k)} \exp(-i\mathbf{k} \cdot \mathbf{r}) - \mu \quad (5.29)$$

where \mathbf{r} corresponds to the coordinate of the neighbor with the position (i, j, k) . A detailed list, including the hopping parameters for each band is found in Appendix C. As expected, the agreement with the LDA data is perfect, see Fig. 5.2. I estimated the strength of the spin-orbit coupling α (see Eq. (5.8) and Appendix C for the precise value) to agree quantitatively with Ref. [120, 121]. The result for the spin-orbit split bands and some cuts through the Fermi surfaces are shown in Fig. 5.4 and in Fig. 5.5, respectively.

From this tight-binding fit, it is now easy to construct the Fermi surface for the β and γ band which is displayed in Fig. 5.3. The Fermi surface is in quite good agreement with the reconstruction from Hashimoto *et al.* in Ref. [122]. Apart from the fact, that there is no Fermi surface from the α band, there are two topological differences: First, the small electron pocket around the Γ point in the γ band which is absent in Hashimoto's reconstruction, and second, the 8 small tubes pointing close to the X-point in the β band, which are also not seen in Hashimoto *et al.*. However, Samokhin *et al.* [120, 121] show small pockets at the same position in the β band, where the tubes end in Fig. 5.3(a). That is, there are still some differences between the published Fermi surface reconstructions and my result, but the overall shape is quite similar.

With the help of this tight binding-model one can easily calculate the density of states (DoS) corresponding to each band [130]:

$$D(\omega) = \frac{1}{4\pi^3} \int_{B.Z.} dk^3 \delta(\omega - \xi_{\mathbf{k}}) . \quad (5.30)$$

Again, details of the calculation can be found in Appendix D.3. The result (without SOC) is

5 Dynamical spin and charge responses in CePt₃Si

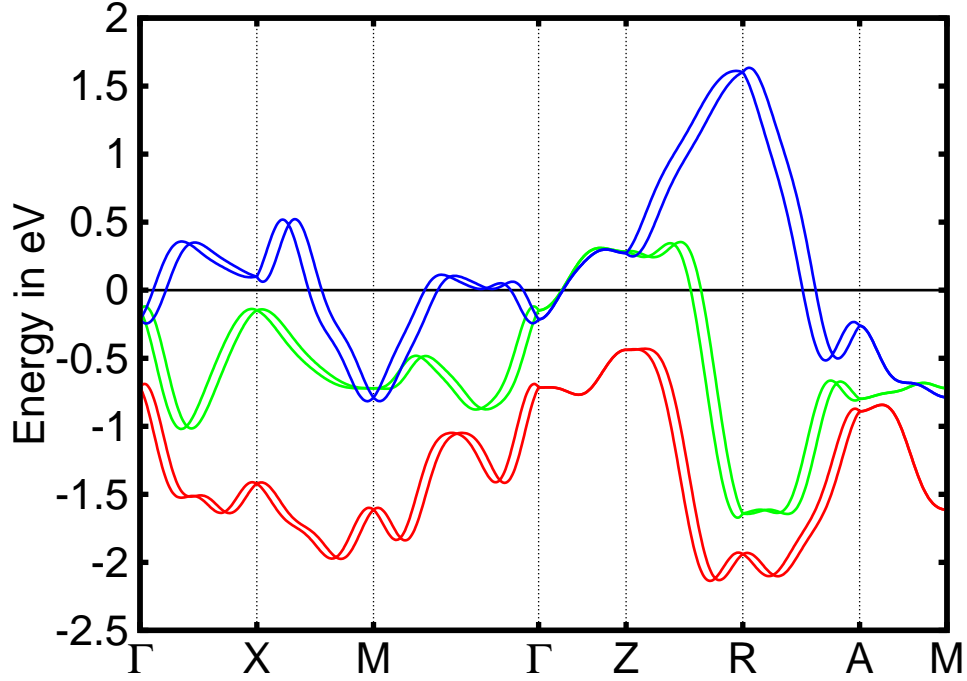


Figure 5.4: Band structure model with spin-orbit coupling for the α (red), β (green) and γ band (blue) of CePt₃Si.

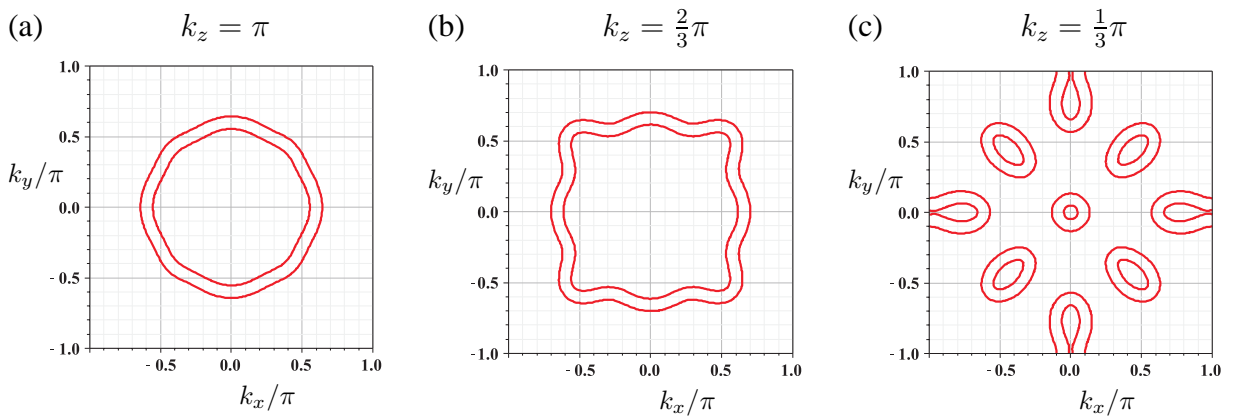


Figure 5.5: Cuts through the spin-orbit split β bands of CePt₃Si for (a) $k_z = \pi$, (b) $k_z = 2/3\pi$ and (c) $k_z = 1/3\pi$.

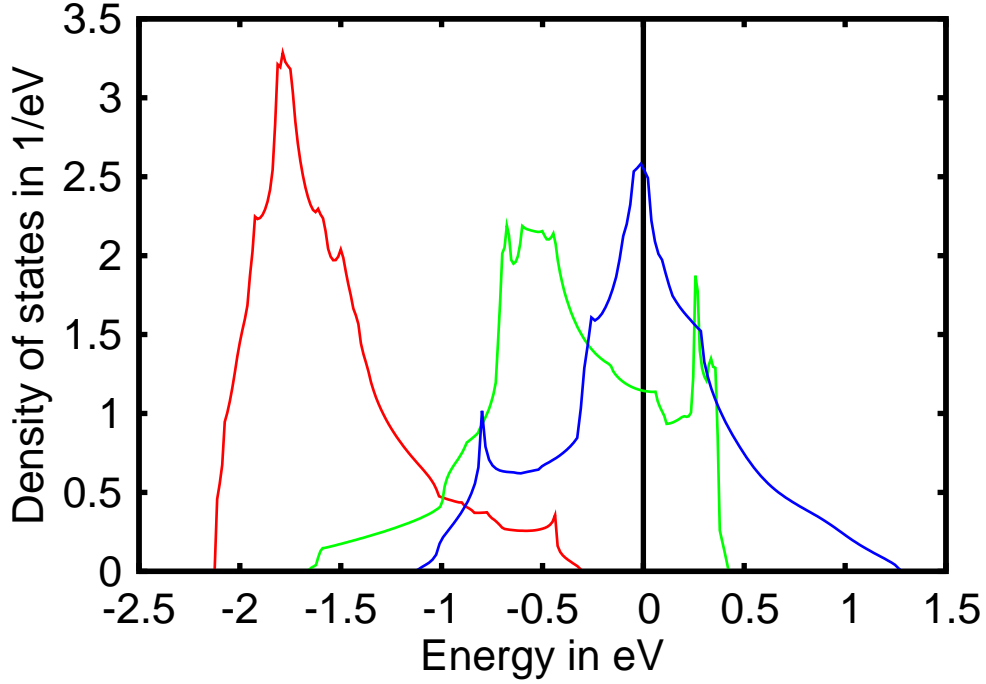


Figure 5.6: Density of states for the α (red) β (green) and γ band (blue) of CePt₃Si.

shown in Fig. 5.6. Obviously, the α band has zero DoS at the Fermi surface. The β band combines 31% of the DoS and the γ band the remaining 61% at the Fermi edge. This is in contradiction to Samokhin *et al.* [120, 121] who obtained the opposite result with the β band contributing 70% to the DoS and the γ band 24%. I assume that this is an effect from the Ce-4f electrons which flatten especially the β band close to the Fermi surface, leading to such a high DoS. Thus, despite the low DoS of the β band, I will rely to the published results and analyze in the following the nesting properties of this band. Another reason for a closer examination of the β band might be the interesting shape, which is clearly not quasi two dimensional, like the γ band.

5.3.2 Fermi surface nesting

Nesting between sheets of the Fermi surfaces is described by the so-called nesting-function, which is identical to the imaginary part of the susceptibility: $\Im\chi(\mathbf{q}, \omega)$ evaluated in the limit $\omega \rightarrow 0$. For finite frequencies this is known as dynamical nesting⁷. Since the numerical results are only available for finite frequencies, I chose here $\omega = 1, 1\text{meV}$, which is very close to zero compared to the bandwidth of about 2eV. To simplify matters, I switched off the spin-orbit coupling. However, differences in $\Im\chi(\mathbf{q}, \omega)$ between calculations with and without SOC are small and will be discussed in the following Section 5.4.1 about inelastic neutron scattering.

⁷Note that the real part of the susceptibility for $\omega = 0$ can be peaked at different position for strong dynamical nesting.

5 Dynamical spin and charge responses in CePt₃Si

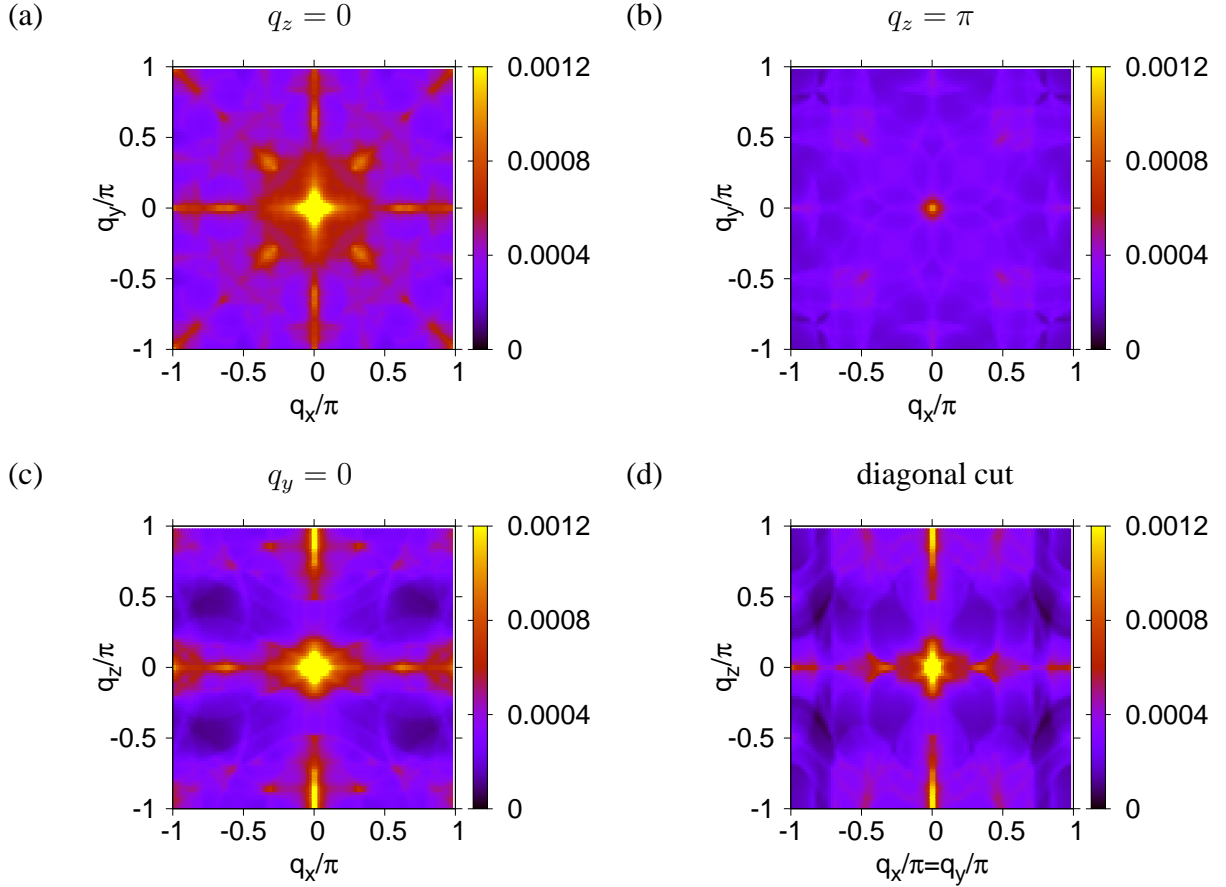


Figure 5.7: Nesting function $\Im\chi(\mathbf{q}, \omega)$ for the β band of CePt₃Si, evaluated at $\omega = 1.1$ meV.

Note that in the normal state, without SOC, the spin susceptibility (see Section 5.2) becomes diagonal and isotropic. Furthermore, the spin and charge susceptibilities are equal (at least in the normal state). Thus, only one term [namely the $i = j = \alpha = \beta = 0$ term from Eq. (5.23)] instead of 12 has to be evaluated. The result is shown in Fig. 5.7. From these cuts through different planes across the Brillouin zone, one can clearly identify the following nesting vectors (ordered by the intensity in $\Im\chi$):

$$\begin{aligned}
 Q_0 &= (0, 0, 0) \\
 Q_1 &= (0, 0, \pi) \\
 Q_2 &= (\pi, \pi, 0) \\
 Q_3 &= (0.6\pi, 0, 0) \\
 Q_4 &= (\pi, 0, 0) \\
 Q_5 &= (0.3\pi, 0.3\pi, 0) \\
 Q_6 &= (0.3\pi, 0, 0.87\pi) .
 \end{aligned} \tag{5.31}$$

At this stage, one might wonder about the peak at the center of the Brillouin zone, because

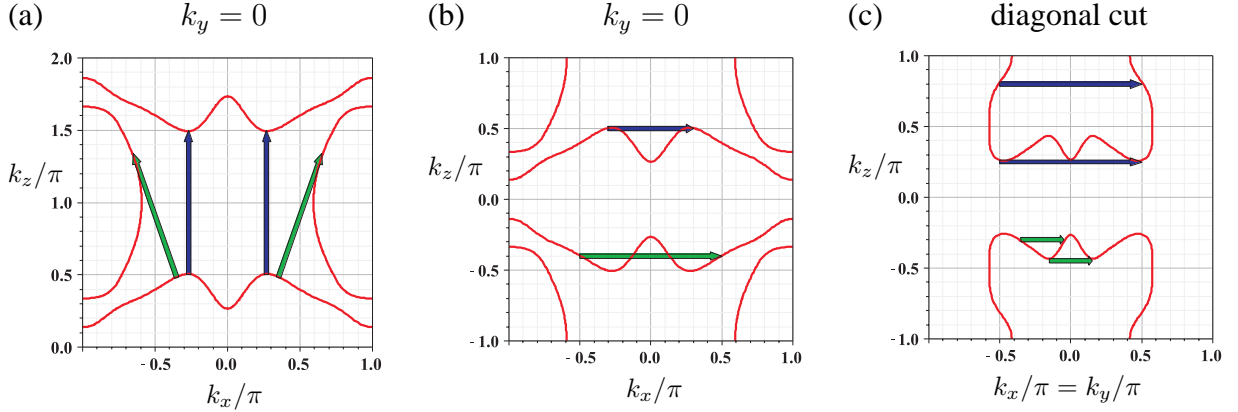


Figure 5.8: Nesting vectors for the β band of CePt₃Si. (a) $Q_1 = (0, 0, \pi)$ in blue and $Q_6 = (0.3\pi, 0, 0.87\pi)$ in green (b) $Q_3 = (0.6\pi, 0, 0)$ in blue and $Q_4 = (\pi, 0, 0)$ in green (c) $Q_2 = (\pi, \pi, 0)$ in blue and $Q_5 = (0.3\pi, 0.3\pi, 0)$ in green.

from the Lindhard expression for the normal state [72, 130]

$$\chi^{\text{Lindhard}}(\mathbf{q}, \omega) = \sum_{\mathbf{k}} \frac{f(\xi_{\mathbf{k}}) - f(\xi_{\mathbf{k}+\mathbf{q}})}{\omega - (\xi_{\mathbf{k}+\mathbf{q}} - \xi_{\mathbf{k}}) + i\delta}, \quad (5.32)$$

$$\chi_0''^{\text{Lindhard}}(\mathbf{q}, \omega) = -\pi \sum_{\mathbf{k}} [f(\xi_{\mathbf{k}}) - f(\xi_{\mathbf{k}+\mathbf{q}})] \delta(\omega - \xi_{\mathbf{k}+\mathbf{q}} + \xi_{\mathbf{k}}) \quad (5.33)$$

such a peak is not expected. For the homogeneous limit ($\mathbf{q} \rightarrow 0$) and for finite frequencies, the Lindhard response (the imaginary and real part) vanishes since the numerator becomes zero:

$$\chi_0^{\text{Lindhard}}(\mathbf{q} \rightarrow 0, \omega \neq 0) = 0 \quad (5.34)$$

This raises an important issue: The method I described in Section 5.2 goes beyond the Lindhard expression, since it starts from the spectral function. The damping $\delta_0 = 2\text{meV}$ can be seen as quasiparticle width. Such a linewidth is not included in the Lindhard expression. For finite damping δ_0 in the Green's functions, I get with the substitutions $x = \omega/\delta_0$ and $y = \xi_{\mathbf{k}}/\delta_0$:

$$\chi''(\mathbf{q} = 0, \omega) = \frac{N_{\text{F}}}{\pi^2} \left\langle \int_{-\infty}^{\infty} dy \frac{1}{x(x^2 + 4)} \left\{ x \arctan(x + y) + x \arctan(x - y) + \ln \frac{[(x + y)^2 + 1][(x - y)^2 + 1]}{(y^2 + 1)^2} \right\} \right\rangle_{\text{FS}}. \quad (5.35)$$

The last term drops out by integration and the remaining integration is performed, assuming just now a spherical Fermi surface:

$$\chi''(\mathbf{q} = 0, \omega) = \frac{N_{\text{F}}}{\pi} \frac{2x}{x^2 + 4}. \quad (5.36)$$

5 Dynamical spin and charge responses in CePt₃Si

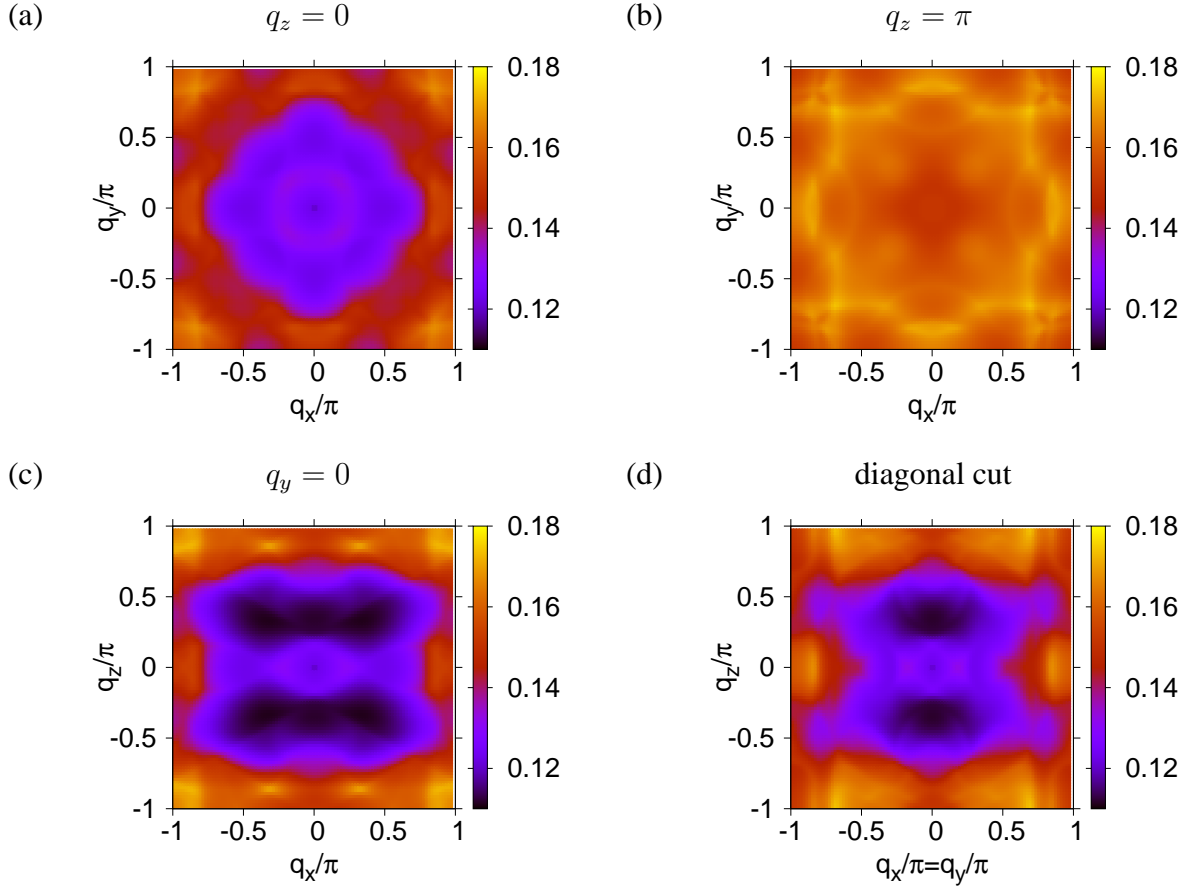


Figure 5.9: Real part of the susceptibility for the β band of CePt₃Si without ASOC, evaluated at $\omega = 1.1\text{meV}$.

One finds that $\chi''(\mathbf{q} = 0, \omega)$ is peaked at $\omega^{max} = 2\delta_0$, and the Lindhard response is recovered in the limit $\delta_0 \ll \omega$. Even though the Fermi surface of this model is by far not spherical, this estimation is in perfect agreement with the numerical results⁸, and thus explains the quasiparticle peak at $\mathbf{q} = 0$.

Comparing the nesting vectors Q_1, \dots, Q_6 listed in Eq. (5.31) with the band structure model, one can identify the nesting Fermi surface sheets in the β band of CePt₃Si. In Fig. 5.8 some representative examples are sketched in. Note that due to the representation as 2D cuts through the Brillouin zone, it is difficult to see that the nesting conditions are actually fulfilled along curves on the Fermi surface. Apart from the $\mathbf{q} = 0$ peak, the nesting vector $Q_1 = (0, 0, \pi)$ is clearly the strongest (see Fig. 5.7) even though it is smeared out along the q_z axis⁹. This can be attributed to the strong antiferromagnetic spin fluctuations in the vicinity of an AFM order with exactly this ordering vector $Q_1 = (0, 0, \pi)$. Therefore, I conclude that nesting along Q_1 plays an

⁸The dependence on ω and δ_0 is reproduced except for a scaling factor, which is due to the non-spherical band structure.

⁹Close to the AFM instability this peak might strongly be enhanced by an RPA treatment.

important role in CePt₃Si, since it may explain at least partially the staggered AFM order in this compound, which supports this itinerant model.

So far published calculations dealt only with the static and, therefore, the real part of the susceptibility, see e.g. Yanase *et al.* [114]. This is a good approximation if dynamic nesting is not important. However, I find that the real part (see Fig. 5.9) differs significantly from the imaginary part of the susceptibility (see Fig. 5.7). Instead of a peak at the AFM wave-vector in $\Re\chi$ as seen by Yanase, I find a saddle point (Fig. 5.9) at this position, which might be due to the different parameterization of the band structure.

5.4 Results

With the band structure model of Section 5.3.1, it is now possible to calculate different response functions and to discuss the effect of spin fluctuations for the Cooper-pairing. Here, different parts of the spin or charge susceptibility are important. The inelastic neutron scattering (INS) cross section is obtained from the imaginary part of the dynamical spin susceptibility and will be addressed in Section 5.4.1. Experimental work on INS has already been published in Ref. [131, 132], mainly for the antiferromagnetic state. Let me remind, that all numerical results use the β band of CePt₃Si for $T = 0$. Nevertheless, the calculations are done for the normal state without antiferromagnetic ordering. For this reason, a comparison to the cited experiments, mainly about the magnon dispersion, is not possible.

The pairing interaction for a weak-coupling model, based on spin fluctuation exchange, uses the real part of the static spin and charge susceptibilities. In Section 5.4.2, I will present a sign analysis for possible superconducting pairing states. Finally, in Section 5.4.3, I calculate Kohn anomalies, using the real part of the dynamical charge susceptibility. Kohn anomalies in CePt₃Si have not yet been measured. However, excellent experimental work in lead and niobium [133] suggests promising results.

5.4.1 Inelastic neutron scattering

In general, the dynamical magnetic (or spin) susceptibility $\chi_{ij}(\mathbf{q}, \omega)$ is a (3×3) second-rank tensor which depends on transferred momentum \mathbf{q} and frequency ω . The indices $i, j = x, y, z$ run over the three spatial dimensions, since the (static, i.e. $\omega = 0$) susceptibility connects the magnetic field \mathbf{B} ($\mathbf{B} = \mu\mathbf{H}$; \mathbf{H} : applied field) with the magnetic moment \mathbf{M} : $M_i = \sum_j \chi_{ij} B_j$. The dynamical spin susceptibility can be decomposed into a symmetric and antisymmetric component according to Ref. [134]:

$$\chi_{ij}(\mathbf{q}, \omega) = \chi_{ij}^{(S)}(\mathbf{q}, \omega) + \chi_{ij}^{(A)}(\mathbf{q}, \omega) , \quad (5.37)$$

with $\chi_{ij}^{(S)} = \chi_{ji}^{(S)}$ and $\chi_{ij}^{(A)} = -\chi_{ji}^{(A)}$. The antisymmetric tensor is uniquely related to an axial vector [here denoted by $\mathbf{C}(\mathbf{q}, \omega)$] via

$$\chi_{ij}^{(A)}(\mathbf{q}, \omega) = -i\epsilon_{ijk} C_k(\mathbf{q}, \omega) . \quad (5.38)$$

5 Dynamical spin and charge responses in CePt₃Si

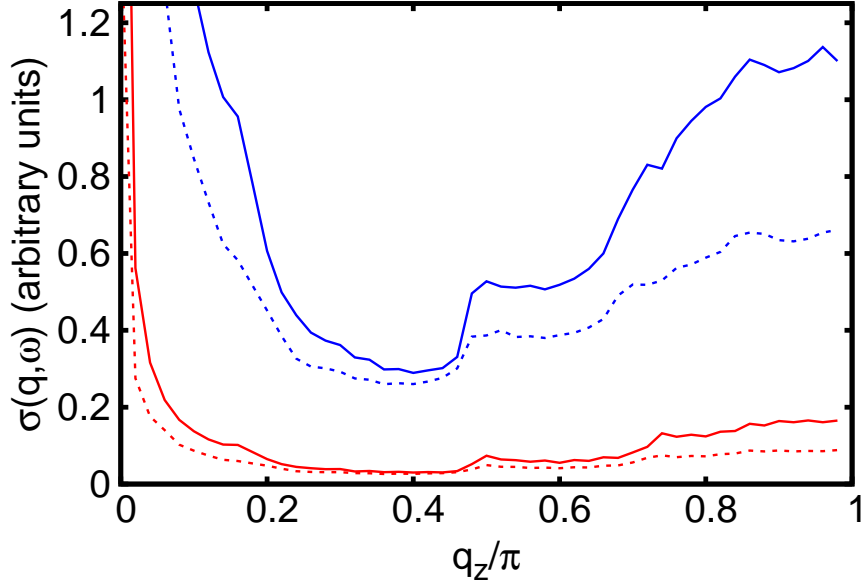


Figure 5.10: Calculated INS along q_z in CePt₃Si for $\omega = 1.1\text{meV}$ (red) and $\omega = 11\text{meV}$ (blue), with (dotted) and without (solid) ASOC.

With the following parameterization

$$\chi^{(A)}(\mathbf{q}, \omega) = \begin{pmatrix} 0 & -\chi_{xy}^{(A)} & \chi_{xz}^{(A)} \\ \chi_{xy}^{(A)} & 0 & -\chi_{yz}^{(A)} \\ -\chi_{xz}^{(A)} & \chi_{yz}^{(A)} & 0 \end{pmatrix}, \quad (5.39)$$

$$\mathbf{C}(\mathbf{q}, \omega) = -i \begin{pmatrix} \chi_{yz}^{(A)} \\ \chi_{xz}^{(A)} \\ \chi_{xy}^{(A)} \end{pmatrix}, \quad (5.40)$$

the inelastic cross section $\sigma(\mathbf{q}, \omega)$ for neutron scattering can be written as [134]:

$$\sigma(\mathbf{q}, \omega) = \frac{1}{\pi} \frac{k_f}{k_i} \left[1 - \exp\left(-\frac{\omega}{T}\right) \right]^{-1} \quad (5.41)$$

$$\times \left[\text{“nuclear scattering”} + r^2 F_m^2 \sum_{ij} (\delta_{ij} - \hat{q}_i \hat{q}_j) \Im \chi_{ij}^{(S)} + \text{“polarized neutrons”} \right].$$

The term in the first line is the so-called Bose-factor, the first term in the brackets is due to nuclear scattering and the last one vanishes for non-polarized neutrons. F_m is the magnetic form factor of the ion, $r = 5.4 \times 10^{-13}$ cm and $\hat{\mathbf{q}} = \mathbf{q}/|\mathbf{q}|$. More details, especially for polarized neutrons can be found in Ref. [134]. However, I am interested in the second term, which is

relevant for the scattering on electrons:

$$\begin{aligned} \sum_{ij} (\delta_{ij} - \hat{q}_i \hat{q}_j) \chi_{ij}^{(S)''} &= \chi_{xx}^{(S)''} (1 - \hat{q}_x^2) + \chi_{yy}^{(S)''} (1 - \hat{q}_y^2) + \chi_{zz}^{(S)''} (1 - \hat{q}_z^2) \\ &\quad - 2\chi_{xy}^{(S)''} \hat{q}_x \hat{q}_y - 2\chi_{xz}^{(S)''} \hat{q}_x \hat{q}_z - 2\chi_{yz}^{(S)''} \hat{q}_y \hat{q}_z . \end{aligned} \quad (5.42)$$

For some special cases the above expression simplifies considerably: If e.g. $\hat{\mathbf{q}} = \hat{\mathbf{e}}_z$, i.e. one performs a scan along the [001]-axis (used, for example, to determine the spin-wave dispersion in Ref. [131]), the cross section is proportional to¹⁰:

$$\sigma(\mathbf{q} = (0, 0, q_z), \omega) \propto \Im (\chi_{xx}^{(S)} + \chi_{yy}^{(S)}) \quad (5.43)$$

That means, all off-diagonal components drop out and only the sum of the susceptibilities “perpendicular” to the \mathbf{q} -vector remain. Since the diagonal components of the spin susceptibility are by definition symmetric, one can identify $\chi_{ii}^{(S)} = \chi_{ii}$. In the normal state, without ASOC, the spin susceptibility is isotropic $\chi_{ij} = \chi \delta_{ij}$ and the well-known connection $\sigma(\mathbf{q}, \omega) \propto \chi''$ is recovered. Thus, within the notation defined in Section 5.2, the neutron cross section along the q_z direction reads:

$$\sigma(\mathbf{q} = (0, 0, q_z), \omega) \propto \Im [4\chi_{0000}] \quad \text{without ASOC} \quad (5.44)$$

$$\sigma(\mathbf{q} = (0, 0, q_z), \omega) \propto \Im [\chi_{++00} + \chi_{+-00} + \chi_{-+00} + \chi_{--00}] \quad \text{with ASOC} \quad (5.45)$$

Some examples for calculated neutron cross sections are shown in Fig. 5.10 (for typical energies) and Fig. 5.11 (spectrum over the whole bandwidth). Again in Fig. 5.10 one can see the quasiparticle peak at $q_z = 0$ and the AFM peak at $q_z = \pi$. Interestingly, the graph including the ASOC is always smoother than the one without ASOC. The reason for this may be found in the four terms in Eq. (5.45) that contribute to the cross section: For each of these intra- (χ_{++00} , χ_{--00}) and inter-band (χ_{+-00} , χ_{-+00}) terms, the nesting condition is a little bit different. Averaging over all these momentum-shifted peaks, leads to a smoother result. Furthermore, for both frequencies in Fig. 5.10, the graph without ASOC lies below the one with ASOC. As can be seen in Fig. 5.11, this is due to a shift in spectral weight from lower frequencies to higher ones.

Finally, I want to describe an attempt which was not successful. With the published data for the spin-wave dispersion for CePt₃Si [131], I wanted to build a \mathbf{q} -dependent RPA model, which then could have been used to renormalize the calculated spin susceptibility. The spin-wave dispersion for a two-sublattice commensurate antiferromagnet, which is realized in CePt₃Si, is given by [131]

$$\omega(\mathbf{q}) = \sqrt{[J(\mathbf{Q}_{AFM}) - J(\mathbf{q})][J(\mathbf{Q}_{AFM}) - J(\mathbf{Q}_{AFM} + \mathbf{q})]} , \quad (5.46)$$

with the antiferromagnetic wave-vector $\mathbf{Q}_{AFM} = (0, 0, \pi)$ and with the exchange integrals $J(\mathbf{q})$ in the Fourier representation $J(\mathbf{q}) = \sum_{\mathbf{r}} J(\mathbf{r}) e^{-i\mathbf{q} \cdot \mathbf{r}}$ where \mathbf{r} runs over all (next-)nearest neigh-

¹⁰after correction for the Bose-factor

5 Dynamical spin and charge responses in CePt₃Si

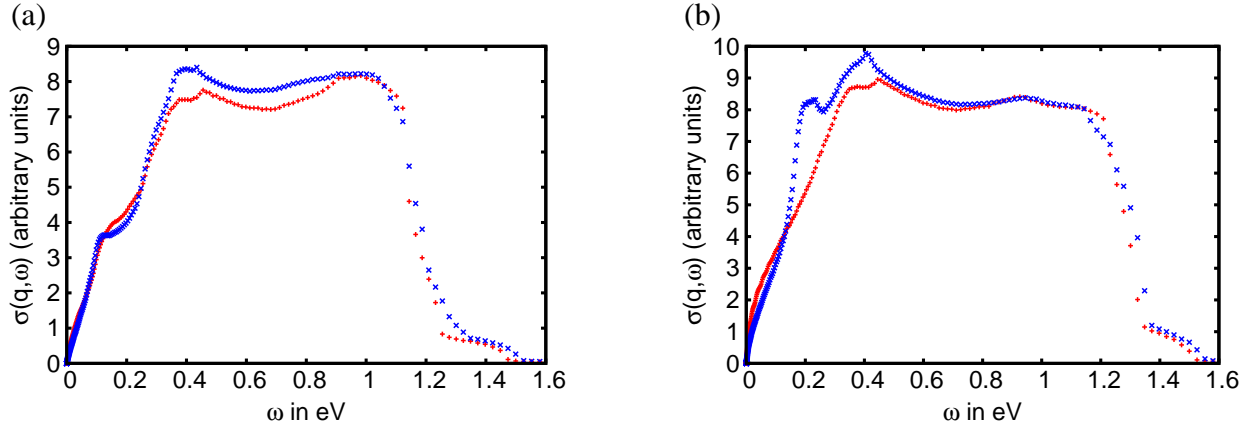


Figure 5.11: Calculated INS spectra for CePt₃Si: ω -scan for CePt₃Si with (red) and without (blue) ASOC for the wave vector $\mathbf{q} = (0, 0, 0.5\pi)$ (a) and $\mathbf{q} = (0, 0, \pi)$ (b).

bors. For the $J_1 - J_7$ -model, proposed in Ref. [131], the following parameterization is used ¹¹

$$\begin{aligned}
 J(\mathbf{q}) = & 2J_1(\cos q_x + \cos q_y) + 4J_2 \cos q_x \cos q_y + 2J_3 \cos q_z + 4J_4(\cos q_x + \cos q_y) \cos q_z \\
 & + 8J_5 \cos q_x \cos q_y \cos q_z + 2J_6 [\cos(2q_x) + \cos(2q_y)] \\
 & + 2J_7 [\cos(3q_x) + \cos(3q_y)] ,
 \end{aligned} \tag{5.47}$$

where the constants $J_1 - J_7$ are fitted to the experimental results. This model neglects completely the \mathbf{q} -dependence of the spin susceptibility. Therefore, I wanted to use a more sophisticated model. The bare spin susceptibility $\chi(\mathbf{q}, \omega)$ is calculated from the band structure and then submitted to an RPA-treatment, which includes a \mathbf{q} -dependent coupling constant:

$$\chi^{\text{RPA}}(\mathbf{q}, \omega) = \frac{\chi(\mathbf{q}, \omega)}{1 - J(\mathbf{q})\chi(\mathbf{q}, \omega)} . \tag{5.48}$$

Then, the real and imaginary part read

$$\begin{aligned}
 \Re\chi^{\text{RPA}}(\mathbf{q}, \omega) &= \frac{\chi' - J(\mathbf{q})|\chi_0|^2}{(1 - J(\mathbf{q})\chi')^2 + J^2(\mathbf{q})\chi''^2} \\
 \Im\chi^{\text{RPA}}(\mathbf{q}, \omega) &= \frac{\chi''}{(1 - J(\mathbf{q})\chi')^2 + J^2(\mathbf{q})\chi''^2} ,
 \end{aligned} \tag{5.49}$$

and the spin-wave dispersion is obtained from the maximum of $\Im\chi^{\text{RPA}}(\mathbf{q}, \omega)$ for constant \mathbf{q} . The exchange integrals $J_1 - J_7$ are adjusted, using a simulated annealing procedure so that the spin-wave dispersion agrees with the experimental results. Unfortunately, it was not possible to find parameters $J_1 - J_7$ with satisfying result. I attribute this to a break-down of the itinerant description. A solution to this problem might be to include the antiferromagnetism in a model as proposed in Ref. [114]. However, from the computational point of view such an increase of the

¹¹The lattice constants $a=b$ and c are set to unity.

dimension for a dynamical calculation is at least very demanding.

5.4.2 Consequences for the Cooper–pairing

Based on the numerical results for the spin and charge susceptibility in the normal state, it is now possible to construct a superconducting pairing interaction mediated by spin fluctuations in order to shed light on the pairing scenario in CePt₃Si. As discussed in the introduction of this section, the susceptibility is calculated in the normal state, and to simplify matters, the static case ($\omega = 0$) is considered here. Thus, in contrast to the previous section, the real part of the susceptibility is decisive. In the following, I combine a model proposed by Takimoto *et al.* [135] with numerical results obtained by the method of this chapter. Finally, I will provide simple arguments from sign considerations of the gap equation for the superconducting pairing state.

The starting point is the superconducting gap equation, where one needs the following extended definition for the superconducting order parameter. As mentioned in Chapter 1, the superconducting $\mathbf{d}_{\mathbf{k}}$ -vector needs to be parallel to the spin–orbit vector $\boldsymbol{\gamma}_{\mathbf{k}}$ (if the triplet contribution to the gap is not strongly suppressed). In general, one may then write

$$\mathbf{d}(\mathbf{k}) = \phi(\mathbf{k})\boldsymbol{\gamma}_{\mathbf{k}} \quad (5.50)$$

$$\Delta_{\pm}(\mathbf{k}) = \psi(\mathbf{k}) \pm \phi(\mathbf{k})|\boldsymbol{\gamma}_{\mathbf{k}}|, \quad (5.51)$$

where the symmetry of the momentum dependence of $\phi(\mathbf{k})$ is the same as that of the spin–singlet contribution $\psi(\mathbf{k})$ [136]. For this order parameter, the weak–coupling gap equation reads according to Takimoto *et al.* [135]

$$\begin{pmatrix} \psi(\mathbf{k}) \\ d_x(\mathbf{k}) \\ d_y(\mathbf{k}) \end{pmatrix} = \sum_{\mathbf{q}} \begin{pmatrix} -V_{ss}(\mathbf{q}) & V_{sx}(\mathbf{q}) & V_{sy}(\mathbf{q}) \\ V_{xs}(\mathbf{q}) & V_{xx}(\mathbf{q}) & -V_{xy}(\mathbf{q}) \\ V_{ys}(\mathbf{q}) & -V_{yx}(\mathbf{q}) & V_{yy}(\mathbf{q}) \end{pmatrix} \begin{pmatrix} F_s(\mathbf{k} - \mathbf{q}) \\ F_x(\mathbf{k} - \mathbf{q}) \\ F_y(\mathbf{k} - \mathbf{q}) \end{pmatrix}, \quad (5.52)$$

with the following diagonal pairing interaction due to spin and charge fluctuations¹²:

$$V_{ss}(\mathbf{q}) = U^2 [-\chi_{cc}^{\text{RPA}}(\mathbf{q}) + \chi_{xx}^{\text{RPA}}(\mathbf{q}) + \chi_{yy}^{\text{RPA}}(\mathbf{q}) + \chi_{zz}^{\text{RPA}}(\mathbf{q})] + U \quad (5.53)$$

$$V_{xx}(\mathbf{q}) = U^2 [\chi_{cc}^{\text{RPA}}(\mathbf{q}) - \chi_{xx}^{\text{RPA}}(\mathbf{q}) + \chi_{yy}^{\text{RPA}}(\mathbf{q}) + \chi_{zz}^{\text{RPA}}(\mathbf{q})] \quad (5.54)$$

$$V_{yy}(\mathbf{q}) = U^2 [\chi_{cc}^{\text{RPA}}(\mathbf{q}) + \chi_{xx}^{\text{RPA}}(\mathbf{q}) - \chi_{yy}^{\text{RPA}}(\mathbf{q}) + \chi_{zz}^{\text{RPA}}(\mathbf{q})]. \quad (5.55)$$

The off–diagonal components of the pairing interaction

$$V_{xy}(\mathbf{q}) = V_{yx}(\mathbf{q}) = U^2 [\chi_{xy}^{\text{RPA}}(\mathbf{q}) + \chi_{yx}^{\text{RPA}}(\mathbf{q})] \quad (5.56)$$

$$V_{sx}(\mathbf{q}) = -V_{xs}(\mathbf{q}) = iU^2 [\chi_{yz}^{\text{RPA}}(\mathbf{q}) - \chi_{zy}^{\text{RPA}}(\mathbf{q})] \quad (5.57)$$

$$V_{sy}(\mathbf{q}) = -V_{ys}(\mathbf{q}) = iU^2 [\chi_{zx}^{\text{RPA}}(\mathbf{q}) - \chi_{xz}^{\text{RPA}}(\mathbf{q})] \quad (5.58)$$

¹²It is convenient for the following analysis to use a different sign convention compared to Takimoto *et al.*, where the pairing interactions are positive.

5 Dynamical spin and charge responses in CePt₃Si

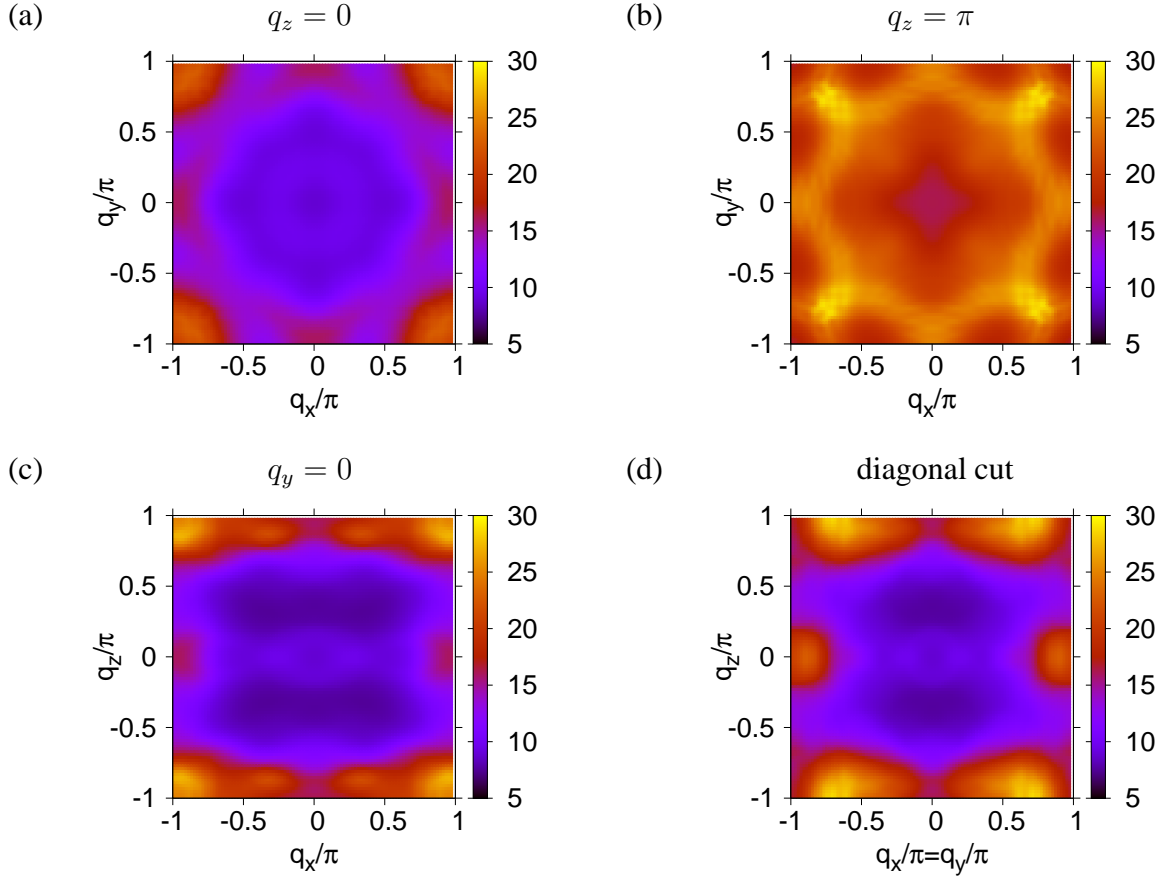


Figure 5.12: Pairing interaction $V_{ss}(\mathbf{q})$ for the singlet channel of the β band in CePt₃Si.

lead to a coupling of the singlet and triplet channel and are small compared to the diagonal components. The RPA renormalization reads:

$$\chi_{cc}^{\text{RPA}}(\mathbf{q}) = \frac{\chi_{cc}(\mathbf{q})}{1 + 2U\chi_{cc}(\mathbf{q})} \quad \text{charge} \quad (5.59)$$

$$\chi^{\text{RPA}}(\mathbf{q}) = \frac{\chi(\mathbf{q})}{1 - 2U\chi(\mathbf{q})} \quad \text{spin} \quad (5.60)$$

Thereby, the charge (χ_{cc}) and spin (χ) susceptibility are calculated numerically using Eqs. (5.12)–(5.15) through the procedure described in Section 5.2 and in Appendix D. Since the gap equation is confined to the weak-coupling limit, the real part of the susceptibility is taken for $\omega \rightarrow 0$. The Matsubara frequency-integrated anomalous Green's functions on the right-hand side of the gap equation are defined as follows

$$F_s(\mathbf{k}) = \frac{1}{2} (\psi_{\mathbf{k}}\varphi_+ + \mathbf{d}_{\mathbf{k}} \cdot \hat{\gamma}_{\mathbf{k}}\varphi_-) \quad (5.61)$$

$$F_\alpha(\mathbf{k}) = \frac{1}{2} \hat{\gamma}_\alpha(\mathbf{k}) (\psi_{\mathbf{k}}\varphi_- + \mathbf{d}_{\mathbf{k}} \cdot \hat{\gamma}_{\mathbf{k}}\varphi_+) , \quad (5.62)$$

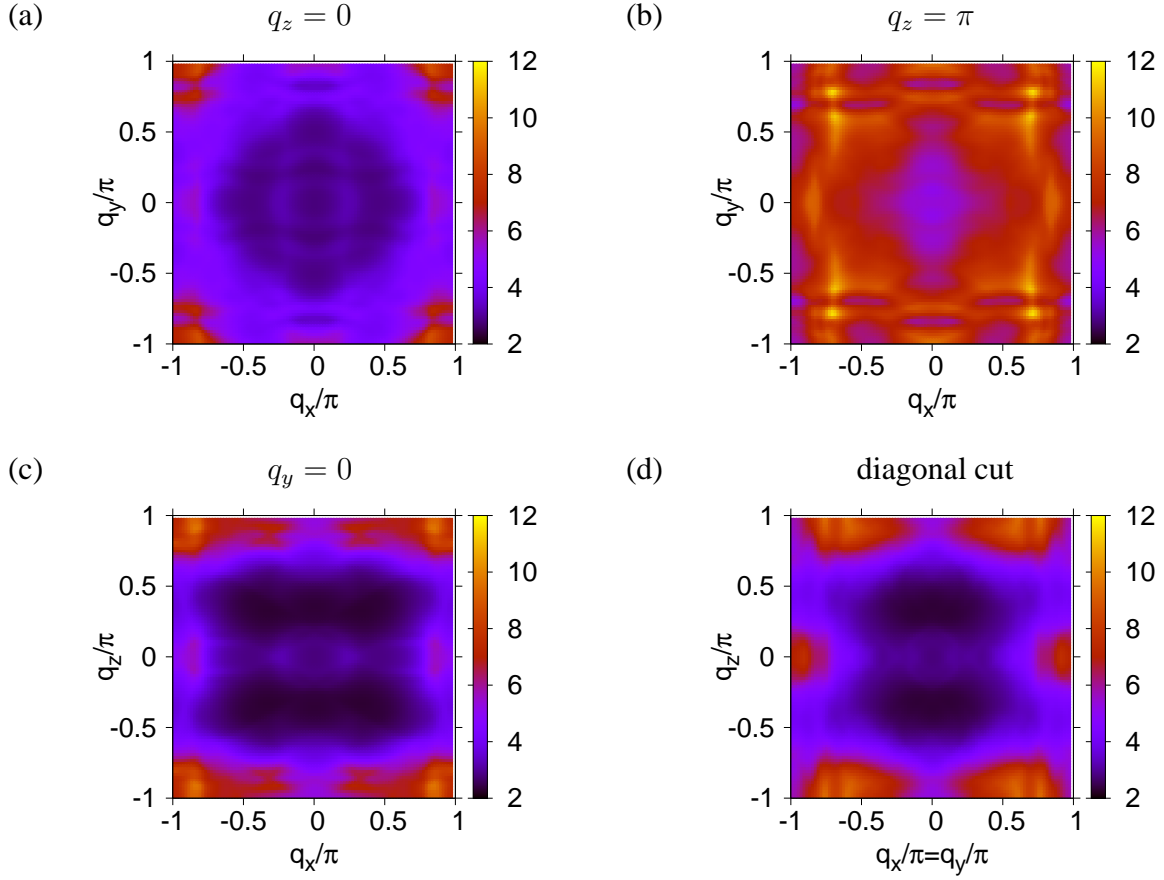


Figure 5.13: Pairing interaction $V_{xx}(\mathbf{q})$ for the triplet channel (\mathbf{d}_x) of the β band in CePt_3Si . The pairing interaction $V_{yy}(\mathbf{q})$ for the second component of the triplet channel (\mathbf{d}_y) is obtained by exchanging q_x and q_y .

with the abbreviation

$$\varphi_{\pm} = \frac{1}{2E_{+}(\mathbf{k})} \tanh \frac{E_{+}(\mathbf{k})}{2k_{\text{B}}T} \pm \frac{1}{2E_{-}(\mathbf{k})} \tanh \frac{E_{-}(\mathbf{k})}{2k_{\text{B}}T} . \quad (5.63)$$

Note that there is no gap equation for the triplet component $d_z(\mathbf{k})$, since $\mathbf{d}(\mathbf{k}) \parallel \boldsymbol{\gamma}(\mathbf{k})$ and $\gamma_z(\mathbf{k}) = 0$ for Rashba-type of SOC as in CePt_3Si . The previous form of the gap Equation (5.52) is rather inconvenient. In order to discuss the consequences for the pairing from the spin and charge susceptibilities, I made the following approximations to simplify the gap equation:

- The gap equation is linearized and particle–hole asymmetric terms are neglected.
- The assumption that $\chi_{\alpha\beta}$ and, therefore, $V_{\alpha\beta}$ is diagonal. For CePt_3Si , the off–diagonal components of $\chi_{\alpha\beta}$ are small compared to the diagonal components. In the centrosymmetric case the off–diagonal elements vanish identically.

5 Dynamical spin and charge responses in CePt₃Si

The result is a decoupled gap equation for the singlet and triplet component

$$\psi(\mathbf{k}) = - \sum_{\mathbf{k}'} V_{ss}(\mathbf{k} - \mathbf{k}') \frac{1}{2} \left[\frac{1}{2\xi_+(\mathbf{k}')} \tanh \frac{\xi_+(\mathbf{k}')}{2k_B T} + \frac{1}{2\xi_-(\mathbf{k}')} \tanh \frac{\xi_-(\mathbf{k}')}{2k_B T} \right] \psi(\mathbf{k}') \quad (5.64)$$

$$\mathbf{d}_\alpha(\mathbf{k}) = \sum_{\mathbf{k}'} V_{\alpha\alpha}(\mathbf{k} - \mathbf{k}') \frac{1}{2} \left[\frac{1}{2\xi_+(\mathbf{k}')} \tanh \frac{\xi_+(\mathbf{k}')}{2k_B T} + \frac{1}{2\xi_-(\mathbf{k}')} \tanh \frac{\xi_-(\mathbf{k}')}{2k_B T} \right] \mathbf{d}_\alpha(\mathbf{k}'), \quad (5.65)$$

with the pairing interaction given in Eqs. (5.53)–(5.55). Note that the pairing interaction for all channels $V_{ss}(\mathbf{q})$, $V_{xx}(\mathbf{q})$ and $V_{yy}(\mathbf{q})$ are positive on the whole Brillouine zone.

In Fig. 5.12 and in Fig. 5.13, the numerical results for the singlet and triplet pairing interaction are displayed for different cuts through the Brillouine zone. Here, the on-site interaction $U = 286\text{meV}$ was chosen, such that an RPA-enhancement of at most a factor of 10 was obtained. The pairing interaction for singlet and triplet looks similar with a strongly enhanced plane at $q_z = \pi$ in both cases and some minor contributions at the edges of the Brillouine zone in the $q_z = 0$ plane. Note that the triplet pairing interactions $V_{xx}(\mathbf{q})$ and $V_{yy}(\mathbf{q})$ are for symmetry reasons identical up to a rotation by 90° around the q_z axis. The asymmetry along the q_x , q_y directions [see Fig. 5.13(a) and (b)] is a direct consequence of the ASOC. Off-diagonal components in the spin susceptibility, which would provide a coupling between the singlet and triplet order parameter, are supposed to be of the same order of magnitude as this asymmetry.

The main difference between Fig. 5.12 and Fig. 5.13 is the magnitude of the pairing interaction, which is stronger by an overall factor of about 2 – 3. Thus, a closer look at the singlet pairing interaction is appropriate, where the strongest peak is found for the skew vector $Q = (0.75\pi, 0.75\pi, \pi)$. This nesting vector connects the opposite parts of the bottom and top sheet of the Fermi surface, see Fig. 5.15. Reminding that $V_{ss} > 0$, a sign change in the superconducting order parameter $\psi_{\mathbf{k}}$ would be needed to satisfy the singlet gap Equation (5.64) with this nesting vector. In Fig. 5.14 some common superconducting states are displayed on the Fermi surface. These illustrations show, that it is difficult to satisfy the singlet gap equation with extended s -wave¹³ or d -wave states, since none of these singlet order parameters shows a sign change across the diagonal. The only possibility to satisfy the gap equation is provided by p -wave states (or higher angular momenta), which is, of course, not allowed for the singlet gap Equation (5.64). That is to say, the singlet component of the gap equation for the strongest nesting vector remains without solution, while it would be in favor of a superconducting p -wave state (see Fig. 5.15).

The situation for the triplet gap Equation (5.65) is different: Here, the pairing interaction requires either small momentum transfers or no sign change for the order parameter. For small momentum transfers $\mathbf{q} \rightarrow 0$ and therefore $\mathbf{k} \approx \mathbf{k}'$, the triplet gap equation has a solution for any positive pairing interaction. However, Fig. 5.13(a), (c) or (d) show little weight around the center of the Brillouine zone. Hence, the second possibility with larger momentum transfer \mathbf{Q} and sign change for the areas of the order parameter, which are connected by \mathbf{Q} , has to be taken

¹³Simple s -wave is not possible due to the required sign change of the order parameter. For extended s -wave pairing it is possible to connect some isolated points on the Fermi surface with opposite sign of the order parameter – however, this will strongly depend on the Fermi surface.

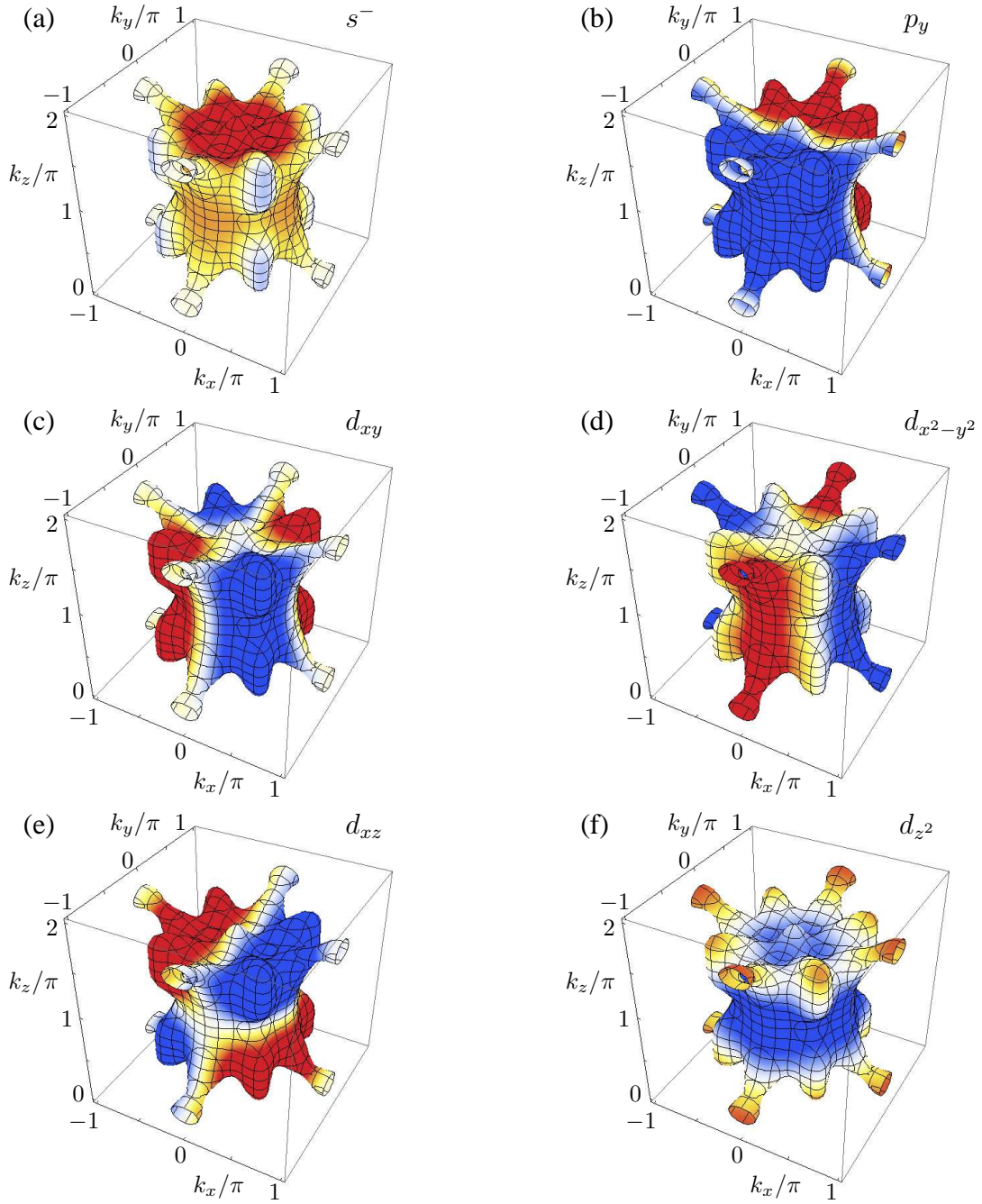


Figure 5.14: Projections of superconducting pairing states on the β band of CePt_3Si . Red/blue areas denote a positive/negative order parameter. The superconducting states are described by (a) $\phi_{\mathbf{k}} = \cos k_x + \cos k_y$ (extended s -wave), (b) $\phi_{\mathbf{k}} = \sin k_y$ (p_y -wave), (c) $\phi_{\mathbf{k}} = \sin k_x \sin k_y$ (d_{xy} -wave), (d) $\phi_{\mathbf{k}} = \cos k_x - \cos k_y$ ($d_{x^2-y^2}$ -wave), (e) $\phi_{\mathbf{k}} = \sin k_x \sin k_z$ (d_{xz} -wave) and (f) $\phi_{\mathbf{k}} = 2 \cos k_z - \cos k_x - \cos k_y$ (d_{z^2} -wave).

5 Dynamical spin and charge responses in CePt₃Si

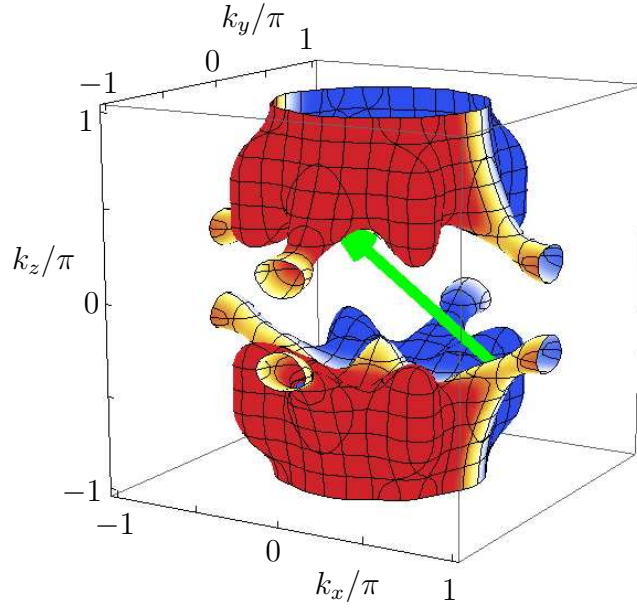


Figure 5.15: Important nesting vector $\mathbf{Q} = (0.75\pi, 0.75\pi, \pi)$ (green) for the singlet pairing interaction on the β band of CePt₃Si. The coloring corresponds to the p_y -wave state, displayed in Fig. 5.14(b).

into account. Just like in the singlet case, the pairing interaction $V_{xx}(\mathbf{q})$ is strongest in the $q_z = \pi$ plane with one small but important difference. Because of the anisotropy along the q_x and q_y direction, as seen in Fig. 5.13(b), all nesting vectors $\mathbf{Q} = (q_x, q_y, \pi)$ with $q_y < q_x$ are enhanced due to the ASOC. Without ASOC, the triplet pairing interactions for the $d_x(\mathbf{k})$ - and $d_y(\mathbf{k})$ -component are equal $V_{xx}(\mathbf{q}) = V_{yy}(\mathbf{q})$, and they would reflect the full tetragonal symmetry. The enhancement for $q_y < q_x$ can be seen best by comparing the intensity of $V_{xx}(\mathbf{q})$ in Fig. 5.13(b) along the q_x and q_y axes or in the vicinity of the split peak close to the diagonal. All nesting vectors $\mathbf{Q} = (q_x, q_y, \pi)$ with $q_y < q_x$ are in favor of a p_y -state (compared to a p_x -state), which shows no sign change along the k_x direction [see Fig. 5.14(b)]. For $V_{xx}(\mathbf{q})$, the favored p_y -state corresponds exactly to the $d_x(\mathbf{k})$ -component of the triplet order parameter with $\mathbf{d}_{\mathbf{k}} \parallel \boldsymbol{\gamma}_{\mathbf{k}}$ and the simple model for $\boldsymbol{\gamma}_{\mathbf{k}} = (-\sin k_y, \sin k_x, 0)$. The analog reasoning holds for the pairing interaction $V_{yy}(\mathbf{q})$, which corresponds to $d_y(\mathbf{k})$. That is to say, the triplet gap Equation (5.65) is solved by a p -wave state that is given by the antisymmetric $\boldsymbol{\gamma}_{\mathbf{k}}$ -vector.

To summarize the results from this sign considerations for the superconducting order parameter, it can be stated that the singlet part of the decoupled gap equation can hardly be fulfilled. Except for some isolated points on the Fermi surface, it is possible to construct a weakly attractive pairing interaction for an extended s -wave state, otherwise the singlet gap equation remains without solution (at least for the strongest nesting vectors). The triplet gap equation on the other hand prefers a p -wave state, which is just given by a $\mathbf{d}_{\mathbf{k}}$ -vector that is supposed to be parallel to $\boldsymbol{\gamma}_{\mathbf{k}}$. It turns out that this triplet state is supported by small momentum transfers and an additional contribution is directly related to the ASOC. Thus, for an increasing Rashba-type of SOC, the pairing interaction favors a triplet state. For CePt₃Si the above sign considerations suggest,

$$D_\lambda(\mathbf{q}, i\nu_m) = D_\lambda^{(0)}(\mathbf{q}, i\nu_m) + |M_{\mathbf{q}\lambda}|^2 \chi(\mathbf{q}, i\nu_m) + \dots$$

Figure 5.16: Feynman diagram to calculate Kohn anomalies.

that the triplet contribution to the superconducting gap is considerably larger than the singlet contribution, which is confirmed by experiments (see Chapter 1).

5.4.3 Kohn anomalies in CePt₃Si

Kohn anomalies are calculated from the Dyson equation for the phonon propagator (see e.g. Ref. [137] or for Kohn anomalies in superconductors Ref. [138]). The bare phonon Green's function reads [116]:

$$D_\lambda^{(0)}(\mathbf{q}, i\nu_m) = \frac{2\Omega_{\mathbf{q}\lambda}}{(i\nu_m)^2 - \Omega_{\mathbf{q}\lambda}^2}, \quad (5.66)$$

with the unrenormalized phonon dispersion $\Omega_{\mathbf{q}\lambda}$ of the phonon branch λ . Evaluating the simple Dyson equation for the phonon propagator in Fig. 5.16 by associating each phonon line with a matrix element $|M_{\mathbf{q}\lambda}|^2$, one gets immediately the renormalized phonon Green's function:

$$\begin{aligned} D_\lambda(\mathbf{q}, i\nu_m) &= \frac{D_\lambda^{(0)}(\mathbf{q}, i\nu_m)}{1 - D_\lambda^{(0)}(\mathbf{q}, i\nu_m)|M_{\mathbf{q}\lambda}|^2\chi(\mathbf{q}, i\nu_m)} \\ &= \frac{2\Omega_{\mathbf{q}\lambda}}{(i\nu_m)^2 - \Omega_{\mathbf{q}\lambda}^2 - 2\Omega_{\mathbf{q}\lambda}|M_{\mathbf{q}\lambda}|^2\chi(\mathbf{q}, i\nu_m)}. \end{aligned} \quad (5.67)$$

In the presence of an ASOC the bare polarization bubble is calculated as follows

$$\chi^{(0)}(\mathbf{q}, i\nu_m) = -\frac{2}{\beta} \sum_{\mathbf{k}, i\omega_n} \text{Tr} \left[\hat{\mathbf{G}}(\mathbf{k}, i\omega_n) \hat{\mathbf{G}}(\mathbf{k} + \mathbf{q}, i\omega_n + i\nu_m) \right], \quad (5.68)$$

which is (up to a prefactor) the zeroth component $[\chi_{00}(\mathbf{q}, i\nu_m)]$ of the susceptibility tensor defined in Eq. (5.1). Thus, the evaluation is completely analog to Section 5.2. Again, the susceptibility can be decomposed into 12 terms which are evaluated independently using Eq. (5.22) and

5 Dynamical spin and charge responses in CePt₃Si

Eq. (5.23):

$$\begin{aligned} \chi^{(0)}(\mathbf{q}, i\nu_m) = \frac{1}{2} [& \chi_{++00} + \chi_{++xx} + \chi_{++yy} \\ & + \chi_{+-00} - \chi_{+-xx} - \chi_{+-yy} \\ & + \chi_{-+00} - \chi_{-+xx} - \chi_{-+yy} \\ & + \chi_{--00} + \chi_{--xx} + \chi_{--yy}] . \end{aligned} \quad (5.69)$$

After an analytical continuation according to $i\nu_m \rightarrow \omega + i\delta$, the renormalized phonon dispersion is now calculated from the poles of the phonon Green's function in Eq. (5.67), i.e. from $[D_\lambda(\mathbf{q}, \omega)]^{-1} = 0$. The result reads:

$$\omega^2 = \Omega_{\mathbf{q}\lambda}^2 + 2\Omega_{\mathbf{q}\lambda}|M_{\mathbf{q}\lambda}|^2\chi(\mathbf{q}, \omega) . \quad (5.70)$$

It can easily be seen from Eq. (5.69), that many inter- and intra-band terms contribute to the susceptibility. From these terms, one may expect Kohn anomalies at smaller momentum transfers that correspond to the distance between two spin-orbit split Fermi surfaces [139, 140, 141]. Let me continue with some remarks to the above Eq. (5.70). Clearly it is a self-consistent equation in the renormalized phonon frequency ω . It turns out, that the first iteration (i.e. replacing ω by $\Omega_{\mathbf{q}\lambda}$ on the right-hand side) gives already results that are sufficiently close to the limiting value¹⁴. The Kohn anomalies are caused by peaks in the real part of the susceptibility. The imaginary part contributes to the linewidth, i.e. imaginary part of ω . From Eq. (5.70), one gets at the same time, the phonon dispersion and the linewidth.

In order to compare the above expressions to previous work on two dimensional electron gas done by Pletyukhov *et al.* [141, 142], I evaluated Eq. (5.68) in the Lindhard approximation [143], i.e. for non-interacting electrons but including a Rashba-type of SOC¹⁵:

$$\chi^{(0)}(\mathbf{k}, i\nu_m) = 4 \sum_{\mathbf{k}} \sum_{\alpha, \beta} \frac{f[\xi_\alpha(\mathbf{k})] - f[\xi_{\alpha\beta}(\mathbf{k} + \mathbf{q})]}{i\nu_m + \xi_\alpha(\mathbf{k}) - \xi_{\alpha\beta}(\mathbf{k} + \mathbf{q})} [1 + \beta \hat{\gamma}_{\mathbf{k}} \cdot \hat{\gamma}_{\mathbf{k} + \mathbf{q}}] . \quad (5.71)$$

This coincides with the results of Pletyukhov *et al.*. Note that Eq. (5.69), which is used for all figures in this section, goes clearly beyond the above Lindhard expression: First, it is not restricted to two dimensions and the special Rashba-type of SOC (but can deal with any type of ASOC for three dimensional Brillouin zones), and second I use the spectral representation to include also quasiparticle lifetime effects.

Here, I take Coulomb repulsion through a Hubbard U into account, leading to an RPA renormalization according to $\chi(\mathbf{q}, \omega) = \chi^{(0)}(\mathbf{q}, \omega) / [1 - U\chi^{(0)}(\mathbf{q}, \omega)]$ with $U = 572\text{meV}$. The U was chosen such that the bare susceptibility is enhanced by at most a factor of 10. As an illustration, the RPA enhancement is shown in Fig. 5.17. There, the real part of the static susceptibility¹⁶

¹⁴ $\chi(\omega)$ is calculated on a non-equidistant grid (see Appendix D). If $\omega - \Omega_{\mathbf{q}\lambda}$ is smaller than the grid spacing, the iteration converged.

¹⁵Here, the expression $\alpha\beta$ in $\xi_{\alpha\beta}$ denotes the product of both indices.

¹⁶In contrast to the imaginary part of $\Im\chi(\omega = 0, \mathbf{q}) = 0$, the real part can be evaluated through the Kramers-Kronig

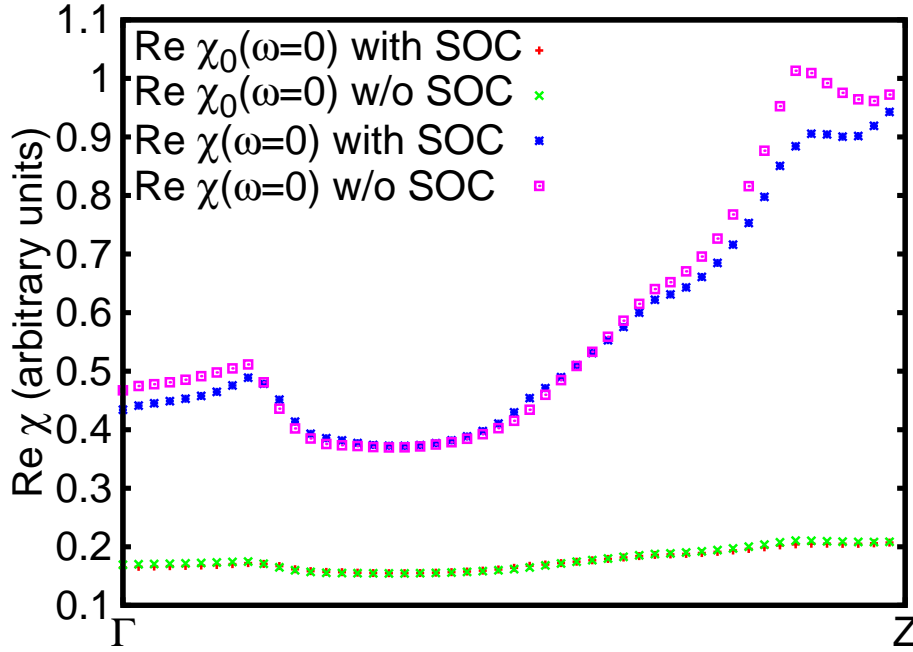


Figure 5.17: RPA enhancement of $\Re\chi_0(\omega = 0)$ for CePt₃Si along Γ Z with and without SOC.

is displayed before and after the RPA treatment along the q_z axis with and without ASOC. Note that the real part is responsible for the magnitude of the Kohn anomaly. Again, as for INS in Section 5.4.1, the result with ASOC is significantly smoother, especially for larger momenta.

The LDA calculation for the phonon dispersion in CePt₃Si was done by Heid [123], using density–functional perturbation theory¹⁷. It bases on the experimental structure of CePt₃Si determined by Bauer *et al.* [2], whereas the electronic structure was taken from LaPt₃Si plus one additional background charge (corresponding to the Ce–4f electron). This calculation, shown in Fig. 5.18, uses the Ce mass (however, the La mass leads to approximately the same results). The internal parameters (i.e. the position of the atoms inside the unit cell) were not optimized, i.e. there might be some residual forces.

In order to proceed, one needs the matrix–elements $|M_{\mathbf{q},\lambda}|^2$, which are provided by Heid’s LDA calculations [123]. A simple linear model for the averaged matrix–elements of a typical phonon branch then reads¹⁸:

$$|M_{\mathbf{q}}|^2(p) = \frac{t_1^2}{100}p; \quad p \in [0; 1]. \quad (5.72)$$

relation precisely for $\omega = 0$.

¹⁷A review about this linear–response method is found in Ref. [144].

¹⁸In general, the matrix–elements are also \mathbf{k} –dependent. Then, these matrix–elements have to be included into the momentum–sum of the spin susceptibility. However, I make the usual assumption, that this \mathbf{k} –dependence is weak.

5 Dynamical spin and charge responses in CePt₃Si

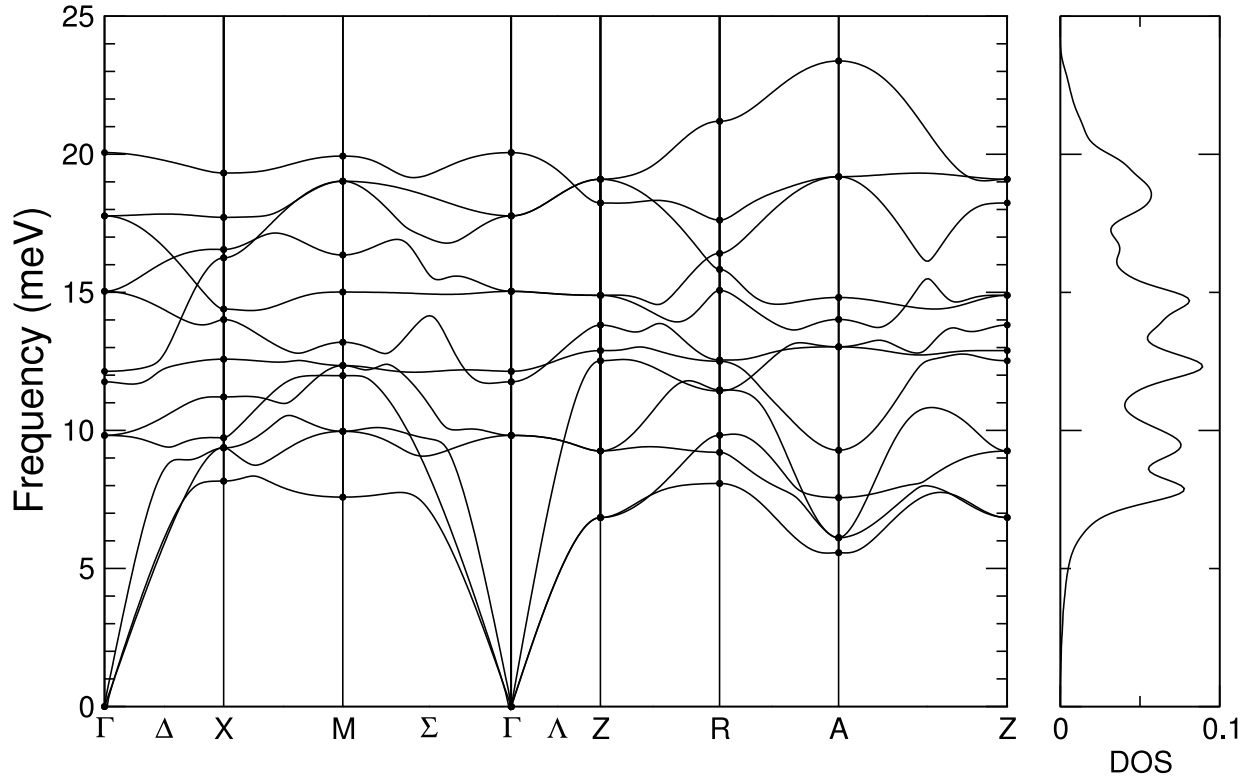


Figure 5.18: LDA calculation of the phonon dispersion for CePt₃Si by Heid [123]. The dots mark evaluated points in the Brillouin zone and the solid lines represent interpolations. The right-hand side displays the phonon density of states.

Here p parameterizes the distance from the Γ -point to the boundary of the Brillouin zone. The dependence on the phonon branch λ was neglected, since the matrix-elements for the lowest TA and LA modes were comparable. However, if experimental data for a comparison were available, it would be easy to include this polarization effect.

Further, I used the following interpolations of the LDA data shown in Fig. 5.18 through the lowest lying phonons as bare phonon dispersion:

$$\begin{aligned} \Omega_{\mathbf{q}} &= 0.062t_1 \sin\left(\frac{\pi}{2}p\right) && \text{for } \Gamma Z, && (5.73) \\ \Omega_{\mathbf{q}} &= 0.074t_1 \sin\left(\frac{\pi}{2}p\right) && \text{for } \Gamma X, \\ \Omega_{\mathbf{q}} &= 0.08t_1 \sin\left(\frac{\pi}{2}p\right) + 0.012t_1 \sin\left(\frac{3\pi}{2}p\right) && \text{for } \Gamma M. \end{aligned}$$

Of course, the LDA calculation contains already corrections from the static polarization bubble. That is, if the LDA calculation would be performed on a finer mesh, Kohn anomalies might

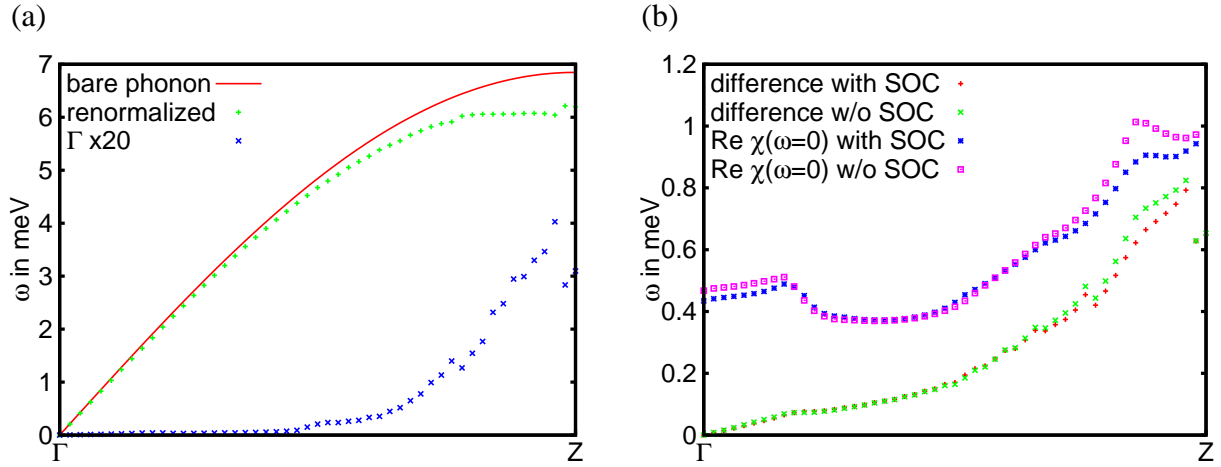


Figure 5.19: Kohn anomalies for the β band of CePt_3Si with ASOC along ΓZ . The solid (red) line in (a) represents the bare phonon dispersion from Eq. (5.73), the green symbols are the result for the renormalized phonon dispersion. The blue symbols represent the phonon linewidth Γ which is scaled by a factor 20. In (b), the differences between the bare phonon dispersion and the renormalized phonon dispersion are plotted in red (with ASOC) and green (without ASOC). Furthermore, the underlying real part of the static charge susceptibility $\Re\chi(\omega = 0)$ is shown with (blue) and without (magenta) ASOC for comparison.

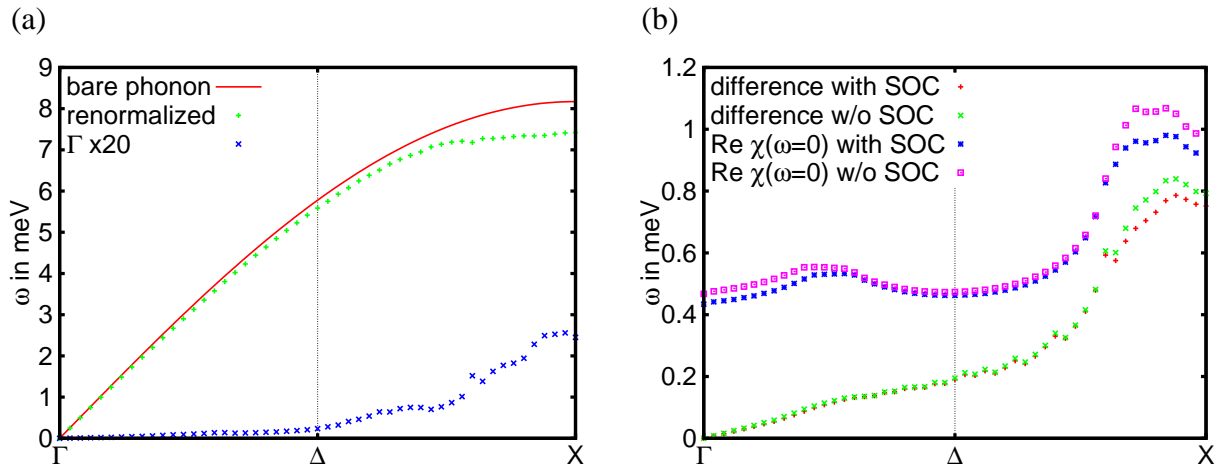


Figure 5.20: Kohn anomalies for the β band of CePt_3Si with ASOC along ΓX . Same coloring as in Fig. 5.19.

5 Dynamical spin and charge responses in CePt_3Si

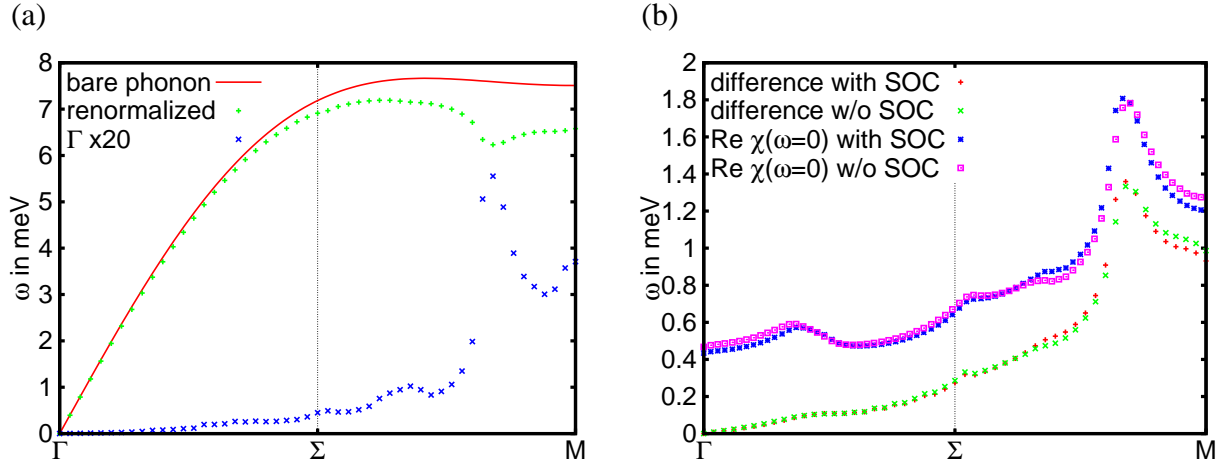


Figure 5.21: Kohn anomalies for the β band of CePt_3Si with ASOC along ΓM . Same coloring as in Fig. 5.19.

become visible¹⁹. On the other hand, effects from the ASOC were not included in this LDA approach²⁰. Hence, in order to fit experimental data, first the Kohn anomalies calculated in the static limit without ASOC should be subtracted to obtain the bare phonon dispersion, and only then, the dynamical results including the ASOC should be included. Since I have only two data points along one direction in the Brillouin zone (compare Fig. 5.18), such an expensive procedure is superfluous. However, here I am interested in the effects of the ASOC on Kohn anomalies. Therefore, it is convenient to use the above phonon dispersion for the calculation with and without ASOC. Otherwise a direct comparison would not be possible.

Fig. 5.21(a) shows a comparatively strong Kohn anomaly close to the M -point, which is seen even better in the linewidth or by subtracting the bare phonon dispersion from the renormalized one [see Fig. 5.21(b)]. As in the previous sections, the difference between switching on/off the ASOC is tiny and in contrast to the predictions of Ref. [139, 140, 141] (for 2D systems), the results in Fig. 5.19, Fig. 5.20 and Fig. 5.21 do not show additional Kohn anomalies at smaller momenta. I attribute this to the different nesting conditions for the inter- and intra-band contributions together with the relatively broad and small peaks in the real part of the susceptibility (see Fig. 5.17). This is also a question of dimensionality: low-dimensional systems tend to show deeper and sharper Kohn anomalies [146]. The linewidths shown in Figs. 5.20–5.21 are comparable with experimental results (concerning the increase to the zone boundary and the maximum value), e.g. on Pb and Nb which experiences also a strong SOC [133].

¹⁹This depends also on the accuracy of the calculation, especially for small Kohn anomalies as observed in bulk materials. Further, the linewidth has to be calculated separately, e.g. using Ref. [145].

²⁰Furthermore, it is not obvious which diagrams are included in DFT methods as LDA, since this is a non-diagrammatic approach.

5.5 Summary

In this chapter, I introduced a method to calculate efficiently the dynamical spin and charge susceptibilities in NCS for arbitrary ASOC in the whole three dimensional Brillouin zone at low temperatures in the normal state close to the AFM phase. The method uses the spectral function as input and has therefore the potential to go clearly beyond a Lindhard analysis. For this purpose, it would be desirable to use, for instance, the spectral function obtained from (future) ARPES experiments to compare the calculated spin and charge responses to other experiments like INS and eventually develop an RPA model to renormalize the susceptibilities. The results in this chapter can be seen as a proof of principle, that dynamic calculations including ASOC are possible. For the first time, the dynamic nesting function is evaluated and shows a pronounced peak at the antiferromagnetic wave vector $\mathbf{Q} = (0, 0, \pi)$ for the β band of CePt₃Si. Differences between the real and imaginary part of the susceptibility for $\omega \rightarrow 0$ provide evidences for non negligible dynamic nesting. The difference for the calculated INS spectra and for the Kohn anomalies with and without ASOC is tiny. The predicted additional peaks at small momenta are not visible due to an overlap of many broad peaks originating from up to twelve inter- and intra-band terms. Calculated Kohn anomalies (assuming an RPA enhancement of about a factor ten) suggest that experiments might be promising. A sign analysis of the weak-coupling gap equation including a pairing interaction based on spin fluctuations points towards a strong triplet component in the superconducting order parameter of CePt₃Si. Furthermore, I showed in this case that with increasing strength of the ASOC a larger triplet contribution is favored.

6 Summary

Non-centrosymmetric superconductors (NCS) have now been studied for six years and they are still of special interest, since theory predicts the possibility of a mixed singlet–triplet order parameter. A lot of experimental and theoretical work has been initiated due to this unique property. The majority of NCS are well described by a BCS–like theory, however there are also many compounds with exotic and surprising properties, as listed in the introduction. One of them is CePt_3Si , which was studied in the last part of this thesis. The unconventional superconducting state in such a compound necessitates a generalized description of response and transport functions in such NCS.

I set up the basic equations for a linear response and transport theory in NCS, discussed the gauge invariance of this theory, found a new gauge mode with unconventional dispersion and derived gauge invariant expressions for various response and transport functions. As a case study, I considered in detail the electronic Raman response. For this purpose, I used a kinetic equation approach. Starting from a von Neumann equation, I derived a generalized Boltzmann equation which is a 4×4 matrix equation in particle–hole (Nambu) and spin space. I solved this set of coupled equations in ω – \mathbf{q} space by finding the appropriate transformations which diagonalized them by first performing a $\text{SU}(2)$ rotation into the so–called band basis and then applying a Bogoliubov–transformation into quasiparticle space. The transport equations could be solved analytically for an extended momentum and frequency range ($\omega \ll E_F$ and $|\mathbf{q}| \ll k_F$). The theory is particle–hole symmetric, applies to any kind of antisymmetric spin–orbit coupling (ASOC) and is gauge invariant. As an example, I derived expressions for the normal and superfluid density as well as for the specific heat capacity in the presence of an ASOC. A comparison with a simple local equilibrium analysis revealed perfect agreement, as expected. A straightforward generalization of this kinetic theory could include, for example, effects from impurity scattering. I have performed such an analysis together with Einzel in Ref. [71] for centrosymmetric superconductors.

The gauge invariance of the kinetic theory is by itself an interesting theoretical topic. I demonstrated the gauge invariance by assuming a separable ansatz for the pairing interaction. For non–vanishing ASOC, two phase fluctuations are obtained, belonging to both spin–orbit split bands. Only by taking those two phase fluctuations into account, I could prove the gauge invariance of the transport theory. In addition to the gauge invariance that is connected to the particle conservation on each band separately, the phase fluctuations also give rise to a generalized Josephson relation for NCS, which is derived for the first time in this thesis. It turned out that two gauge modes are present in NCS. I calculated the slope of both gauge modes in the limiting case of vanishing ASOC and without taking the long range Coulomb interaction into account. The first gauge mode can be identified as the Anderson–Bogoliubov mode, which is present in any (singlet or triplet) superconductor. The second gauge mode is unique to NCS with a characteristic

6 Summary

slope that depends on the symmetry of the ASOC. The effect of Coulomb interaction, which usually shifts the gauge modes to the plasma frequency, remains a topic of further investigations as well as the influence of these gauge modes on response and transport functions. Furthermore, the connection to collective modes in two-band superconductors predicted by Leggett [90] and recently experimentally observed in MgB_2 [91] is worth additional research.

As application of the kinetic theory, I calculated the electronic (pair-breaking) Raman response in NCS for zero temperature and in the clean limit. With regard to the most interesting NCS, I analyzed the Raman response for an ASOC of tetragonal (point group $\mathcal{G} = C_{4v}$) and cubic (point group $\mathcal{G} = O$) symmetry. I provided both, analytical and numerical results: First, I provided analytical expressions for the Raman vertex for both point groups. Second, I evaluated the electronic Raman response for the limiting case of a purely triplet order parameter and third, I analyzed the mixed parity state in a case by case study, revealing a characteristic two peak structure for NCS and the exact peak and kink position in the spectra as well as the low frequency power laws. Further, I provided numerical calculations covering all relevant cases from weak to strong triplet-singlet ratio. It turned out that this ratio can easily be deduced from the peak positions in the electronic Raman response. As a result, I propose a new method to determine this unknown triplet-singlet ratio in parity-violating NCS. The experimental examination is still outstanding but might be promising, especially for NCS with higher T_c . A topic of further investigations might be the consequence of the new gauge mode on the electronic Raman response. A very recent publication by Klein [92] discussed this topic for two-band superconductors like MgB_2 with interesting results concerning the screening contribution in the electronic Raman response. Nevertheless, it remains unclear to what extent the results for two-band superconductors can be adopted for NCS. Of course, a more material specific calculation, which takes the actual Fermi surface into account, is still an outstanding issue. However, this should be done in cooperation with experimental work.

Finally, I introduced an efficient numerical method to calculate the dynamical spin and charge responses in NCS, using all symmetries of the problem via discrete cosine and sine transformations. In detail, the spin and charge susceptibilities for CePt_3Si in the whole three dimensional Brillouin zone was calculated. Since such an evaluation is rather expensive with respect to memory and computation time, I confined the analysis to the normal state without magnetic order but for low temperatures. With the spectral function as a starting point, the method has the potential to go clearly beyond a Lindhard analysis. For further investigations it might, for example, be desirable to use the spectral function obtained from ARPES experiments in order to calculate the spin and charge responses. Instead, I provided a parameterization of the three closest bands to the Fermi surface, using LDA calculations by Heid [123]. For all subsequent calculations I used the β band with the most interesting nesting features, although I found a smaller density of states (31%) compared to Samokhin *et al.* [120, 121], who attributed 70% of the density of states (DoS) to the β band. I argue that this difference is due to an approximation for the Ce-4f electrons: in Heid's LDA calculation they were treated as background charge. Thus the low-lying f-bands, which can be seen in Samokhin's calculation, are missing in my model. Clearly these f-bands flatten especially the β band dispersion close to the Fermi surface leading to such a high DoS. The dynamic nesting function was evaluated and showed a pronounced peak at the antiferromagnetic wave vector $\mathbf{Q} = (0, 0, \pi)$ for the β band. Large differences between the real

and imaginary part of the susceptibility for $\omega \rightarrow 0$ provide evidences for non-negligible dynamic nesting. Further, using this band structure, I calculated as an example inelastic neutron scattering cross sections for the q_z axis and Kohn anomalies for different scans through the Brillouin zone with and without ASOC. In both cases, the difference from the ASOC were small and additional peaks for small momenta, predicted in Ref. [139, 140, 141] were not observed. I attribute this to the higher dimensionality and to an overlap of many broad peaks originating from up to twelve inter- and intra-band terms. Calculated Kohn anomalies suggest that experiments might be promising although Kohn anomalies are usually hard to detect in three dimensional compounds. All previous work on the spin and charge susceptibilities in NCS (including microscopic pairing theories as, for example, in Ref. [50, 51, 52]) was restricted to the static susceptibility and thus neglected dynamical nesting effects. In this sense, the results can be seen as a proof of the principle that dynamic calculations on the whole Brillouin zone, including ASOC, are possible. Using numerical results for the spin- and charge susceptibility and a model proposed by Takimoto *et al.* [135], I qualitatively analyzed the superconducting pairing interaction. In this model, the pairing interaction is constructed from spin fluctuations. One can hardly find a solution to the singlet part of the weak-coupling gap equation. The triplet part of this decoupled gap equation prefers a p -wave state, where the corresponding $\mathbf{d}_{\mathbf{k}}$ -vector is proportional to the antisymmetric spin-orbit coupling vector $\boldsymbol{\gamma}_{\mathbf{k}}$. Furthermore, it turns out that an increasing Rashba-type of spin-orbit coupling strengthens the triplet contribution to the superconducting gap. Solving the gap equation with a dynamical pairing interaction, based on the spin and charge susceptibilities calculated in this thesis, would be a natural continuation of this work. Further improvements might concern the inclusion of an antiferromagnetic order or even a superconducting gap in such a calculation.

Coming back to the questions raised in the introduction, this leads me to the following conclusions: I could successfully extend a kinetic formalism for various response and transport functions to describe NCS. The discussion of the gauge invariance of this theory led to the discovery of a new gauge mode with unusual dispersion. I showed detailed calculations of the dynamical spin and charge susceptibilities in the three dimensional momentum space and in presence of an ASOC. A pairing interaction based on spin fluctuations shows in particular for CePt₃Si that the triplet contribution to the order parameter increases with a Rashba-type of spin-orbit coupling. Through a sign analysis of the decoupled gap equation, it becomes clear that the triplet contribution is considerably larger than the singlet contribution to the gap in CePt₃Si. For this case, a threshold behavior is expected in the Raman spectra. Using this kinetic approach to calculate the electronic Raman response, revealed a new experimental method to determine the unknown triplet-singlet ratio of the superconducting order parameter.

Appendix A

Small \mathbf{q} -expansion

For small wave numbers, i.e. $\mathbf{q} \rightarrow 0$, the Tsuneto and related functions, which play an important role in the matrix-elements N_{ij} [see Eq. (2.55)], will simplify considerably. Taking into account terms to the order $O(\eta_{\mathbf{k}}^2)$ with $\eta_{\mathbf{k}} = \mathbf{v}_{\mathbf{k}} \cdot \mathbf{q}$, I obtain the well-known expression for the Tsuneto-function [147]

$$\lim_{\mathbf{q} \rightarrow 0} \lambda_{\lambda}(\mathbf{k}) = -4\Delta_{\lambda}^2(\mathbf{k}) \frac{(\omega^2 - \eta_{\mathbf{k}}^2)\theta_{\lambda}(\mathbf{k}) + \eta_{\mathbf{k}}^2\phi_{\lambda}(\mathbf{k})}{\omega^2[\omega^2 - 4E_{\lambda}^2(\mathbf{k})] - \eta_{\mathbf{k}}^2[\omega^2 - 4\xi_{\lambda}^2(\mathbf{k})]}, \quad (\text{A.1})$$

where

$$\phi_{\lambda}(\mathbf{k}) = -\frac{\partial n_{\lambda}(\mathbf{k})}{\partial \xi_{\lambda}(\mathbf{k})} = \frac{\xi_{\lambda}^2(\mathbf{k})}{E_{\lambda}^2(\mathbf{k})} y_{\lambda}(\mathbf{k}) + \frac{\Delta_{\lambda}^2(\mathbf{k})}{E_{\lambda}^2(\mathbf{k})} \theta_{\lambda}(\mathbf{k}) \quad (\text{A.2})$$

is the derivative of the electron distribution function in the band λ and

$$y_{\lambda}(\mathbf{k}) = -\frac{\partial f[E_{\lambda}(\mathbf{k})]}{\partial E_{\lambda}(\mathbf{k})} = \frac{1}{4k_{\text{B}}T} \frac{1}{\cosh^2\left(\frac{E_{\lambda}(\mathbf{k})}{2k_{\text{B}}T}\right)} \quad (\text{A.3})$$

is the derivative of the quasiparticle distribution function.

The following limits are also of interest: the homogenous limit ($\mathbf{q} = 0$), e.g. for the Raman response and the static limit ($\omega = 0$), used in local equilibrium situations

$$\lambda_{\lambda}(\mathbf{k}, \mathbf{q} = 0) = \frac{4\Delta_{\lambda}^2(\mathbf{k})\theta_{\lambda}(\mathbf{k})}{4E_{\lambda}^2(\mathbf{k}) - \omega^2} \quad (\text{A.4})$$

$$\lim_{\omega \rightarrow 0} \lim_{\mathbf{q} \rightarrow 0} \lambda_{\lambda}(\mathbf{k}) = \phi_{\lambda}(\mathbf{k}) - y_{\lambda}(\mathbf{k}). \quad (\text{A.5})$$

For the following small \mathbf{q} -expansion I omitted the band label λ for better readability:

$$\lim_{\mathbf{q} \rightarrow 0} \theta_{\mathbf{k}}^+ = 2\theta_{\mathbf{k}} + \frac{\eta_{\mathbf{k}}^2}{4E_{\mathbf{k}}^2} \left[\frac{\Delta_{\mathbf{k}}^2 - 2\xi_{\mathbf{k}}^2}{E_{\mathbf{k}}^2} (y_{\mathbf{k}} - \theta_{\mathbf{k}}) - \frac{\xi_{\mathbf{k}}^2}{E_{\mathbf{k}}} f_{\mathbf{k}}'' \right] \quad (\text{A.6a})$$

$$\lim_{\mathbf{q} \rightarrow 0} \theta_{\mathbf{k}}^- = \frac{\eta_{\mathbf{k}}\xi_{\mathbf{k}}}{E_{\mathbf{k}}^2} (y_{\mathbf{k}} - \theta_{\mathbf{k}}) \quad (\text{A.6b})$$

$$\lim_{\mathbf{q} \rightarrow 0} \Phi_{\mathbf{k}} = \phi_{\mathbf{k}} + \frac{\eta_{\mathbf{k}}^2}{4E_{\mathbf{k}}^2} \frac{\Delta_{\mathbf{k}}^2(\Delta_{\mathbf{k}}^2 - 4\xi_{\mathbf{k}}^2)}{2E_{\mathbf{k}}^4} (y_{\mathbf{k}} - \theta_{\mathbf{k}}) - \frac{\eta_{\mathbf{k}}^2\xi_{\mathbf{k}}^2}{4E_{\mathbf{k}}^2} \left[\frac{\Delta_{\mathbf{k}}^2}{E_{\mathbf{k}}} f_{\mathbf{k}}'' + \frac{\xi_{\mathbf{k}}^2}{6E_{\mathbf{k}}^3} f_{\mathbf{k}}''' \right] \quad (\text{A.6c})$$

Appendix A Small q -expansion

$$\begin{aligned}\delta\theta_{\mathbf{k}} &= \frac{\theta_{\mathbf{k}}^+}{2} - \theta_{\mathbf{k}} \\ &= \frac{\eta_{\mathbf{k}}^2}{8E_{\mathbf{k}}^2} \left[\frac{\Delta_{\mathbf{k}}^2 - 2\xi_{\mathbf{k}}^2}{E_{\mathbf{k}}^2} (y_{\mathbf{k}} - \theta_{\mathbf{k}}) - \frac{\xi_{\mathbf{k}}^2}{E_{\mathbf{k}}} f_{\mathbf{k}}'' \right]\end{aligned}\quad (\text{A.6d})$$

$$\begin{aligned}\delta\phi_{\mathbf{k}} &= \Phi_{\mathbf{k}} - \phi_{\mathbf{k}} \\ &= \frac{\eta_{\mathbf{k}}^2}{4E_{\mathbf{k}}^2} \frac{\Delta_{\mathbf{k}}^2(\Delta_{\mathbf{k}}^2 - 4\xi_{\mathbf{k}}^2)}{2E_{\mathbf{k}}^4} (y_{\mathbf{k}} - \theta_{\mathbf{k}}) - \frac{\eta_{\mathbf{k}}^2 \xi_{\mathbf{k}}^2}{4E_{\mathbf{k}}^2} \left[\frac{\Delta_{\mathbf{k}}^2}{E_{\mathbf{k}}} f_{\mathbf{k}}'' + \frac{\xi_{\mathbf{k}}^2}{6E_{\mathbf{k}}^3} f_{\mathbf{k}}''' \right],\end{aligned}\quad (\text{A.6e})$$

where $f_{\mathbf{k}}^{(n)}$ denotes the n th derivative of $f(E_{\mathbf{k}})$ with respect to $E_{\mathbf{k}}$. Furthermore, I find the following expansions:

$$\lim_{q \rightarrow 0} \eta_{\mathbf{k}}^+ = 2E_{\mathbf{k}} \left(1 + \frac{\eta_{\mathbf{k}}^2 \Delta_{\mathbf{k}}^2}{8E_{\mathbf{k}}^4} \right) \quad (\text{A.7a})$$

$$\lim_{q \rightarrow 0} \eta_{\mathbf{k}}^- = \frac{\xi_{\mathbf{k}}}{E_{\mathbf{k}}} \eta_{\mathbf{k}} \left(1 - \frac{\eta_{\mathbf{k}}^2 \Delta_{\mathbf{k}}^2}{8E_{\mathbf{k}}^4} \right) \quad (\text{A.7b})$$

$$\lim_{q \rightarrow 0} \tilde{y}_{\mathbf{k}} = y_{\mathbf{k}} - \frac{\eta_{\mathbf{k}}^2}{8E_{\mathbf{k}}^2} \left(\frac{\Delta_{\mathbf{k}}^2}{E_{\mathbf{k}}} \nu_{\mathbf{k}}'' + \frac{\xi_{\mathbf{k}}^2}{3} \nu_{\mathbf{k}}''' \right) \quad (\text{A.7c})$$

$$\lim_{q \rightarrow 0} \Theta_{\mathbf{k}} = \theta_{\mathbf{k}} + \frac{\eta_{\mathbf{k}}^2}{8E_{\mathbf{k}}^2} \left[\frac{\Delta_{\mathbf{k}}^2}{E_{\mathbf{k}}} (y_{\mathbf{k}} - \theta_{\mathbf{k}}) - \frac{\xi_{\mathbf{k}}^2}{E_{\mathbf{k}}} \nu_{\mathbf{k}}'' \right]. \quad (\text{A.7d})$$

The ten products of coherence-factors in Eq. (2.50) have the following explicit form:

$$\left[q_{\mathbf{k}}^{(s)} \right]^2 = \frac{1}{2} \frac{E_{\mathbf{k}+} E_{\mathbf{k}-} + \xi_{\mathbf{k}+} \xi_{\mathbf{k}-} - s \Delta_{\mathbf{k}}^2}{E_{\mathbf{k}+} E_{\mathbf{k}-}} \quad (\text{A.8a})$$

$$\left[p_{\mathbf{k}}^{(s)} \right]^2 = \frac{1}{2} \frac{E_{\mathbf{k}+} E_{\mathbf{k}-} - \xi_{\mathbf{k}+} \xi_{\mathbf{k}-} + s \Delta_{\mathbf{k}}^2}{E_{\mathbf{k}+} E_{\mathbf{k}-}} \quad (\text{A.8b})$$

$$q_{\mathbf{k}}^{(+)} q_{\mathbf{k}}^{(-)} = \frac{1}{2} \frac{E_{\mathbf{k}-} \xi_{\mathbf{k}+} + E_{\mathbf{k}+} \xi_{\mathbf{k}-}}{E_{\mathbf{k}+} E_{\mathbf{k}-}} \quad (\text{A.8c})$$

$$p_{\mathbf{k}}^{(+)} p_{\mathbf{k}}^{(-)} = \frac{1}{2} \frac{E_{\mathbf{k}-} \xi_{\mathbf{k}+} - E_{\mathbf{k}+} \xi_{\mathbf{k}-}}{E_{\mathbf{k}+} E_{\mathbf{k}-}} \quad (\text{A.8d})$$

$$q_{\mathbf{k}}^{(s)} p_{\mathbf{k}}^{(s)} = \frac{\Delta_{\mathbf{k}} \xi_{\mathbf{k}+} + s \xi_{\mathbf{k}-}}{2 E_{\mathbf{k}+} E_{\mathbf{k}-}} \quad (\text{A.8e})$$

$$q_{\mathbf{k}}^{(-)} p_{\mathbf{k}}^{(+)} = \frac{\Delta_{\mathbf{k}} E_{\mathbf{k}+} + E_{\mathbf{k}-}}{2 E_{\mathbf{k}+} E_{\mathbf{k}-}} \quad (\text{A.8f})$$

and the small q -limit of each coherence-factors reads:

$$\lim_{q \rightarrow 0} q_{\mathbf{k}}^{(+)} = \frac{\xi_{\mathbf{k}}}{E_{\mathbf{k}}} \left(1 - \frac{\eta_{\mathbf{k}}^2 \Delta_{\mathbf{k}}^2}{4E_{\mathbf{k}}^4} \right) \quad (\text{A.9a})$$

$$\lim_{q \rightarrow 0} q_{\mathbf{k}}^{(-)} = 1 - \frac{\eta_{\mathbf{k}}^2 \Delta_{\mathbf{k}}^2}{8E_{\mathbf{k}}^4} \quad (\text{A.9b})$$

$$\lim_{\mathbf{q} \rightarrow 0} p_{\mathbf{k}}^{(+)} = \frac{\Delta_{\mathbf{k}}}{E_{\mathbf{k}}} \left(1 + \frac{\eta_{\mathbf{k}}^2 \xi_{\mathbf{k}}^2}{4E_{\mathbf{k}}^4} \right) \quad (\text{A.9c})$$

$$\lim_{\mathbf{q} \rightarrow 0} p_{\mathbf{k}}^{(-)} = \frac{\eta_{\mathbf{k}} \Delta_{\mathbf{k}}}{2E_{\mathbf{k}}^2} . \quad (\text{A.9d})$$

Appendix B

Derivation of the Raman vertices

In order to derive the relevant expressions for the polarization–dependent Raman vertices, I start from a general dispersion relation for tetragonal symmetry (C_{4v})

$$\begin{aligned}
 \epsilon_{\mathbf{k}} = & \sum_{n=1}^{\infty} \sum_{r=0}^{\infty} a_{n,r}^{C_{4v}} [\cos(nk_x a) + \cos(nk_y a)] \cos(rk_z c) \\
 & + \sum_{n=0}^{\infty} \sum_{r=0}^{\infty} b_{n,r}^{C_{4v}} \cos(nk_x a) \cos(nk_y a) \cos(rk_z c) \\
 & + \sum_{n=1}^{\infty} \sum_{m=1}^{\infty} \sum_{r=0}^{\infty} c_{n,m,r}^{C_{4v}} [\cos(nk_x a) \cos(mk_y a) + \cos(mk_x a) \cos(nk_y a)] \cos(rk_z c)
 \end{aligned} \tag{B.1}$$

and for the cubic symmetry (O)

$$\begin{aligned}
 \epsilon_{\mathbf{k}} = & \sum_{n=1}^{\infty} a_n^O [\cos(nk_x a) + \cos(nk_y a) + \cos(nk_z a)] \\
 & + \sum_{n=0}^{\infty} b_n^O \cos(nk_x a) \cos(nk_y a) \cos(nk_z a) \\
 & + \sum_{n=1}^{\infty} \sum_{m=1}^{n-1} c_{n,m}^O [\cos(mk_x a) \cos(mk_y a) \cos(nk_z a) \\
 & + \cos(mk_x a) \cos(nk_y a) \cos(mk_z a) + \cos(nk_x a) \cos(mk_y a) \cos(mk_z a)] \\
 & + \sum_{n=2}^{\infty} \sum_{m=1}^{n-1} \sum_{r=0}^{m-1} d_{n,m,r}^O [\cos(nk_x a) \cos(mk_y a) \cos(rk_z a) \\
 & + \cos(nk_x a) \cos(rk_y a) \cos(mk_z a) + \cos(mk_x a) \cos(nk_y a) \cos(rk_z a) \\
 & + \cos(rk_x a) \cos(nk_y a) \cos(mk_z a) + \cos(mk_x a) \cos(rk_y a) \cos(nk_z a) \\
 & + \cos(rk_x a) \cos(mk_y a) \cos(nk_z a)] .
 \end{aligned} \tag{B.2}$$

Time reversal symmetry allows only for even functions of momentum \mathbf{k} in the energy dispersion. Furthermore, the dispersion must be invariant under all symmetry elements of the point group \mathcal{G} of the crystal. For small momentum transfers and nonresonant scattering, the Raman tensor is

Appendix B Derivation of the Raman vertices

given by the effective-mass approximation

$$\gamma(\mathbf{k}) = m \sum_{i,j} \hat{\mathbf{e}}_i^S \frac{\partial^2 \epsilon(\mathbf{k})}{\partial k_i \partial k_j} \hat{\mathbf{e}}_j^I, \quad (\text{B.3})$$

where $\hat{\mathbf{e}}^{S,I}$ denote the unit vectors of the scattered and incident polarization light, respectively. The light polarization vectors select elements of the Raman tensor according to

$$\gamma_{\mathbf{k}}^{IS} = \mathbf{e}^I \cdot \gamma_{\mathbf{k}}^{(R)} \cdot \mathbf{e}^S, \quad (\text{B.4})$$

where the Raman tensor $\gamma_{\mathbf{k}}$ can be decomposed into its symmetry components and later expanded into Fermi surface harmonics:

$$\gamma_{\mathbf{k}}^{C_{4v}} = \begin{pmatrix} \gamma_{A_1^{(1)}} + \gamma_{B_1} & \gamma_{B_2} & \gamma_{E^{(1)}} \\ \gamma_{B_2} & \gamma_{A_1^{(1)}} - \gamma_{B_1} & \gamma_{E^{(2)}} \\ \gamma_{E^{(1)}} & \gamma_{E^{(2)}} & \gamma_{A_1^{(2)}} \end{pmatrix} \quad (\text{B.5})$$

$$\gamma_{\mathbf{k}}^O = \begin{pmatrix} \gamma_{A_1} + \gamma_{E^{(1)}} - \sqrt{3}\gamma_{E^{(2)}} & \gamma_{T_2^{(1)}} & \gamma_{T_2^{(2)}} \\ \gamma_{T_2^{(1)}} & \gamma_{A_1} + \gamma_{E^{(1)}} + \sqrt{3}\gamma_{E^{(2)}} & \gamma_{T_2^{(3)}} \\ \gamma_{T_2^{(2)}} & \gamma_{T_2^{(3)}} & \gamma_{A_1} - 2\gamma_{E^{(1)}} \end{pmatrix}. \quad (\text{B.6})$$

Here I have omitted all non-Raman active symmetries such as A_{2g} . The vertices $A_1^{(1)}$ and $A_1^{(2)}$ are equal up to some constants determined by the band structure, and the vertices for $E^{(1)}$ and $E^{(2)}$ in C_{4v} differ only by a rotation of the azimuthal angle ϕ by $\pi/2$. Since this rotation is an element of the corresponding point groups, these vertices are identical, too. The same holds for $T_2^{(1)}$, $T_2^{(2)}$ and $T_2^{(3)}$. Therefore, the upper indices will be omitted in the following (whenever possible). For the tetragonal group C_{4v} the A_1 , B_1 , B_2 and E symmetries are Raman active in backscattering geometry. Relevant polarizations for this group are:

$$\begin{aligned} \gamma_{\mathbf{k}}^{xx} &= \gamma_{\mathbf{k}}^{A_1} + \gamma_{\mathbf{k}}^{B_1} & \gamma_{\mathbf{k}}^{x'x'} &= \gamma_{\mathbf{k}}^{A_1} + \gamma_{\mathbf{k}}^{B_2} \\ \gamma_{\mathbf{k}}^{yy} &= \gamma_{\mathbf{k}}^{A_1} - \gamma_{\mathbf{k}}^{B_1} & \gamma_{\mathbf{k}}^{y'y'} &= \gamma_{\mathbf{k}}^{A_1} - \gamma_{\mathbf{k}}^{B_2} \\ \gamma_{\mathbf{k}}^{xy} &= \gamma_{\mathbf{k}}^{B_2} & \gamma_{\mathbf{k}}^{x'y'} &= \gamma_{\mathbf{k}}^{B_1} \\ \gamma_{\mathbf{k}}^{xz} &= \gamma_{\mathbf{k}}^E & \gamma_{\mathbf{k}}^{RR} &= \gamma_{\mathbf{k}}^{A_1} \\ \gamma_{\mathbf{k}}^{yz} &= \gamma_{\mathbf{k}}^E & \gamma_{\mathbf{k}}^{LL} &= \gamma_{\mathbf{k}}^{A_1} \\ \gamma_{\mathbf{k}}^{zz} &= \gamma_{\mathbf{k}}^{A_1} & \gamma_{\mathbf{k}}^{RL} &= \gamma_{\mathbf{k}}^{B_1} - i\gamma_{\mathbf{k}}^{B_2}. \end{aligned} \quad (\text{B.7})$$

The cubic group O reveals three Raman active symmetries, namely A_1 , ($E^{(1)}$, $E^{(2)}$), and T_2 (still assuming backscattering geometry). The relevant polarizations are:

$$\gamma_{\mathbf{k}}^{xx} = \gamma_{\mathbf{k}}^{A_1} + \gamma_{\mathbf{k}}^{E^{(1)}} - \sqrt{3}\gamma_{\mathbf{k}}^{E^{(2)}} \quad \gamma_{\mathbf{k}}^{x'x'} = \gamma_{\mathbf{k}}^{A_1} + \gamma_{\mathbf{k}}^{E^{(1)}} + \gamma_{\mathbf{k}}^{T_2}$$

$$\begin{aligned}
\gamma_{\mathbf{k}}^{yy} &= \gamma_{\mathbf{k}}^{A_1} + \gamma_{\mathbf{k}}^{E^{(1)}} + \sqrt{3}\gamma_{\mathbf{k}}^{E^{(2)}} & \gamma_{\mathbf{k}}^{y'y'} &= \gamma_{\mathbf{k}}^{A_1} + \gamma_{\mathbf{k}}^{E^{(1)}} - \gamma_{\mathbf{k}}^{T_2} \\
\gamma_{\mathbf{k}}^{xy} &= \gamma_{\mathbf{k}}^{T_2} & \gamma_{\mathbf{k}}^{x'y'} &= -\sqrt{3}\gamma_{\mathbf{k}}^{E^{(2)}} \\
\gamma_{\mathbf{k}}^{xz} &= \gamma_{\mathbf{k}}^{T_2} & \gamma_{\mathbf{k}}^{RR} &= \gamma_{\mathbf{k}}^{A_1} + \gamma_{\mathbf{k}}^{E^{(1)}} \\
\gamma_{\mathbf{k}}^{yz} &= \gamma_{\mathbf{k}}^{T_2} & \gamma_{\mathbf{k}}^{LL} &= \gamma_{\mathbf{k}}^{A_1} + \gamma_{\mathbf{k}}^{E^{(1)}} \\
\gamma_{\mathbf{k}}^{zz} &= \gamma_{\mathbf{k}}^{A_1} - 2\gamma_{\mathbf{k}}^{E^{(1)}} & \gamma_{\mathbf{k}}^{RL} &= -\sqrt{3}\gamma_{\mathbf{k}}^{E^{(2)}} - i\gamma_{\mathbf{k}}^{T_2}.
\end{aligned} \tag{B.8}$$

Here, I have defined the unit polarization vectors $\hat{\mathbf{x}}' = (\hat{\mathbf{x}} + \hat{\mathbf{y}})/\sqrt{2}$ and $\hat{\mathbf{y}}' = (\hat{\mathbf{x}} - \hat{\mathbf{y}})/\sqrt{2}$. L and R denote left and right circularly polarized light with positive and negative helicity, respectively ($\mathbf{e}^L = (\hat{\mathbf{x}} + i\hat{\mathbf{y}})/\sqrt{2}$, $\mathbf{e}^R = (\hat{\mathbf{x}} - i\hat{\mathbf{y}})/\sqrt{2}$). Note that in a backscattering configuration the polarization vectors $\mathbf{e}^{I,S}$ are pinned to the coordinate system of the crystal axes. Therefore, some caution is advised when choosing the proper helicity for the scattered polarization vector \mathbf{e}^S . Although the Raman vertices $E^{(1)}$ and $E^{(2)}$ seem to look completely different, the Raman response turns out to be exactly the same. From a tight-binding analysis one obtains the same (band structure) prefactors for both vertices, thus $\gamma_{\mathbf{k}}^{E^{(1)}}$ and $\sqrt{3}\gamma_{\mathbf{k}}^{E^{(2)}}$ generate both the same Raman response. Note that it is not possible to measure A_1 and $E^{(1)}$ independently in backscattering geometry with the crystal c-axis aligned parallel to the laser beam.

The Raman vertices are extracted from the band structure by comparing the symmetry components of the Raman tensor with the second derivative of the energy dispersion. This can be done by solving a set of 6 coupled linear equations – the 6 equations correspond exactly to the 6 free components of the symmetric tensor of inverse effective-mass and to the 6 symmetry elements (vertices) to be determined. Finally I make a series expansion in \mathbf{k} , in order to get the angular dependence of the vertices on the Fermi surface. The results for the tetragonal point group C_{4v} are

$$\gamma_{A_1}^{(R)} = \sum_{k=0}^{\infty} \sum_{l=0}^{l \leq k/2} \gamma_{k,l}^{(R)} \cos 4l\phi \sin^{2k} \theta \tag{B.9a}$$

$$\gamma_{B_1}^{(R)} = \sum_{k=1}^{\infty} \sum_{l=1}^{l \leq (k+1)/2} \gamma_{k,l}^{(R)} \cos(4l - 2)\phi \sin^{2k} \theta \tag{B.9b}$$

$$\gamma_{B_2}^{(R)} = \sum_{k=1}^{\infty} \sum_{l=1}^{l \leq (k+1)/2} \gamma_{k,l}^{(R)} \sin(4l - 2)\phi \sin^{2k} \theta \tag{B.9c}$$

$$\gamma_E^{(R)} = \sum_{k=1}^{\infty} \sum_{l=1}^{\infty} \gamma_{k,l}^{(R)} \sin(2l - 1)\phi \sin 2k\theta \tag{B.9d}$$

and for the cubic point group O , I obtain

$$\gamma_{A_1}^{(R)} = \sum_{k=0}^{\infty} \sum_{l=0}^{l \leq k/2} \gamma_{k,l}^{(R)} \cos 4l\phi \sin^{2k} \theta \tag{B.10a}$$

Appendix B Derivation of the Raman vertices

$$\gamma_{E^{(1)}}^{(R)} = \gamma_0^{(R)}(2 - 3 \sin^2 \theta) + \dots \quad (\text{B.10b})$$

$$\gamma_{E^{(2)}}^{(R)} = \sum_{k=1}^{\infty} \sum_{l=1}^{l \leq (k+1)/2} \gamma_{k,l}^{(R)} \cos(4l - 2)\phi \sin^{2k} \theta \quad (\text{B.10c})$$

$$\gamma_{T_2}^{(R)} = \sum_{k=1}^{\infty} \sum_{l=1}^{l \leq (k+1)/2} \gamma_{k,l}^{(R)} \sin(4l - 2)\phi \sin^{2k} \theta \quad (\text{B.10d})$$

in a backscattering–geometry experiment ($z\bar{z}$). The leading terms in this expansion of $\gamma_{\mathbf{k}}^{(R)}$ are also illustrated in Table B.1 for the tetragonal point group and in Table B.2 for the cubic point group.

Table B.1: Spherical representation of the first terms in the series expansion for the Raman vertices of tetragonal symmetry. In A_1 symmetry also the second term ($\sin^2 \theta$) is illustrated, because the first term does not contribute to the Raman response.

symmetry	vertex	spherical plot
A_1	$1, \sin^2 \theta$	
B_1	$\cos(2\phi) \sin^2 \theta$	
B_2	$\sin(2\phi) \sin^2 \theta$	
E	$\sin(\phi) \sin(2\theta)$	

Appendix B Derivation of the Raman vertices

Table B.2: Spherical representation of the first terms in the series expansion for the Raman vertices of cubic symmetry. In A_1 symmetry also the second term ($\sin^2 \theta$) is illustrated, because the first term does not contribute to the Raman response.

symmetry	vertex	spherical plot
A_1	$1, \sin^2 \theta$	
$E^{(1)}$	$2 - 3 \sin^2 \theta$	
$E^{(2)}$	$\cos(2\phi) \sin^2 \theta$	
T_2	$\sin(2\phi) \sin(2\theta)$	

Appendix C

Tight-binding fit

The band structure which is used to calculate the spin- and charge-susceptibility is obtained from a fit to an LDA calculation performed by Heid. The LDA calculation was performed for LaPt₃Si plus one negative background charge in order to account for the one 4f electron. The calculation was done without spin-orbit coupling on a grid with 11×11×9 (=1089) k-points in the irreducible Brillouine zone, which corresponds to a 20×20×16 grid in the whole Brillouinzone. The k-space anisotropy of the spin-orbit coupling is given by Eq. (5.10):

$$\hat{\gamma}_{\mathbf{k}} = \frac{1}{v_{\text{avg}}} \begin{pmatrix} -v_y(\mathbf{k}) \\ v_x(\mathbf{k}) \\ 0 \end{pmatrix} \quad (\text{C.1})$$

$$v_{\text{avg}}^2 = \int_{\text{B.Z.}} d\mathbf{k} [v_x^2(\mathbf{k}) + v_y^2(\mathbf{k})] \quad (\text{C.2})$$

$$v_{x,y} = \frac{\partial \xi_{\mathbf{k}}}{\partial k_{x,y}} \quad (\text{C.3})$$

An estimation for the strength of the spin-orbit interaction g_{\perp} was obtained from a comparison with Ref. [120, 121]. The tight-binding coefficients were evaluated from a least squares fit via repeated simulated annealing with more weight close to the Fermi surface¹. I considered a simple tetragonal lattice and used a tight-binding fit including 4th nearest neighbor model. For the tetragonal symmetry of CePt₃Si this implies 74 hopping terms plus the chemical potential as fitting parameters. This task is not overdetermined because the dispersion is known at 1089 k-points. Furthermore this large number of terms in the dispersion does not slow down the calculation of the spin or charge susceptibility. Instead, it provides a simple approach to interpolate between the LDA-results. In general, the band structure can be written as

$$\xi_{\mathbf{k}} = \sum_{(i,j,k) \neq (0,0,0)} t_{(i,j,k)} \exp(-i\mathbf{k} \cdot \mathbf{r}) - \mu, \quad (\text{C.4})$$

where \mathbf{r} corresponds to the coordinate of the (i, j, k) th neighbor ($i, j, k \in 0, \pm 1, \pm 2, \dots$). Note that for tetragonal symmetry 2, 4 or even 8 terms can be collected to form the hopping terms t_1, t_2, t_3, \dots . The tight-binding terms are labeled in the following way, where the expression in

¹The weighting-function decreases smoothly by a factor of 9 to the farthest part of the Fermi surface.

Appendix C Tight-binding fit

the brackets denote a representative coordinate (i, j, k) of the corresponding hopping-term ².

t_1	$(0, 1, 0)$	$2 \cos(k_y) + 2 \cos(k_x)$
t_2	$(1, 1, 0)$	$4 \cos(k_x) \cos(k_y)$
t_3	$(0, 2, 0)$	$2 \cos(2k_y) + 2 \cos(2k_x)$
t_4	$(1, 2, 0)$	$4 \cos(k_x) \cos(2k_y) + 4 \cos(2k_x) \cos(k_y)$
t_5	$(2, 2, 0)$	$4 \cos(2k_x) \cos(2k_y)$
t_6	$(0, 3, 0)$	$2 \cos(3k_y) + 2 \cos(3k_x)$
t_7	$(1, 3, 0)$	$4 \cos(k_x) \cos(3k_y) + 4 \cos(3k_x) \cos(k_y)$
t_8	$(2, 3, 0)$	$4 \cos(2k_x) \cos(3k_y) + 4 \cos(3k_x) \cos(2k_y)$
t_9	$(3, 3, 0)$	$4 \cos(3k_x) \cos(3k_y)$
t_{10}	$(0, 4, 0)$	$2 \cos(4k_y) + 2 \cos(4k_x)$
t_{11}	$(1, 4, 0)$	$4 \cos(k_x) \cos(4k_y) + 4 \cos(4k_x) \cos(k_y)$
t_{12}	$(2, 4, 0)$	$4 \cos(4k_x) \cos(2k_y) + 4 \cos(2k_x) \cos(4k_y)$
t_{13}	$(3, 4, 0)$	$4 \cos(3k_x) \cos(4k_y) + 4 \cos(4k_x) \cos(3k_y)$
t_{14}	$(4, 4, 0)$	$4 \cos(4k_x) \cos(4k_y)$
t_{15}	$(0, 0, 1)$	$2 \cos(k_z)$
t_{16}	$(0, 1, 1)$	$4 \cos(k_z)(\cos(k_y) + \cos(k_x))$
t_{17}	$(1, 1, 1)$	$8 \cos(k_x) \cos(k_y) \cos(k_z)$
t_{18}	$(0, 2, 1)$	$4 \cos(k_z)(\cos(2k_y) + \cos(2k_x))$
t_{19}	$(1, 2, 1)$	$8 \cos(k_z)(\cos(2k_x) \cos(k_y) + \cos(k_x) \cos(2k_y))$
t_{20}	$(2, 2, 1)$	$8 \cos(2k_x) \cos(2k_y) \cos(k_z)$
t_{21}	$(0, 3, 1)$	$4 \cos(k_z)(\cos(3k_y) + \cos(3k_x))$
t_{22}	$(1, 3, 1)$	$8 \cos(k_z)(\cos(k_x) \cos(3k_y) + \cos(3k_x) \cos(k_y))$
t_{23}	$(2, 3, 1)$	$8 \cos(k_z)(\cos(2k_x) \cos(3k_y) + \cos(3k_x) \cos(2k_y))$
t_{24}	$(3, 3, 1)$	$8 \cos(3k_x) \cos(3k_y) \cos(k_z)$
t_{25}	$(0, 4, 1)$	$4 \cos(k_z)(\cos(4k_y) + \cos(4k_x))$
t_{26}	$(1, 4, 1)$	$8 \cos(k_z)(\cos(k_x) \cos(4k_y) + \cos(4k_x) \cos(k_y))$
t_{27}	$(2, 4, 1)$	$8 \cos(k_z)(\cos(2k_x) \cos(4k_y) + \cos(4k_x) \cos(2k_y))$
t_{28}	$(3, 4, 1)$	$8 \cos(k_z)(\cos(3k_x) \cos(4k_y) + \cos(4k_x) \cos(3k_y))$
t_{29}	$(4, 4, 1)$	$8 \cos(4k_x) \cos(4k_y) \cos(k_z)$
t_{30}	$(0, 0, 2)$	$2 \cos(2k_z)$
t_{31}	$(0, 1, 2)$	$4 \cos(2k_z)(\cos(k_y) + \cos(k_x))$
t_{32}	$(1, 1, 2)$	$8 \cos(k_x) \cos(k_y) \cos(2k_z)$
t_{33}	$(0, 2, 2)$	$4 \cos(2k_z)(\cos(2k_y) + \cos(2k_x))$
t_{34}	$(1, 2, 2)$	$8 \cos(2k_z)(\cos(2k_x) \cos(k_y) + \cos(k_x) \cos(2k_y))$
t_{35}	$(2, 2, 2)$	$8 \cos(2k_x) \cos(2k_y) \cos(2k_z)$
t_{36}	$(0, 3, 2)$	$4 \cos(2k_z)(\cos(3k_y) + \cos(3k_x))$
t_{37}	$(1, 3, 2)$	$8 \cos(2k_z)(\cos(k_x) \cos(3k_y) + \cos(3k_x) \cos(k_y))$
t_{38}	$(2, 3, 2)$	$8 \cos(2k_z)(\cos(2k_x) \cos(3k_y) + \cos(3k_x) \cos(2k_y))$
t_{39}	$(3, 3, 2)$	$8 \cos(3k_x) \cos(3k_y) \cos(2k_z)$
t_{40}	$(0, 4, 2)$	$4 \cos(2k_z)(\cos(4k_y) + \cos(4k_x))$

²Here, and for the numerical calculations the lattice parameters $a = b$ and c are set to unity.

$$\begin{aligned}
t_{41} & (1, 4, 2) : 8 \cos(2k_z)(\cos(k_x) \cos(4k_y) + \cos(4k_x) \cos(k_y)) \\
t_{42} & (2, 4, 2) : 8 \cos(2k_z)(\cos(2k_x) \cos(4k_y) + \cos(4k_x) \cos(2k_y)) \\
t_{43} & (3, 4, 2) : 8 \cos(2k_z)(\cos(3k_x) \cos(4k_y) + \cos(4k_x) \cos(3k_y)) \\
t_{44} & (4, 4, 2) : 8 \cos(4k_x) \cos(4k_y) \cos(2k_z) \\
t_{45} & (0, 0, 3) : 2 \cos(3k_z) \\
t_{46} & (0, 1, 3) : 4 \cos(3k_z)(\cos(k_y) + \cos(k_x)) \\
t_{47} & (1, 1, 3) : 8 \cos(k_x) \cos(k_y) \cos(3k_z) \\
t_{48} & (0, 2, 3) : 4 \cos(3k_z)(\cos(2k_y) + \cos(2k_x)) \\
t_{49} & (1, 2, 3) : 8 \cos(3k_z)(\cos(2k_x) \cos(k_y) + \cos(k_x) \cos(2k_y)) \\
t_{50} & (2, 2, 3) : 8 \cos(2k_x) \cos(2k_y) \cos(3k_z) \\
t_{51} & (0, 3, 3) : 4 \cos(3k_z)(\cos(3k_y) + \cos(3k_x)) \\
t_{52} & (1, 3, 3) : 8 \cos(3k_z)(\cos(k_x) \cos(3k_y) + \cos(3k_x) \cos(k_y)) \\
t_{53} & (2, 3, 3) : 8 \cos(3k_z)(\cos(2k_x) \cos(3k_y) + \cos(3k_x) \cos(2k_y)) \\
t_{54} & (3, 3, 3) : 8 \cos(3k_x) \cos(3k_y) \cos(3k_z) \\
t_{55} & (0, 4, 3) : 4 \cos(3k_z)(\cos(4k_y) + \cos(4k_x)) \\
t_{56} & (1, 4, 3) : 8 \cos(3k_z)(\cos(k_x) \cos(4k_y) + \cos(4k_x) \cos(k_y)) \\
t_{57} & (2, 4, 3) : 8 \cos(3k_z)(\cos(2k_x) \cos(4k_y) + \cos(4k_x) \cos(2k_y)) \\
t_{58} & (3, 4, 3) : 8 \cos(3k_z)(\cos(3k_x) \cos(4k_y) + \cos(4k_x) \cos(3k_y)) \\
t_{59} & (4, 4, 3) : 8 \cos(4k_x) \cos(4k_y) \cos(3k_z) \\
t_{60} & (0, 0, 4) : 2 \cos(4k_z) \\
t_{61} & (0, 1, 4) : 4 \cos(4k_z)(\cos(k_y) + \cos(k_x)) \\
t_{62} & (1, 1, 4) : 8 \cos(k_x) \cos(k_y) \cos(4k_z) \\
t_{63} & (0, 2, 4) : 4 \cos(4k_z)(\cos(2k_y) + \cos(2k_x)) \\
t_{64} & (1, 2, 4) : 8 \cos(4k_z)(\cos(2k_x) \cos(k_y) + \cos(k_x) \cos(2k_y)) \\
t_{65} & (2, 2, 4) : 8 \cos(2k_x) \cos(2k_y) \cos(4k_z) \\
t_{66} & (0, 3, 4) : 4 \cos(4k_z)(\cos(3k_y) + \cos(3k_x)) \\
t_{67} & (1, 3, 4) : 8 \cos(4k_z)(\cos(k_x) \cos(3k_y) + \cos(3k_x) \cos(k_y)) \\
t_{68} & (2, 3, 4) : 8 \cos(4k_z)(\cos(2k_x) \cos(3k_y) + \cos(3k_x) \cos(2k_y)) \\
t_{69} & (3, 3, 4) : 8 \cos(3k_x) \cos(3k_y) \cos(4k_z) \\
t_{70} & (0, 4, 4) : 4 \cos(4k_z)(\cos(4k_y) + \cos(4k_x)) \\
t_{71} & (1, 4, 4) : 8 \cos(4k_z)(\cos(k_x) \cos(4k_y) + \cos(4k_x) \cos(k_y)) \\
t_{72} & (2, 4, 4) : 8 \cos(4k_z)(\cos(2k_x) \cos(4k_y) + \cos(4k_x) \cos(2k_y)) \\
t_{73} & (3, 4, 4) : 8 \cos(4k_z)(\cos(3k_x) \cos(4k_y) + \cos(4k_x) \cos(3k_y)) \\
t_{74} & (4, 4, 4) : 8 \cos(4k_x) \cos(4k_y) \cos(4k_z)
\end{aligned}$$

Appendix C Tight-binding fit

The band structure fit for the β band of CePt₃Si yields

$$\begin{aligned}
 t_1 &= 1.000000 & t_2 &= 0.358493 & t_3 &= -0.331107 & t_4 &= -0.239777 \\
 t_5 &= 0.152182 & t_6 &= 0.191377 & t_7 &= -0.030291 & t_8 &= 0.071605 \\
 t_9 &= 0.116762 & t_{10} &= 0.039128 & t_{11} &= 0.032885 & t_{12} &= -0.063346 \\
 t_{13} &= 0.039534 & t_{14} &= 0.056700 & t_{15} &= 0.026333 & t_{16} &= -0.581673 \\
 t_{17} &= -0.550543 & t_{18} &= 0.295727 & t_{19} &= 0.245089 & t_{20} &= 0.101670 \\
 t_{21} &= -0.024705 & t_{22} &= -0.025429 & t_{23} &= 0.015342 & t_{24} &= 0.057998 \\
 t_{25} &= 0.015041 & t_{26} &= -0.015057 & t_{27} &= 0.006583 & t_{28} &= -0.018151 \\
 t_{29} &= 0.006012 & t_{30} &= -0.957762 & t_{31} &= -0.050089 & t_{32} &= 0.082644 \\
 t_{33} &= 0.114648 & t_{34} &= 0.011217 & t_{35} &= 0.010295 & t_{36} &= -0.024208 \\
 t_{37} &= 0.005362 & t_{38} &= 0.000841 & t_{39} &= -0.034375 & t_{40} &= -0.019411 \\
 t_{41} &= 0.004461 & t_{42} &= 0.006155 & t_{43} &= -0.000725 & t_{44} &= -0.005928 \\
 t_{45} &= -0.142076 & t_{46} &= -0.022716 & t_{47} &= 0.066993 & t_{48} &= -0.018927 \\
 t_{49} &= 0.014536 & t_{50} &= -0.019409 & t_{51} &= 0.029159 & t_{52} &= 0.005648 \\
 t_{53} &= -0.023640 & t_{54} &= -0.009391 & t_{55} &= -0.003495 & t_{56} &= 0.007018 \\
 t_{57} &= 0.005883 & t_{58} &= -0.000134 & t_{59} &= 0.002172 & t_{60} &= -0.099237 \\
 t_{61} &= -0.001039 & t_{62} &= 0.013199 & t_{63} &= 0.031846 & t_{64} &= -0.003015 \\
 t_{65} &= -0.038766 & t_{66} &= 0.008778 & t_{67} &= 0.016811 & t_{68} &= 0.000073 \\
 t_{69} &= -0.002996 & t_{70} &= -0.021220 & t_{71} &= -0.002964 & t_{72} &= 0.003475 \\
 t_{73} &= 0.005178 & t_{74} &= -0.000642 & & & &
 \end{aligned} \tag{C.5}$$

$$\mu = 3.502108 ,$$

with a band filling of 79% and an average Fermi surface velocity of $v_{\text{avg}} = 5.67$. All energies for the β band are in units of $t_1 = 110\text{meV}$.

The band structure fit for the α band of CePt₃Si yields

$$\begin{aligned}
t_1 &= 1.0000000000 & t_2 &= 1.1178001181 & t_3 &= -0.1410421595 & t_4 &= 0.0111206866 \\
t_5 &= 0.4606822361 & t_6 &= -0.1930080172 & t_7 &= -0.0206163996 & t_8 &= -0.0843128680 \\
t_9 &= 0.0283846721 & t_{10} &= 0.0301898255 & t_{11} &= -0.0016314998 & t_{12} &= 0.1321370343 \\
t_{13} &= 0.0004517330 & t_{14} &= -0.0337674838 & t_{15} &= -0.2949050094 & t_{16} &= -0.1929239743 \\
t_{17} &= -0.5307504915 & t_{18} &= 0.0374165878 & t_{19} &= 0.0878828981 & t_{20} &= -0.0279976298 \\
t_{21} &= 0.1560826003 & t_{22} &= 0.1085002201 & t_{23} &= 0.0079798286 & t_{24} &= -0.0116885434 \\
t_{25} &= 0.0021459710 & t_{26} &= 0.0198868041 & t_{27} &= 0.0182870364 & t_{28} &= 0.0015452003 \\
t_{29} &= 0.0093740937 & t_{30} &= 0.6908026711 & t_{31} &= 0.0474742444 & t_{32} &= 0.0054831515 \\
t_{33} &= -0.2514351956 & t_{34} &= 0.0024786220 & t_{35} &= 0.1021525091 & t_{36} &= 0.0385854454 \\
t_{37} &= -0.0321245747 & t_{38} &= 0.0135155493 & t_{39} &= 0.0148221376 & t_{40} &= 0.0266323284 \\
t_{41} &= 0.0102369900 & t_{42} &= -0.0038180767 & t_{43} &= -0.0040011344 & t_{44} &= -0.0003175090 \\
t_{45} &= 0.0338374626 & t_{46} &= 0.0285164402 & t_{47} &= -0.0150683613 & t_{48} &= 0.0050793228 \\
t_{49} &= -0.0301460101 & t_{50} &= 0.0079961794 & t_{51} &= -0.0283918016 & t_{52} &= 0.0047951579 \\
t_{53} &= 0.0062649306 & t_{54} &= -0.0063695654 & t_{55} &= 0.0013259022 & t_{56} &= 0.0006566319 \\
t_{57} &= -0.0044342855 & t_{58} &= -0.0030729050 & t_{59} &= -0.0014544178 & t_{60} &= 0.0938227199 \\
t_{61} &= 0.0011495392 & t_{62} &= 0.0004766283 & t_{63} &= -0.0489321791 & t_{64} &= -0.0027245761 \\
t_{65} &= 0.0154413697 & t_{66} &= -0.0019055742 & t_{67} &= -0.0068828978 & t_{68} &= 0.0018700372 \\
t_{69} &= 0.0072284189 & t_{70} &= 0.0053892621 & t_{71} &= -0.0015550213 & t_{72} &= 0.0028751649 \\
t_{73} &= 0.0000006775 & t_{74} &= 0.0015909850 & & & &
\end{aligned}$$

$$\mu = 16.3470040783 ,$$

(C.6)

with a band filling of 100% and an average Fermi surface velocity of $v_{\text{avg}} = 5.94$. All energies for the α band are in units of $t_1 = 94.8\text{meV}$.

Appendix C Tight-binding fit

The band structure fit for the γ band of CePt₃Si yields

$$\begin{aligned}
 t_1 &= 1.0000000000 & t_2 &= -0.9863811694 & t_3 &= -0.0443368655 & t_4 &= -0.1001570806 \\
 t_5 &= -0.0881807558 & t_6 &= 0.1024991958 & t_7 &= 0.0386095277 & t_8 &= -0.0744509386 \\
 t_9 &= -0.0757677586 & t_{10} &= 0.0118515101 & t_{11} &= 0.0057126110 & t_{12} &= 0.0186993542 \\
 t_{13} &= -0.0274816592 & t_{14} &= -0.0357290040 & t_{15} &= -1.0178540886 & t_{16} &= -0.1505399388 \\
 t_{17} &= 0.2657876240 & t_{18} &= -0.1392880068 & t_{19} &= 0.0507704098 & t_{20} &= -0.0136928392 \\
 t_{21} &= 0.0033060425 & t_{22} &= 0.0017467623 & t_{23} &= -0.0165076881 & t_{24} &= -0.0146710760 \\
 t_{25} &= -0.0250342549 & t_{26} &= 0.0163487800 & t_{27} &= -0.0168667925 & t_{28} &= 0.0123139569 \\
 t_{29} &= -0.0019879082 & t_{30} &= 0.0942887273 & t_{31} &= -0.0981892595 & t_{32} &= -0.1041405791 \\
 t_{33} &= 0.0676645801 & t_{34} &= 0.0479353882 & t_{35} &= -0.0565567613 & t_{36} &= -0.0396506599 \\
 t_{37} &= 0.0387860395 & t_{38} &= -0.0163599983 & t_{39} &= -0.0036732412 & t_{40} &= -0.0278015863 \\
 t_{41} &= 0.0055942211 & t_{42} &= 0.0109728517 & t_{43} &= -0.0021006428 & t_{44} &= -0.0005992281 \\
 t_{45} &= 0.0373775930 & t_{46} &= 0.0055582039 & t_{47} &= 0.0016125044 & t_{48} &= -0.0001577827 \\
 t_{49} &= 0.0124204469 & t_{50} &= -0.0042163248 & t_{51} &= -0.0379666852 & t_{52} &= -0.0200240936 \\
 t_{53} &= 0.0063743217 & t_{54} &= 0.0287118487 & t_{55} &= 0.0083141516 & t_{56} &= 0.0020636029 \\
 t_{57} &= -0.0130591564 & t_{58} &= 0.0065672078 & t_{59} &= -0.0006983135 & t_{60} &= 0.0053095940 \\
 t_{61} &= -0.0015232407 & t_{62} &= -0.0005436420 & t_{63} &= -0.0094508036 & t_{64} &= 0.0019553688 \\
 t_{65} &= 0.0086236334 & t_{66} &= -0.0078038493 & t_{67} &= -0.0012953419 & t_{68} &= -0.0013943071 \\
 t_{69} &= 0.0031465533 & t_{70} &= 0.0131697214 & t_{71} &= 0.0067105992 & t_{72} &= -0.0042129027 \\
 t_{73} &= -0.0027824194 & t_{74} &= -0.0030127833 & & & &
 \end{aligned}$$

$$\mu = -2.584748075 , \tag{C.7}$$

with a band filling of 20% and an average Fermi surface velocity of $v_{\text{avg}} = 4.35$. All energies for the γ band are in units of $t_1 = 129.9$ meV.

Appendix D

Algorithms to calculate the DoS and susceptibility

A schematic data flow of the algorithm used to calculate one component of the spin or charge susceptibility is displayed in Fig. D.1. Let me comment the different steps:

- First, two grids with dimension $500 \times 500 \times 500$ are filled with band structure data for each of the two bands (band dispersion, $\hat{\gamma}_{\mathbf{k}}$ -vector and in the superconducting state also the value of the gap and the coherence factors on the Brillouine zone). The grid represents 1/8th of the Brillouine zone, in order to account for the tetragonal and time reversal symmetry.
- ω -loop:
The susceptibility can be evaluated at arbitrary frequencies. Since the real part of the susceptibility is calculated via Kramers-Kronig, I need to cover the whole bandwidth. For INS and Kohn anomalies, only the low-frequency contribution is important. Therefore, I chose a non-equidistant ω -sampling according to ω^4 . For all calculations in this thesis 300 frequencies were evaluated.
- ν -loop:
The ν integration, see Eq. (5.22), goes from $-\omega \dots 0$ (plus a margin of $15k_B T$, which should be sufficiently large for finite temperatures). In this range, 200 frequencies are evaluated and then integrated using the Simpson-rule.
- Both grids are then filled with the spectral function for the corresponding frequency. For the calculation of the spectral function, the symmetry along the diagonal ΓZ is also taken into account.
- DCT/DST and multiplication:
According to the symmetry of $\hat{\gamma}_i$, either a discrete cosine or a discrete sine transformation is performed (see Appendix D.1). I used the FFTw-library [148, 149] which is much faster, than e.g. algorithms from Numerical recipes [150]. The discrete trigonometric transformations (DTT) are performed in each dimension separately. Unfortunately, these transforms are associated with different index-shifts for each dimensions (if the convolution involves the $\gamma_{\mathbf{k}}$ -vectors). Furthermore, the DTT-libraries avoid to store zeros, which

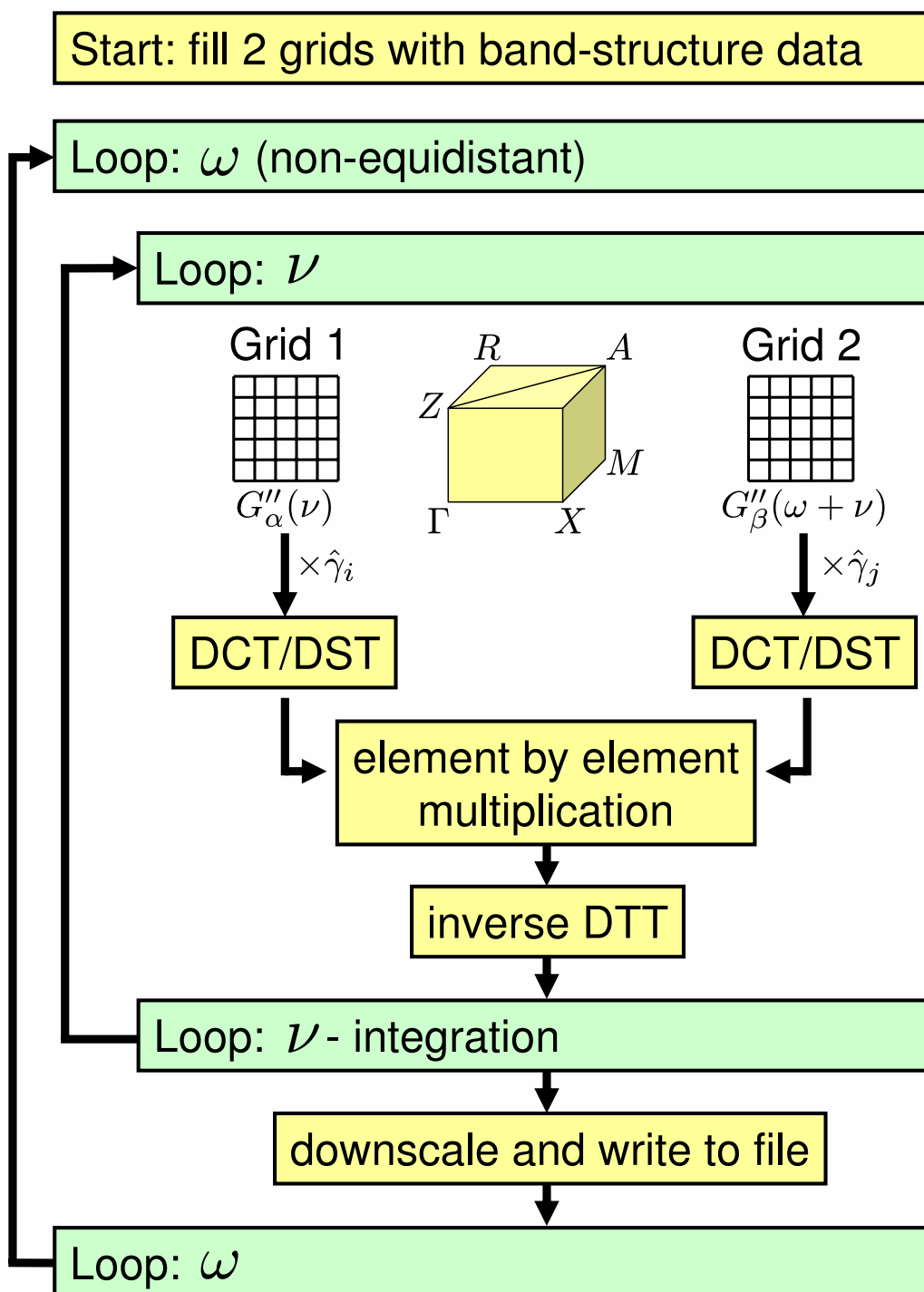


Figure D.1: Schematic data flow of the algorithm, calculating the dynamical q -dependent susceptibility.

are e.g. needed when a different inverse transform is used. This leads to the problem, that the size of the grid is not constant: The inverse transform needs one more sample in each dimension. Because of these index-shifts, one has to take care of the element by element multiplication. In each dimension, 4 different cases have to be taken into account, dependent on whether the right and/or left sample is stored or not.

- Inverse DTT:
The inverse DTT is always a DCT, since the multiplication of two even or two odd functions is always even.
- Downscaling:
The data volume from 300 frequencies times a $500 \times 500 \times 500$ grid in \mathbf{q} -space would be too large and too unhandy to store. Therefore, a trilinear interpolation in \mathbf{q} -space is applied (see Appendix D.2) to downscale the grid to a $100 \times 100 \times 100$ mesh. Thus, the data volume for each data file (12 terms for a single entry in the susceptibility tensor have to be evaluated) shrinks from hypothetically 37GB to 300MB. Note that only the imaginary part of the susceptibility is stored. The real part is calculated when the data file is read out. Then, the Kramers–Kronig transform takes only a few seconds.

D.1 Numerical convolution

In order to calculate the susceptibility, one has to evaluate the following expression (see Section 5.2):

$$C_{\alpha\beta ij}(\epsilon, \nu) = \frac{1}{\pi^2} [\hat{\gamma}_i G''_{\alpha}(\epsilon)] \otimes [G''_{\beta}(\nu) \hat{\gamma}_j] . \quad (\text{D.1})$$

$$(\text{D.2})$$

Instead of applying the cross-correlation theorem, it is more convenient to first introduce the following abbreviations ¹

$$f(\mathbf{k}) = \hat{\gamma}_i(\mathbf{k}) G''_{\alpha}(\mathbf{k}, \epsilon) \quad (\text{D.3})$$

$$g(\mathbf{k}) = \hat{\gamma}_j(\mathbf{k}) G''_{\beta}(\mathbf{k}, \nu) \quad (\text{D.4})$$

$$h(\mathbf{q}) = f(\mathbf{k}) \otimes g(\mathbf{k}) = \int_{B.Z.} d\mathbf{k} f(\mathbf{k}) g(\mathbf{k} + \mathbf{q}) \quad (\text{D.5})$$

¹It is not common to write down explicitly the argument of the function when using the symbolic notation for cross-correlations or convolutions. However, here it is necessary, because the functions f, g can be even or odd w.r.t. one component of \mathbf{k} .

Appendix D Algorithms to calculate the DoS and susceptibility

and then convert the cross-correlation \otimes into a convolution \star ²

$$h(q_l) = \begin{cases} f(k_l) \star g(k_l) & \text{for } f: \text{ even, } f(-k_l) = f(k_l) \\ -f(k_l) \star g(k_l) & \text{for } f: \text{ odd, } f(-k_l) = -f(k_l) \end{cases} \quad (\text{D.6})$$

where I used

$$f(k_l) \otimes g(k_l) = f^*(-k_l) \star g(k_l) = f(-k_l) \star g(k_l) \quad (\text{D.7})$$

and the fact that $f = f^*$ is real.

At this stage, a closer look at the symmetry of the $\hat{\gamma}$ vector in each dimension for the Rashba-type of SOC is appropriate. From the definition of $\hat{\gamma}$ in Eq. (5.10) one obtains:

$$\begin{aligned} \hat{\gamma}_x(-k_x, k_y, k_z) &= \hat{\gamma}_x(\mathbf{k}) && \rightarrow \text{even} && \rightarrow \text{DCT} \\ \hat{\gamma}_x(k_x, -k_y, k_z) &= -\hat{\gamma}_x(\mathbf{k}) && \rightarrow \text{odd} && \rightarrow \text{DST} \\ \hat{\gamma}_x(k_x, k_y, -k_z) &= \hat{\gamma}_x(\mathbf{k}) && \rightarrow \text{even} && \rightarrow \text{DCT} \\ \hat{\gamma}_y(-k_x, k_y, k_z) &= -\hat{\gamma}_y(\mathbf{k}) && \rightarrow \text{odd} && \rightarrow \text{DST} \\ \hat{\gamma}_y(k_x, -k_y, k_z) &= \hat{\gamma}_y(\mathbf{k}) && \rightarrow \text{even} && \rightarrow \text{DCT} \\ \hat{\gamma}_y(k_x, k_y, -k_z) &= \hat{\gamma}_y(\mathbf{k}) && \rightarrow \text{even} && \rightarrow \text{DCT} \end{aligned} \quad (\text{D.8})$$

with the abbreviations ‘‘DST’’=‘‘Discrete Sine Transformation’’ and ‘‘DCT’’=‘‘Discrete Cosine Transformation’’.

The discretization of Eq. (D.6) leads to a circular convolution $\langle \dots \odot \dots \rangle$, defined in Ref. [118]. Adopting the notation of this publication, it turns out that only one of the 40 possible convolutions in the (anti)symmetric case is compatible with a feasible data alignment and with the provided DTT algorithms by FFTw [149]. The data alignment and the corresponding trigonometric transforms for the symmetric and antisymmetric case are shown in Fig. D.2 and Fig. D.3, respectively. In particular, the discretized convolutions read:

- even symmetry
 $\langle \text{HSHS} \odot \text{HSHS} \rangle \rightarrow \text{WSWS}$
 $h(n-1) = C_{1e}^{-1} \{C_{2e}[f(n)] \times C_{2e}[g(n)]\}$
- odd symmetry
 $\langle \text{HAHA} \odot \text{HAHA} \rangle \rightarrow \text{WSWS}$
 $h(n-1) = -C_{1e}^{-1} \{S_{2e}[f(n)] \times S_{2e}[g(n)]\}$

Here I used the following abbreviations (conform with Ref. [118]):

$$[C_{1e}]_{mn} = \begin{cases} 1 & \text{for } n = 0 \\ (-1)^m & \text{for } n = N \\ 2 \cos\left(\frac{\pi mn}{N}\right) & \text{otherwise} \end{cases} \quad \text{for } m, n = 0, \dots, N \quad (\text{D.9})$$

²The convolution is separately performed in each dimension, which is indicated by indexing the momentum.

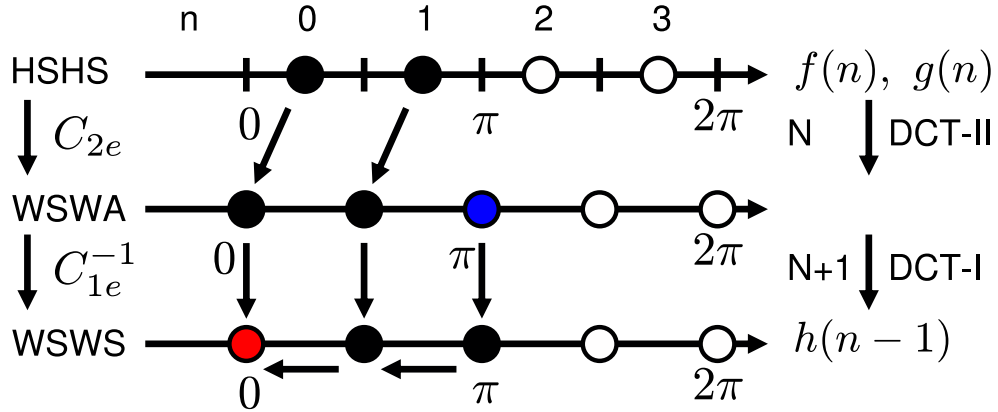


Figure D.2: Data alignment for a symmetric convolution of the length $N = 2$. Note that the length of the output has increased by one sample, since the black circles denote actually stored data points and the white circles denote data points that are not stored due to symmetry reasons. Arrows denote the shifts of the indices by 0, 1/2 or 1 sample in the corresponding step. At the place of the blue circle, a zero has to be filled and the content of the array corresponding to the red circle has to be deleted/overwritten. On the left-hand side of this diagram the notation from Ref. [118] is used and on the right-hand side the corresponding names for the algorithms e.g. in Ref. [148] is displayed.

$$[C_{2e}]_{mn} = 2 \cos\left(\frac{\pi m(n + 1/2)}{N}\right) \quad \text{for } m, n = 0, \dots, N - 1 \quad (\text{D.10})$$

$$[S_{2e}]_{mn} = 2 \sin\left(\frac{\pi m(n + 1/2)}{N}\right) \quad \text{for } \begin{cases} m = 0, \dots, N \\ n = 0, \dots, N - 1 \end{cases} \quad (\text{D.11})$$

The denominations for the symmetries of the data array with respect to the left and right boundary are also explained in Ref. [118]:

- WS : whole sample symmetric
- WA : whole sample antisymmetric
- HS : half sample symmetric
- HA : half sample antisymmetric

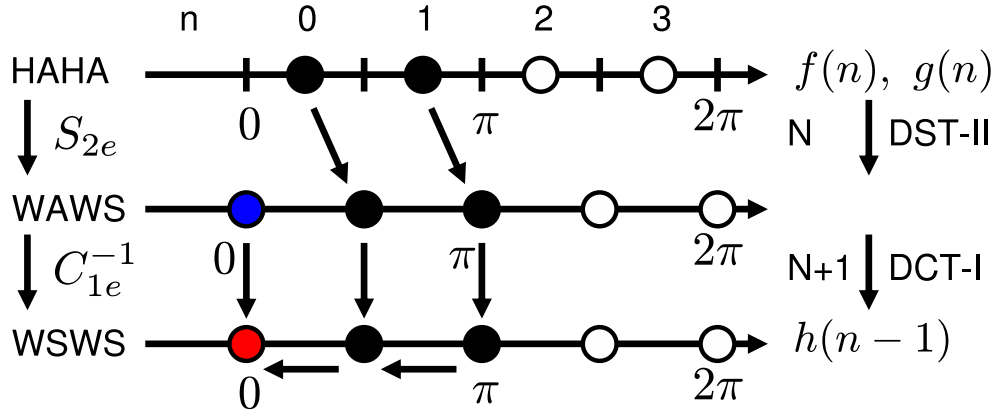


Figure D.3: Data alignment for an antisymmetric convolution of the length $N = 2$. Note that also in this case the length of the output has increased by one sample. The symbols are explained in Fig. D.2

D.2 Trilinear interpolation

In order to interpolate the value of a function at the position (x, y, z) between the 8 closest lattice points in a cubic grid³, it is convenient to define first, the nearest neighbors

$$\begin{aligned}
 P_1 &= (\lfloor x \rfloor, \lfloor y \rfloor, \lfloor z \rfloor) & P_2 &= (\lceil x \rceil, \lfloor y \rfloor, \lfloor z \rfloor) \\
 P_3 &= (\lceil x \rceil, \lceil y \rceil, \lfloor z \rfloor) & P_4 &= (\lfloor x \rfloor, \lceil y \rceil, \lfloor z \rfloor) \\
 P_5 &= (\lfloor x \rfloor, \lfloor y \rfloor, \lceil z \rceil) & P_6 &= (\lceil x \rceil, \lfloor y \rfloor, \lceil z \rceil) \\
 P_7 &= (\lceil x \rceil, \lceil y \rceil, \lceil z \rceil) & P_8 &= (\lfloor x \rfloor, \lceil y \rceil, \lceil z \rceil)
 \end{aligned}$$

with $\lfloor x \rfloor = \text{floor}(x)$ (C-syntax) and $\lceil x \rceil = \text{ceil}(x)$ (C-syntax). The value of the function at position i is denoted by f_i . Furthermore, one can define the distances to point P_1 , which is the closest to the origin:

$$\begin{aligned}
 \Delta x &= x - \lfloor x \rfloor & (D.12) \\
 \Delta y &= y - \lfloor y \rfloor \\
 \Delta z &= z - \lfloor z \rfloor .
 \end{aligned}$$

The interpolated value f then reads:

$$\begin{aligned}
 f &= f_1 (1 - \Delta x)(1 - \Delta y)(1 - \Delta z) & + f_5 (1 - \Delta x)(1 - \Delta y)\Delta z & (D.13) \\
 &+ f_2 \Delta x(1 - \Delta y)(1 - \Delta z) & + f_6 \Delta x(1 - \Delta y)\Delta z \\
 &+ f_3 \Delta x\Delta y(1 - \Delta z) & + f_7 \Delta x\Delta y\Delta z \\
 &+ f_4 (1 - \Delta x)\Delta y(1 - \Delta z) & + f_8 (1 - \Delta x)\Delta y\Delta z .
 \end{aligned}$$

³The lattice constants are set to unity, hence the interpolation can be done on a cubic instead of a tetragonal lattice.

D.3 DoS in 3D

The density of states (DoS) in three dimension was calculated using the so-called Simplex–algorithm after Eschrig [151]. In the normal state, the DoS is given by (see, for example, Ashcroft/Mermin [130]):

$$D(\omega) = \frac{1}{4\pi^3} \int_{B.Z.} dk^3 \delta(\omega - \xi_{\mathbf{k}}) . \quad (\text{D.14})$$

Using the notation of Ref. [151], one can identify $a_i \equiv 1$ and $\Sigma_i \equiv 0$. Thus, the contribution of each simplex in three dimensions ($i,j=0,1,2,3$) to the integral simplifies to:

$$J(\omega, v, \epsilon_i) = 3v \sum_j^{\epsilon_j < \omega} \frac{(\omega - \epsilon_j)^2}{\prod_{i(\neq j)} (\epsilon_i - \epsilon_j)} , \quad (\text{D.15})$$

with $D(\omega) = \sum J(\omega, v, \epsilon_i)$, where the sum includes all simplices with the same volume v . In three dimensions, it is convenient to subdivide cubes into 6 tetrahedrons with equal volume (without loss of accuracy also 5 tetrahedrons with different volume could further reduce the computational effort). Labeling the corners of one cube (with edge length $h = \pi/N$) according to

$$\begin{array}{llll} 1 : (0, 0, 0) & 2 : (h, 0, 0) & 3 : (h, h, 0) & 4 : (0, h, 0) \\ 5 : (0, 0, h) & 6 : (h, 0, h) & 7 : (h, h, h) & 8 : (0, h, h) \end{array} \quad (\text{D.16})$$

I get the following 6 tetrahedrons:

tetra- hedron	corners 0 1 2 3
(I)	2 3 1 6
(II)	5 3 1 6
(III)	5 3 7 6
(IV)	5 3 7 4
(V)	5 3 1 4
(VI)	5 7 8 4

(D.17)

This special choice prevents divisions by zero for energy–dispersions with the following symmetry $\xi(k_x, k_y, k_z) = \xi(k_y, k_x, k_z)$, which is present for the point groups C_{4v} and O .

Bibliography

- [1] P. W. Anderson. Structure of “triplet” superconducting energy gaps. *Phys. Rev. B* **30**, 4000 (1984).
- [2] E. Bauer, G. Hilscher, H. Michor, C. Paul, E. W. Scheidt, A. Griбанov, Y. Seropegin, H. Noël, M. Sigrist, and P. Rogl. Heavy fermion superconductivity and magnetic order in noncentrosymmetric CePt₃Si. *Phys. Rev. Lett.* **92**, 027003 (2004).
- [3] E. Bauer, I. Bonalde, and M. Sigrist. Superconductivity and normal state properties of non-centrosymmetric CePt₃Si: A status report. *Low Temp. Phys.* **31**, 748 (2005).
- [4] P. A. Frigeri, D. F. Agterberg, and M. Sigrist. Spin susceptibility in superconductors without inversion symmetry. *New J. Phys.* **6**, 115 (2004).
- [5] P. A. Frigeri, D. F. Agterberg, A. Koga, and M. Sigrist. Superconductivity without inversion symmetry: MnSi versus CePt₃Si. *Phys. Rev. Lett.* **92**, 097001 (2004).
- [6] P. A. Frigeri, D. F. Agterberg, A. Koga, and M. Sigrist. Erratum: Superconductivity without inversion symmetry: MnSi versus CePt₃Si [Phys. Rev. Lett. 92, 097001 (2004)]. *Phys. Rev. Lett.* **93**, 099903 (2004).
- [7] N. Metoki, K. Kaneko, T. D. Matsuda, A. Galatanu, T. Takeuchi, S. Hashimoto, T. Ueda, R. Settai, Y. Ōnuki, and N. Bernhoeft. Magnetic structure and the crystal field excitation in heavy-fermion antiferromagnetic superconductor CePt₃Si. *J. Phys.: Condens. Matter* **16**, L207 (2004).
- [8] A. Amato, E. Bauer, and C. Baines. Coexistence of magnetism and superconductivity in the heavy-fermion superconductor CePt₃Si. *Phys. Rev. B* **71**, 092501 (2005).
- [9] W. Higemoto, Y. Haga, T. D. Matsuda, Y. Ōnuki, K. Ohishi, T. U. Ito, A. Koda, S. R. Saha, and R. Kadono. Possible unconventional superconductivity and magnetism in CePt₃Si probed by muon spin rotation and relaxation. *J. Phys. Soc. Jpn.* **75**, 124713 (2006).
- [10] H. Mukuda, S. Nishide, A. Harada, K. Iwasaki, M. Yogi, M. Yashima, Y. Kitaoka, M. Tsujino, T. Takeuchi, R. Settai, Y. Ōnuki, E. Bauer, K. M. Itoh, and E. E. Haller. Multiband superconductivity in heavy fermion compound CePt₃Si without inversion symmetry: An NMR study on a high-quality single crystal. *J. Phys. Soc. Jpn.* **78**, 014705 (2009).
- [11] M. Nicklas, G. Sparn, R. Lackner, E. Bauer, and F. Steglich. Effect of hydrostatic pressure on the ambient pressure superconductor CePt₃Si. *Physica B* **359**, 386 (2005).

Bibliography

- [12] N. Tateiwa, Y. Haga, T. D. Matsuda, S. Ikeda, T. Yasuda, T. Takeuchi, R. Settai, and Y. Ōnuki. Novel pressure phase diagram of heavy fermion superconductor CePt₃Si investigated by ac calorimetry. *J. Phys. Soc. Jpn.* **74**, 1903 (2005).
- [13] N. Tateiwa, Y. Haga, T.D. Matsuda, E. Yamamoto, S. Ikeda, T. Takeuchi, R. Settai, and Y. Ōnuki. Thermodynamic studies on non centrosymmetric superconductors by ac calorimetry under high pressures. *arXiv:cond-mat/0710.2580* (2006).
- [14] M. Nicklas, F. Steglich, J. Knolle, I. Eremin, R. Lackner, and E. Bauer. Pair breaking by nonmagnetic impurities in the noncentrosymmetric superconductor CePt₃Si. *Phys. Rev. B* **81**, 180511 (2010).
- [15] I. Bonalde, W. Brämer-Escamilla, and E. Bauer. Evidence for line nodes in the superconducting energy gap of noncentrosymmetric CePt₃Si from magnetic penetration depth measurements. *Phys. Rev. Lett.* **94**, 207002 (2005).
- [16] K. Izawa, Y. Kasahara, Y. Matsuda, K. Behnia, T. Yasuda, R. Settai, and Y. Ōnuki. Line nodes in the superconducting gap function of noncentrosymmetric CePt₃Si. *Phys. Rev. Lett.* **94**, 197002 (2005).
- [17] M. Yogi, Y. Kitaoka, S. Hashimoto, T. Yasuda, R. Settai, T. D. Matsuda, Y. Haga, Y. Ōnuki, P. Rogl, and E. Bauer. Evidence for a novel state of superconductivity in noncentrosymmetric CePt₃Si: A Pt-NMR study. *Phys. Rev. Lett.* **93**, 027003 (2004).
- [18] M. Yogi, Y. Kitaoka, S. Hashimoto, T. Yasuda, R. Settai, T. D. Matsuda, Y. Haga, Y. Ōnuki, P. Rogl, and E. Bauer. ¹⁹⁵Pt NMR study on noncentrosymmetric heavy-fermion superconductor CePt₃Si. *Journal of Physics and Chemistry of Solids* **67**, 522 (2006).
- [19] E.-W. Scheidt, F. Mayr, G. Eickerling, P. Rogl, and E. Bauer. Double specific heat anomaly of the superconducting state of CePt₃Si. *J. Phys.: Condens. Matter* **17**, L121 (2005).
- [20] Y. Aoki, A. Sumiyama, G. Motoyama, Y. Oda, T. Yasuda, R. Settai, and Y. Ōnuki. AC/DC susceptibility of the heavy-fermion superconductor CePt₃Si under pressure. *arXiv:cond-mat/0709.0834* (2007).
- [21] P. Badica, T. Kondo, and K. Togano. Superconductivity in a new pseudo-binary Li₂B(Pd_{1-x}Pt_x)₃ (x=0-1) boride system. *J. Phys. Soc. Jpn.* **74**, 1014 (2005).
- [22] K.-W. Lee and W. E. Pickett. Crystal symmetry, electron-phonon coupling, and superconducting tendencies in Li₂Pd₃B and Li₂Pt₃B. *Phys. Rev. B* **72**, 174505 (2005).
- [23] S. Chandra, S. M. Jaya, and M. C. Valsakumar. Electronic structure of Li₂Pd₃B and Li₂Pt₃B. *Physica C: Superconductivity* **432**, 116 (2005).
- [24] K. Togano, P. Badica, Y. Nakamori, S. Orimo, H. Takeya, and K. Hirata. Superconductivity in the metal rich Li-Pd-B ternary boride. *Phys. Rev. Lett.* **93**, 247004 (2004).

- [25] H. Takeya, S. Kasahara, M. El Massalami, T. Mochiku, K. Hirata, and K. Togano. Physical properties of $\text{Li}_2\text{Pd}_3\text{B}$ and $\text{Li}_2\text{Pt}_3\text{B}$ superconductors. *PRICM 6: Sixth Pacific Rim International Conference on Advanced materials and Processing Pts 1-3*, 561, 2079 (2007).
- [26] U. Eibenstein and W. Jung. $\text{Li}_2\text{Pd}_3\text{B}$ and $\text{Li}_2\text{Pt}_3\text{B}$: Ternary lithium borides of palladium and platinum with boron in octahedral coordination. *J. Solid State Chem.* **133**, 21 (1997).
- [27] T. Akazawa, H. Hidaka, T. Fujiwara, T. C. Kobayashi, E. Yamamoto, Y. Haga, R. Settai, and Y. Ōnuki. Pressure-induced superconductivity in ferromagnetic UIr without inversion symmetry. *J. Phys.: Condens. Matter* **16**, L29 (2004).
- [28] T. C. Kobayashi, S. Fukushima, H. Hidaka, H. Kotegawa, T. Akazawa, E. Yamamoto, Y. Haga, R. Settai, and Y. Ōnuki. Pressure-induced superconductivity in ferromagnet UIr without inversion symmetry. *Physica B* **378**, 355 (2006).
- [29] J. Linder, A. H. Nevidomskyy, and A. Sudbø. Nontrivial interplay of superconductivity and spin-orbit coupling in noncentrosymmetric ferromagnets. *Phys. Rev. B* **78**, 172502 (2008).
- [30] W. H. Lee, H. K. Zeng, Y. D. Yao, and Y. Y. Chen. Superconductivity in the Ni based ternary carbide LaNiC_2 . *Physica C* **266**, 138 (1996).
- [31] V. K. Pecharsky, L. L. Miller, and K. A. Gschneidner. Low-temperature behavior of two ternary lanthanide nickel carbides: Superconducting LaNiC_2 and magnetic CeNiC_2 . *Phys. Rev. B* **58**, 497 (1998).
- [32] A. D. Hillier, J. Quintanilla, and R. Cywinski. Evidence for time-reversal symmetry breaking in the noncentrosymmetric superconductor LaNiC_2 . *Phys. Rev. Lett.* **102**, 117007 (2009).
- [33] A. Subedi and D. J. Singh. Electron-phonon superconductivity in noncentrosymmetric LaNiC_2 : First-principles calculations. *Phys. Rev. B* **80**, 092506 (2009).
- [34] T. Klimczuk, Q. Xu, E. Morosan, J. D. Thompson, H. W. Zandbergen, and R. J. Cava. Superconductivity in noncentrosymmetric $\text{Mg}_{10}\text{Ir}_{19}\text{B}_{16}$. *Phys. Rev. B* **74**, 220502 (2006).
- [35] G. Mu, Y. Wang, L. Shan, and H.-H. Wen. Possible nodeless superconductivity in the noncentrosymmetric superconductor $\text{Mg}_{12-\delta}\text{Ir}_{19}\text{B}_{16}$. *arXiv:cond-mat/0708.3479* (2007).
- [36] K. Tahara, Z. Li, H. X. Yang, J. L. Luo, S. Kawasaki, and G.-q. Zheng. Superconducting state in the noncentrosymmetric $\text{Mg}_{9.3}\text{Ir}_{19}\text{B}_{16.7}$ and $\text{Mg}_{10.5}\text{Ir}_{19}\text{B}_{17.1}$ revealed by NMR. *Phys. Rev. B* **80**, 060503 (2009).
- [37] G. Amano, S. Akutagawa, T. Muranaka, Y. Zenitani, and J. Akimitsu. Superconductivity at 18 K in yttrium sesquicarbide system, Y_2C_3 . *J. Phys. Soc. Jpn.* **73**, 530 (2004).

Bibliography

- [38] R. Kadono, M. Hiraishi, M. Miyazaki, K. H. Satoh, S. Takeshita, S. Kuroiwa, S. Saura, and J. Akimitsu. Magnetic response of noncentrosymmetric superconductor La_2C_3 : Effect of double-gap and spin-orbit interaction. *arXiv:cond-mat/0809.1274* (2008).
- [39] G. Schuck, S. M. Kazakov, K. Rogacki, N. D. Zhigadlo, and J. Karpinski. Crystal growth, structure, and superconducting properties of the β -pyrochlore KOs_2O_6 . *Phys. Rev. B* **73**, 144506 (2006).
- [40] K. V. Samokhin and V. P. Mineev. Gap structure in noncentrosymmetric superconductors. *Phys. Rev. B* **77**, 104520 (2008).
- [41] N. Kimura, K. Ito, K. Saitoh, Y. Umeda, H. Aoki, and T. Terashima. Pressure-induced superconductivity in noncentrosymmetric heavy-fermion CeRhSi_3 . *Phys. Rev. Lett.* **95**, 247004 (2005).
- [42] N. Aso, H. Miyano, H. Yoshizawa, N. Kimura, T. Komatsubara, and H. Aoki. Incommensurate magnetic order in the pressure-induced superconductor CeRhSi_3 . *J. Magn. Magn. Mater.* **310**, 602 (2007).
- [43] N. Tateiwa, Y. Haga, T.D. Matsuda, S. Ikeda, E. Yamamoto, Y. Okuda, Y. Miyauchi, R. Settai, and Y. Ōnuki. High pressure study on the strong-coupling superconductivity in non-centrosymmetric compound CeIrSi_3 . *arXiv:cond-mat/0709.2199* (2007).
- [44] N. Kimura, Y. Umeda, T. Asai, T. Terashima, and H. Aoki. Magnetic and superconducting properties of LaRhSi_3 and CeRhSi_3 with the non-centrosymmetric crystal structure. *J. Phys. Soc. Jpn.* **76**, 044708 (2007).
- [45] G. Eguchi, D. C. Peets, M. Kriener, Y. Maeno, E. Nishibori, Y. Kumazawa, K. Banno, S. Maki, and H. Sawa. The fully-gapped noncentrosymmetric 5d-electron superconductors CaIrSi_3 and CaPtSi_3 . *arXiv:cond-mat/1006.4807* (2010).
- [46] T. Shibayama, M. Nohara, H. A. Katori, Y. Okamoto, and Z. Hiroi an H. Takagi. Superconductivity in Rh_2Ga_9 and Ir_2Ga_9 without inversion symmetry. *arXiv:cond-mat/0706.0577* (2007).
- [47] Y. L. Zuev, V. A. Kuznetsova, R. Prozorov, M. D. Vannette, M. V. Lobanov, D. K. Christen, and J. R. Thompson. *s*-wave superconductivity in non-centrosymmetric Re_3W probed by magnetic penetration depth. *arXiv:cond-mat/0707.1905* (2007).
- [48] P. A. Frigeri, D. F. Agterberg, I. Milat, and M. Sigrist. Phenomenological theory of the *s*-wave state in superconductors without an inversion center. *Eur. Phys. J. B* **54**, 435 (2006).
- [49] Y. Tada, N. Kawakami, and S. Fujimoto. Spin fluctuations and superconductivity in non-centrosymmetric heavy fermion systems CeRhSi_3 and CeIrSi_3 . *Phys. Rev. B* **81**, 104506 (2010).

- [50] Y. Tada, N. Kawakami, and S. Fujimoto. Microscopic mechanism and pairing symmetry of superconductivity in the noncentrosymmetric heavy fermion systems CeRhSi₃ and CeIrSi₃. *J. Phys. Soc. Jpn.* **77**, 054707 (2008).
- [51] Y. Yanase and M. Sigrist. Non-centrosymmetric superconductivity and antiferromagnetic order: Microscopic discussion of CePt₃Si. *J. Phys. Soc. Jpn.* **76**, 043712 (2007).
- [52] T. Yokoyama, S. Onari, and Y. Tanaka. Enhanced triplet superconductivity in noncentrosymmetric systems. *Phys. Rev. B* **75**, 172511 (2007).
- [53] K. V. Samokhin. Spin susceptibility of noncentrosymmetric superconductors. *Phys. Rev. B* **76**, 094516 (2007).
- [54] B. Liu and I. Eremin. Impurity resonance states in noncentrosymmetric superconductor CePt₃Si: A probe for Cooper-pairing symmetry. *Phys. Rev. B* **78**, 014518 (2008).
- [55] I. Bonalde, R. L. Ribeiro, W. Braemer-Escamilla, C. Rojas, E. Bauer, A. Prokofiev, Y. Haga, T. Yasuda, and Y. Ōnuki. Unusual behaviours and impurity effects in the noncentrosymmetric superconductor CePt₃Si. *New J. Phys.* **11**, 055054 (2009).
- [56] A. Vorontsov, I. Vekhter, and M. Eschrig. Andreev bound states in non-centrosymmetric superconductors. *Physica B* **403**, 1095 (2008).
- [57] A. B. Vorontsov, I. Vekhter, and M. Eschrig. Surface bound states and spin currents in noncentrosymmetric superconductors. *Phys. Rev. Lett.* **101**, 127003 (2008).
- [58] S. Fujimoto. Unambiguous probe of parity mixing of Cooper pairs in noncentrosymmetric superconductors. *Phys. Rev. B* **79**, 220506 (2009).
- [59] Y. Tanaka, Y. Mizuno, T. Yokoyama, K. Yada, and M. Sato. Anomalous Andreev bound state in non-centrosymmetric superconductors. *arXiv:cond-mat/1006.3544* (2010).
- [60] C. F. Miclea, A. C. Mota, M. Sigrist, F. Steglich, T. A. Sayles, B. J. Taylor, C. A. McElroy, and M. B. Maple. Vortex avalanches in the noncentrosymmetric superconductor Li₂Pt₃B. *Phys. Rev. B* **80**, 132502 (2009).
- [61] C. F. Miclea, A. C. Mota, M. Nicklas, R. Cardoso, F. Steglich, M. Sigrist, A. Prokofiev, and E. Bauer. Extreme vortex pinning in the noncentrosymmetric superconductor CePt₃Si. *Phys. Rev. B* **81**, 014527 (2010).
- [62] N. Hiasa, T. Saiki, and R. Ikeda. Vortex lattice structure dependent on pairing symmetry in Rashba superconductors. *Phys. Rev. B* **80**, 014501 (2009).
- [63] M. Sato, Y. Takahashi, and S. Fujimoto. Non-abelian topological order in *s*-wave superfluids of ultracold fermionic atoms. *Phys. Rev. Lett.* **103**, 020401 (2009).
- [64] Y. Tanaka, T. Yokoyama, A. V. Balatsky, and N. Nagaosa. Theory of topological spin current in noncentrosymmetric superconductors. *Phys. Rev. B* **79**, 060505 (2009).

Bibliography

- [65] H. Q. Yuan, D. F. Agterberg, N. Hayashi, P. Badica, D. Vandervelde, K. Togano, M. Sigrist, and M. B. Salamon. s -wave spin-triplet order in superconductors without inversion symmetry: $\text{Li}_2\text{Pd}_3\text{B}$ and $\text{Li}_2\text{Pt}_3\text{B}$. *Phys. Rev. Lett.* **97**, 017006 (2006).
- [66] K. V. Samokhin. Spin-orbit coupling and semiclassical electron dynamics in noncentrosymmetric metals. *Annals of Physics* **324**, 2385 (2009).
- [67] G. Dresselhaus. Spin-orbit coupling effects in zinc blende structures. *Phys. Rev.* **100**, 580 (1955).
- [68] V. M. Edelstein. Characteristics of the Cooper pairing in two-dimensional noncentrosymmetric electron systems. *Zh. Eksp. Teor. Fiz.* **95**, 2151 (1989).
- [69] L. P. Gor'kov and E. I. Rashba. Superconducting 2D system with lifted spin degeneracy: Mixed singlet-triplet state. *Phys. Rev. Lett.* **87**, 037004 (2001).
- [70] H. Q. Yuan, D. Vandervelde, M. B. Salamon, P. Badica, and K. Togano. A penetration depth study on $\text{Li}_2\text{Pd}_3\text{B}$ and $\text{Li}_2\text{Pt}_3\text{B}$. *arXiv:cond-mat/0506771* (2005).
- [71] D. Einzel and L. Klam. Response, relaxation and transport in unconventional superconductors. *J. Low Temp. Phys.* **150**, 57 (2008).
- [72] N. D. Mermin. Lindhard dielectric function in the relaxation-time approximation. *Phys. Rev. B* **1**, 2362 (1970).
- [73] L. Klam, D. Manske, and D. Einzel. Chapter in “Physical properties of non-centrosymmetric superconductors”, unpublished. Springer, Heidelberg.
- [74] M. Bakr, A. P. Schnyder, L. Klam, D. Manske, C. T. Lin, B. Keimer, M. Cardona, and C. Ulrich. Electronic and phononic Raman scattering in detwinned $\text{YBa}_2\text{Cu}_3\text{O}_{6.95}$ and $\text{Y}_{0.85}\text{Ca}_{0.15}\text{Ba}_2\text{Cu}_3\text{O}_{6.95}$: s -wave admixture to the $d_{x^2-y^2}$ -wave order parameter. *Phys. Rev. B* **80**, 064505 (2009).
- [75] D. Pines and P. Nozières. *The theory of quantum liquids*. W. A. Benjamin, New York (1966).
- [76] O. Betbeder-Matibet and P. Nozières. Transport equations in clean superconductors. *Annals of Physics* **51**, 392 (1969).
- [77] P. Wölfle. Kinetic theory of anisotropic fermi superfluids. *J. Low Temp. Phys.* **22**, 157 (1976).
- [78] T. Tsuneto. Transverse collective excitations in superconductors and electromagnetic absorption. *Phys. Rev.* **118**, 1029 (1960).
- [79] L. Klam. Transport und Ramanstreuung in unkonventionellen Supraleitern. *Diploma thesis* (2006).

- [80] A. J. Leggett. A theoretical description of the new phases of liquid He^3 . *Rev. Mod. Phys.* **47**, 331 (1975).
- [81] A. J. Leggett. Erratum: A theoretical description of the new phases of liquid He^3 . *Rev. Mod. Phys.* **48**, 357 (1976).
- [82] D. Einzel. Analytic two-fluid description of unconventional superconductivity. *J. Low Temp. Phys.* **131**, 1 (2003).
- [83] Y. Nambu. Nobel lecture: Spontaneous symmetry breaking in particle physics: A case of cross fertilization. *Rev. Mod. Phys.* **81**, 1015 (2009).
- [84] N. N. Bogoljubov. On a new method in the theory of superconductivity. *Nuovo Cimento* **7**, 794 (1958).
- [85] P. W. Anderson. Coherent excited states in the theory of superconductivity: Gauge invariance and the Meissner effect. *Phys. Rev.* **110**, 827 (1958).
- [86] Vollhardt, D. and Wölfle, P. *The superfluid phases of helium 3*. Taylor and Francis, London (1990).
- [87] Wölfle, P. Collisionless collective modes in superfluid He-3. *Physica B* **90**, 96 (1977).
- [88] H. Monien, K. Scharnberg, L. Tewordt, and N. Schopohl. Effects of spin-orbit interaction and crystal fields on superconducting p -wave pair states and their collective excitations in cubic systems. *Phys. Rev. B* **34**, 3487 (1986).
- [89] H. Monien, K. Scharnberg, L. Tewordt, and N. Schopohl. Effects of spin-orbit interaction and crystal fields on superconducting p -wave pair states and their collective excitations in cubic systems. *J. Low Temp. Phys.* **65**, 13 (1986).
- [90] A. J. Leggett. Number-phase fluctuations in two-band superconductors. *Progress of Theoretical Physics* **36**, 901 (1966).
- [91] G. Blumberg, A. Mialitsin, B. S. Dennis, M. V. Klein, N. D. Zhigadlo, and J. Karpinski. Observation of Leggett's collective mode in a multiband MgB_2 superconductor. *Phys. Rev. Lett.* **99**, 227002 (2007).
- [92] M. V. Klein. Theory of Raman scattering from Leggett's collective mode in a multiband superconductor: Application to MgB_2 . *Phys. Rev. B* **82**, 014507 (2010).
- [93] P. W. Anderson. Plasmons, gauge invariance, and mass. *Phys. Rev.* **130**, 439 (1963).
- [94] J. Goldstone. Field theories with superconductor solutions. *Nuovo Cimento* **19**, 154 (1961).
- [95] P. Wölfle. Observability of order parameter collective modes in heavy fermion superconductors. *Physics Letters A* **119**, 40 (1986).

Bibliography

- [96] Wölfle, P. Collective modes in unconventional superconductors. *J. Low Temp. Phys.* **95**, 191 (1994).
- [97] R. Sooryakumar and M. V. Klein. Raman scattering by superconducting-gap excitations and their coupling to charge-density waves. *Phys. Rev. Lett.* **45**, 660 (1980).
- [98] P. B. Littlewood and C. M. Varma. Gauge-invariant theory of the dynamical interaction of charge density waves and superconductivity. *Phys. Rev. Lett.* **47**, 811 (1981).
- [99] P. J. Hirschfeld, W. O. Putikka, and P. Wölfle. Electromagnetic power absorption by collective modes in unconventional superconductors. *Phys. Rev. Lett.* **69**, 1447 (1992).
- [100] T. P. Devereaux and R. Hackl. Inelastic light scattering from correlated electrons. *Rev. Mod. Phys.* **79**, 175 (2007).
- [101] T. P. Devereaux and D. Einzel. Electronic raman scattering in superconductors as a probe of anisotropic electron pairing. *Phys. Rev. B* **51**, 16336 (1995).
- [102] T. P. Devereaux and D. Einzel. Erratum: Electronic Raman scattering in superconductors as a probe of anisotropic electron pairing. *Phys. Rev. B* **54**, 15547 (1996).
- [103] H.-Y. Kee, K. Maki, and C. H. Chung. Raman spectra of triplet superconductivity in Sr_2RuO_4 . *Phys. Rev. B* **67**, 180504 (2003).
- [104] H.-Y. Kee, K. Maki, and C. H. Chung. Raman spectra in chiral superconductors. *Physica B* **408**, 789 (2004).
- [105] M. Miura, S. Higashitani, M. Yamamoto, and K. Nagai. Raman spectra of spin-triplet superconductor Sr_2RuO_4 . *Physica B* **383**, 82 (2006).
- [106] D. Manske, C. T. Rieck, R. Das Sharma, A. Bock, and D. Fay. Screening of the B_{1g} Raman response in d -wave superconductors. *Phys. Rev. B* **56**, R2940 (1997).
- [107] M. V. Klein and S. B. Dierker. Theory of Raman scattering in superconductors. *Phys. Rev. B* **29**, 4976 (1984).
- [108] H. Monien and A. Zawadowski. Theory of Raman scattering with final-state interaction in high- T_c BCS superconductors: Collective modes. *Phys. Rev. B* **41**, 8798 (1990).
- [109] D. K. Morr and A. V. Chubukov. Resonant Raman scattering in antiferromagnets. *Phys. Rev. B* **56**, 9134 (1997).
- [110] M. C. Krantz and M. Cardona. Raman scattering by electronic excitations in semiconductors and in high T_c superconductors. *J. Low Temp. Phys.* **99**, 205 (1995).
- [111] T. Strohm and M. Cardona. Electronic Raman scattering in $\text{YBa}_2\text{Cu}_3\text{O}_7$ and other superconducting cuprates. *Phys. Rev. B* **55**, 12725 (1997).

- [112] L. Klam, D. Einzel, and D. Manske. Electronic Raman scattering in noncentrosymmetric superconductors. *Phys. Rev. Lett.* **102**, 027004 (2009).
- [113] L. V. Gasparov, P. Lemmens, N. N. Kolesnikov, and G. Güntherodt. Electronic Raman scattering in $Tl_2Ba_2CuO_{6+\delta}$: Symmetry of the order parameter, oxygen doping effects, and normal-state scattering. *Phys. Rev. B* **58**, 11753 (1998).
- [114] Y. Yanase and M. Sigrist. Superconductivity and magnetism in non-centrosymmetric system: application to $CePt_3Si$. *J. Phys. Soc. Jpn.* **77**, 124711 (2008).
- [115] Y. Yanase and M. Sigrist. Magnetic properties in non-centrosymmetric superconductors with and without antiferromagnetic order. *J. Phys. Soc. Jpn.* **76**, 124709 (2007).
- [116] G. D. Mahan. *Many-particle physics*. Kluwer Academic, Plenum Publ., New York (2000).
- [117] T. Ohkochi, T. Toshimitsu, H. Yamagami, S.-i. Fujimori, A. Yasui, Y. Takeda, T. Okane, Y. Saitoh, A. Fujimori, Y. Miyauchi, Y. Okuda, R. Settai, and Y. Ōnuki. Observation of itinerant Ce 4f electronic states in $CeIrSi_3$ studied by angle-resolved Ce 3d \rightarrow 4f resonance photoemission spectroscopy. *J. Phys. Soc. Jpn.* **78**, 084802 (2009).
- [118] S. A. Martucci. Symmetric convolution and the discrete sine and cosine transforms. *IEEE Trans. Signal Process.* **42**, 1038 (1994).
- [119] R. Settai, T. Takeuchi, and Y. Ōnuki. Recent advances in Ce-based heavy-fermion superconductivity and Fermi surface properties. *J. Phys. Soc. Jpn.* **76**, 051003 (2007).
- [120] K. V. Samokhin, E. S. Zijlstra, and S. K. Bose. $CePt_3Si$: An unconventional superconductor without inversion center. *Phys. Rev. B* **69**, 094514 (2004).
- [121] K. V. Samokhin, E. S. Zijlstra, and S. K. Bose. Erratum: $CePt_3Si$: An unconventional superconductor without inversion center [Phys. Rev. B **69**, 094514 (2004)]. *Phys. Rev. B* **70**, 069902 (2004).
- [122] S. Hashimoto, T. Yasuda, T. Kubo, H. Shishido, T. Ueda, R. Settai, T. D. Matsuda, Y. Haga, H. Harima, and Y. Ōnuki. The de Haas-van Alphen effect and the Fermi surface in $CePt_3Si$ and $LaPt_3Si$. *J. Phys.: Condens. Matter* **16**, L287 (2004).
- [123] R. Heid. private communications.
- [124] Y. Ōnuki, T. Yasuda, H. Shishido, S. Hashimoto, T. Ueda, R. Settai, T. D. Matsuda, Y. Haga, and H. Harima. Fermi surface properties of $CePt_3Si$ and $LaPt_3Si$. *Physica B* **359**, 368 (2005).
- [125] T. Takeuchi, T. Yasuda, M. Tsujino, H. Shishido, R. Settai, H. Harima, and Y. Ōnuki. Specific heat and de Haas-van Alphen experiments on the heavy-fermion superconductor $CePt_3Si$. *J. Phys. Soc. Jpn.* **76**, 014702 (2007).

Bibliography

- [126] V. P. Mineev and K. V. Samokhin. De Haas–van Alphen effect in metals without an inversion center. *Phys. Rev. B* **72**, 212504 (2005).
- [127] bilbao crystallographic server. <http://www.cryst.ehu.es>.
- [128] B. Meyer and C. Elsässer and F. Lechermann and M. Fähnle. FORTRAN90 program for mixed-basis-pseudopotential calculations for crystals. (*Max-Planck-Institut für Metallforschung, Stuttgart*).
- [129] R. Heid and K.-P. Bohnen. Linear response in a density-functional mixed-basis approach. *Phys. Rev. B* **60**, R3709 (1999).
- [130] N. W. Ashcroft and N. D. Mermin. *Solid state physics*. Brooks/Cole Thomson Learning, Singapore (2006).
- [131] B. Fåk, S. Raymond, D. Braithwaite, G. Lapertot, and J.-M. Mignot. Low-energy magnetic response of the noncentrosymmetric heavy-fermion superconductor CePt₃Si studied via inelastic neutron scattering. *Phys. Rev. B* **78**, 184518 (2008).
- [132] T. Willers, B. Fåk, N. Hollmann, P. O. Körner, Z. Hu, A. Tanaka, D. Schmitz, M. Enderle, G. Lapertot, L. H. Tjeng, and A. Severing. Crystal-field ground state of the noncentrosymmetric superconductor CePt₃Si: A combined polarized soft x-ray absorption and polarized neutron study. *Phys. Rev. B* **80**, 115106 (2009).
- [133] P. Aynajian, T. Keller, L. Boeri, S. M. Shapiro, K. Habicht, and B. Keimer. Energy gaps and Kohn anomalies in elemental superconductors. *Science* **319**, 1509 (2008).
- [134] S. V. Maleev. Polarized neutron scattering in magnets. *Phys. Usp.* **45**, 569 (2002).
- [135] T. Takimoto and P. Thalmeier. Triplet Cooper pair formation by anomalous spin fluctuations in non-centrosymmetric superconductors. *J. Phys. Soc. Jpn.* **78**, 103703 (2009).
- [136] S. Fujimoto. Magnetoelectric effects in heavy-fermion superconductors without inversion symmetry. *Phys. Rev. B* **72**, 024515 (2005).
- [137] D. Allender, J. W. Bray, and J. Bardeen. Theory of fluctuation superconductivity from electron-phonon interactions in pseudo-one-dimensional systems. *Phys. Rev. B* **9**, 119 (1974).
- [138] Michael E. Flatté. Kohn anomalies in superconductors. *Phys. Rev. B* **50**, 1190 (1994).
- [139] G.-H. Chen and M. E. Raikh. Small- q anomaly in the dielectric function and high-temperature oscillations of the screening potential in a two-dimensional electron gas with spin-orbit coupling. *Phys. Rev. B* **59**, 5090 (1999).
- [140] M. E. Raikh and G. H. Chen. Spin-orbit anomaly in the dielectric function of 2D electron gas. *Physica E* **6**, 783 (2000).

- [141] M. Pletyukhov and V. Gritsev. Screening in the two-dimensional electron gas with spin-orbit coupling. *Phys. Rev. B* **74**, 045307 (2006).
- [142] M. Pletyukhov and S. Konschuh. Charge and spin density response functions of the clean two-dimensional electron gas with Rashba spin-orbit coupling at finite momenta and frequencies. *Eur. Phys. J. B* **60**, 29 (2007).
- [143] J. Lindhard. On the properties of a gas of charged particles. *Matematisk-fysiske meddelelser* **28**, 1 (1954).
- [144] S. Baroni, S. de Gironcoli, A. Dal Corso, and P. Giannozzi. Phonons and related crystal properties from density-functional perturbation theory. *Rev. Mod. Phys.* **73**, 515 (2001).
- [145] P. B. Allen. Neutron spectroscopy of superconductors. *Phys. Rev. B* **6**, 2577 (1972).
- [146] Kröger, J. Electron-phonon coupling at metal surfaces. *Rep. Prog. Phys.* **69**, 899 (2006).
- [147] P. J. Hirschfeld, P. Wölfle, J. A. Sauls, D. Einzel, and W. O. Putikka. Electromagnetic absorption in anisotropic superconductors. *Phys. Rev. B* **40**, 6695 (1989).
- [148] M. Frigo and S. G. Johnson. The design and implementation of FFTW3. *Proceedings of the IEEE* **93**, 216 (2005).
- [149] M. Frigo and S. G. Johnson. <http://www.fftw.org>.
- [150] W. H. Press, S. A. Teukolsky, and W. T. Vetterling. *Numerical recipes*. Cambridge Univ. Press, New York (2007).
- [151] H. Eschrig. *Optimized LCAO method*. Springer, Berlin / Heidelberg (1989).

Acknowledgments

First of all, I want to thank Prof. Dr. Walter Metzner for the great opportunity to work on my thesis in his group at the Max–Planck–Institut für Festkörperforschung in Stuttgart. I appreciated the discussions, enjoyed the privilege of attending many workshops and conferences, and had a very nice time in his group. Many thanks go to my supervisor Dr. Dirk Manske for the choice of this very interesting topic and for his helpful advice. He encouraged me in all circumstances and always had an open ear for my problems. Furthermore, I want to thank my external supervisor Prof. Dr. Giniyat Khaliullin for the inspiring discussions in my PhD committee and I wish to thank Prof. Dr. Alejandro Muramatsu for co–refereeing this thesis.

In particular, I wish to thank Prof. Dr. Manfred Sigrist for the opportunity to participate and give a talk in his workshop about non–centrosymmetric superconductors. I am greatly thankful to be able to contribute a chapter in a book about “Physical properties of non–centrosymmetric superconductors” edited by Prof. Dr. Ernst Bauer and him. I enjoyed the discussions during the numerous mutual visits and I am looking forward to further collaboration in his group. Special thank is devoted to Dr. Dietrich Einzel, who supervised me during my diploma thesis. I learned from him the kinetic equation approach, which is also used in this thesis and appreciated in particular his proofreading of this thesis. Furthermore, I am thankful for the extensive discussions and his contributions to two, and hopefully many more, publications. Many thanks go to Dr. Rolf Heid, who provided the LDA calculations for the electron and phonon dispersions in this thesis.

Dr. Hans–Georg Libuda is gratefully acknowledged as the coordinator of the International Max Planck Research School for Advanced Materials. As a member of this research school, I had the opportunity to help in the organization of an internal workshop. I enjoyed numerous additional workshops, guided tours through different departments and institutes, additional lectures and supplementary help in all possible circumstances. Many thanks go to Prof. Dr. Manfred Fähnle and Prof. Dr. Jörg Wrachtrup for the opportunity to give a tutorial lesson in thermodynamic and solid state physics, respectively.

Furthermore, I wish to thank Dr. Philip M. R. Brydon and Dr. Andreas Schnyder for many helpful discussions and some inspiring ideas. I want to acknowledge Dr. Mohammed Bakr for the opportunity to provide a theoretical contribution to a publication. Many thanks go to Prof. Dr. Heinz Barentzen for group theoretical support and to Dr. Klaus Doll for some help about crystallographic questions. Furthermore, I wish to thank Prof. Dr. Johannes Waldmann for helpful remarks and ideas on how to calculate a convolution through a discrete trigonometric transform. Also, I would like to thank all members in the “Abteilung Metzner” and in the research school for the great atmosphere.

Finally, I would like to thank my parents for their support and also my grandmother for the accommodation during the last months at the Max–Planck–Institut.

Curriculum vitae

Name: Ludwig Klam
Geburtsdaten: 26.07.1980 in Heidenheim an der Brenz

AUSBILDUNG

- 05/2007 – 10/2010 Doktorarbeit zum Thema „Unconventional properties of non-centrosymmetric superconductors“ am Max-Planck-Institut für Festkörperforschung, Stuttgart
- 10/2001 – 11/2006 Diplomstudiengang Physik an der TU München mit Diplomarbeit zum Thema „Transport und Ramanstreuung in unkonventionellen Supraleitern“ am Walther-Meißner-Institut, Garching
- 07/2000 – 04/2001 Grundwehrdienst (Luftwaffe)
- 1991 – 2000 Willibald-Gymnasium Eichstätt

TÄTIGKEITEN IN DER LEHRE

- WS 2008/09 Betreuung einer Übungsgruppe zur Vorlesung „Theoretische Physik 6 – Thermostatistik“ an der Universität Stuttgart bei Prof. Dr. Föhnle
- SS 2008 Betreuung einer Übungsgruppe zur Vorlesung „Experimentalphysik 6 – Festkörperphysik“ an der Universität Stuttgart bei Prof. Dr. Wrachtrup

PREISE UND AUSZEICHNUNGEN

- 5/2007 Stipendium der International Max Planck Research School for Advanced Materials (IMPRS-AM)
- 2000 Landessieger Bayern Jugend forscht (Physik) zum Thema: „Simulation von Interferenzen an speziellen Gittern“
- 1999 1. Preis Bundeswettbewerb Mathematik
- 1997 3. Preis Regionalwettbewerb Jugend Musiziert

SONSTIGES

- 2009 Doktorandensprecher der Max-Planck-Institute (FKF und MF)
- 2008 Übungsgruppenleiter am Hochschulsport in Hohenheim

